ANALYSIS OF A THREE-DIMENSIONAL RAILWAY VEHICLE-TRACK SYSTEM AND DEVELOPMENT OF A SMART WHEELSET

Md. Rajib Ul Alam Uzzal

A thesis

In the Department of

Mechanical and Industrial Engineering

Presented in Partial Fulfillment of the Requirements

for the Degree of Doctor of Philosophy at

Concordia University

Montreal, Quebec, Canada

March 2012

© Md. Rajib Ul Alam Uzzal, 2012

ABSTRACT

ANALYSIS OF A THREE-DIMENSIONAL RAILWAY VEHICLE-TRACK SYSTEM AND DEVELOPMENT OF A SMART WHEELSET

Md. Rajib Ul Alam Uzzal
Concordia University, 2012

Wheel flats are the sources of high magnitude impact forces at the wheel-rail interface, which can induce high levels of local stresses leading to fatigue damage, and failure of various vehicle and track components. With demands for increased load and speed, the issue of wheel flats and a strategy for effective maintenance and in-time replacement of defective wheels has become an important concern for heavy haul operators. A comprehensive coupled vehicle-track model is thus required in order to predict the impact forces and the resulting component stresses in the presence of wheel flats.

This study presents the dynamic response of an Euler- Bernoulli beam supported on two-parameter Pasternak foundation subjected to moving load as well as moving mass. Dynamic responses of the beam in terms of normalized deflection and bending moment have been investigated for different velocity ratios under moving load and moving mass conditions. The effect of moving load velocity on dynamic deflection and bending moment responses of the beam have been investigated. The effect of foundation parameters such as, stiffness and shear modulus on dynamic deflection and bending moment responses have also been investigated for both moving load and moving mass at constant speeds.

This dissertation research concerns about modeling of a three-dimensional railway vehicle-track model that can accurately predict the wheel-rail interactions in the presence of wheel defects. This study presents a three-dimensional track system model using two Timoshenko beams supported on discrete elastic supports, where the sleepers are considered as rigid masses, and the rail pad and ballast as spring-damper elements. The vehicle system is modeled as a three-dimensional 17- DOF lumped mass model comprising a full car body, two bogies and four wheelsets. The railway track is modeled as a pair of three-dimensional flexible beams that considers two parallel Timoshenko beams periodically supported by lumped masses representing the sleepers.

The wheel-rail contact is modeled using nonlinear Hertzian contact theory. The developed model is validated with the existing measured data and analytical solutions available in literature. The nonlinear model is then employed to investigate the wheel-rail impact forces that arise in the wheel-rail interface due to the presence of single as well as multiple wheel flats.

The effects of single and multiple wheel flats on the responses of vehicle and track components in terms of displacements and acceleration responses are investigated for both defective wheel and the flat-free wheel. The characteristics of the bounce, pitch and roll motions of the bogie due to a single wheel flat are also investigated. The study shows that nonlinear railpad and ballast model gives better prediction of the wheel-rail impact force than that of the linear model when compared with the experimental data. The results clearly show that presence of wheel flat within the same wheelset has significant effect on the impact force, displacement and acceleration responses of that wheelset.

This study further presents the modeling of a MEMS based accelerometer in order to detect the presence of a wheel flat in the railway vehicle. The proposed accelerometer can survive in a dynamic shock environment with acceleration up to ±150g. Simulations of the accelerometer are performed under various operating conditions in order to determine the optimum configuration.

This thesis is dedicated with all my heart to

my beloved parents, Md. Moksed Ali, and Most. Rawshan Ara Begum, whose continuous support and encouragement throughout my educational career.

ACKNOWLEDGEMENTS

I would like to thank my co-supervisors Dr. R. B. Bhat and Dr. A. K. W. Ahmed for their continued intellectual guidance, encouragement throughout the course of this research. I would also like to take this opportunity to express my gratitude to Dr. S. Rakheja for the advice I received from him towards the scope and direction of this dissertation.

I would also like to thank my examination committee members for their assistance and time during the course of this work, in particular, Dr. I. Stiharu. Special thanks are due to Canadian National (CN) Railway, Quebec Govt. Transportation Dept. and Concordia University for their financial support throughout the course of this dissertation.

My eternal thanks and gratitude to my parents-in-law, sister and sister-in-law for their moral support made this achievement possible. I would also like to express my deepest gratitude to my wife, Syeda Rubyat Shahid, for her understanding, encouragement and limitless patience during this study. Thanks to my wonderful baby boy, Razeen Alam, who has been one of the sources of inspiration in completing this thesis. I am also thankful to all my friends in Concordia, specially, Santosh, Suresh, Saeedi and Azadeh for their help and support.

Above all, I thank to Almighty Allah for giving me the strength to complete this research.

TABLE OF CONTENTS

CHAPTER 1

INTRODUCTION AND LITERATURE REVIEW

CHAPTER 2

STEADY STATE RESPONSE OF ELASTICALLY SUPPORTED CONTINUOUS BEAM UNDER A MOVING LOAD/MASS

CHAPTER 3

VEHICLE-TRACK SYSTEM MODEL AND ITS NATURAL FREQUENCIES

CHAPTER 4

MODEL VALIDATION AND DYNAMIC RESPONSE OF VEHICLE-TRACK SYSTEM DUE TO WHEEL FLAT

CHAPTER 5

IMPACT RESPONSE DUE TO MULTIPLE WHEEL FLATS

CHAPTER 6

DEVELOPMENT OF A SMART WHEELSET

CHAPTER 7

MODELING OF A MEMS BASED ACCELEROMETER FOR AUTOMATIC DETECTION OF WHEEL FLAT

CHAPTER 8

CONCLUSIONS AND RECOMMENDATIONS

LIST OF FIGURES

LIST OF TABLES

NOMENCLATURE

SYMBOL	**DESCRIPTION**
c	Damping coefficient per unit length of the beam (N.s/m^2)
d_V	Displacement vector of the vehicle subsystem (m)
$\dot{\mathrm{d}}_\mathrm{V}$	Velocity vector of the vehicle subsystem (m/s)
$\ddot{\mathrm{d}}_\mathrm{V}$	Acceleration vector of the vehicle subsystem (m/s^2)
d_T	Displacement vector of the track subsystem (m)
$\dot{\mathrm{d}}_\mathrm{T}$	Velocity vector of the track subsystem (m/s)
$\ddot{\mathrm{d}}_\mathrm{T}$	Acceleration vector of the track subsystem (m/s^2)
g	Gravitational acceleration (kg. m/s^2)
g_{ap}	Distance between two adjacent electrodes (m)
j	Number of wheels considered in the vehicle model (j=1-8)
k	Number of rail mode corresponding to the sleeper position (k =1, … K)
k_1	Shear coefficient of beam (N)
k_f	Foundation stiffness per unit length (N/m^2)
k_r	Timoshenko shear coefficient of rail beam
l_b	Half of the wheelset distance in longitudinal direction (m)
l_c	Half of the car bogie distance in longitudinal direction (m)
l_p	half of the primary suspension distance in lateral direction (m)
l_s	Half of the secondary suspension distance in lateral direction (m)

m	Total mass of the accelerometer (kg)
$\overline{m}$	Unit mass of the beam element (kg/m)
m_r	Rail mass per unit length (kg/m)
$m_{central}$	Mass of the central plate of the accelerometer (kg)
$m_{fingers}$	Mass of the fingers of the accelerometer (kg)
$q_k(t)$	k th mode displacement of beam
$\dot{q}_k(t)$	k th mode velocity of beam
$\ddot{q}_k(t)$	k th mode acceleration of beam
$r(t)$	Wheel flat profile function
$\overline{r}$	Radius of gyration of the beam cross-section (m)
v	Vehicle speed (m/s)
x	Longitudinal coordinate along the length of the beam (m)
x_i	Position of the sleeper ($i = 1, 2, 3,\ldots\ldots N$)
x_{Gj}	Position of the wheel (j=1-8)
A	Rail cross sectional area,
A_0	Overlap area between the fingers in the sensing region (m^2)
C_{bi}	Ballast damping at the location of ith sleeper (N-s/m), ($i = 1, 2, 3,\ldots\ldots N$)
C_H	Non-linear Hertzian spring constant (N/m$^{3/2}$)

C_p	Primary suspension damping (Ns/m)
C_{pri}	Railpad damping at the location of ith sleeper (N-s/m), ($i = 1, 2, 3, \ldots\ldots N$)
C_s	Secondary suspension damping (Ns/m)
C_v	Damping matrix of the vehicle (N-s/m),
D_f	Flat depth (mm)
E	Elastic modulus of rail (N/ m^2)
EI	Rail bending stiffness (N-m^2)
E_P	Young’s modulus of polysilicon (N/m^2)
F	Electrostatic force (N)
F_{RSi}	Rail/sleeper contact force ($i = 1, 2, 3, \ldots\ldots N$)
F_{VT}	Interface force vector between the vehicle and track (N)
G	Shear modulus of the rail (N/m^2)
H	Height of the polysilicon beam (m)
I	Rail second moment of area (m^4)
J_{bx}	Roll moment of inertia of the bogie (kg-m^2)
J_{by}	Pitch moment of inertia of the bogie (kg-m^2)
J_{cx}	Roll moment of inertia of the car body (kg-m^2)
J_{cy}	Pitch moment of inertia of the car body (kg-m^2)

J_{wx}	Roll moment of inertia of the wheelset (kg-m^2)
K	Total number of modes of the rail
K_{bi}	Ballast stiffness at the location of *i*th sleeper (N/m), ($i = 1, 2, 3, \ldots\ldots N$)
K_C	Spring constant of the accelerometer (N/m)
K_p	Primary suspension stiffness (N/m)
K_{pri}	Railpad stiffness at the location of *i*th sleeper (N/m), ($i = 1, 2, 3, \ldots\ldots N$)
K_s	Secondary suspension stiffness (N/m)
K_v	Stiffness matrix of the vehicle (N/m)
L	Total length of the rail (m)
L_f	Flat length (mm)
L_s	Half of the lateral distance between left and right end railpads (m)
M	Sectional bending moment acting on beam element (N-m)
M_{b1}	Front bogie mass (kg)
M_{b2}	Rear bogie mass (kg)
M_c	Car body mass (kg)
M_{si}	Sleeper mass of the *i*th sleeper (kg), ($i = 1, 2, 3, \ldots\ldots N$)
M_v	Mass matrix of the vehicle (kg)
M_w	Mass of the wheelset (kg)

N	Number of the sleepers/ballasts
$N_{\psi}(k,x)$	k th mode shape functions of the rotation of the rail
$N_{z}(k,x)$	k th mode shape functions of the vertical deflection of the rail
P_a	Constant axial force acting on beam element (N)
P_{WRj}	Contact forces developed at the wheel-rail interface (N), (j=1-8)
P_{WRlj}	Contact forces developed at the left wheel-rail interface (N), (j=1-4)
P_{WRrj}	Contact forces developed at the right wheel-rail interface (N), (j=1-4)
$P\delta(x-vt)$	Moving load per unit length (N/m)
R	Wheel radius (m)
$\overline{R}$	Rotary inertial moment of the beam element (kg-m^2)
U	Sectional shear force acting on beam element (N)
V	Potential difference between two electrodes (volt)
V_0	Output voltage to the electrical circuit of the accelerometer (Volt)
V_C	Volume of the central plate of the accelerometer (m^3)
V_{pi}	Pull in voltage (Volt)
V_s	Input voltage to the electrical circuit of the accelerometer (Volt)
W	Width of the polysilicon beam (m)
W_C	Energy stored into the capacitor (Joules)

$Y(x)$	Mode shape function
Y_k	k th rail mode shape
$Z_0(t)$	Wheel/rail irregularities function
Z_{b1}	Vertical displacement of the front bogie (m)
$\dot{Z}_{b1}$	Vertical velocity of the front bogie (m/s)
$\ddot{Z}_{b1}$	Vertical acceleration of the front bogie (m/s^2)
Z_{b2}	Vertical displacement of the rear bogie (m)
$\dot{Z}_{b2}$	Vertical velocity of the rear bogie (m/s)
$\ddot{Z}_{b2}$	Vertical acceleration of the rear bogie (m/s^2)
Z_c	Vertical displacement of the car body (m)
$\dot{Z}_c$	Vertical velocity of the car body (m/s)
$\ddot{Z}_c$	Car body acceleration (m/s^2)
$Z_k(t)$	k th mode vertical displacement of the rail
$Z_{rl}(x,t)$	Vertical displacement of the left rail beam (m)
$Z_{rr}(x,t)$	Vertical displacement of the right rail beam (m)
$Z_{sli}(t)$	Vertical displacement of the ith sleeper at the left end pad location (m), (i = 1, 2, 3,…… N)
$\dot{Z}_{sli}(t)$	Vertical velocity of the ith sleeper at the left end pad location (m/s), (i = 1, 2,

	3,…… N)
$Z_{sri}(t)$	Vertical displacement of the ith sleeper at the right end pad location (m), ($i = 1, 2, 3,\ldots\ldots N$)
$\dot{Z}_{sri}(t)$	Vertical velocity of the ith sleeper at the right end pad location (m/s), ($i = 1, 2, 3,\ldots\ldots N$)
$Z_{si}(t)$	Vertical displacement of the ith sleeper (m), ($i = 1, 2, 3,\ldots\ldots N$)
$\dot{Z}_{si}(t)$	Vertical velocity of the ith sleeper (m/s), ($i = 1, 2, 3,\ldots\ldots N$)
$\ddot{Z}_{si}$	Vertical acceleration of the ith sleeper (m/s), ($i = 1, 2, 3,\ldots\ldots N$)
Z_{w1}	Vertical displacement of the 1st wheelset (m)
$\dot{Z}_{w1}$	Vertical velocity of the 1st wheelset (m/s)
$\ddot{Z}_{w1}$	Vertical acceleration of the 1st wheelset (m/s^2)
Z_{w2}	Vertical displacement of the 2nd wheelset (m)
$\dot{Z}_{w2}$	Vertical velocity of the 2nd wheelset (m/s)
$\ddot{Z}_{w2}$	Vertical acceleration of the 1st wheelset (m/s^2)
Z_{w3}	Vertical displacement of the 3rd wheelset (m)
$\dot{Z}_{w3}$	Vertical velocity of the 3rd wheelset (m/s)
$\ddot{Z}_{w3}$	Vertical acceleration of the 3rd wheelset (m/s^2)
Z_{w4}	Vertical displacement of the 4th wheelset (m)

$\dot{Z}_{w4}$	Vertical velocity of the 4th wheelset (m/s)
$\ddot{Z}_{w4}$	Vertical acceleration of the 4th wheelset (m/s^2)
Z_{wlj}	Vertical displacement of the left wheel for a particular Wheelset, (j=1-4)
Z_{wrj}	Vertical displacement of the right wheel for a particular Wheelset, (j=1-4)
δ	Dirac delta function
ε_0	Permittivity of the free space (F/m)
η	Shear distortion of the beam element (m)
θ_{b1}	Pitch angular displacement of the front bogie (rad)
$\dot{\theta}_{b1}$	Pitch angular velocity of the front bogie (rad/s)
$\ddot{\theta}_{b1}$	Pitch angular acceleration of the front bogie (rad/s^2)
θ_{b2}	Pitch angular displacement of the rear bogie (rad)
$\dot{\theta}_{b2}$	Pitch angular velocity of the rear bogie (rad/s)
$\ddot{\theta}_{b2}$	Pitch angular acceleration of the rear bogie (rad/s^2)
θ_c	Pitch angular displacement of the car body (rad)
$\dot{\theta}_c$	Pitch angular velocity of the car body (rad/s)
$\ddot{\theta}_c$	Pitch angular acceleration of the car body (rad/s^2)
ρ	Rail density (kg/m^3)
ρ_C	Density of the central plate of the accelerometer (kg/m^3)

ρ_r	Unit mass of the beam on Pasternak foundation (kg/m)
ϕ_{b1}	Roll angular displacement of the front bogie (rad)
$\dot{\phi}_{b1}$	Roll angular velocity of the front bogie (rad/s)
$\ddot{\phi}_{b1}$	Roll angular acceleration of the front bogie (rad/s^2)
ϕ_{b2}	Roll angular displacement of the rear bogie (rad)
$\dot{\phi}_{b2}$	Roll angular velocity of the rear bogie (rad/s)
$\ddot{\phi}_{b2}$	Roll angular acceleration of the rear bogie (rad/s^2)
ϕ_c	Roll angular displacement of the car body (rad)
$\dot{\phi}_c$	Roll angular velocity of the car body (rad/s)
$\ddot{\phi}_c$	Roll angular acceleration of the car body (rad/s^2)
$\phi_{si}(t)$	Roll angular displacement of the *i*th sleeper (rad), ($i = 1, 2, 3, \ldots\ldots N$)
$\dot{\phi}_{si}(t)$	Roll angular velocity of the *i*th sleeper (rad/s), ($i = 1, 2, 3, \ldots\ldots N$)
$\ddot{\phi}_{si}$	Roll angular acceleration of the *i*th sleeper (rad/s), ($i = 1, 2, 3, \ldots\ldots N$)
ϕ_{w1}	Roll angular displacement of the 1st wheelset (rad)
ϕ_{w2}	Roll angular displacement of the 2nd wheelset (rad)
ϕ_{w3}	Roll angular displacement of the 3rd wheelset (rad)
ϕ_{w4}	Roll angular displacement of the 4th wheelset (rad)

$\dot{\phi}_{w1}$	Roll angular velocity of the 1st wheelset (rad/s)
$\dot{\phi}_{w2}$	Roll angular velocity of the 2nd wheelset (rad/s)
$\dot{\phi}_{w3}$	Roll angular velocity of the 3rd wheelset (rad/s)
$\dot{\phi}_{w4}$	Roll angular velocity of the 4th wheelset (rad/s)
$\ddot{\phi}_{w1}$	Roll angular acceleration of the 1st wheelset (rad/s^2)
$\ddot{\phi}_{w2}$	Roll angular acceleration of the 2nd wheelset (rad/s^2)
$\ddot{\phi}_{w3}$	Roll angular acceleration of the 3rd wheelset (rad/s^2)
$\ddot{\phi}_{w4}$	Roll angular acceleration of the 4th wheelset (rad/s^2)
ψ	Rotational angle of the beam element (rad)
ω	Natural frequency of the rail beam (rad/s)
ω_0	Resonant frequency of the accelerometer (rad/s)
ω_c	Cut-off frequency (rad/s)
ω_{di}	Damped natural frequency of the i'th component of the vehicle (rad/s), (i = 1, 2,…17)
ω_{ni}	Natural frequency of the i'th component of the vehicle (rad/s), (i = 1, 2,…17)
Δz	Wheel-rail overlap in vertical direction
$\Psi_k(t)$	k th mode rotation of the rail

CHAPTER 1

INTRODUCTION AND LITERATURE REVIEW

1.1 INTRODUCTION

Railway transportation is an efficient means of conveyance of passengers and goods. It is safe, economical and environment friendly too. Canada has one of the largest rail networks in the world with over 48,000 km of track, used primarily for freight handling [1]. Association of American Railroads (AAR) and Transport Canada regulations, standards and programs work to make railway system safer, secure, accessible, competitive and more environmentally responsible. In Canada, there are two major transcontinental freight railway systems, the Canadian National (CN) and Canadian Pacific (CP) Railway. With highest revenue and large physical size of its rail network, Canadian National (CN) is the largest railway in Canada spanning from Atlantic coast in Nova Scotia to Pacific coast in British Columbia. In a very recent announcement, the Association of American Railroads (AAR) has stated that U.S. freight railroads are planning to spend a record $12 billion on capital improvements in year 2011 whereas it was $10.7 billion in 2010 [2]. According to Rail Association of Canada (RAC), Canada spends approximately $9 billion per year in railway sector [3]. Study shows that Rail system moves over 70 million people and 75 per cent of all surface goods every year in Canada. Furthermore, it is growing throughout Canada every year for its economical and environment friendly operation and its more than 35,000 employees help provide safe and secure access to national and international markets for its customers, enabling Canada to successfully grow and compete in the 21st century [3].

In typical North American freight cars, the car body is supported on a pair of trucks or bogies. In a typical freight truck, as shown in Fig. 1.1, the wheelset to side frame connection consists of only a bearing and bearing adapter with associated friction. The lateral and yaw motions of the wheelsets relative to the side frames are thus generally very small. The elastomeric pads between the bearing adapter and the sideframe, however, form the primary suspension, whose stiffness is usually considered in the modeling process. The bolster is connected to the sideframes by a combination of vertical springs, as shown, in parallel with the friction plates, which constitute the secondary suspension. The lateral motion is restricted by the bolster gibs. The dry friction at the centerplate together with the stiffness of continuous contact with the side bearings resists the truck rotation relative to the centerplate.

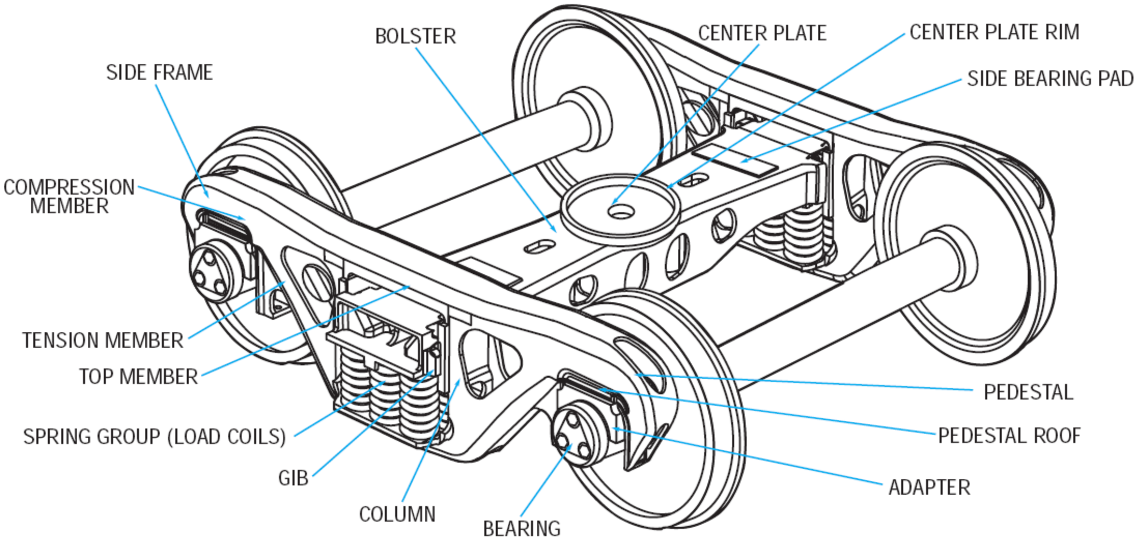

Fig. 1.1: A three-piece freight car truck

The conventional railway track structure consists of various discrete subsystem layers representing the rails, sleepers, railpads, fasteners, ballast, sub-ballast, and the sub-grade. Rails are connected to the sleepers through rail-pads and fasteners, which are supported by the ballast. The ballast bed rests on a sub-ballast layer, which forms the transition layer to the subgrade. The different layers of the track structure are shown in Fig. 1.2. The modern rail is made of steel and its cross section is derived from an I-profile that serves as a carrier of the vertical load of the train that is distributed over the sleepers. Railpads are usually synthetic materials to provide some cushioning effect between the rail and the sleeper. The properties of the pads affect the overall track stiffness, while soft railpads attenuate the high frequency vibration and permit larger deflection due to load. The modeling of the track structure thus necessitates identification of appropriate parameters of the railpad, apart from other structural layers.

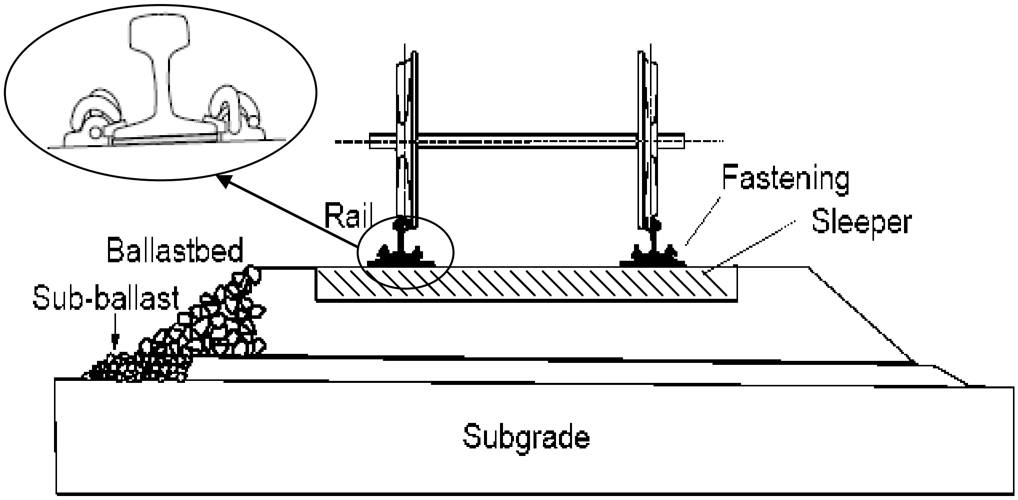

Fig. 1.2: Various layers of the track structure

1.2 LITERATURE REVIEW

The dynamic wheel-rail interactions in the presence of wheel/rail defects require accurate characterization of the complex wheel-rail contact model particularly in the presence of interface defects. With the significant increase of train speed and axle load, the vibrations of the coupled vehicle and track system due to a single or multiple wheel flats are further intensified adversely affecting the safe operation of trains. Furthermore, the presence of nonlinearity in between the wheel-rail contact points and the track components makes the analysis more complex. In order to analyze the railway coupled vehicle-track interaction in the presence of wheel/rail defects, numerous studies have been carried out to date. These studies include both analytical and experimental analyses of vehicle-track interactions in the presence of wheel/rail defects. A vast majority of these studies are analytical which incorporate one or two-dimensional vehicle and track models in order to predict wheel-rail impact force due the presence of wheel and rail defects [4-18]. A very few studies have been carried out field measurement of impact loads and accelerations caused by the wheel and rail defects [4, 19, 20, 21]. A comprehensive review on different types of dynamic vehicle and track models and the sources of the wheel-rail impact forces has been presented by Knothe and Grassie [22]. Another comprehensive review on the effects of wheel defects on vehicle and track components has been presented by Barke and Chiu [23]. In order to have accurate prediction through the analysis, detailed study of the modeling of vehicle, track and wheel/rail defects is required. The relevant reported studies, grouped under relevant topics, are thus reviewed and discussed in the following subsections in order to build essential background and to formulate the scope of this dissertation research.

1.2.1 Railway beam under moving load and mass:

The dynamic behavior of beams on elastic foundations subjected to moving loads or masses has been investigated by many researchers, especially in Railway Engineering. The modern trend towards higher speeds in the railways has further intensified the research in order to accurately predict the vibration behavior of the railway track. These studies mostly considered the Winkler elastic foundation model that consists of infinite closely-spaced linear springs subjected to a moving load [24-28]. These models are also termed as one-parameter models [29]. These one-parameter models, as shown in Fig. 1.3, have been extensively employed in early studies to investigate the vibration of beams subjected to moving loads. In case of moving mass, studies are limited to single [30-42] or multiple span [43, 44] beams with different boundary conditions and without any elastic supports. A very few studies considered one parameter foundation model for prediction of beam responses subjected to a moving mass [45-47]. However, these one parameter models do not accurately represent the continuous characteristics of practical foundations since it assumes no interaction among the lateral springs. Moreover, it also results in overlooking the influence of the soil on either side of the beam [48].

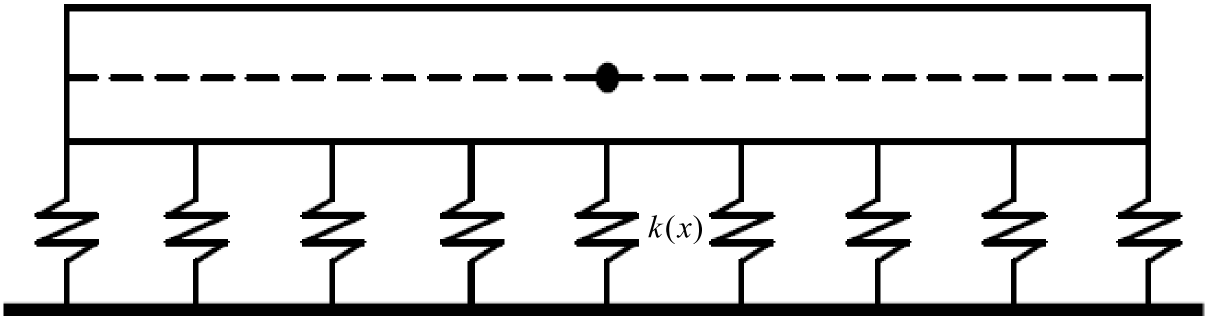

Fig. 1.3: Beam structure resting on Winkler foundation.

In order to overcome the limitations of the one parameter model, several two-parameter models, also known as Pasternak models, have been proposed for the analysis of the dynamic behavior of beams under moving loads [49-51]. A two-parameter Pasternak foundation model excited by a moving force is shown in Fig. 1.4. All of these models are mathematically equivalent and differ only in foundation parameters. However, dynamic response of the beam supported on a two parameter foundation model under a moving mass is not investigated so far. Moreover, the effects of shear modulus and foundation stiffness on deflection and bending moment responses of the beam supported by Pasternak foundation have also never been investigated in the presence of a moving mass.

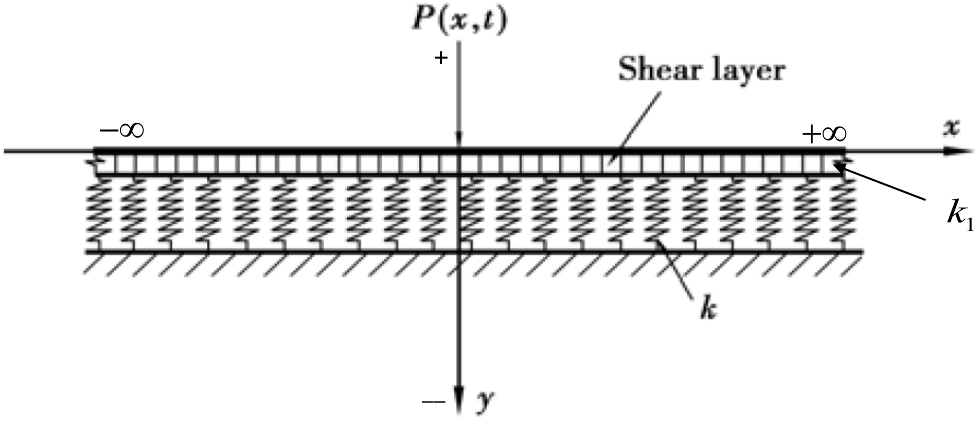

Fig. 1.4: Infinite beam model on Pasternak foundation subjected to a moving load [50].

In order to capture the distributed stresses accurately, a three-parameter model has been developed for cohesive and non-cohesive soil foundations [52-54]. This model, as shown in Fig. 1. 5, offers the continuity in the vertical displacements at the boundaries between the loaded and the unloaded surfaces of the soil [55]. In the analysis of vibration of beams under the moving loads and masses, the beam has been modeled as either a Timoshenko beam [30, 47, 48, 56-61], or an Euler-Bernoulli beam [24-29, 32-38, 43, 50, 51, 62- 64]. The analytical solution of the vibration of infinite beams under the moving load has received considerable attention by researchers [24, 28, 51, 65, 66]. In the case of two-parameter model, studies are scarce due to the model complexity and difficulties in estimating parameter values [51, 65-67]. In recent years, a growing interest on the vibration of the beam under moving load arises in railway industry because of the use of beam type structure as simplified physical model for railway track and pavements [26, 28, 68].

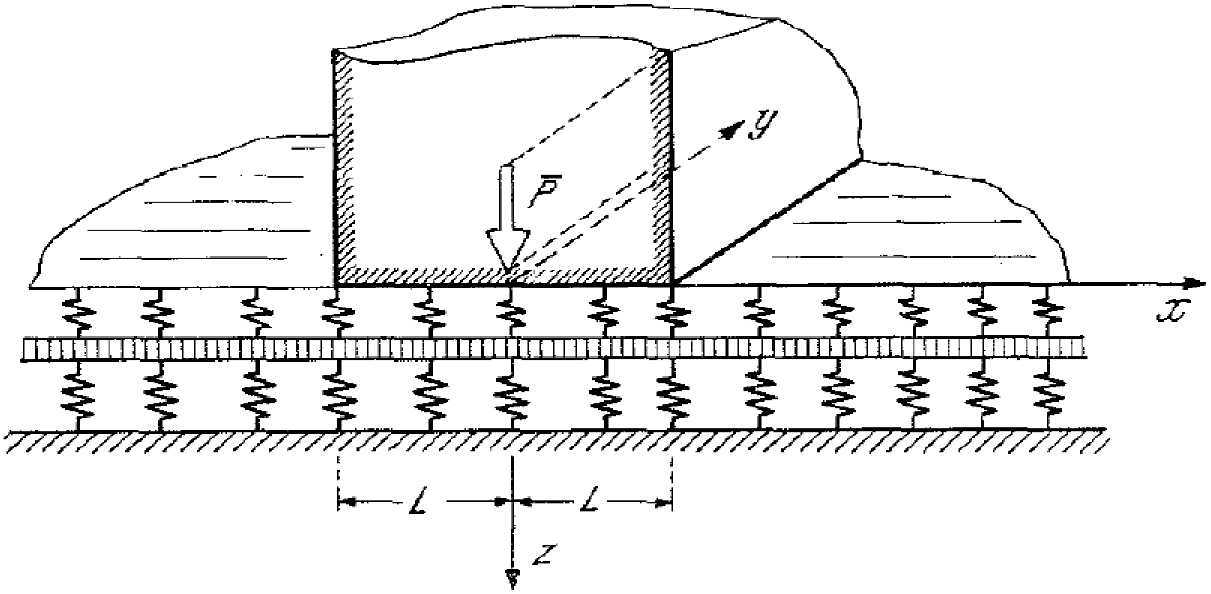

Fig. 1. 5: A three-parameter foundation model developed by Kerr [52]

Apart from the one-, two- or three- parameter foundation models, poroelastic half space model of the foundation is also common in the dynamic analysis of a beam due to a moving oscillating load [69, 71], or moving point load [70, 72-76]. These half-space models can be single layer [71, 72, 74-76], or multiple layers [70, 73]. Responses of the beams in terms of displacements [69-76], bending moments [70], accelerations [71] and shear force [70] have been analyzed in these studies. Studies with multilayer half space show that the response calculated for the multi-layered case exhibits higher frequencies and larger amplitudes than the response obtained for a uniform half-space [70, 73].

1.2.2 Vehicle system model:

In analyzing the interaction between the train and the track, the vehicle system can be modeled as one-dimensional, two-dimensional, or three-dimensional model. The simplest vehicle model is a single DOF one dimensional model, which considers a single wheel with static force representing the static load due to the car and bogie where the contact between the wheel and rail is maintained by either linear or non-linear spring. This model is shown in Fig. 1. 6. This model has been applied in a number of published studies concerned with dynamic wheel-rail interactions [5, 18, 19], and is considered sufficient for high frequency vibration analysis considering the interaction between the wheel and rail with surface irregularities. However, this model is insufficient in a number of scenarios, namely: (i) to evaluate the effects of vehicle suspensions on the impact loads caused by a wheel flat; (ii) to analyze the contributions due to pitch and roll motions of the vehicle on wheel-rail impact load; and (iii) to investigate the effect of multiple defects in different wheelsets.

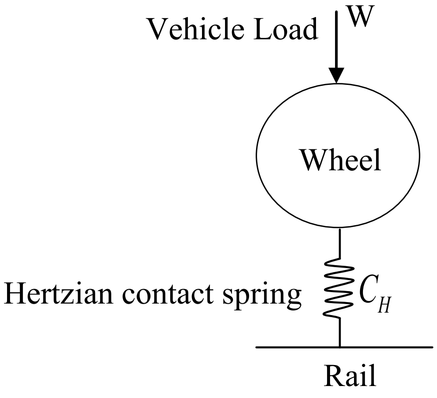

Fig. 1. 6: A single DOF one dimensional vehicle model

Several two- or three- DOF vehicle models have been evolved those employ car, bogie, a single wheelset, and primary and secondary suspensions [4, 6, 7]. A three-DOF one-dimensional model is shown in Fig. 1.7. This model permits the analysis of influence of car body and suspension on the wheel-rail impact loads, while the pitch and roll dynamic responses could not be evaluated.

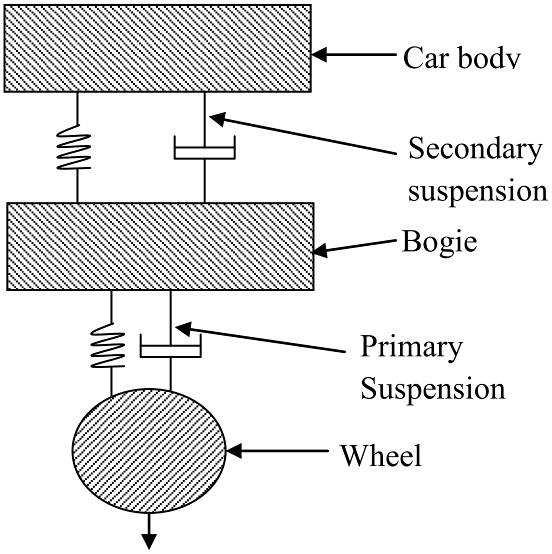

Fig. 1. 7: A three-DOF one-dimensional vehicle model [4]

Alternatively, two-dimensional or in-plane models those include half of the car body and two bogies and four wheelsets have been most widely formulated and applied for studies on wheel-rail interactions. A two-dimensional model can be either a pitch-plane or a roll-plane model. A vast majority of the studies dealing with the two-dimensional vehicle model employ the pitch-plane vehicle model in order to incorporate the pitch effect of the vehicle on wheel-rail impact force [8, 9, 10, 77], while some studies employ roll-plane vehicle models in order to incorporate the influence of the roll dynamics [11, 12]. A four-DOF two-dimensional pitch plane vehicle model, as shown in Fig. 1.8, has been developed by Nielsen and Igeland [77] in order to study the influence of wheel and rail imperfections on vehicle-track interaction. This model has been further employed by Dong [8] and Cai [9] in order to simulate the vehicle-track interaction under wheel defects.

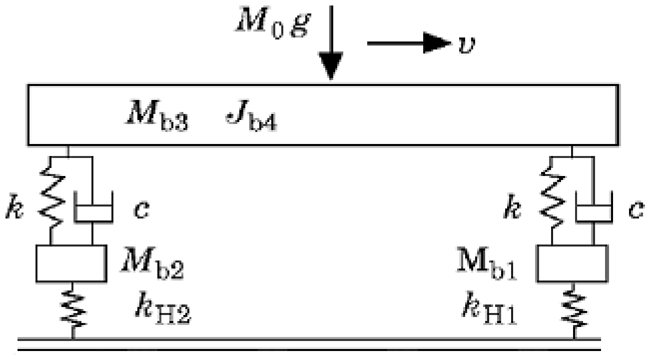

Fig. 1. 8: Four-DOF two-dimensional pitch-plane vehicle model [77].

Unlike the pitch-plane vehicle model, little effort has been made to develop a roll- plane two-dimensional vehicle model in order to study the contribution due to roll dynamics. A two-dimensional vehicle model in the roll plane consists of a wheelset, side frame and car body connected together through the primary and secondary suspension, as shown in Fig. 1.9 [11, 78]. These models permit the study of effects of wheel defects within the opposite wheels.

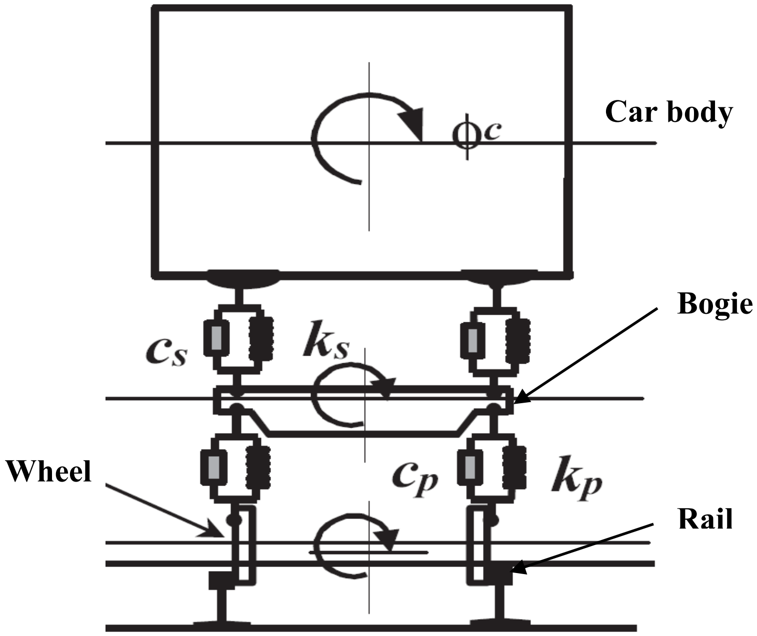

Fig. 1. 9: A typical roll-plane vehicle model with several DOF [11]

Several two-dimensional vehicle models have also been formulated with 10-12 DOF that consist of half bogie and a quarter of the car body weight and include the pitch motion of both the car body and bogie [13, 15]. Such a model would be sufficient to analyze the dynamic interaction between the leading and trailing bogie and wheels and effect of the cross wheel defects. However, contributions due to either pitch or roll motion of the car body and bogies have to be neglected in such models.

A number of comprehensive three-dimensional vehicle models have been developed in recent years [16, 79, 80] incorporating a full or half of the car body, two bogies, and two wheelsets, as shown in Fig. 1. 10. Such models permit dynamic coupling between the leading and trailing bogies. These vehicle models are employed to investigate the wheel-rail impact force and track component force due to rail joints [81], sleeper voids [82], curved tracks [83, 84, 85, 86], random track irregularities [87, 88, 89], wheel flats [90], rail corrugation [91] and out-of-roundness (OOR) of wheel [92, 93]. Several three-dimensional railway vehicle-track models have also been developed in order to study vehicle-track-bridge interactions in the absence of wheel/rail defects [94, 95, 96]. However, the effects of multiple wheel flats on the wheel-rail impact forces and their consequences have never been investigated with these full three-dimensional vehicle models.

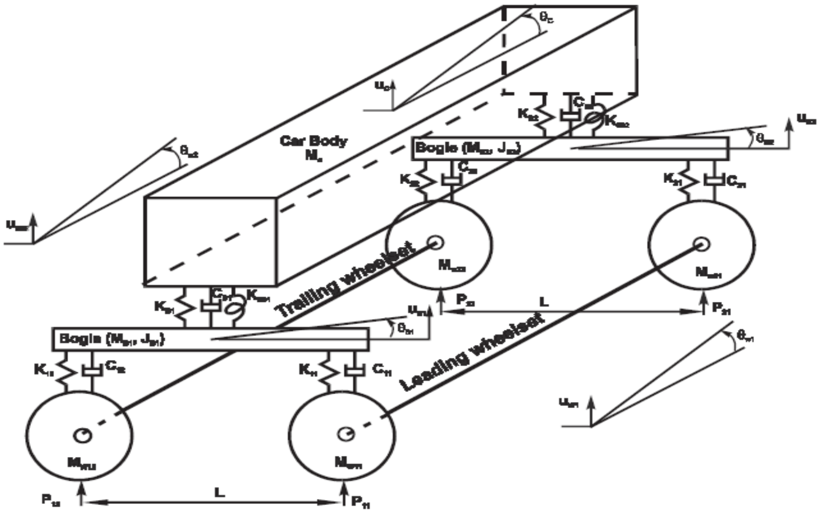

Fig. 1. 10: A three-dimensional 10-DOF vehicle model [16]

Sun et al. [97] developed a comprehensive three dimensional vehicle model, as shown in Fig. 1. 11, in order to study lateral and vertical dynamics of the wagon-track system. Such a model provides all the advantages of roll, pitch plane models, and quite adequate for the investigation of the influences of coupled vertical, pitch, and lateral dynamics of the vehicle. Furthermore, under certain conditions, the pitch and roll motions of the car body and bogie that could enhance the wheel-rail impact force caused by the wheel and rail irregularities can be adequately investigated. Moreover, the investigation of the cross wheel effects of the four wheels of a bogie and the leading and trailing wheelsets can be effectively carried out.

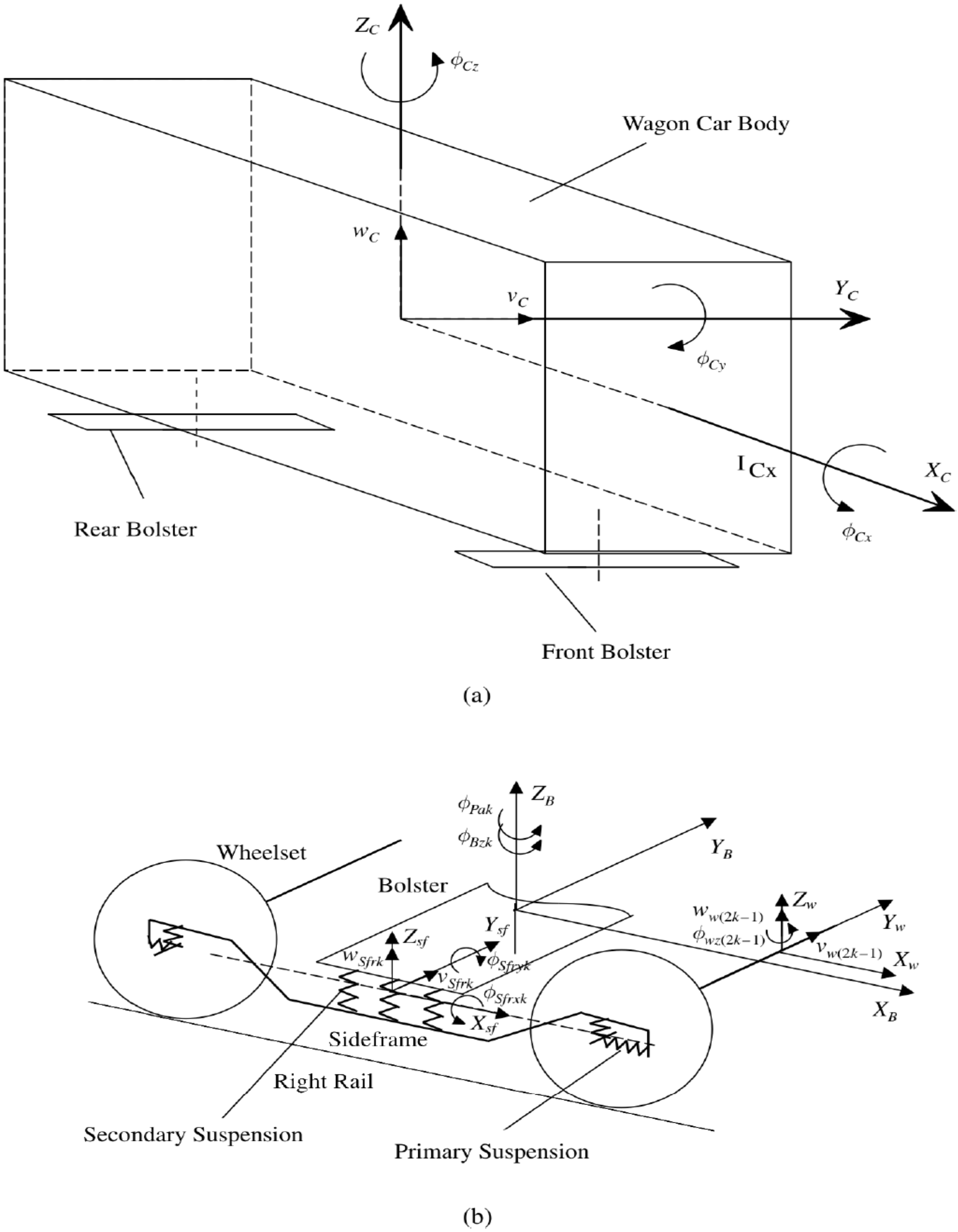

Fig. 1. 11: A three-dimensional vehicle model developed by Sun et al. [97], (a) car body; (b) bogie.

1.2.3 Track system model:

The reported track system models for analysis of dynamic train-track interactions can be grouped into three categories, namely: (i) lumped parameter models; (ii) rail beam on continuous supports; and (iii) rail beam on discrete supports. Among the reported track system models, lumped parameter model is the simplest and the earliest model that includes a single effective rigid mass supported on track of two or more layers of sleepers and ballasts connected by linear spring and damping elements [98]. This model was employed to study the formation of rail corrugations and wheel/rail impact forces due to wheel OOR defects. In early analyses, as shown in Fig. 1.12, a single-layer continuous track model was used where the track was treated as a finite/infinite rail beam on an elastic foundation and subject to a moving load [4, 99]. Such a model is considered to represent the track system fairly well, and can provide a closed form analytical solution. Furthermore, there is a possibility to replace the subsoil foundation by the frequency and wave number dependent stiffness. However, this model presents certain limitations, such as the sleeper mass cannot be adequately distributed over the rail and dynamic behavior of sleeper cannot be investigated.

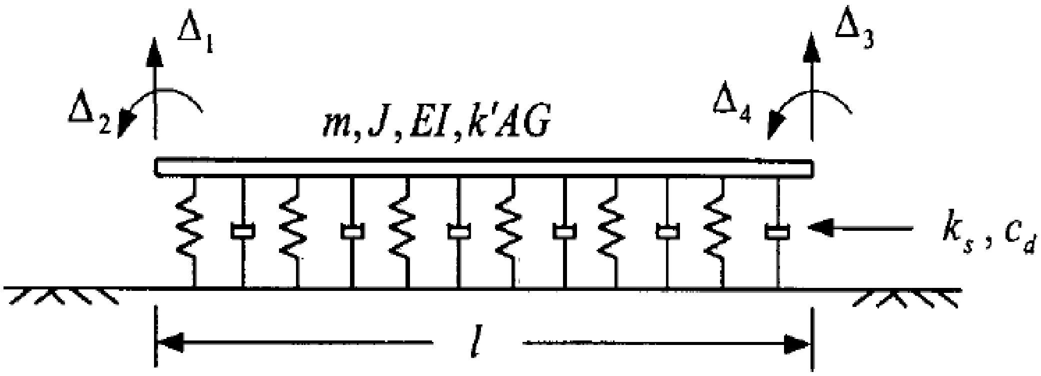

Fig. 1.12: Finite beam on single-layer continuous elastic foundation [99]

Alternatively, a two-layer continuous track model that consists of two Timoshenko beams supported on continuous spring-damper elements has been developed by Bitzenbauer and Dinkel [100]. Similar models have also been applied by many researchers to study rail corrugations, wheel-rail noise generation, wheel-rail impact loads due to rail joints and to investigate the dynamic interaction problems between a moving vehicle and substructure [100, 101, 102]. The model, as shown in Fig. 1.13, enables analysis of dynamic behavior of the sleeper considering both symmetric and asymmetric bending modes, while only limited information could be derived for dynamic behavior of the total track system.

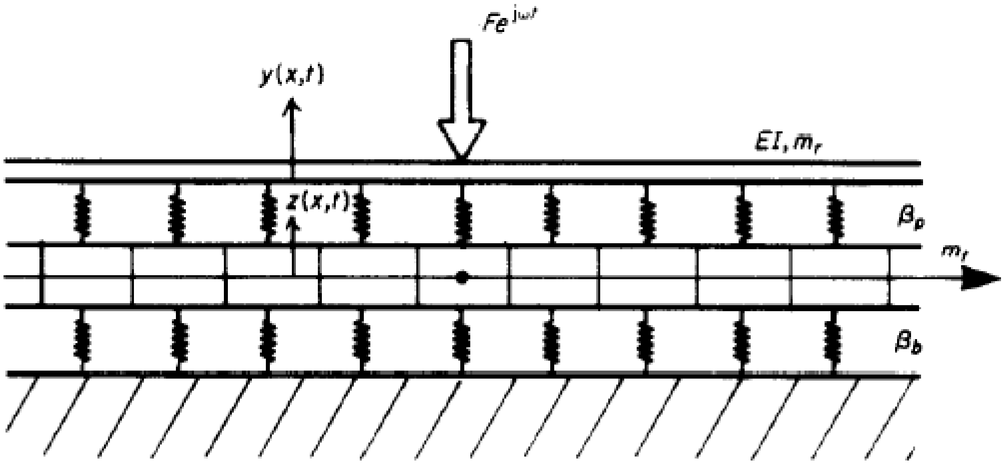

Fig. 1. 13: A two-layer continuous track model [101]

In the analysis of impact forces generated at the wheel-rail interface caused by wheel and rail defects, the rail beam models on discrete supports have been most widely used in order to include the effect of discrete sleeper support into the impact analysis [20, 93, 104]. Similar models have also been used to study the effect of OOR wheel profiles, the dynamic response of vehicle and track under high-speed conditions and noise emissions caused by wheel and rail defects [77, 105]. These models show the advantage of capturing the responses corresponding to three resonance frequencies of the track structure, the rail and the sleeper [106]. A two-layer discrete track model is shown in Fig. 1.14.

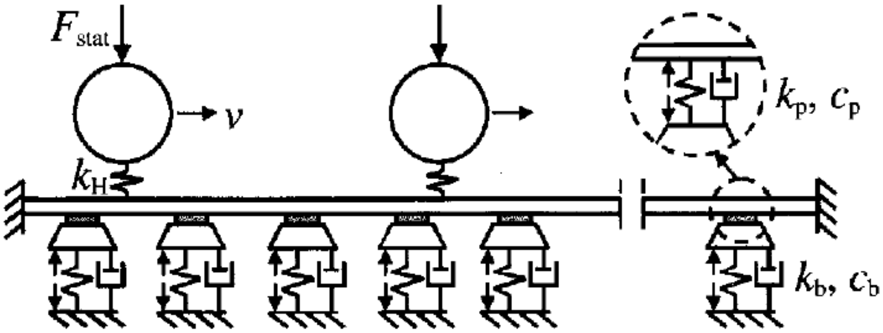

Fig. 1. 14: Two-layer discrete track model [19]

Three-layer track models have also been formulated where the ballast is modeled as a massive mass in addition to the sleeper mass. These models have been employed by Zhai and Cai [13, 15] to study the wheel-rail impact loads due to wheel flats and rail joints, and Jin et al. [6, 14] to study the effect of rail corrugations on vertical dynamics of the vehicle and track. Oscarsson [107] also used this model to simulate the train-track interactions with stochastic track properties. Ishida and Ban [7] developed a five layers track model, as shown in Fig. 1.15, in order to analyze the effect of different types of wheel flats in terms of impact loads and rail acceleration where the ballast is divided into three different layers coupled through damping and spring elements. This model permits analysis of the response of ballast at different positions to the excitation at wheel-rail interface. The model results, however, did not show substantial advantage in enhancing the dynamic wheel-rail impact load prediction ability when compared to the simpler models.

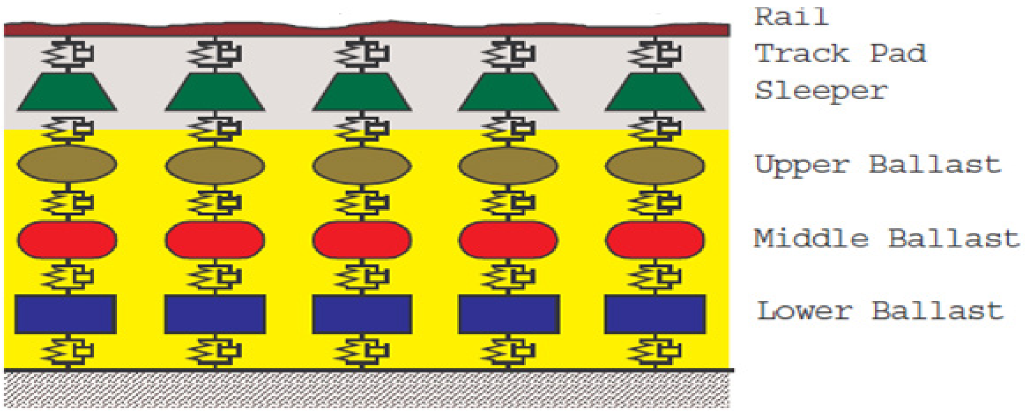

Fig. 1. 15: A comprehensive five-layer discrete track model developed by Ishida and Ban [7].

Apart from the track system modeling, modeling of the track components, such as rail, sleeper, railpad, ballast, also varies depending upon the purpose of studies. The rail is mostly modeled as a continuous beam, either as an Euler-Bernoulli beam or a Timoshenko beam. The Euler beam model of the rail has been used in many studies on dynamic analysis of the vehicle-track system to study the effects of wheel flats [88, 108], rail corrugation [6, 14, 91], rail dipped joints [109], rail welds [81, 108], bridge-train interactions [110] and OOR defects [93]. However, the Euler beam model neglects shear deformation and rotational inertia of the rail which may yield overestimation of the dynamic force in the high frequency range. Thus, lateral dynamic studies that involve lateral flexibility of the rail web may not be suitable with this model. Furthermore, it has been reported that Euler beam representation of the rail is adequate for the rail response to vertical excitation for frequencies less than about 500 Hz, while for Timoshenko beam model it is up to 2.5 kHz [22]. Timoshenko beam model of rail has, thus, been widely employed in order to study the dynamic interaction between the wheel and rail in the presence of wheel and/or rail imperfections, effect of nonlinearity and railpad stiffness on wheel-rail impact and noise generation [18, 103, 105, 111, 112]. In recent years, several number of studies have employed Timoshenko beam to model the rail in order to analyze the vehicle-track interactions due to the wheel flats [78, 113, 114] and track irregularities [81, 87, 115]. A Timoshenko rail beam four-layer track model is shown in Fig. 1. 16.

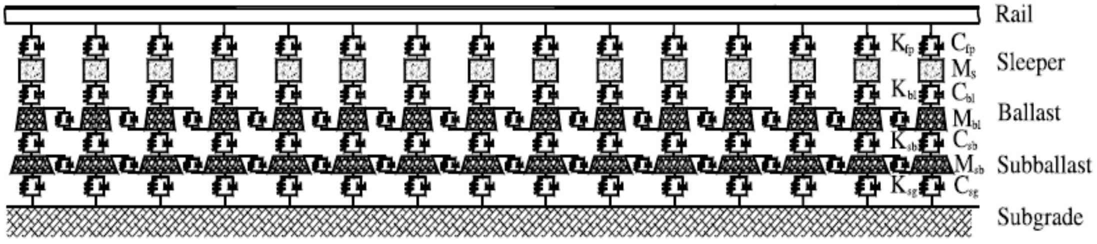

Fig. 1. 16: A Timoshenko rail beam four-layer track model [113]

Railpads are used to support the rail, and to protect sleepers from wear and damage. Railpad is generally modeled using spring elements [104, 116] or combined spring and damping elements [6, 14, 93, 108] to form either continuous or discrete rail support. A state-dependent three-parameter viscoelastic railpad model has been developed by Anderson and Oscarsson [5] in order to study the dynamic behavior of pad under low and high frequency excitations. Different types of pad models utilized in railway vehicle-track interaction analysis in the presence of wheel and rail defects are shown in Fig. 1. 17. In a continuous rail support, the railpad is continuously placed under the rail beam [99, 100], whereas the discrete models consider the visco-elastic pad model at a point on the rail foot at the center of the sleeper support to investigate the wheel-rail interactions [10, 18, 23, 104, 108].

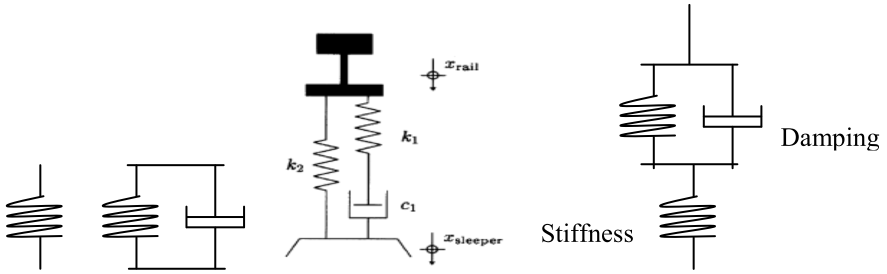

(a) (b) (c) (d)

Fig. 1. 17: Different types of rail pad model: (a) one-parameter; (b) two-parameter; and (c) and (d) three-parameter.

In the analysis of vehicle-track interactions in the presence of wheel and rail defects, a sleeper can be considered either as a transverse beam with either uniform or variable cross section [118] or as discrete mass [6, 10, 14, 105, 107] on an elastic foundation representing the ballast. These studies have invariably concluded that sleeper modeled as a rigid mass is adequate for prediction of dynamic vehicle-track interaction force, while the bending stiffness is neglected that may yield an overestimation of impact force at higher speeds. The ballast is generally modeled as parallel spring-damper elements [4, 8, 10, 93, 103, 104, 105] or as rigid masses those are interconnected by the shear springs and dashpots [6, 13, 14, 15]. The latter model permits analysis of distributed ballast deflections under excitations at the wheel-rail interface. However, the ballasts do not greatly affect the wheel-rail contact forces due to their distant placement from the wheel-rail contact [119].A comprehensive ballast model developed by Zhai et al. [13, 15] that considers shear interaction between the ballast masses is shown in Fig. 1. 18.

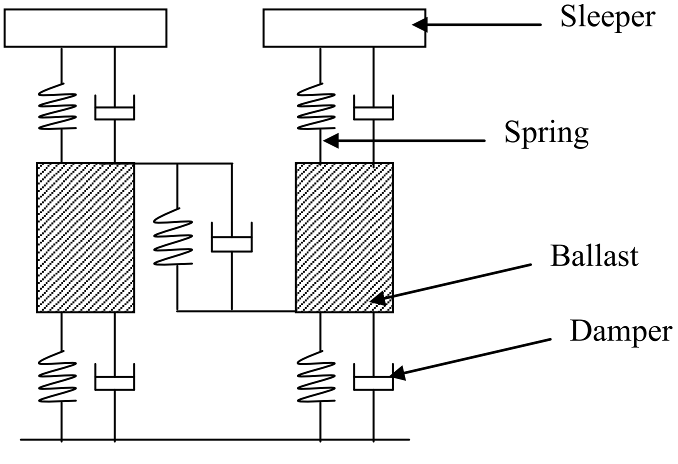

Fig. 1. 18: Ballast model considering the stiffness and damping in shear [13, 15]

The elastic properties of the track system can be modeled with either linear or nonlinear stiffnesses and damping. Although the properties of railpad and ballast in practice are nonlinear, a vast majority of the studies involving vehicle-track interaction in the presence of wheel and rail defects considered the linear properties of the railpad stiffness and damping [4, 8, 9, 13, 14, 16, 83, 88]. The analytical studies of wheel-rail impact loads due to wheel and rail defects showed reasonably good agreements with measured peak contact force in the presence of wheel defects [13, 21]. The difference between the predicted peak wheel-rail impact loads and the measured data is, however, very high in case of high vehicle speed [4, 8]. The predicted wheel-rail impact loads were compared using linear and nonlinear rail track properties by Johansson and Nielsen [19]. The study concluded that a linear track model yields lower magnitudes of the impact loads than the nonlinear track model in low and medium speed range. However, at higher speeds, more than 70 km/h, both models predicted higher impact forces than the measured data. The nonlinear properties of the railpad are included in a very few studies in order to investigate the wheel-rail interaction in the presence of wheel/rail defects [105, 117]. These studies showed considerable differences in the results due to linear and nonlinear track models. Dahlberg [117] claimed the necessity of a nonlinear track model when the load to the railpad and ballasts varies significantly because of the dramatic change in the railpad and ballasts stiffness with change in loads. However, these studies simplify the vehicle model to a single wheel model only, which do not consider the pitch and roll motion of the car body and bogie. Change in the static and dynamic stiffness of nonlinear railpad due to change in the load is shown in Fig. 1. 19.

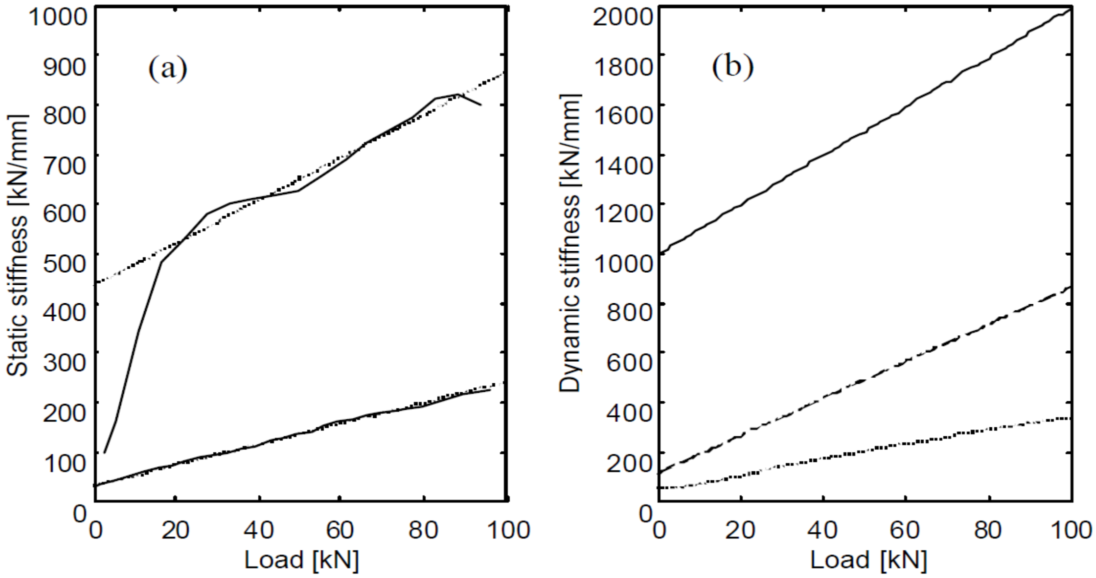

Fig. 1. 19: (a) static stiffness of non-linear pads, — measured , ···· approximated. The upper curves are for the stiff pad and the lower curves are for the medium pad; (b) dynamic stiffness of non-linear pads, — stiff pad, --- medium pad, ···· soft pad [105].

1.2.4 Wheel-rail contact model:

Wheel-rail contact points couple the vehicle model with the track model. The accurate and reliable prediction of wheel-rail impact force largely depends upon the accuracy of the wheel-rail contact model. A number of theories have been evolved to accurately describe the dynamic wheel-rail contact point. The vast majority of the analytical studies considered linear [114, 120, 121, 122, 123, 124, 125] or non-linear [5, 13, 14, 15, 97, 103, 107, 126, 127] Hertzian contact model in order to study the wheel-rail interactions due to wheel/rail defects. Hertzian contact model, as shown in Fig. 1. 20, is perhaps the simplest and most widely used to characterize the rolling contact in railway vehicle. A major disadvantage of non-linear Hertzian contact model is that it underestimates the impact force at low speeds and overestimates the impact force at higher speeds [112]. It has been suggested that a linearized contact spring could adequately represent the wheel-rail contact when variations in the overlap are very small [121]. The linearized contact spring has been widely used to study the rail corrugations, vibration due to high frequency irregularities on wheel-rail tread, and noise generations [102, 121, 127, 128]. The linearization, however, yields overestimation of the contact stiffness in the vicinity of discontinuity and thereby the impact loads [8].

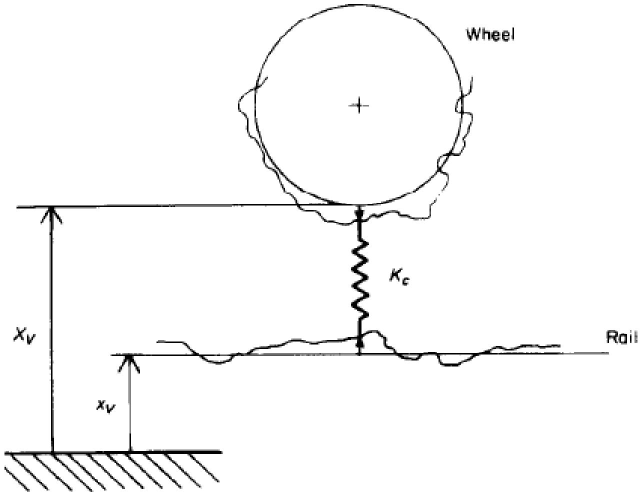

Fig. 1. 20: A single point wheel-rail contact model applied by Tassilly and Vincent [125]

Kalker [129] proposed a Non-Hertzian contact model based on predicted contact area and shape, which requires extensive computation as the contact area must be established as a function of wheel angular position relative to the rail. A study of vehicle-track interaction by Baeza et al. [130] has used the non-Hertzian contact model for a wheel with flat. The study stated that it is not viable to solve this contact model simultaneously with the integration of differential equation of motion. Alternate methods to calculate the wheel-rail contact forces using non–Hertzian contact patch have been reported by Pascal and Sauvage [131]. The solutions of contact problems for an elliptical contact zone are presented by Kalker [132] and Shen et al.

[133], and later mostly used by others for analysis of wheel-rail squealing noise [134], corrugation studies [135], and interaction due to rail irregularities [136] etc.

For analysis of vehicle system dynamics, instead of using single-point contact, multiple point wheel-rail contact models were used in [137, 138, 139, 140]. Several multipoint contact models based on elliptic and non-elliptic profile are cited in [139]. A multiple point contact model, as shown in Fig. 1. 21, has been developed by Dong [8] based on Hertzian static contact theory in order to study the wheel-rail impact load due to wheel flat. This model has also been employed later by Hou et al [90] and Sun et al [97] for the same purpose. Both of these studies reported that multiple contact model shows good correlation between the predicted and experimental data, except for some overestimations of wheel-rail impact load at a speed of 70 km/h [97]. These studies, nevertheless, assume that contact region is symmetric about the vertical axis, and the results obtained are very similar to those predicted by Hertzian point contact model. A recent study by Zhu [78] developed a multipoint adaptive contact model to account for the asymmetric contact as the flat enters the rail. Further study is, however, required to establish the spring stiffness for the model.

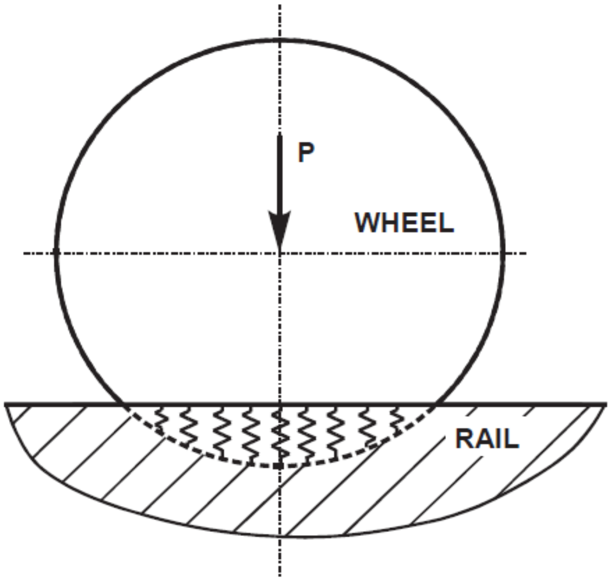

Fig. 1. 21: Multipoint wheel-rail contact model.

1.2.5 Wheel defects:

Railway wheel defects are generally attributed to the imperfections caused by the misalignment and fixation, manufacturing flaws, and those caused by the operation of the vehicle. These defects are termed as wheel flat, shelling, spalling, shattering, corrugation, eccentricity, etc. Several comprehensive reviews on various types of wheel defects, their effect on wheel-rail impact loads, and vehicle and track components have been described in [20, 23].

Wheel shelling is a type of wheel defect that is caused by loss of materials from the wheel tread and is assumed as the result of rolling contact fatigue. Moyar and Stone [139] carried out a study on formation of railway wheel shelling due to thermal effect and concluded that periodic rail chill has a strong effect on shelling in the case of hot-braked treads. Wheel spalling is another type of wheel defect that has been associated with rolling contact fatigue. Railway wheel spalling is assumed to occur as the result of fine thermal cracks joining to produce the loss of a small piece of tread material. It has been observed that spalling appears shortly after reprofiling due to the lack of inspection [142]. A railway wheel with shelling defect is shown in Fig. 1. 22.

Fig. 1. 22: Wheel shelling defect.

Apart from the wheel shelling, a number of studies have investigated the impact loads caused by various other types of surface defects and their propagation. These include wheel Out Of Roundness (OOR), wheel spalling, wheel shelling, and wheel and rail corrugation. The clamping of wheel during reprofiling is known to be a cause of periodic OOR, while non-periodic OOR are caused by unbalances in the wheelset or by inhomogeneous material properties of the wheel. Both of these types of OOR are usually found in disc-braked wheel sets [143]. It has been concluded that for a vehicle speed up to 145 km/h, the effect of the wheelset unbalances on dynamic responses of the vehicle is small and negligible [140].

. The formation of the wheel OOR, their experimental detection, mathematical model to predict impact load due to wheel OOR and criteria for removal of OOR wheels have been thoroughly discussed in a comprehensive review presented by Barke and Chiu [23], and Nielsen and Johansson [20].

Among all the types of wheel defects, wheel flat is the most common type encountered by railway industry [8]. The impact load due to wheel flats induces high-frequency vibrations of the track that causes damage to track components, which may also be high enough to shear the rail [7, 13, 15]. Wheel flats thus affect track maintenance and the reliability of the vehicle's rolling elements [130]. In addition to safety and economic considerations, these defects reduce passenger comfort and significantly increase the intensity of noise [120]. Due to the modern trend in increasing the speed and wheel load of the vehicle, replacement of defective wheels and in-time maintenance of the track has become an important concern for heavy haul operators. In order to predict the wheel-rail impact load accurately, it is necessary to develop the effective impact load prediction tools. A wide range of mathematical models have thus evolved to characterize the geometry of wheel flats in order to investigate the impact loads [7, 8, 15, 90, 103].

In order to control the adverse effect of wheel flats and ensure the safe operation of the railroads, various railroad organizations have set the criteria for removal of wheels with flats primarily based on flat size and the impact load produced by the flat. The American Association of Railroad (AAR) has set the criteria to replace the wheel from the service for 50.8 mm long single flat or 38.1mm long two adjoining flats [144]. The AAR also states that a wheel should be replaced if the peak impact forces due to single flat approaches the 222.41 to 266.89 kN range

[145]. According to Transport Canada safety regulations, a railway car may not continue in service if one of its wheels has a flat of more than 63.50 mm in length or two adjoining flats each of which is more than 50.80 mm [1]. Swedish Railway sets the condemning limit for a wheel flat based on a flat length of 40 mm and flat depth of 0.35 mm [17]. According to UK Rail safety and standard board [146], freight vehicle with axle load equal to or over 17.5 tonnes a wheel with flat length exceeding 70 mm must be taken out of service. These removal criteria for defective wheels are based on the damage potential of the wheel flat and mostly the magnitude of the wheel-rail impact force due to the wheel flat. The presence of multiple flats either within a single wheel or within a multiple wheels of a freight car that could lead to considerably different magnitudes of impact loads is not properly addressed by the current guidelines. The Transport Canada guidelines also stipulate the threshold lengths of two adjoining flats in a single wheel, while the basis for the threshold values is not known. Furthermore, the contributions due to roll and pitch dynamics of the car and relative positions of different wheel flats with wide variations in relative positions between the flats on the wheel-rail impact forces were not investigated.

In order to predict the wheel-rail impact load accurately, it is necessary to develop the effective impact load prediction tools. A wide range of mathematical descriptions have thus evolved to characterize the geometry of wheel flats in order to investigate the impact loads [7, 8, 13, 16, 103]. Wheel flats have been classified as chord type flat, cosine type flat and combined flat based on the flat geometries. As shown in Fig. 1. 23, a newly formed fresh flat with relatively sharp edges is known as chord type flat. This type of flat model has been widely used in various studies on wheel-rail impact load, rail acceleration, and noise [7, 16, 103]. However, it has been shown that the chord type flat model overestimates the wheel-rail impact load [7].

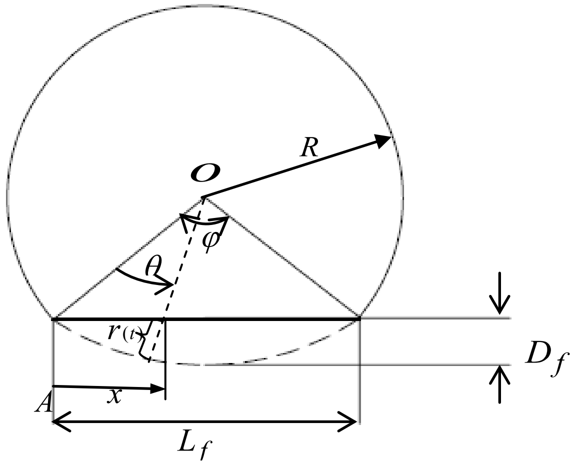

Fig. 1. 23: Chord type wheel flat model.

With continued service, the edges of the chord type flat become rounded under repeated impact loads. This type of flat can be modeled as haversine flat, which is widely used for analysis of dynamic behavior of rail vehicles and tracks together with the wheel-rail impact load due to flat [8, 13]. The impact force response predicted by a haversine wheel flat generally shows good agreement with experimental data [7, 8]. However, in reality, the shape of the wheel flat is neither purely chord type nor purely haversine shape. In an attempt to make a model that represents a real wheel flat shape, a combined wheel flat model was introduced by Ishida and Ban [7]. This model, however, did not show notable advantages over a haversine flat model. Although the presence of the multiple flats within a wheel or axle is very common in practice, a vast majority of the studies consider only a single flat. A few recent studies have also investigated the effects of multiple wheel flats on the force responses of the direct and cross wheel-rail impact point [78, 97, 119]. A typical wheel flat and the model of a wheel with multiple wheel flats are shown in Fig. 1. 24.

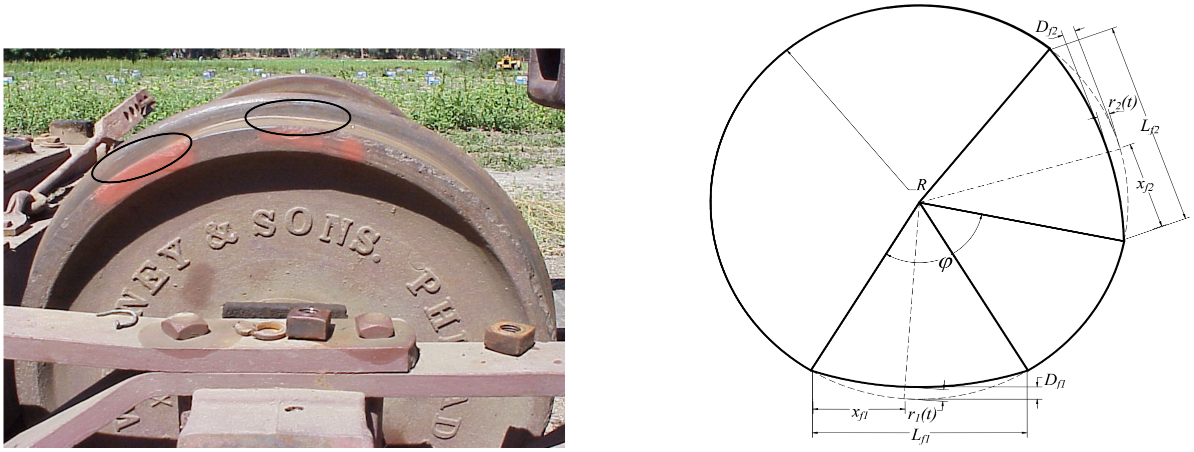

(a) (b)

Fig. 1. 24: A railway wheel (a) with two flats; (b) model with two haversine type flats.

Experimental and theoretical studies on impact loads due to wheel flats have been described by Johansson and Nielsen [20], Newton and Clark [4] and Fermer and Nielsen [21]. These studies revealed that impact loads produced by wheel defects are not always easily detectable by visual inspection of the wheel and a nonlinear track model yields more accurate prediction of the wheel-rail impact force due to wheel defects than the linear track model. Early experimental studies carried out by Jenkins et al [147] and Frederick [148] showed the effect of vehicle and track parameters on vertical dynamic forces in the presence of wheel flats and rail joints. A recent experimental study on vertical wheel-rail contact force in the presence of track irregularities has been carried out by Gullers et al. [149]. The experimental study to observe the flat growth has been carried out by Jergeus et al. [142]. The study concluded that the rate of growth of wheel flat is very high at the beginning and it is thus essential to take the wheelset out of service as soon as possible when a wheel flat is observed.

1.2.6 Simulation methods:

There are two different techniques widely used in the analysis of moving load and moving mass problems. These are Fourier transformation method and generalized mode or assumed mode method. Fryba [24] presented a detailed solution of the moving load problem where the beam was modeled as infinitely long Euler-Bernoulli beam resting on Winkler foundation. A vast majority of the studies dealing with the moving load problems utilized the Fourier transformation method to solve the governing differential equations arising from either Euler-Bernoulli or Timoshenko theory [24, 28, 51, 65, 66]. The responses of the infinite beam under moving load supported on either Winkler or Pasternak foundation were studied by means of Fourier transforms and using Green's function in [25, 66, 150]. Mead and Mallik [151], and Cai et al. [152] presented an approximate "assumed mode" method to study the space-averaged response of infinitely long periodic beams subjected to convected loading and moving force, respectively. These methods are applicable to the forced vibration analysis of an infinite continuous beam subjected to arbitrary excitations. In order to consider the effect of non linearity in beam analysis, Finite Element Analysis (FEA) of an infinite beam has been carried out in [153-155]. In these studies, FEA has been adopted to perform the analysis of nonlinear dynamic structure under moving loads where the load varies with both time and space.

In moving force problem, the magnitude of the moving force has been assumed to be constant by neglecting the inertia forces of a moving mass. However, in case of moving mass, the interaction force consists of inertia of the mass, centrifugal force, etc. Hence, the velocity of the moving mass, structural flexibility, and the mass ratio of the moving mass to structure play important roles on the overall interaction process. A closed-form solution to a moving mass problem is obtained by Michaltos et al. [32] by approximating the solution without the effect of the mass. By using the method of Green functions, the effects of the system parameters on the dynamic response of the beam subjected to a moving mass have been studied by Ting et al. [36], Foda and Abduljabbar [37], and Sadiku and Leipholz [39]. The method of the eigenfunction expansion in series or modal analysis has been employed by Akin and Mofid [41], Bowe and Mullarkey [42], Ichikawa et al. [43], Stanisic and Lafayette [46], and Lee [47]. Lou et al. [60], Yavari et al. [61], Vu-Quoc and Olsson [62], Bajer and Dyniewicz [63], and Cifuentes [64] investigated the dynamic response of single and multi span beams subjected to a moving mass by using finite element method.

To analyze the wheel-rail interactions in presence of wheel/rail defects, two different techniques, namely, Frequency domain and Time domain techniques are widely used. Frequency domain technique has been used to study the impact load due to wheel defects, track irregularities and the formation of corrugations [93, 122, 135]. This technique takes less time to analyze and is effective for the prediction of the frequency response related to excitation. However, it is limited to investigation of the linear models only. When nonlinearity is present either in vehicle-track system model or in contact model, it is necessary to adopt the solution process in time domain. Time domain analysis can be further classified into modal analysis method and finite element method. Modal analysis method has been used to study the wheel-rail impact load due to wheel flats and rail joints, noise generation and rail corrugations [6, 13, 14, 15, 119, 134]. This method has the advantage of fast computing when the local variations of the track are small. However, many modes are required to exactly model the track in order to have accurate prediction of the track behavior. Alternatively, use of finite element method for solution of train-track interaction has become more attractive due to the recent progress in computer capacity. Finite element method has been applied to study the impact load due to wheel and rail defects and formation of OOR in wheel profiles [18, 89, 112, 113, 147]. The extreme adaptability and flexibility of finite element method have made it a powerful tool to solve PDE over complex domain. However, the accuracy of the obtained solution is usually a function of the mesh resolution and the solution often requires substantial amount of computer and user time, particularly when extensive parametric study is required.

1.2.7 Detection of wheel defects:

Imperfections on the wheel tread and rail surface can have detrimental influence on both vehicle and track components such as vehicle bogies, wheelsets, bearings, rails and railpads. The high impact forces from a defective wheel cause stress in the rail, and in extreme cases can break the track or cause the wheel to jump off the track, resulting in derailment. The continuous repetitions of impacts on rail, together with the high forces involved, cause rapid deterioration of both rolling and fixed railway equipment. If ignored or underestimated, the fault will wear out materials up to the breakdown. Thus, various methods have been proposed for detecting flat wheels. One method is to employ inspectors to listen to the trains as they move through a particular location. In some cases, flat wheels are identified through routine inspections when the cars are being serviced. These methods employ a range of technologies from optical systems that gauge the wheels in real time to sensors that look for vibrations and stress levels.

Continuous wavelet transform has been applied to vibration signal analysis of railway wheels in order to detect the wheel tread defects by Belotti et al. [156] and Yue et al. [157]. Belotti et al. [156] has shown a wheel-flat diagnostic tool by using wavelet transform method, as shown in Fig. 1. 25. In this study, an experimental layout was designed to develop and to validate a reliable, effective, and low-cost wheel-flat diagnostic tool. The method implies the detection of the wheel flats through the measurement of peak acceleration by the use of several accelerometers placed in fixed positions on the rail. The results obtained from experimental study validate the theoretical model and demonstrates the advantages of wavelet-based detection of signatures. However, the wired connections between the accelerometer and the analysis house make the overall system bulky. Furthermore, the entire train has to pass through the specific test section that can be far from the train operating area.

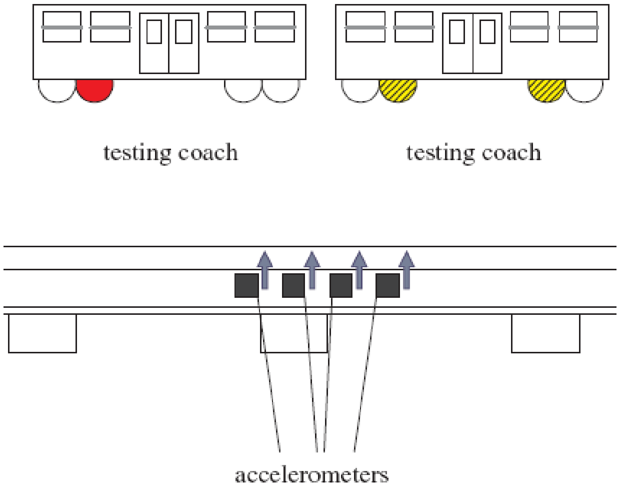

Fig. 1. 25: Testing train scheme with damaged wheels represented by deep marked and instrumented rail where the arrows near the accelerometers indicate their measuring axes [156].

The detection of wheel flats with fiber optic sensors has been reported by Anderson [158]. In this method, the screen is fixed between the end of the fiber and the active area of the detector, and the pinhole is sized to have the same diameter as the RMS value of the bright/dark spots in the speckle pattern, as shown in Fig. 1.26. When the fiber is disturbed the speckle pattern changes. As the speckle pattern changes, bright and dark fringes pass over the pinhole, resulting in a time varying signal that is indicative of the vibration of the fiber. For small perturbations, the frequency of this signal is equal to the frequency of the physical disturbance. The advantages of the pinhole/detector system are low cost and simplicity. For visible and near-infrared light, large-area detectors are readily available for modest cost, and can be readily assembled with a built-in pinhole and fiber-optic connector, making field assembly simple and straight forward. However, the design has poor optical efficiency, wasting up to 90% or more of the incident light, which is attributed to the limiting aperture of the pinhole. Furthermore, the placement of the fiber on the underside of the metal grating alongside the track makes the system rather complicated. Several different types of optical sensors have been applied in order to detect wheel and rail defects with fair accuracy and high resolutions [159, 160].

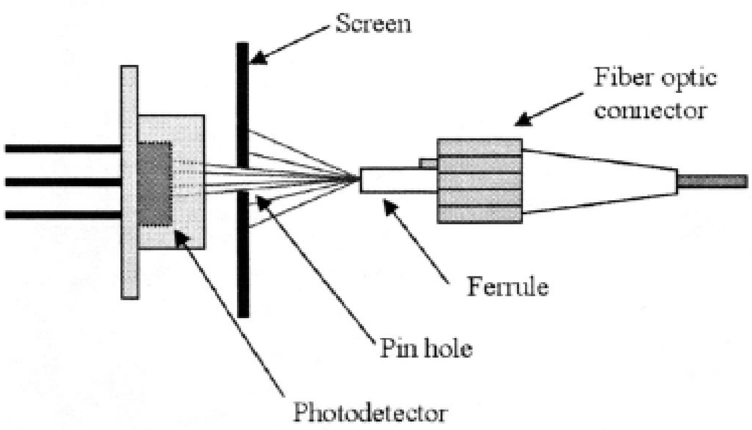

Fig. 1. 26: Detector and pinhole assembly used to measure temporal changes in speckle pattern [159].

Another method of detecting wheel flats employs scanning with laser beam [161], as shown in Fig. 1. 27. The entire module consists of a detector to send and receive radiation signals after the scanning of the wheel. The module also has a smart electronics box (SEB) that contains digital signal processors and connection to the wayside personal computer (PC) for further analysis. Wheel flats can be clearly detected from the unique signature and the gradients between scans at different heights on the wheel. Similar technique has also been applied by Kenderian et al. [162] in order to detect dynamic railroad defects.

Ultrasound technique has often been used as a non-destructive technique in order to inspect the defects of rail wheel [163-167]. The methods consist of sending an ultrasound pulse over the rolling surface to detect echoes produced by the defects. The inspections can be carried out manually or by expensive and complex installations. In both cases, however, long inspection time is required. Moreover, ultrasound techniques use high frequencies that cannot penetrate certain type of defects because of excessive attenuation [166].

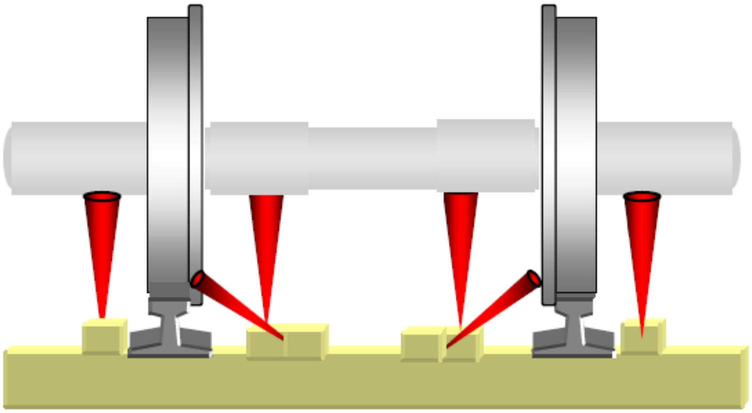

Fig. 1. 27: Positioning of scanner assemblies to view inner bearing, outer bearing, and wheels [161]

Acoustic method for detection of wheel flats is also available in literatures [168, 169]. In this method, sound from a passing train is recorded and the particular sound caused by the impact between a wheel flat and the supporting rail is distinguished by detecting frequencies in that particular sound. Another method for detection of the presence of the wheel flats rely on the sensing of changes in voltage resulting from a break in the established circuit caused by the wheel flat.

The most common approach to detect wheel defects is based on the analysis of impact loads or accelerations of wheels or rails developed due to the presence of wheel and rail defects in time-domain schemes [170-173]. These methods employ several accelerometers placed on rails in order to detect the wheel/rail defects by inspecting the acceleration levels. Detection of the wheel/rail defects depends on the analysis of the frequency spectrum of the measured rail accelerations. Braccialli et al. [172] presented a description of this type of method based on the cepstrum analysis of rail accelerations. These accelerometers can be MEMS based accelerometers or conventional piezoelectric accelerometers. The vast majority of accelerometers are based on piezoelectric crystals, but they are too big and too clumsy, whereas, MEMS based accelerometers are tiny and are made using a highly enabling technology with a huge commercial potential. They provide lower power and robust sensing. The most common application for MEMS based accelerometers in railway engineering is health monitoring of the track [174-176]. A MEMS based sensor network for rail signal system has been proposed by Fukuta [177]. Lee et al. [178] developed a MEMS based hybrid uniaxial strain transducer in order to monitor the fatigue damage of the rail. However, all these MEMS based sensors are developed to monitor the track only.

1.3 THESIS SCOPES AND OBJECTIVES

From the review of the relevant literature, it is evident that although different types of railway vehicle and track models have been developed in order to study the interaction effect in the presence of wheel and rail defects, very few studies have considered three-dimensional representation of the railway vehicle and track model. Furthermore, although railpad and ballast stiffness and damping properties are nonlinear in practice, a vast majority of the studies has considered the linear properties of railpad and ballast model in dynamic analysis of vehicle-track interaction due to wheel and rail defects.

It is also evident from the review of the relevant literature that a great deal of research efforts has been made in order to predict the wheel-rail impact force in the presence of wheel and rail defects such as, single wheel flat, rail corrugation, etc. These studies have provided guidelines for acceptable limits of wheel flats for the railway transportation industry in order to ensure safe and efficient operation. Although the presence of multiple flats within a wheel or different wheels in the same or different axles have been widely noticed in practice, the vast majority of the efforts focus on the impact interactions due to a single flat only. The influences of multiple flats, and their consequences have not been adequately quantified. Furthermore, the pitch and roll motions of the car body and bogie could adversely affect the wheel-rail impact force caused by the wheel and rail irregularities. A comprehensive three-dimensional vehicle model coupled with a three-dimensional track model is thus required in order to predict the wheel-rail impact loads due to wheel and rail defects.

From the review of the relevant literature, it is also evident that considerable efforts have been made to detect the presence of defects in the wheels and rails. However, all these detection techniques utilize the railway track to mount the sensors, which requires the train to pass through that particular test section of the rail in order to investigate the wheel defects. A train in operation that needs prompt investigation may not be possible by these present techniques i.e. continuous monitoring of all the wheels for detection of the flat is not possible. Furthermore, the present techniques require huge connections of wires to transfer the data from the test section to analysis center. One of the challenges for sensors is the need to operate remotely in harsh environments with exposure to wide temperature ranges as well as rain, snow, slush, dirt and grime. Development of an on-board measuring system is thus required that can be placed on the wheel bearing in order to enable the detection of the wheel defects continuously.

The present dissertation research thus aims to develop a comprehensive three-dimensional dynamic railway vehicle-track model coupled with non-linear railpad and ballast stiffness and damping properties. The developed model must be capable of predicting dynamic responses in terms of force or acceleration in the presence of single as well as multiple flats. Finally, based on the analytical results predicted by the developed model, a smart railway wheelset will be developed with MEMS based accelerometers. The specific objectives of the proposed research are listed below, which are also the expected major contributions:

a) Develop a two-parameter Pasternak foundation model subjected to moving load or moving mass in order to analyze the vibration of Euler-Bernoulli beam of finite and infinite length.

b) Develop a comprehensive three-dimensional railway vehicle-track model using two Timoshenko beams supported by discrete non-linear elastic supports to study the interactions of two sideframe wheels and the wheels within a wheelset taking into account the contribution of vehicle pitch and roll motions.

c) Formulate models for single as well as multiple wheel flats in order to evaluate the impact responses in terms of force or acceleration arising from single as well as multiple wheel flats and investigate the influences of one wheel flat on the force or acceleration imparted at the interface of the adjacent wheel.

d) Investigate the influences of variations in various design and operating parameters on the magnitudes of the impact force or acceleration such as, speed, flat size and relative positions of the flats within the same wheel or wheelsets

e) Develop a smart wheelset that can detect its defect automatically.

f) Design and analyze MEMS based accelerometer for automatic detection of wheel flats.

1.4 ORGANIZATION OF THE THESIS

The first chapter summarizes the highlights of the relevant reported studies on different types of modeling of vehicle and track systems employed in studies related to dynamic responses and railway vehicle track interactions in the presence of wheel defects. The reported studies on different types of wheel defects, analytical and experimental methods for detection of wheel defects are also summarized in this chapter. The scope of the dissertation research is subsequently formulated on the basis of the reviewed literature.

In chapter 2, dynamic response of an infinite Euler-Bernoulli beam under a constant moving load is investigated. The same beam with finite length is further employed to obtain the dynamic response with moving load as well as moving mass. The foundation representing the soil is modeled as both one-parameter Winkler and two-parameter Pasternak model. Fourier transform technique is employed to find the analytical solution of the governing partial differential equation in the case of moving load problem. However, numerical method is employed in the case of moving mass problem. The dynamic responses of the beam in terms of beam deflections, and bending moments have been obtained with different velocity ratios. The effects of shear modulus and foundation stiffness on deflection, bending moment and shear force responses have also been investigated for both damped and undamped cases where the speed varies from below critical to above critical velocity. In case of damped analysis, responses are obtained for both underdamped and overdamped conditions.

In chapter 3, a three-dimensional vehicle model is developed together with a three-dimensional two-layer track model. The two models are coupled by the non-linear Hertzian wheel-rail contact model. The equations of motion of the vehicle and track system are presented along with the parameter values. Modal analysis method is used to analyze the coupled continuous rail track and lumped-parameter vehicle system models. Natural frequencies of the vehicle and track systems are calculated and presented in this chapter. This chapter further presents the validation of the developed vehicle-track system model under wheel flat conditions using both theoretical and experimental results from the literature. The responses obtained from the validated vehicle and track system model in terms of wheel-rail impact force are also presented as functions of operating speed and flat geometry.

In chapter 4, the three-dimensional vehicle-track model developed in chapter 3 is validated in terms of wheel-rail impact force with both experimental and analytical data available in literature. The validation is carried out with both linear and nonlinear properties of railpad and ballast. The validated model is then employed to obtain displacement and acceleration responses of individual vehicle and track components in the presence of single wheel flat. The results are shown for both defective and flat-free wheel. The characteristics of the bogie bounce, pitch and roll motions due to a single wheel flat are also investigated. The analyses are performed with different position of the wheel flats such as in front or rear wheelsets within a front or rear bogie. The response characteristics are also obtained with different flat sizes and vehicle speeds.

In chapter 5, the developed and validated three-dimensional railway vehicle-track model is employed to study the effect of multiple wheel flats on wheel acceleration response. The response characteristics of wheel acceleration are obtained for both left and right wheels within same and different wheelsets for different types of wheel flats and their relative positions. The effects of both direct and cross wheel flats on different wheels within same bogie are also investigated. The effect of bogie pitch and roll motions on overall peak acceleration of the wheel is also investigated in the presence of multiple flats. In order to develop a smart wheelset that can detect its wheel flat size by measurement of the peak wheel acceleration, the relation between the peak wheel acceleration, vehicle speed and the wheel flat size are also presented.

In chapter 6, a MEMS based accelerometer model is developed for automatic detection of wheel flat. The three-dimensional railway vehicle-track model developed in chapter 3 is employed in order to investigate the wheel acceleration level in presence of a single wheel flat. COMSOL Multiphysics software is employed to validate the developed accelerometer model. The simulated responses are compared with the results obtained from the calculations. A self-test region is designed within the accelerometer to facilitate the self-tests/diagnostics of each individual accelerometer. Finally, the stability and maximum stress level of the accelerometer is estimated in order to ensure the safe operation of the sensor.

In chapter 7, major conclusions drawn from this dissertation research are summarized and a few recommendations and suggestions for further studies in this area are presented.

CHAPTER 2

STEADY STATE RESPONSE OF ELASTICALLY SUPPORTED CONTINUOUS BEAM UNDER A MOVING LOAD/MASS

2.1 INTRODUCTION

The dynamic analysis of beam type structures subjected to moving loads or moving masses is important and widespread in railway engineering as a beam resting on soil can be conveniently used to represent the track of railway. As the loads/wheels of the railway move over the beam with a very high speed, the structures over which they move are exposed to very high dynamic forces. It is, thus, necessary to understand and analyze the behaviour of these structures in order to facilitate their use in case of higher speeds and heavier loads. A wide range of analytical studies have thus been evolved in order to accurately predict the vibration of the railway track under moving loads/masses [24-38, 47, 48, 56- 64]. Most of these studies employed one-parameter Winkler foundation model consisting of infinite closely-spaced linear springs subjected to a moving load [24-28]. Although this model is very simple, it does not accurately represent the characteristics of many practical applications. Two-parameter elastic foundations, thus, have been suggested in some studies for the vibration analysis of beams under moving loads [49-51]. These models are also known as Pasternak models, which allow shear interaction between the continuous springs.

The beam, that represents the railway track, can be modeled as either an Euler-Bernoulli beam [30, 47, 48, 56-61] or a Timoshenko beam [32-38, 43, 50, 51, 62- 64] depending upon the physical system. A Timoshenko beam model considers the shear deformation and rotational inertia of the beam. Chen and Huang [57] have graphically shown that an Euler-Bernoulli beam can accurately predict the response of the beam for foundation stiffness up to 10^8 N/m^2.

Therefore, an Euler–Bernoulli beam has been considered in the present analysis, since the foundation stiffness considered is 4.078×10^6 N/m^2, which is much less than the suggested value. Moreover, an Euler–Bernoulli beam model can accurately predict the response since the depth and rotary inertia of the track can be considered small compared to the translational inertia [51]. The differential equation governing the system can be obtained by the dynamic equilibrium of beam resting on elastic foundation subjected to moving load or moving mass.

In the present analysis, dynamic responses of an Euler-Bernoulli beam under constant moving load as well as constant moving mass are investigated. In case of moving load, the exact analysis has been validated by numerical method. However, only numerical method is employed in case of moving mass problem. The foundation representing the soil is modeled as both one-parameter Winkler and two-parameter Pasternak model. The beam and foundation both were assumed to be homogeneous and isotropic. Fourier transform technique is employed to find the analytical solution of the governing partial differential equation in case of moving load problem. Both the static and dynamic responses of the beam in terms of beam deflections, bending moments and shear force have been obtained for both damped and undamped cases with different velocity ratios. The effects of shear modulus and foundation stiffness on deflection and bending moment responses have also been investigated.

2.2 MODELING OF BEAM ON PASTERNAK FOUNDATION

The governing equation of motion of an Euler-Bernoulli beam resting on two-parameter Pasternak foundation and subjected to a moving load or mass, as shown in Fig. 2.1, can be written as [51]:

$$EI\frac{\partial^4 w}{\partial x^4}+\rho_r\frac{\partial^2 w}{\partial t^2}+c\frac{\partial w}{\partial t}-k_1\frac{\partial^2 w}{\partial x^2}+k_f w=F(x,t) \tag{2.1}$$

where, $F\left(x,t\right)=P\delta(x-vt)$ in case of moving load, and $F\left(x,t\right)=\left[Mg-M\frac{\partial^2 w(vt,t)}{\partial t^2}\right]\delta(x-vt)$ in case of moving mass, $w=w(x,t)$ is the transverse deflection of the beam, E is the Young's modulus of elasticity of the beam material, I is the second moment of area of the beam cross section about its neutral axis, ρ_r is the mass per unit length of the beam, c is the coefficient of viscous damping per unit length of the beam, k_1 is the shear parameter of the beam, k_f is the spring constant of the foundation per unit length, $P\delta(x-vt)$ is the applied moving load per unit length, x is the space coordinate measured along the length of the beam, t is the time in second, M is the moving mass, g is the acceleration due to gravity, and δ is the Dirac delta function.

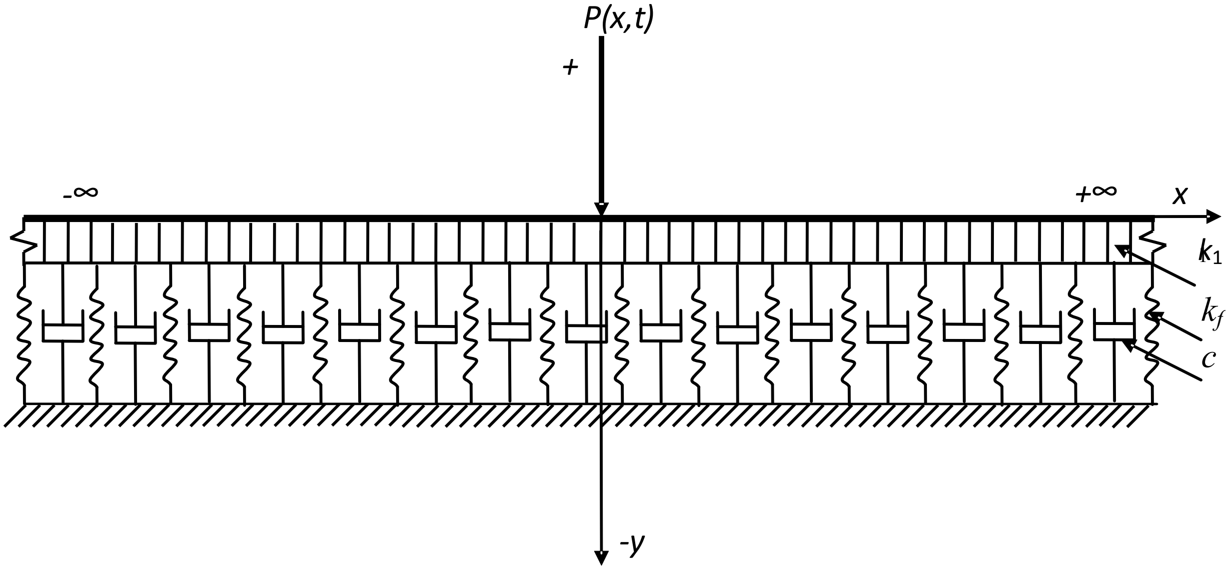

(a)

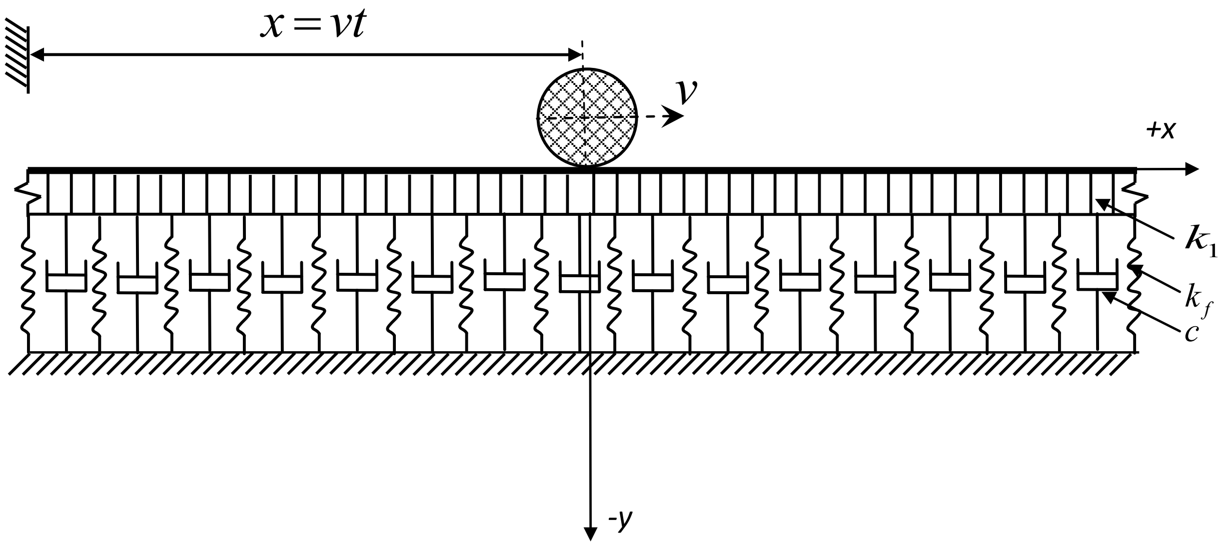

(b)

Fig. 2.1: Beam on Pasternak foundation subjected to a (a) moving load; and (b) moving mass.

Defining the followings, $a = \frac{\rho_r}{2EI}, b^2 = \frac{k_f}{EI}$, $c_1 = \frac{k_1}{2EI}$, $d = \frac{c}{EI}$, Eqn. (2.1) can be written as:

$$\frac{\partial^4 w}{\partial x^4} + 2a\frac{\partial^2 w}{\partial t^2} + d\frac{\partial w}{\partial t} - 2c_1\frac{\partial^2 w}{\partial x^2} + b^2 w = \frac{F}{EI}(x,t) \qquad (2.2)$$

2.3 METHOD OF ANALYSIS FOR A BEAM UNDER MOVING LOAD

The dynamic response of an Euler-Bernoulli beam under constant moving load has been investigated by both Fourier transform technique and modal analysis method. The exact analysis has been validated by the numerical method. This section describes the formulation of the analytical solution of the governing partial differential equation by means of Fourier transform technique. Solutions have been obtained for both damped and undamped conditions, where the speed varies from below to above the critical velocities.

2.3.1 For undamped case (velocity less than the critical):

In case of undamped system, $c = 0$ and for one parameter model, $k_1 = 0$, then Eqn. (2.2) can be written as:

$$\frac{\partial^4 w}{\partial x^4} + 2a\frac{\partial^2 w}{\partial t^2} + b^2 w = \frac{P}{EI}\delta(x - vt) \tag{2.3}$$

Let, $$w^*(\gamma, t) = \int_{-\infty}^{\infty} w(x,t)e^{-i\gamma x}dx \tag{2.4.a}$$

and, $$w(x,t) = \frac{1}{2\pi}\int_{-\infty}^{\infty} w^*(\gamma,t)e^{+i\gamma x}d\gamma \tag{2.4.b}$$

constitute a Fourier transform pair, where, γ is a variable in complex plane. Both sides of Eqn. (2.3) are multiplied by $e^{-i\gamma x}$ and integrated by parts over x from $-\infty$ to $+\infty$. Assuming that w and its space derivatives vanish at $x = \pm\infty$, namely, for $x \to +\infty, x \to -\infty$; $w(x) = w'(x) = w''(x) = w'''(x) = 0$, we get

$$\gamma^4 w^* + b^2 w^* + 2a\frac{d^2 w^*}{dt^2} = \frac{P}{EI}e^{-i\gamma vt} \tag{2.5}$$

The solution of the homogeneous part of Eqn. (2.5) in the presence of light damping dies down and is neglected here. Thus, the steady state solution is given by only the particular integral of Eqn. (2.5).

Substituting $w^* = W^* e^{-i\gamma vt}$ in Eqn. (2.5), we obtain

$$(\gamma^4 + b^2 - 2a\gamma^2 v^2)W^* = \frac{P}{EI} \tag{2.6}$$

or, $$W^* = \frac{P}{EI}\left[\frac{1}{\gamma^4 - 2a\gamma^2 v^2 + b^2}\right] \tag{2.7}$$

or, $w^* = \frac{P}{EI}\left[\frac{1}{\gamma^4 - 2a\gamma^2 v^2 + b^2}\right]e^{-i\gamma vt}$ (2.8)

Thus, from Eqn. (2.4.b) one obtains

$$w(x,t) = \frac{P}{EI}\frac{1}{2\pi}\int_{-\infty}^{\infty}\frac{e^{i\gamma(x-vt)}}{\gamma^4 - 2a\gamma^2 v^2 + b^2}d\gamma \tag{2.9}$$

The integral in Eqn. (2.9) is evaluated by contour integration as discussed below [25]

$$w(x,t) = \frac{P}{EI}\frac{1}{2\pi}(2\pi i)\sum \text{residues at four simple poles.} \tag{2.10}$$

<u>Calculation of the residues:</u>

Let $s(\gamma) = \gamma^4 - 2a\gamma^2 v^2 + b^2 = (\gamma - \gamma_1)(\gamma - \gamma_2)(\gamma - \gamma_3)(\gamma - \gamma_4)$ (2.11)

Let, as shown in Fig. 2.2, the four roots of γ of Eqn. (2.11) be,

$\gamma_1 = \beta + i\alpha$, and $\gamma_3 = -(\beta + i\alpha)$. (2.12)

$\gamma_2 = -\beta + i\alpha$, and $\gamma_4 = \beta - i\alpha$. (2.13)

Substituting the values of γ_i's in terms of α and β from Eqns. (2.12) and (2.13) into Eqn. (2.11), and equating the coefficients of similar terms, we get:

$\alpha^2 + \beta^2 = b$, (2.14)

$\beta^2 - \alpha^2 = av^2$. (2.15)

From Eqns. (2.14) and (2.15), we get

$$\beta = \sqrt{\frac{b + av^2}{2}}, \quad \alpha = \sqrt{\frac{b - av^2}{2}}. \tag{2.16}$$

Poles at γ:

$s(\gamma) = 0 \Rightarrow \gamma^4 - 2a\gamma^2 v^2 + b^2 = 0$.

Assume $v^2 < \frac{b}{a}$, where the critical velocity is given by $v_{cr}^2 = \frac{b}{a}$

For $v < v_{cr}$,

$$\gamma_{1,3}^2 = av^2 + i\sqrt{b^2 - (av^2)^2} \tag{2.17}$$

and, $\gamma_{2,4}^2 = av^2 - i\sqrt{b^2 - (av^2)^2}$ (2.18)

The four poles are shown in Fig. 2. 2, two each on either side of the real axis.

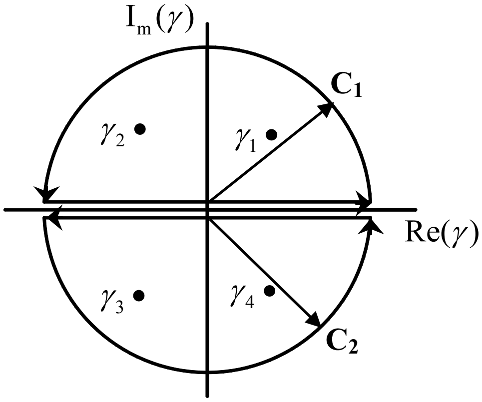

Fig. 2. 2: Position of the poles for velocity less than the critical velocity.

For $\xi(= x - vt) > 0$, considering the contour C_1 (going from $-\infty$ to $+\infty$ on the real axis in order to travel in the counter clock wise direction along the contour), we get,

$w(x,t) = \frac{iP}{EI}$ [Residue at γ_1 + Residue at γ_2].

or, $w(x,t) = \frac{iP}{EI}\left[\frac{e^{i\gamma_1\xi}}{(\gamma_1-\gamma_2)(\gamma_1-\gamma_3)(\gamma_1-\gamma_4)} + \frac{e^{i\gamma_2\xi}}{(\gamma_2-\gamma_1)(\gamma_2-\gamma_3)(\gamma_2-\gamma_4)}\right].$ (2.19)

Substituting γ_i's in terms of α and β, we finally get

$$w(x,t) = \frac{Pe^{-\alpha\xi}}{4EI\alpha\beta b}[\beta\cos\beta\xi + \alpha\sin\beta\xi]. \tag{2.20}$$

Similarly, for $\xi < 0$, considering the contour C_2 (going from $+\infty$ to $-\infty$ on the real axis in order to travel in the counter-clock wise direction along the contour), we get

$$w(x,t) = \frac{iP}{EI}[\text{Residues at } \gamma_3 + \text{Residues at } \gamma_4]. \tag{2.21}$$

$$w(x,t) = \frac{iP}{EI}\left[\frac{e^{i\gamma_3\xi}}{(\gamma_3-\gamma_1)(\gamma_3-\gamma_2)(\gamma_3-\gamma_4)} + \frac{e^{i\gamma_4\xi}}{(\gamma_4-\gamma_1)(\gamma_4-\gamma_2)(\gamma_4-\gamma_3)}\right]. \tag{2.22}$$

Substituting γ_i's in terms of α and β, we finally get

$$w(x,t) = \frac{Pe^{\alpha\xi}}{4EI\alpha\beta b}[\beta\cos\beta\xi - \alpha\sin\beta\xi]. \tag{2.23}$$

Bending moment:

We know, Bending moment, $M(x,t) = EI\dfrac{\partial^2 w(x,t)}{\partial x^2}$ (2.24)

For $\xi > 0$, substituting the value of $w(x,t)$ from Eqn. (2.20) into Eqn. (2.24) and differentiating it twice with respect to x gives:

$$M(x,t) = \frac{-P\beta e^{-\alpha\xi}}{4\alpha b}[\beta\cos\beta\xi + \alpha\sin\beta\xi]. \tag{2.25}$$

Similarly, for $\xi < 0$, substituting the value of $w(x,t)$ from Eqn. (2.23) into Eqn. (2.24) and differentiating it twice with respect to x gives:

$$M(x,t) = \frac{-P\beta e^{\alpha\xi}}{4\alpha b}[\beta\cos\beta\xi - \alpha\sin\beta\xi]. \tag{2.26}$$

Shear force:

We know, Shear force $T(x,t) = EI\dfrac{\partial^3 w(x,t)}{\partial x^3}$ (2.27)

For $\xi > 0$, substituting the value of $w(x,t)$ from Eqn. (2.20) into Eqn. (2.27) and differentiating it three times with respect to x gives:

$$T(x,t) = \frac{P\beta^2 e^{-\alpha\xi}}{4\alpha b}[\beta \sin \beta\xi - \alpha \cos \beta\xi]. \tag{2.28}$$

Similarly, for $\xi < 0$, substituting the value of $w(x,t)$ from Eqn. (2.23) into Eqn. (2.27) and differentiating it three times with respect to x gives:

$$T(x,t) = \frac{P\beta^2 e^{\alpha\xi}}{4\alpha b}[\beta \sin \beta\xi + \alpha \cos \beta\xi]. \tag{2.29}$$

2.3.2 For undamped case (velocity greater than the critical):

For $v > v_{cr}$, Eqns. (2.12) and (2.13) can be written for two parameter model as:

$$\gamma_{1,2,3,4}^2 = -(av^2 - c_1) \pm \sqrt{(av^2 - c_1)^2 - b^2} \tag{2.30}$$

Let, the four roots of γ of Eqn. (2.30) be

$$\begin{aligned} \gamma_1 &= q, \\ \gamma_2 &= -q, \\ \gamma_3 &= r, \\ \gamma_4 &= -r. \end{aligned} \tag{2.31}$$

where, q and r are given by

$$q = \sqrt{\frac{(av^2 - c_1 + b)}{2}} + \sqrt{\frac{(av^2 - c_1 - b)}{2}} \tag{2.32}$$

$$\text{and, } r = \sqrt{\frac{(av^2 - c_1 + b)}{2}} - \sqrt{\frac{(av^2 - c_1 - b)}{2}} \tag{2.33}$$

Thus, the four poles are as shown in Fig. 2.3. For, $\xi(= x - vt) > 0$,

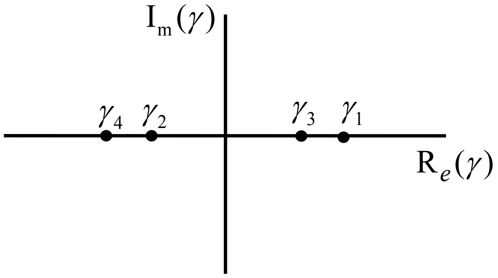

Fig. 2.3: Position of the poles for velocity greater than the critical velocity.

$$w(x,t) = \frac{iP}{EI}\,[\text{Residues at}\,\gamma_1 + \text{Residues at }\,\gamma_2].$$

$$\text{or, } w(x,t) = \frac{iP}{EI}\left[\frac{e^{i\gamma_1\xi}}{(\gamma_1-\gamma_2)(\gamma_1-\gamma_3)(\gamma_1-\gamma_4)} + \frac{e^{i\gamma_2\xi}}{(\gamma_2-\gamma_1)(\gamma_2-\gamma_3)(\gamma_2-\gamma_4)}\right]. \tag{2.34}$$

Substituting γ_i's in terms of q and r, we get

$$w(x,t) = \frac{iP}{EI}\left[\frac{e^{iq\xi}}{2q(q^2-r^2)} - \frac{e^{-iq\xi}}{2q(q^2-r^2)}\right] \tag{2.35}$$

$$= \frac{iP}{EI}\left[\frac{(\cos q\xi + i\sin q\xi) - (\cos q\xi - i\sin q\xi)}{2q(q^2-r^2)}\right]$$

Finally, the deflection of the beam is obtained as

$$w(x,t) = -\frac{P}{qEI(q^2-r^2)}\sin q\xi \tag{2.36}$$

Similarly, for $\xi < 0$, we get

$$w(x,t) = \frac{iP}{EI}\,[\text{Residues at}\,\gamma_3 + \text{Residues at }\,\gamma_4]. \tag{2.37}$$

$$w(x,t) = \frac{iP}{EI}\left[\frac{e^{i\gamma_3\xi}}{(\gamma_3-\gamma_1)(\gamma_3-\gamma_2)(\gamma_3-\gamma_4)} + \frac{e^{i\gamma_4\xi}}{(\gamma_4-\gamma_1)(\gamma_4-\gamma_2)(\gamma_4-\gamma_3)}\right]. \tag{2.38}$$

Substituting γ_i's in terms of q and r, and following the same procedures as outlined in Eqn. (2.35), the equation of beam deflection can be written as

$$w(x,t) = -\frac{P}{rEI(q^2 - r^2)} \sin r\xi \tag{2.39}$$

The expression for bending moment, $M(x,t)$, and shear force, $T(x,t)$, can also be obtained by substituting the value of $w(x,t)$ from Eqns. (2.36) and (2.39) into Eqns. (2.24) and (2.27).

2.3.3 For underdamped case (with two-parameter model):

In the presence of damping, Eqn. (2.9) can be written as

$$w(x,t) = \frac{P}{EI}\frac{1}{2\pi}\int_{-\infty}^{\infty} \frac{e^{i\gamma(x-vt)}}{\gamma^4 - 2a\gamma^2 v^2 + 2c_1\gamma^2 - idv\gamma + b^2} d\gamma \tag{2.40}$$

The integral in Eqn. (2.40) can be expressed as the limit:

$$\int_{-\infty}^{\infty} F(\gamma) d\gamma = \lim_{\mathrm{R}\to\infty} \int_{-\mathrm{R}}^{+\mathrm{R}} \frac{e^{i\gamma(x-vt)}}{\gamma^4 - 2a\gamma^2 v^2 + b^2 + 2c_1\gamma^2 - idv\gamma} d\gamma \tag{2.41}$$

where R is the radius of semicircle *C*.

According to Cauchy's residue theorem, the integral in the counter-clock wise direction around the closed curve C_c consisting of segments *–R*, *+R* and semicircle *C* at limit R = ∞ is

$$\begin{aligned} \oint_{C_c} \frac{e^{i\gamma(x-vt)}}{\gamma^4 - 2a\gamma^2 v^2 + b^2 + 2c_1\gamma^2 - idv\gamma} d\gamma &= \lim_{\mathrm{R}\to\infty} \int_{-\mathrm{R}}^{+\mathrm{R}} \frac{e^{i\gamma(x-vt)}}{\gamma^4 - 2a\gamma^2 v^2 + b^2 + 2c_1\gamma^2 - idv\gamma} d\gamma \\ + \int_{C_c} \frac{e^{i\gamma(x-vt)}}{\gamma^4 - 2a\gamma^2 v^2 + b^2 + 2c_1\gamma^2 - idv\gamma} d\gamma &= 2\pi i \sum_{j=1}^{n} residueF(\gamma)|_{\gamma=\gamma_j} \end{aligned} \tag{2.42}$$

where n=4, is the number of poles in the circle.

The integral in Eqn. (2.40) is evaluated by contour integration as discussed above [179], and we obtain

$$w(x,t) = \frac{P}{EI}\frac{1}{2\pi}(2\pi i)\sum \text{residues at four simple poles.} \tag{2.43}$$

Considering ($k_1 = 0$ and $d = 0$) Let $s(\gamma) = \gamma^4 - 2a\gamma^2 v^2 + b^2$

Poles at $\gamma : s(\gamma) = 0 \Rightarrow \gamma^4 - 2a\gamma^2 v^2 + b^2 = 0$. (2.44)

Therefore, $\gamma^2_{1,2,3,4} = av^2 \pm \sqrt{(av^2)^2 - b^2}$ (2.45)

Assume $v^2 < \dfrac{b}{a}$ where the critical velocity is given by $v^2_{cr} = \dfrac{b}{a}$

For, $v < v_{cr}, \gamma^2_{1,3} = av^2 + i\sqrt{b^2 - (av^2)^2}$. (2.46)

and, $\gamma^2_{2,4} = av^2 - i\sqrt{b^2 - (av^2)^2}$. (2.47)

From Eqn. (2.46), let the two roots of γ be

$\gamma_1 = p + ir$, and $\gamma_3 = q - ir$. (2.48)

Similarly, from Eqn. (2.47) the other two roots of γ are

$\gamma_2 = -p + ir$, and $\gamma_4 = -q - ir$. (2.49)

Let, the poles of the function of the complex variable in the integrand of Eqn. (2.40) be in the form as shown in Fig. 2.4.

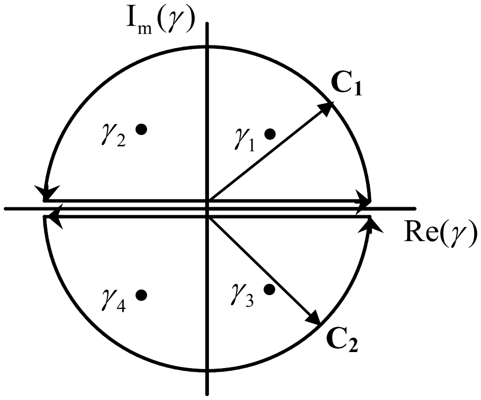

Fig. 2.4: Position of the four poles for damping less than the critical damping.

$$\begin{aligned}\gamma_1 &= p+ir,\\ \gamma_2 &= -p+ir,\\ \gamma_3 &= q-ir,\\ \gamma_4 &= -q-ir.\end{aligned} \tag{2.50}$$

The poles can be determined by the roots of the denominator $Q(\gamma)$ in Eqn. (2.40). The values of p, q, and r are computed from the condition:

$$Q(\gamma)=\gamma^4-2a\gamma^2v^2+2c_1\gamma^2-idv\gamma+b^2=(\gamma-\gamma_1)(\gamma-\gamma_2)(\gamma-\gamma_3)(\gamma-\gamma_4) \tag{2.51}$$

Substituting the values of γ_i's in terms of p, q and r from Eqn. (2.50) into Eqn. (2.51), and equating the coefficients of similar terms, we get:

$$2r^2-p^2-q^2=-2av^2+2c_1, \tag{2.52.a}$$

$$2ri(q^2-p^2)=-idv, \tag{2.52.b}$$

$$(p^2+r^2)(q^2+r^2)=b^2. \tag{2.52.c}$$

From Eqns. (2.52.a) and (2.52.b), we get

$$p^2=av^2-c_1+r^2+\frac{1}{4r}dv, \tag{2.53}$$

$$q^2=av^2-c_1+r^2-\frac{1}{4r}dv, \tag{2.54}$$

By substituting the p and q values in Eqn. (2.52.c), we get

$$r^6+(av^2-c_1)r^4+(\frac{1}{4}a^2v^2-\frac{1}{2}av^2-\frac{1}{4}b^2+\frac{1}{4}c_1^2)r^2-\frac{1}{16}d^2v^2=0 \tag{2.55}$$

Calculating the residues:

For $\xi(=x-vt)>0$, as shown in Fig. 2.4, integrating in the upper half plane:

$$w(x,t)=\frac{iP}{EI}\text{[Residues at } \gamma_1 + \text{ Residues at } \gamma_2\text{]}.$$

or, $$w(x,t)=\frac{iP}{EI}\left[\frac{e^{i\gamma_1\xi}}{(\gamma_1-\gamma_2)(\gamma_1-\gamma_3)(\gamma_1-\gamma_4)}+\frac{e^{i\gamma_2\xi}}{(\gamma_2-\gamma_1)(\gamma_2-\gamma_3)(\gamma_2-\gamma_4)}\right]. \tag{2.56}$$

Substituting γ_i' s in terms of p , q and r (as chosen in Eqn. 2.50), we finally get

$$w(x,t)=\frac{P}{EIp(A_1^2+A_2^2)}\left[(A_1-A_2i)e^{i\gamma_1\xi}+(A_1+A_2i)e^{i\gamma_2\xi}\right] \tag{2.57}$$

$$=\frac{2P}{EIp(A_1^2+A_2^2)}e^{-r\xi}(A_1\cos p\xi+A_2\sin p\xi).$$

Similarly, for $\xi<0$,

$$w(x,t)=\frac{P}{EIq(A_3^2+A_4^2)}\left[(A_3+A_4i)e^{i\gamma_3\xi}+(A_3-A_4i)e^{i\gamma_4\xi}\right] \tag{2.58}$$

$$=\frac{2P}{EIq(A_3^2+A_4^2)}e^{r\xi}(A_3\cos q\xi-A_4\sin q\xi).$$

where, $A_1=pr, \quad A_3=qr,$ (2.59)

$$A_2=r^2-\frac{1}{4}(p^2-q^2), \quad A_4=r^2+\frac{1}{4}(p^2-q^2).$$

When damping is higher than the critical damping, Eqn. (2.54) becomes negative. Therefore, the poles can be designated in this case as shown in Fig. 2.5.

$$\gamma_1=p+ir,\ \gamma_2=-p+ir,\ \gamma_3=-(r-q)i,\ \gamma_4=-(r+q)i. \tag{2.60}$$

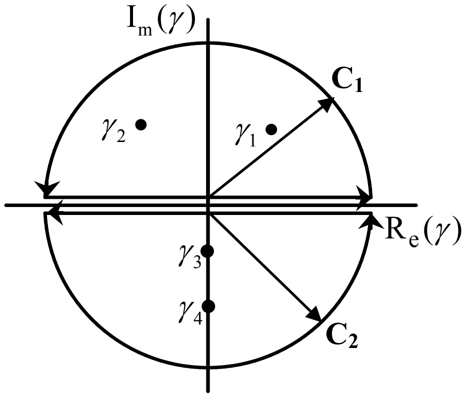

Fig. 2.5: Position of the poles for damping greater than the critical damping.

Using a procedure analogous to that of deriving Eqns. (2.51) and (2.52), we get

$$q^2 = \frac{1}{4r}dv + c_1 - av^2 - r^2. \tag{2.61}$$

The values of p and r continue to be defined by the Eqns. (2.53) and (2.55).

<u>Calculating the residues:</u>

For $\xi(= x - vt) > 0$, as shown in Fig. 2.5, integrating in the upper half plane:

$$w(x,t) = \frac{iP}{EI}\text{[Residues at } \gamma_1 + \text{Residues at } \gamma_2\text{]}.$$

or, $$w(x,t) = \frac{iP}{EI}\left[\frac{e^{i\gamma_1\xi}}{(\gamma_1-\gamma_2)(\gamma_1-\gamma_3)(\gamma_1-\gamma_4)} + \frac{e^{i\gamma_2\xi}}{(\gamma_2-\gamma_1)(\gamma_2-\gamma_3)(\gamma_2-\gamma_4)}\right]. \tag{2.62}$$

Substituting γ_i's in terms of p, q and r (as chosen in Eqn. 2.60), we finally get

$$w(x,t) = \frac{P}{EIp(A_1^2 + A_2^2)}\left[(A_1 - A_2 i)e^{i\gamma_1\xi} + (A_1 + A_2 i)e^{i\gamma_2\xi}\right] \tag{2.63}$$

$$= \frac{2P}{EIp(A_1^2 + A_2^2)}e^{-r\xi}(A_1\cos p\xi + A_2\sin p\xi).$$

Similarly, for $\xi < 0$, integration is carried out in the lower half plane of Fig. 2.5 to get:

$$w(x,t)=\frac{P}{EIq(A_4^2-A_3^2)}\left[(A_3+A_4)e^{(r-q)\xi}-(A_4-A_3)e^{(r+q)\xi}\right] \tag{2.64}$$

where, $A_1 = pr, \qquad A_3 = qr,$ (2.65)

$$A_2 = r^2-\frac{1}{4}(p^2+q^2), \quad A_4 = r^2+\frac{1}{4}(p^2+q^2)\,.$$

2.4 ANALYSIS METHOD FOR A BEAM UNDER MOVING MASS

The deflection modes of continuous beam with simply supported boundary conditions can be obtained from the Euler-Bernoulli equation of the beam. The natural deflection modes and the natural frequencies of a simply supported Euler beam can be expressed as:

$$Y_k(x)=\sin\left(\frac{k\pi x}{l}\right);\text{ and }\ \omega_k=\left(\frac{k\pi}{l}\right)^2\sqrt{\frac{EI}{\rho_r}}\,, \qquad k=1,\,2,\,3\ldots\ldots\ldots K \tag{2.66}$$

where $Y_k(x)$ is the normal mode, ω_k is the corresponding natural frequency and l is the beam length.

The above equations were obtained for the following boundary conditions:

$Y(0)=Y(l)=0$; and $Y''(0)=Y''(l)=0$ (2.67)

Assume a solution of Eqn. (2.1) in the form of a series:

$$w_r\left(x,t\right)=\sum_{k=1}^{K}Y_k(x)q_k(t) \qquad k=1,2,3.....K \tag{2.68}$$

where $Y_k(x)$ are the normal modes of the beam, $q_k(t)$ are the functions of time which have to be found and k is the number of contributing modes. Recalling Eqn. (2.1) for moving mass problem as:

$$EI\frac{\partial^4 w}{\partial x^4}+\rho_r\frac{\partial^2 w}{\partial t^2}+c\frac{\partial w}{\partial t}-k_1\frac{\partial^2 w}{\partial x^2}+k_f w=\left[Mg-M\frac{\partial^2 w(vt,t)}{\partial t^2}\right]\delta(x-vt) \tag{2.69}$$

The substitution of Eqn. (2.66) together with Eqn. (2.68) into the Eqn. (2.69) and using a simplified subscript for differentiation yields:

$$EI\left(\frac{k\pi}{l}\right)^4 \sum_{k=1}^{K} Y_k(x)q_k(t) + \rho_r \sum_{k=1}^{K} Y_k(x)\ddot{q}_k(t) + c\sum_{k=1}^{K} Y_k(x)\dot{q}_k(t) \tag{2.70}$$

$$-k_1\left(\frac{k\pi}{l}\right)^2 \sum_{k=1}^{K} Y_k(x)q_k(t) + k_f \sum_{k=1}^{K} Y_k(x)q_k(t) = \left[Mg - M\sum_{k=1}^{K} Y_k(vt)\ddot{q}_k(t)\right]$$

Multiplying both sides of Eqn. (2.70) by $Y_p(x)$ and integrating along the beam length, applying the orthogonality of functions $Y_q(x)$, and after some rearrangement it becomes

$$\frac{EI}{\rho_r}\left(\frac{k\pi}{l}\right)^4 q_k(t) + \ddot{q}_k(t) + \frac{c}{\rho_r}\dot{q}_k(t) - \frac{k_1}{\rho_r}\left(\frac{k\pi}{l}\right)^2 q_k(t) + \frac{k_f}{\rho_r} q_k(t) \tag{2.71}$$

$$= \frac{2}{\rho_r l}\left[Mg - M\sum_{k=1}^{K} Y_k(vt)\ddot{q}_k(t)\right] Y_p(vt) \qquad \text{for } k = 1,2,3.....K$$

In case of moving load problem, Eqn. (2.71) can be written as:

$$\frac{EI}{\rho_r}\left(\frac{k\pi}{l}\right)^4 q_k(t) + \ddot{q}_k(t) + \frac{c}{\rho_r}\dot{q}_k(t) - \frac{k_1}{\rho_r}\left(\frac{k\pi}{l}\right)^2 q_k(t) + \frac{k_f}{\rho_r} q_k(t) = \frac{2}{\rho_r l} P\sum_{k=1}^{K} Y_k(vt)Y_p(vt) \tag{2.72}$$

for $k = 1,2,3.....K$

Equations (2.71) and (2.72) are sets of coupled ordinary differential equations and a numerical procedure is employed to solve them. A MATLAB predefined function “ode 45” is applied to solve the differential equations in time domain. The equations are solved simultaneously to obtain the deflection and bending moment responses for both moving mass and moving load conditions.

2.5 MODEL VALIDATION

The validity of the present model is examined by comparing the responses in terms of deflection and bending moment of the beam under moving load condition with the analytical results presented in [51]. In this reported study, an infinite Euler–Bernoulli beam of constant cross-section resting on an elastic foundation with both one and two parameters was considered. The beam was subjected to a constant point load moving with a constant speed along the beam. Dynamic responses such as beam deflection, bending moment have been obtained for different velocity ratios. All the parameters considered in the validation are taken from Mallik et al. [51] and presented in Table 2.1. The variations in beam deflection and bending moment responses obtained from the present study is evaluated and compared with those reported in [51], as shown in Fig. 2.6. It can be seen that the deflection and bending moment response predicted by the current model agrees reasonably well with those reported in [51]. The amplitude of deflection and bending moment and the period of vibrations predicted by both models are also in very good agreement, although some differences in the bending moment responses become evident.

Table 2.1: Simulation parameters [51]

Parameters	Assumed values
ρ_r (kg/m)	25
EI (N-m^2)	1.75×10^6
k_f (N/m^2)	40.78×10^5
k_1 (N)	66.6875×10^4
P (N/m)	99.36×10^3

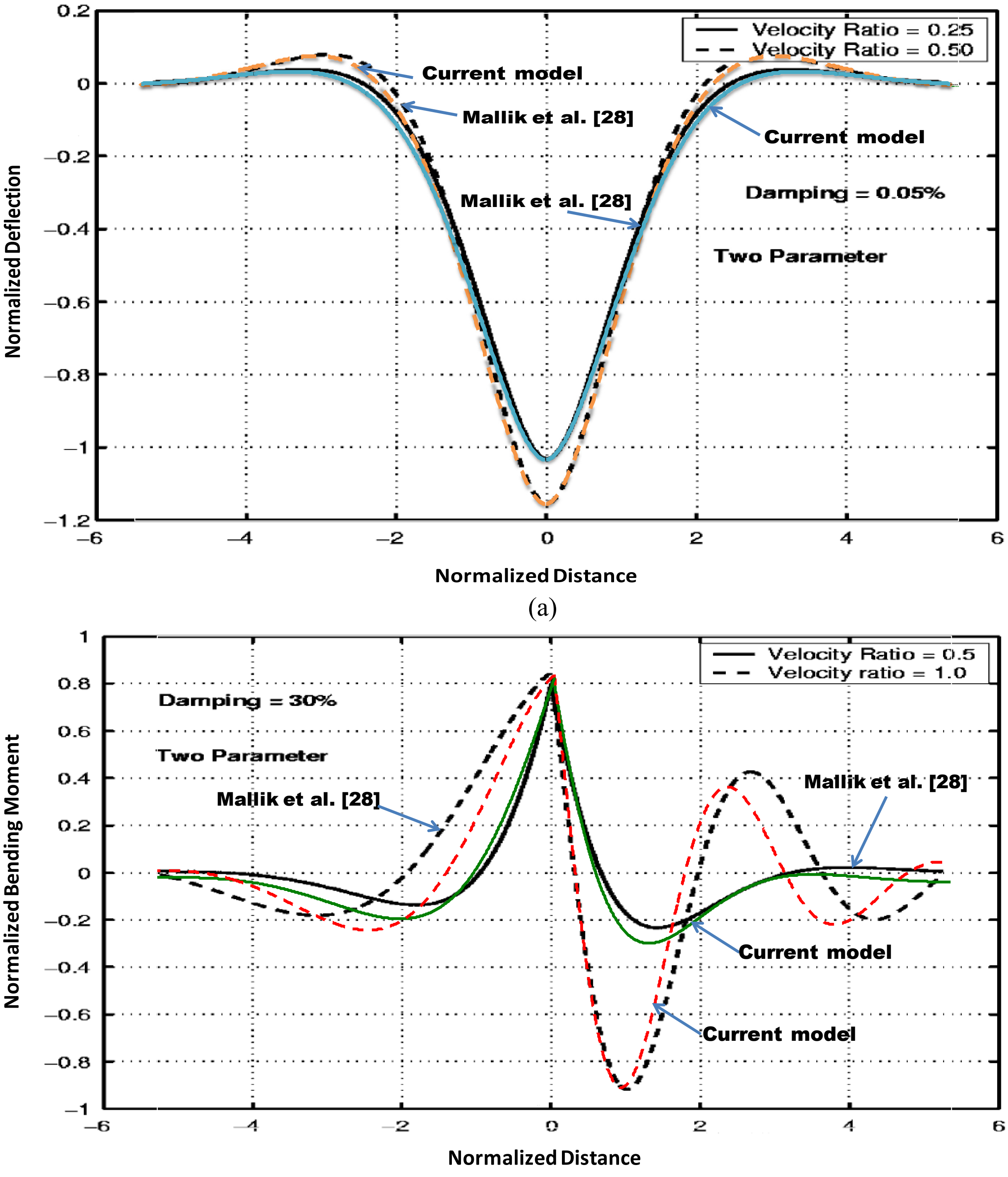

(a)

(b)

Fig. 2. 6: Comparison of beam (a) deflection and (b) bending moment responses of the present model with that reported by Mallik et al. [51].

2.6 RESULTS AND DISCUSSIONS

Numerical computations have been carried out based on the analytical solutions obtained in sections 2.3 and 2.4 for both moving load and moving mass conditions. The normalized dynamic responses in terms of deflection, bending moment and shear force are obtained with respect to the normalized position of the beam. The deflection is normalized by dividing the response obtained by its maximum value under static condition. The normalized distance is obtained by multiplying the distance along the beam (ahead and behind the load) by the coefficient of characteristic wavelength, which can be expressed as [51]: $\lambda = \sqrt{b/2}$. The velocity at which the deflection response shoots up to infinity is known as critical velocity, which can be expressed as: $v_{cr} = \sqrt{(b+c_1)/a}$. The normalized bending moment is obtained by dividing the bending moment response by its maximum value for the static case. Similarly, the normalized shear force is obtained by dividing the bending moment response by its maximum value for the static condition. The parameters used in the present study are given in Table 2.1. The normalized dynamic responses in terms of deflections, bending moment and shear force of the beam are obtained with respect to the normalized position of the beam.

2.6.1 Exact analysis:

The dynamic normalized deflections of a beam resting on two-parameter Pasternak foundation subjected to a moving load with various velocity ratios (v/v_{cr}) are shown in Fig. 2.7. In Fig. 2.7 (a), the results show that the deflections are symmetric about the contact point with moving load for all the selected velocity ratios and the maximum deflections occur beneath the load and die down at a distance far away from the load. In this study, a zero velocity ratio represents static load condition. The negative value of the deflection signifies the downward deflection with the moving load acting downward. A small amount of uplift (positive deflection) occurs at distances away from the load. The figure further shows that the maximum dynamic deflection for both upward and downward deflection increases with increase in the velocity ratios of the moving load.

The normalized deflection responses of the beam for velocities greater than the critical velocity are shown in Fig. 2.7 (b). It can be seen that the deflection at the loading point approaches zero as velocity increases to greater than the critical velocity. Figure 2.7 (b) further shows that increase in velocities decreases the peak deflection of the beam for both front (right hand side of the curve from origin zero) and rear wave (left hand side of the curve from origin zero). The wavelengths of the front waves also decrease with increase in speed. However, the peak deflection values in the rear waves are greater than the front waves for a constant velocity ratio. The figure further shows that point of maximum settlement (downward deflection) occurs behind the load and the distance of this point from the load increases with increasing speed. The figure also illustrates that maximum amount of uplift never dies out although it is far away from the load, which can be attributed to the very low damping ratio ($c / c_{cr} = 0.0005$).

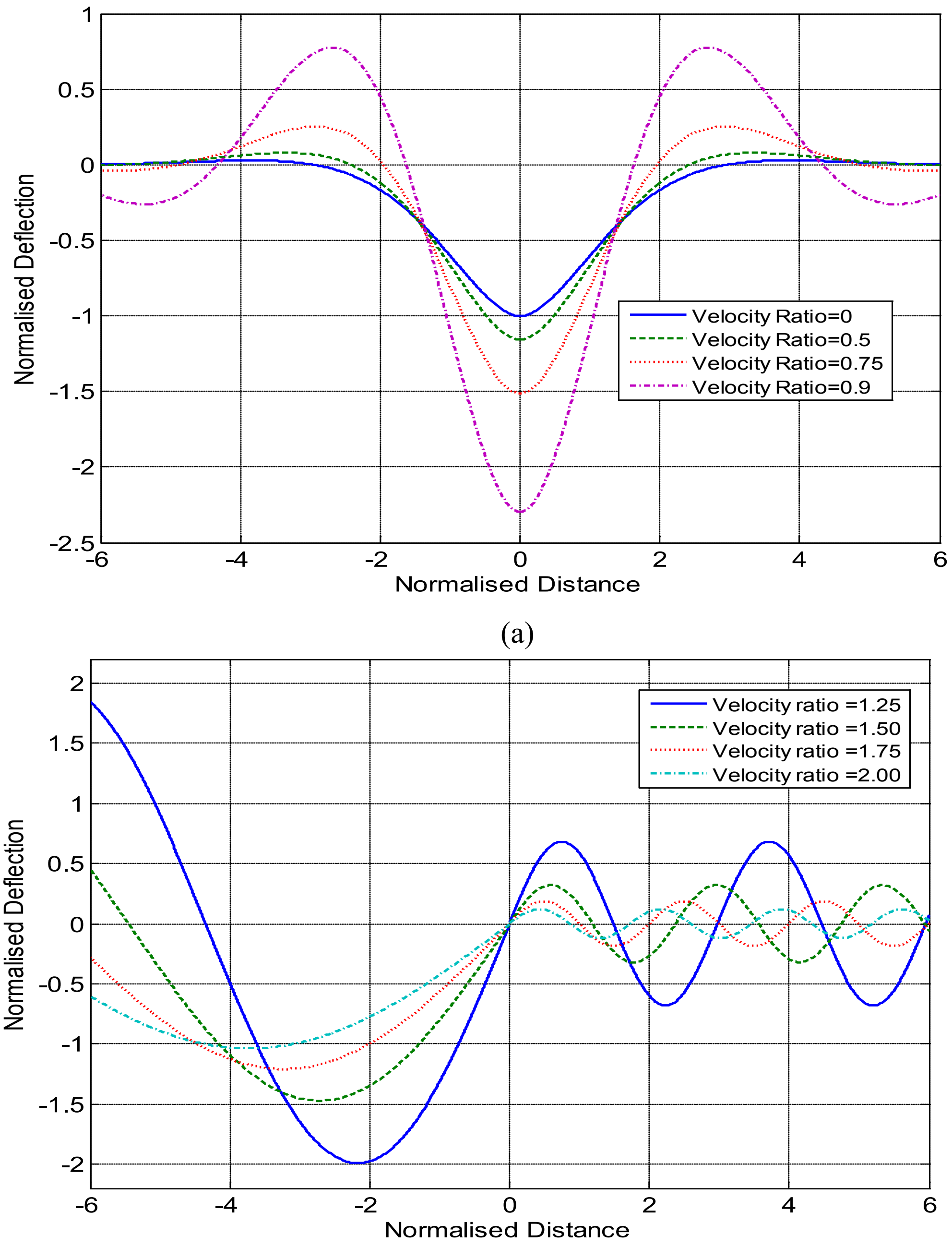

(a)

(b)

Fig. 2. 7: Normalized deflection vs. normalized distance with velocity ratios (a) less than the critical velocity (v/v_{cr} =0, 0.5, 0.75 and 0.9); (b) greater than the critical velocity (v/v_{cr} =1.25, 1.50, 1.75 and 2.0) with damping ratio (c/c_{cr} = 0.0005) for two parameter model.

Figure 2.8 shows the normalized deflection response of the beam for different velocities, which are equal to and less than the critical velocity and for a damping ratio of 0.03. The figure clearly shows, similar to Fig. 2.7 (a), the increase in peak deflection of the beam with increase in speed. The figure further shows that with increase in speed the points of maximum settlements and uplifts shift behind and ahead of the load, respectively. The amount of shifts also increases with increase in speed. However, the peak value of uplift dies down as it is away from the load due to the presence of damping.

The differences in peak magnitude of normalized bending moment and normalized deflection between a one-parameter Winkler and two-parameter Pasternak foundation model are shown in Figs. 2.9 and 2.10. It can be seen from Fig. 2.9 that for a velocity ratio of 0.99 and undamped case, the magnitude of the maximum bending moment is somewhat less for the two parameter model than that for the one parameter model. Similar difference also can be obtained for peak deflection response for a velocity ratio=1.0 and damping ratio=0.30, as shown in Fig. 2.10. These differences can be attributed to the shear interaction between the springs of the foundations that has been considered in two- parameter (Pasternak) foundation model. The maximum difference in the peak value in bending moment is around 6%, while for deflection it is around 3%. The figures further show that despite the differences in peak values in peak magnitude of bending moment and deflection, the wavelengths at the front and rear of the moving load are same for both foundation models.

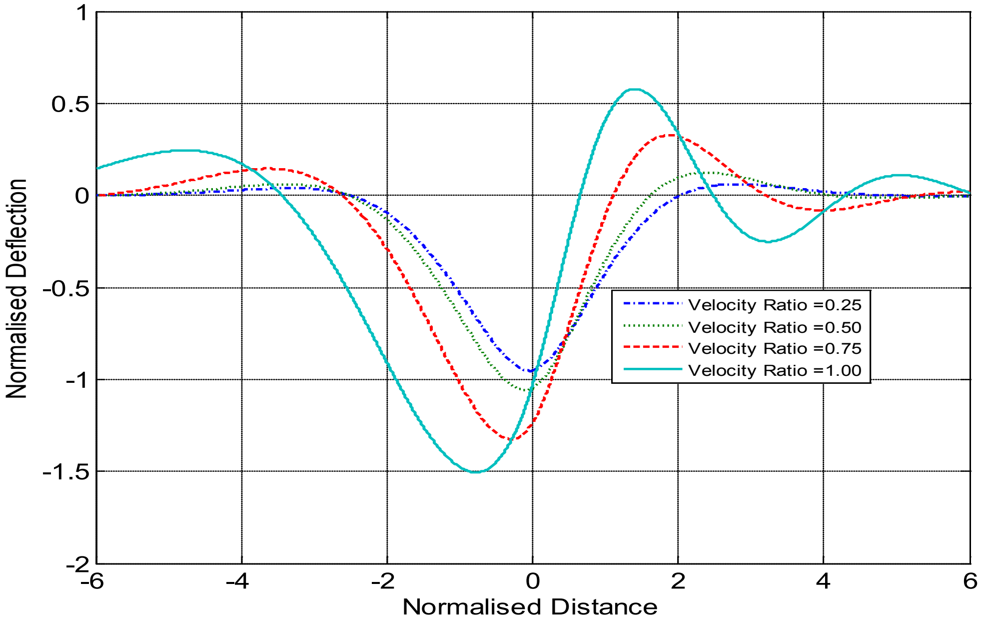

Fig. 2. 8: Normalized deflection vs. normalized distance with different velocity ratios

(v / v_{cr} =0.25, 0.50, 0.75 and 1.0) with damping ratio (c / c_{cr} = 0.03) for two parameter model.

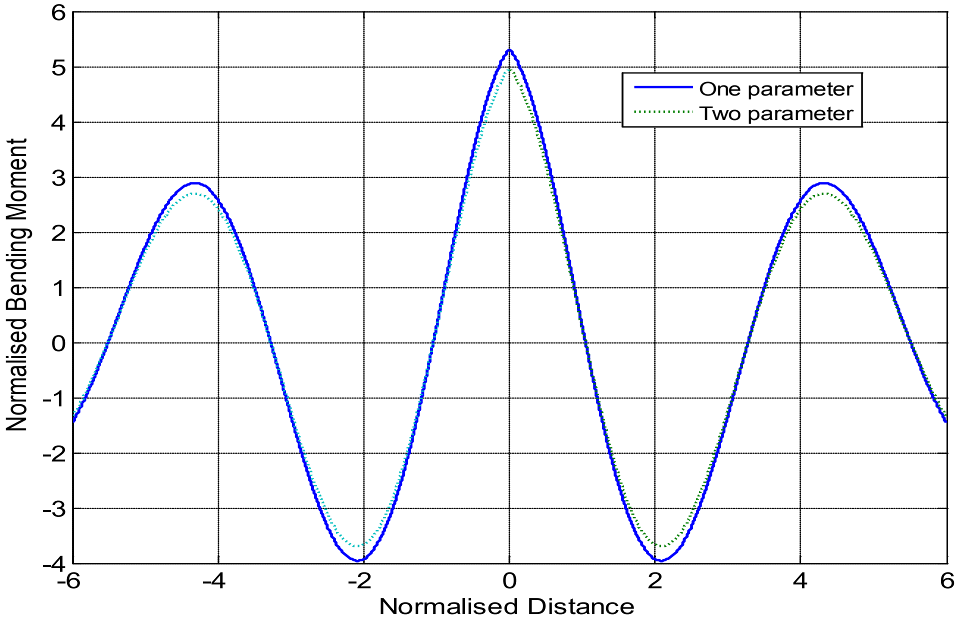

Fig. 2. 9: Normalized bending moment vs. normalized distance without damping for velocity

ratio =0.99 for one and two parameter models.

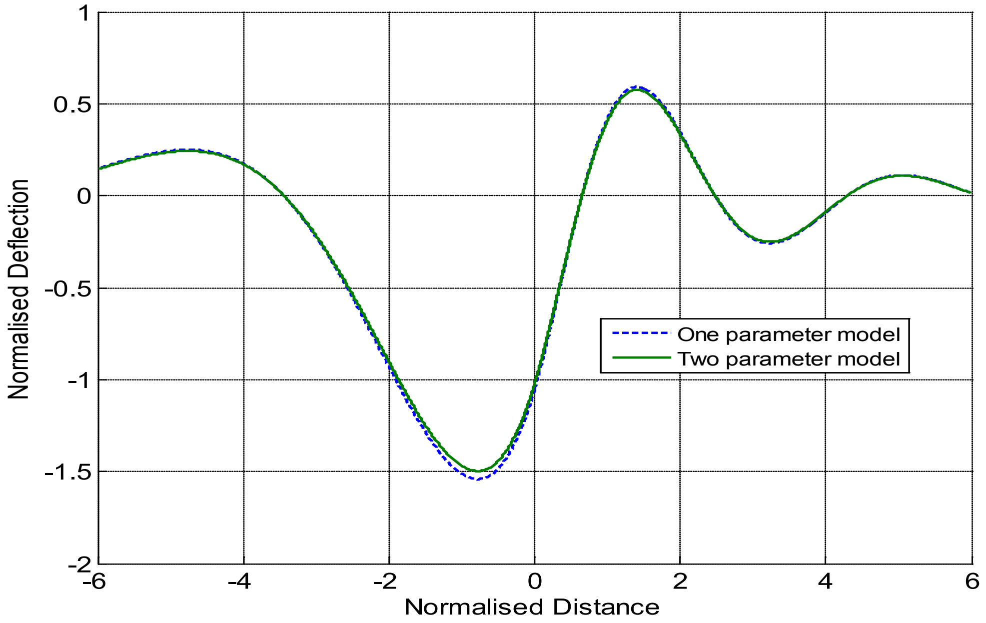

Fig. 2. 10: Normalized deflection vs. normalized Distance with damping ratio=0.30 and velocity ratio =1, for one and two parameter models.

Figure 2.11 shows the deflection responses of the beam with a damping ratio of 0.30 and for velocities above the critical velocity. These responses for beam deflections are similar to the responses, as shown in Fig. 2.7(b), for a very low damping ratio in terms of front and rear waves and shifts of the settlement and uplift. However, decays in peak of the front waves occur as they move away from the center point, which can be attributed to the higher damping ratios. The figure further illustrates that the smaller the velocity ratio the higher is the decay rate.

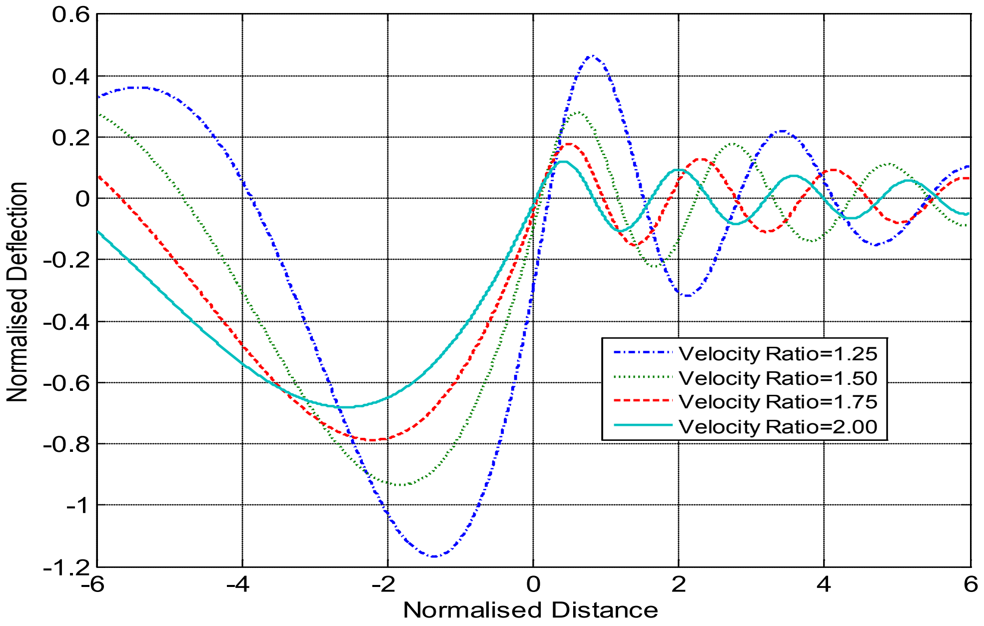

Fig. 2. 11: Normalized deflection vs. normalized distance with different velocity ratios above the critical velocity (v / v_{cr} =1.25, 1.50, 1.75 and 2.0) with damping ratio (c / c_{cr} = 0.3) for two parameter model.

The variations in normalized bending moment (dividing the dynamic bending moment responses by the maximum value of it in static case) for velocities less than and equal to the critical velocity along the beam are shown in Fig. 2.12 (a). The figure shows the absolute value of the bending moment distribution is symmetrical about the load for zero velocity ratio. The figure also shows small variations in the maximum negative bending moment at front and rear of the load for velocities below the critical velocity. The figure further shows that maximum negative bending moment occurs at a point ahead of the load and the magnitude of this peak negative bending moment increases with increase in speed. However, the maximum positive bending moment occurs at the point of the load. With decrease in speed, the maximum negative bending moments at both front and rear of the load shift away from the load.

Figure 2.12 (b) shows the variations in bending moment distribution along the beam for velocities above the critical velocities. Similar to Fig. 2.12 (a), the maximum negative bending moment occurs at a point ahead of the load and shifts away from the load with decrease in speed. The magnitude of this peak negative bending moment, however, decreases with increase in speed. As the speed decreases, the maximum positive bending moment shifts behind the load. The maximum negative bending moment decreases in oscillatory fashion as it moves away from the load, which can be attributed to the viscous damping coefficient of the beam. Similar to the deflection characteristic of the beam, the higher the velocity ratio the smaller is the decay rate.

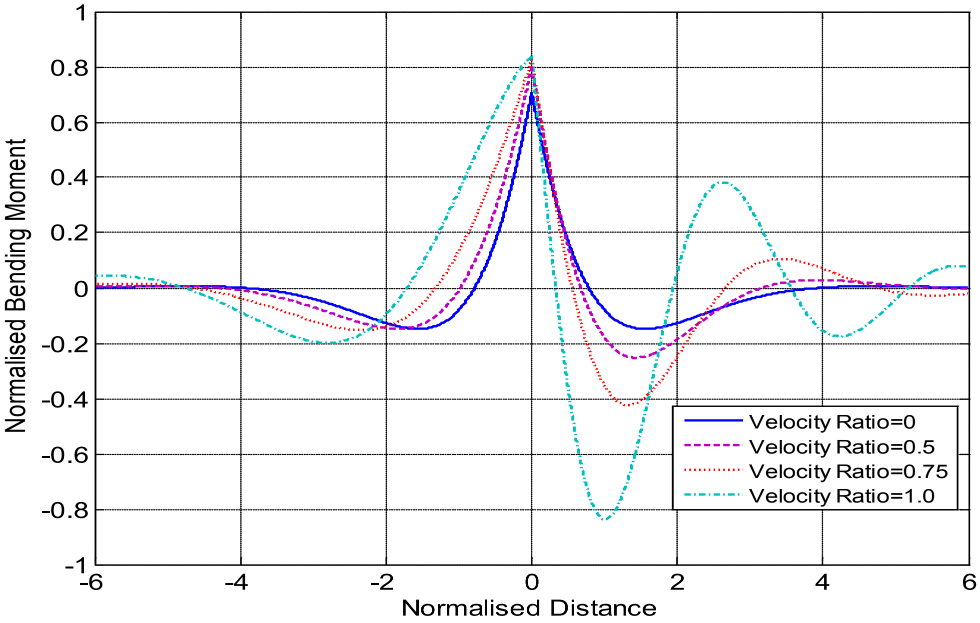

(a)

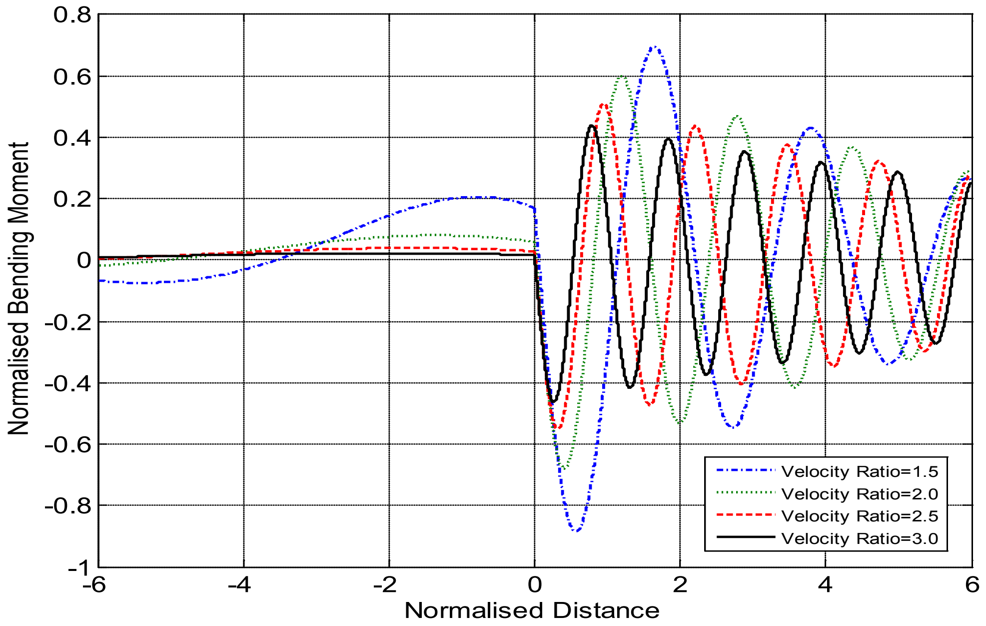

(b)

Fig. 2. 12: Normalized bending moment vs. normalized distance with different velocity ratios (a) (v/v_{cr}=0, 0.50, 0.75 and 1.0); and (b) greater than the critical velocity (v/v_{cr}=1.50, 2.00, 2.50 and 3.00) with damping ratio (c/c_{cr}= 0.3) for two parameter model.

The variations in shear force distribution along the length of the beam for subcritical, critical and supercritical velocities are shown in Figs. 2.13 and 2.14. The damping ratio is considered as 0.1. For all velocities, the maximum negative shear force occurs at a point ahead of the load and shifts away from the load with decrease in speed. For subcritical velocities, as shown in Fig. 2.13, the maximum shear force becomes negative at the point just behind the load whereas it is positive for critical and supercritical velocities, as shown in Fig. 2.14. For supercritical velocities, the peak shear force decreases in oscillatory fashion as it moves away from the load due to the presence of damping. Figure 2.14 further shows that the peak and wavelength of the front waves decrease with increase in speed.

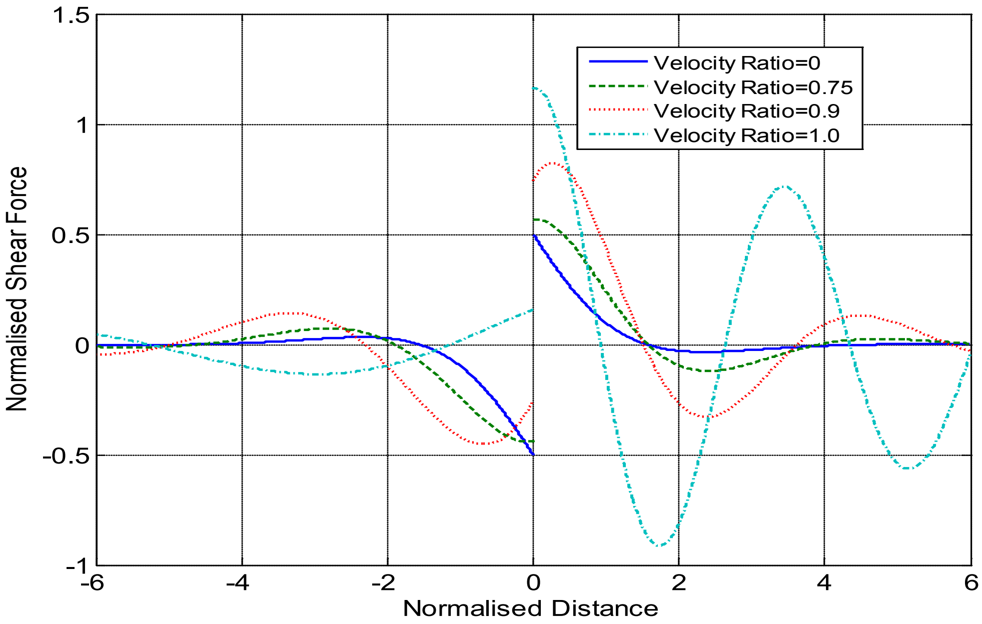

Fig. 2. 13: Normalized shear force vs. normalized distance with different velocity ratios (v / v_{cr} =0,0.75, 0.90 and 1.00) with damping ratio (c / c_{cr} =0.1) for two parameter model.

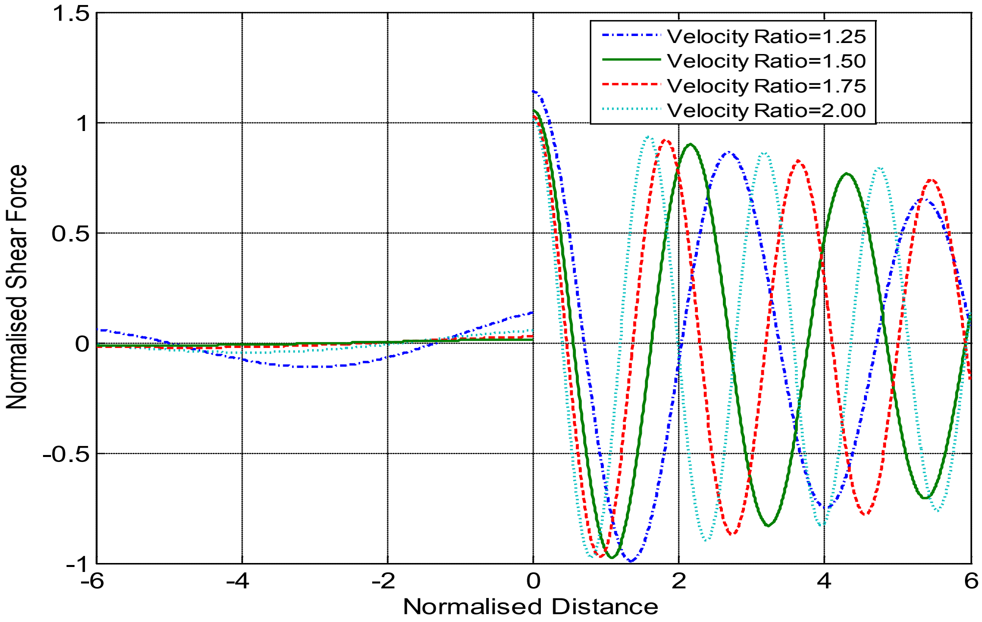

Fig. 2. 14: Normalized shear force vs. normalized distance with different velocity ratios greater than the critical velocity (v / v_{cr} =1.25, 1.50, 1.75 and 2.00) with damping ratio (c / c_{cr} = 0.1).

The variations in shear force distribution along the beam for a combination of different velocity and damping ratios where the damping is higher than the critical damping are shown in Fig. 2.15. It can be seen that at the point of load, maximum positive shear force occurs for the front wave and maximum negative shear force occurs for the rear wave. The responses are similar to those obtained in Fig. 2.13. However, only a few waves can propagate along the beam due to the high damping ratios.

A measure in terms of magnification factor is further defined as the ratio of the maximum dynamic responses to maximum static values. The variations in dynamic magnification factors for deflections and bending moments under, behind and ahead of the load with different velocities and damping ratios are shown in Figs. 2.16-2.19.

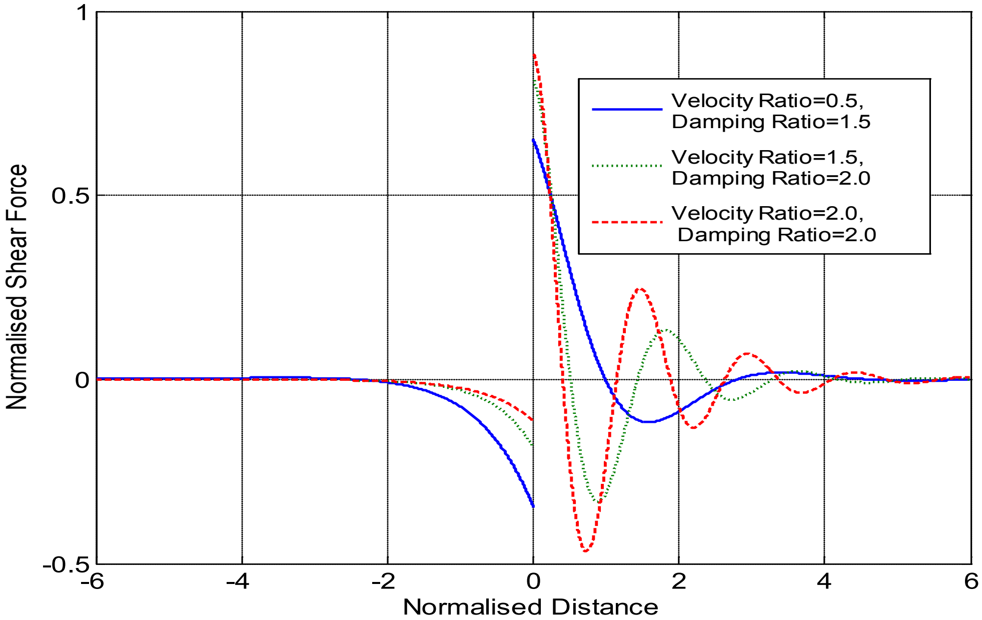

Fig. 2. 15: Normalized shear force vs. normalized distance with different combination of velocity ratios and damping ratios for two parameter model.

Velocities are varied from static-subcritical-critical-supercritical velocities whereas the damping ratios are varied from undamped-underdamped-critically damped-overdamped. The figures clearly show the resemblance in nature to those of frequency response curves of a single degree-of-freedom system. The figures further show that the maximum deflections and bending moments are higher at lighter damping. From Figs. 2.18 and 2.19, it can be seen that the deflection amplitude of the rear wave is much larger than that of the front wave for velocities greater or equal to the critical velocities. For very low velocities ($v / v_{cr} \leq 0.5$), these figures further illustrate that the deflection waves become more symmetrical about the loading point as the speed decreases.

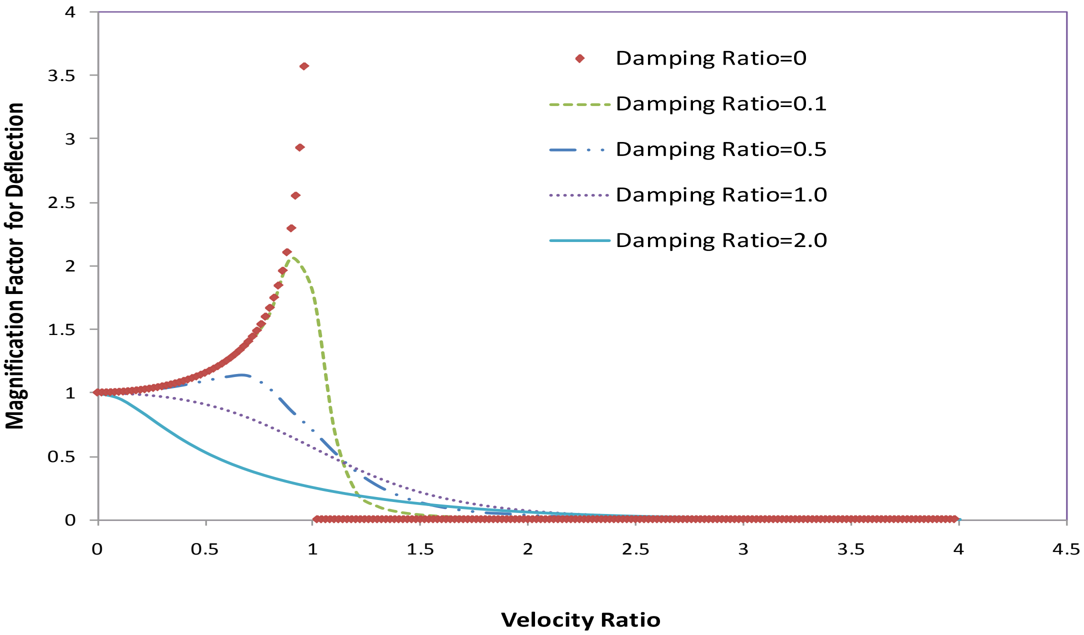

Fig. 2. 16: Dynamic magnification factors for deflection vs. the velocity ratio with different damping ratios under the load for two parameter model.

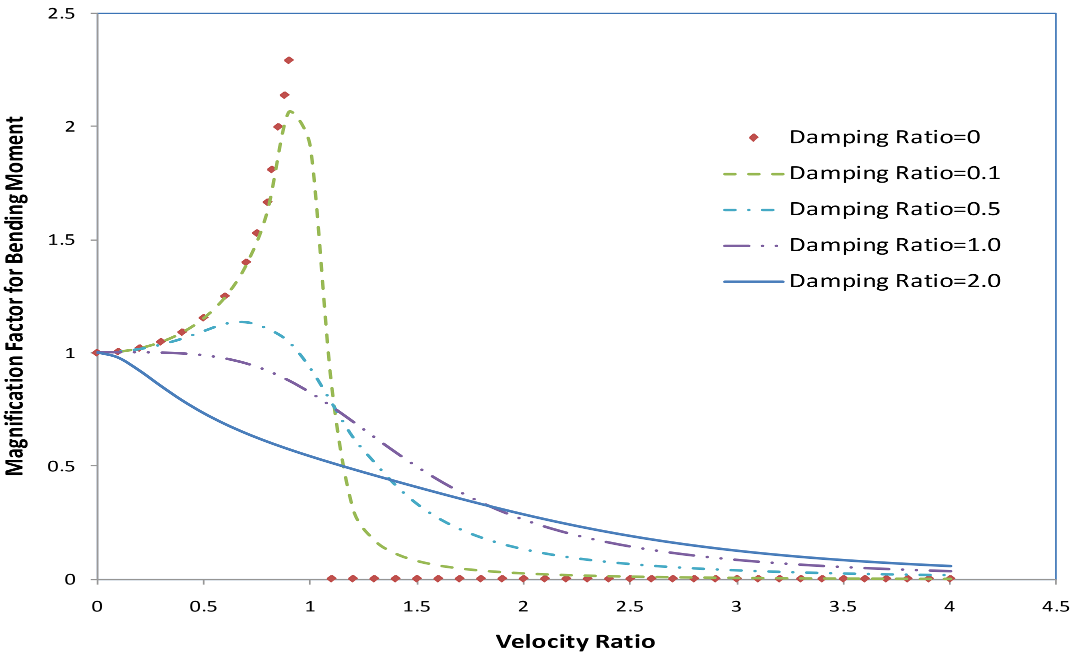

Fig. 2. 17: Dynamic magnification factors for bending moment vs. the velocity ratio with different damping ratios under the load for two parameter model.

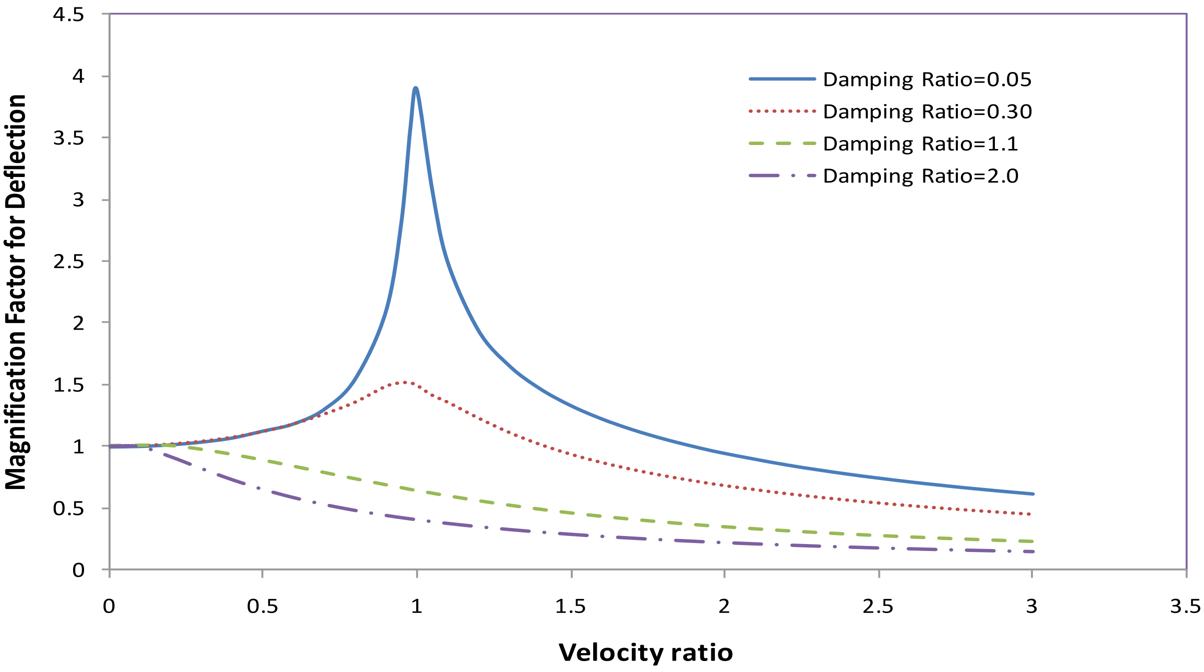

Fig. 2. 18: Dynamic magnification factors for deflection vs. the velocity ratio with different damping ratios behind the load (settlement) for two parameter model.

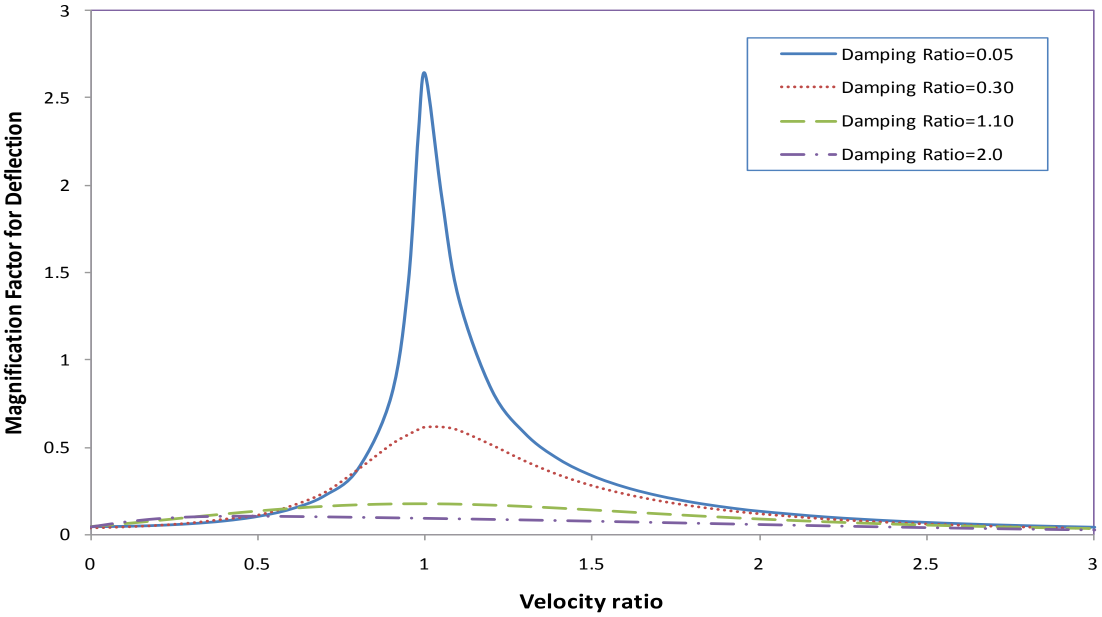

Fig. 2. 19: Dynamic magnification factors for deflection vs. the velocity ratio with different damping ratios ahead of the load (uplift) for two parameter model.

2.6.2 Modal analysis:

Dynamic response of an Euler-Bernoulli beam resting on Pasternak foundation is further investigated using the modal analysis approach under both moving load and moving mass conditions. In case of "moving mass" condition, the mass of the wheel is considered to exert force on the beam equivalent to the moving load. The parameters listed in Table 2.1 are employed in this study and a total of 60 modes have been considered. The normalized dynamic response in terms of deflection, bending moment for both "moving load" and "moving mass" conditions is obtained with respect to the normalized position of the beam.

(i) <u>Comparison between moving load and moving mass responses</u>

Figure 2.20 shows normalized deflection responses for both moving load and moving mass systems with different velocity ratios. The damping ratio of the beam is kept at 0.0005. The figure shows that the maximum deflections occur, for all the given conditions, at the midpoint of the beam. However, the maximum deflection is always higher in case of moving mass, which is attributed to the inertia of the mass. The maximum normalized deflections for moving mass problem are 1.248, 1.582, 1.656, and 1.725 for velocities of 44.12, 88.25, 132.38, and 176.50 km/h, respectively. The maximum normalized deflections for moving load problem are 1.002, 1.003, 1.005, and 1.007 for velocities of 44.12, 88.25, 132.38, and 176.50 km/h, respectively. These results show that the variations in peak normalized deflections for moving mass problem are significant with variations in speed for the given speed range. This variation is not significant for moving load problem. These variations, however, can be significant for higher velocity ratios as shown in Fig. 2.7 (a).

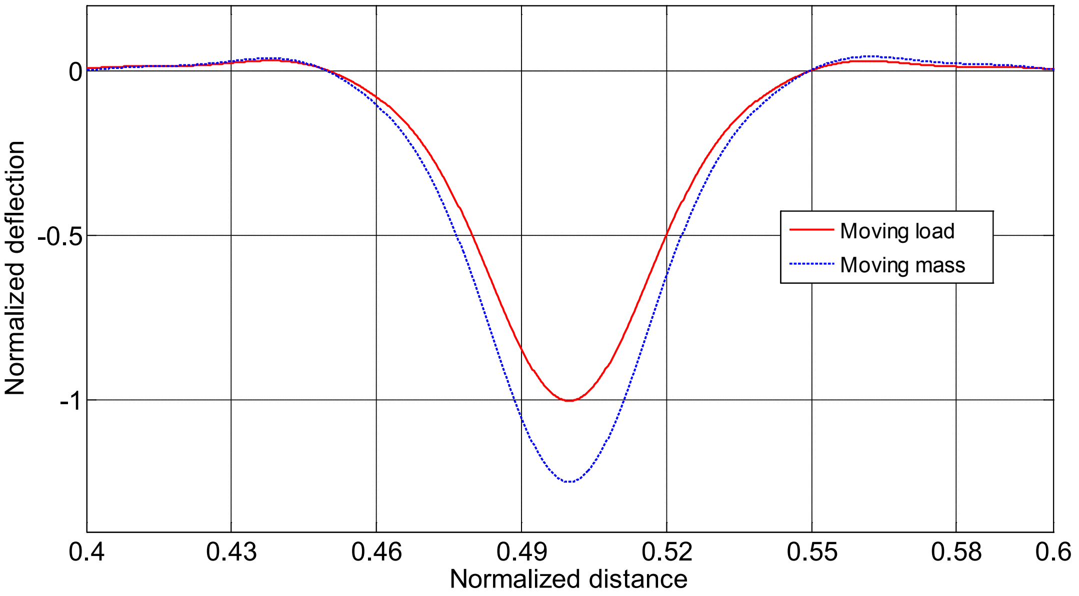

(a)

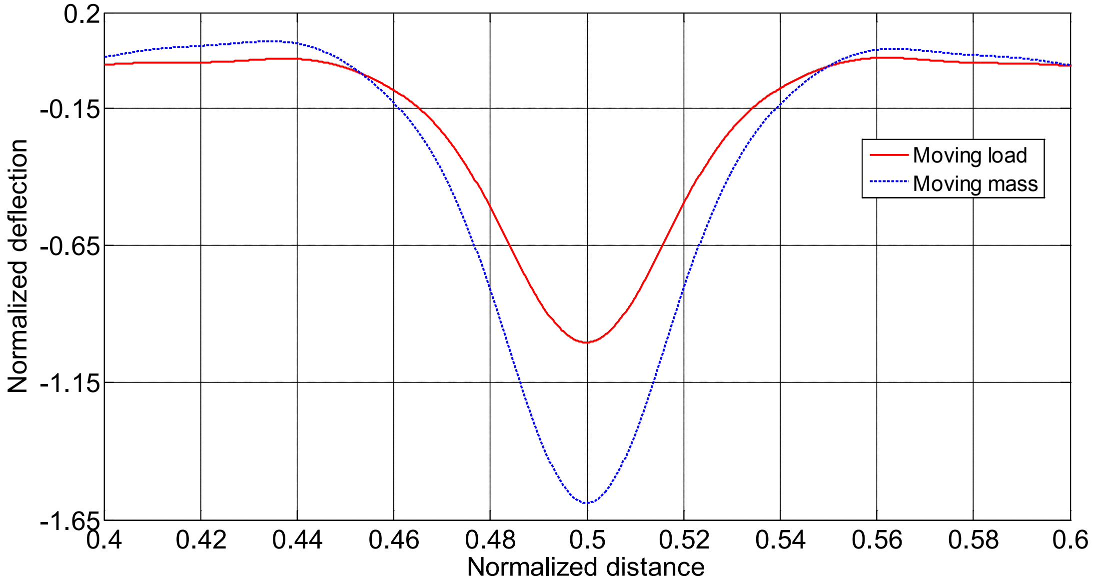
0.2
-0.15
-0.65
-1.15
-1.65
0.4
0.42
0.44
0.46
0.48
0.5
0.52
0.54
0.56
0.58
0.6
Normalized distance
Normalized deflection
Moving load
Moving mass

(b)

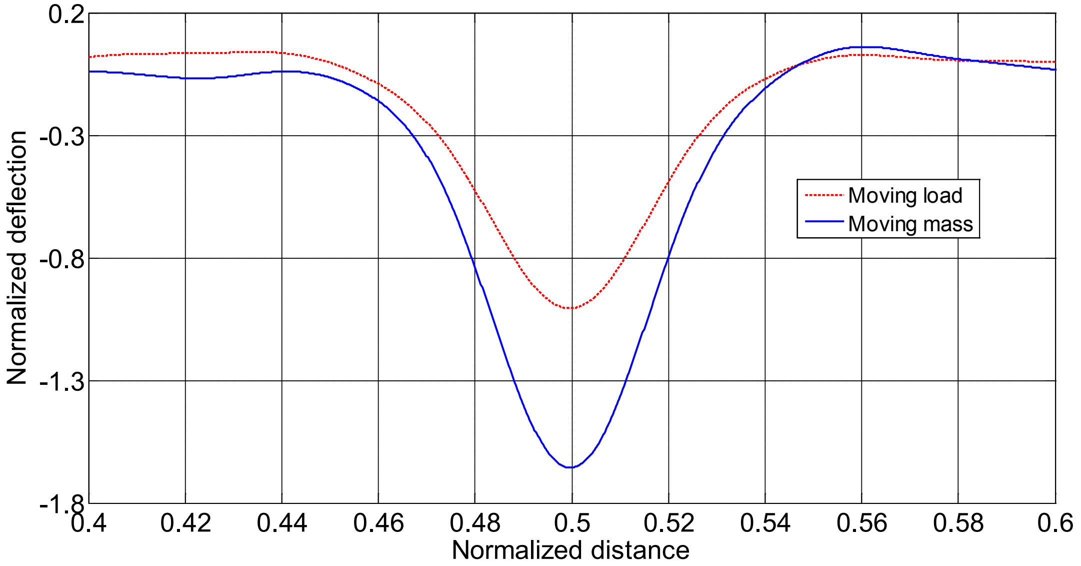
0.2
-0.3
-0.8
-1.3
-1.8
0.4
0.42
0.44
0.46
0.48
0.5
0.52
0.54
0.56
0.58
0.6
Normalized distance
Normalized deflection
Moving load
Moving mass

(c)

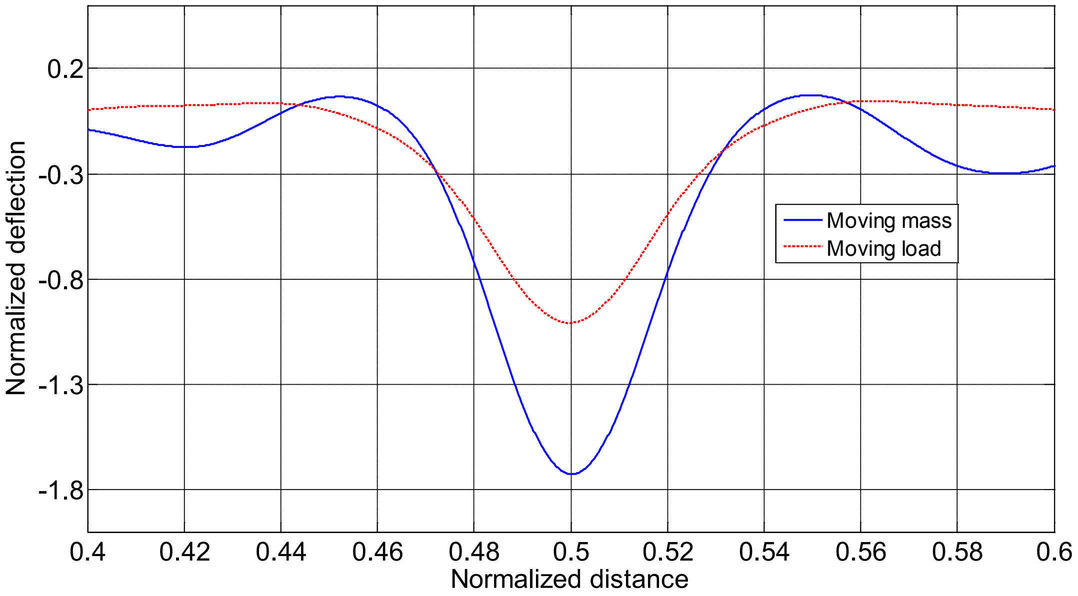

(d)

Fig. 2. 20: Normalized deflection response with different velocity ratios; (a) velocity ratio=0.025; (b) velocity ratio=0.05; (c) velocity ratio=0.075; (d) velocity ratio=0.1.

The variations in normalized bending moment response for both moving load and moving mass systems with different velocity ratios are shown in Fig. 2.21. Similar to the deflection response, the maximum bending moments occur beneath the load for all the given conditions. Figure 2.21 shows that the maximum bending moment is always higher for moving mass system irrespective of the speed. The maximum normalized bending moments for moving mass problem are 0.8767, 1.104, 1.211, and 1.326 for velocities of 44.12, 88.25, 132.38, and176.50 km/h, respectively. In case of moving load problem, the maximum normalized bending moments are 0.7063, 0.7096, 0.7127, and 0.7157 for velocities of 44.12, 88.25, 132.38, and 176.50 km/h, respectively. The figures further show that the peak bending moments increase significantly with increase in speeds in case of moving mass problem for the considered speed range. Thus, simplification of the moving vehicle into a moving load in analysis of dynamic vehicle-track interactions can result in lower prediction of the deflections and bending moments of the track. In case of moving load, the increment is not so pronounced which can be attributed to the considered speed ratios. For higher speed ratios, as shown in Fig. 2.12 (a), this increment is significant. It can be concluded that considering the moving load instead of moving mass essentially neglects the inertia of the mass, centrifugal force, velocity of the moving mass which in turn gives us the inaccurate prediction of the deflections, bending moments and contact forces that arise in between the contact points.

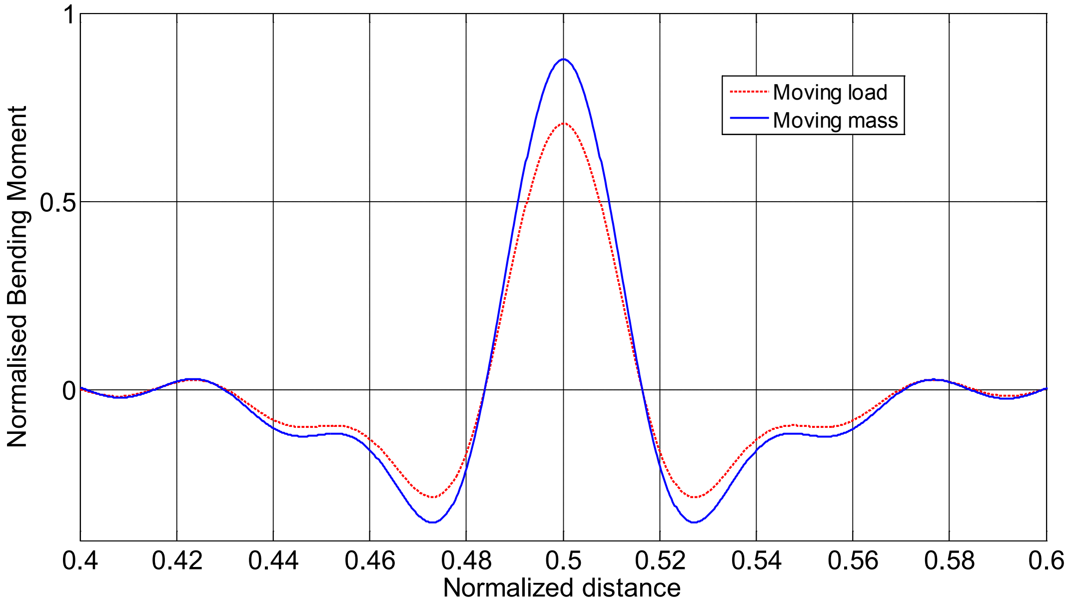

(a)

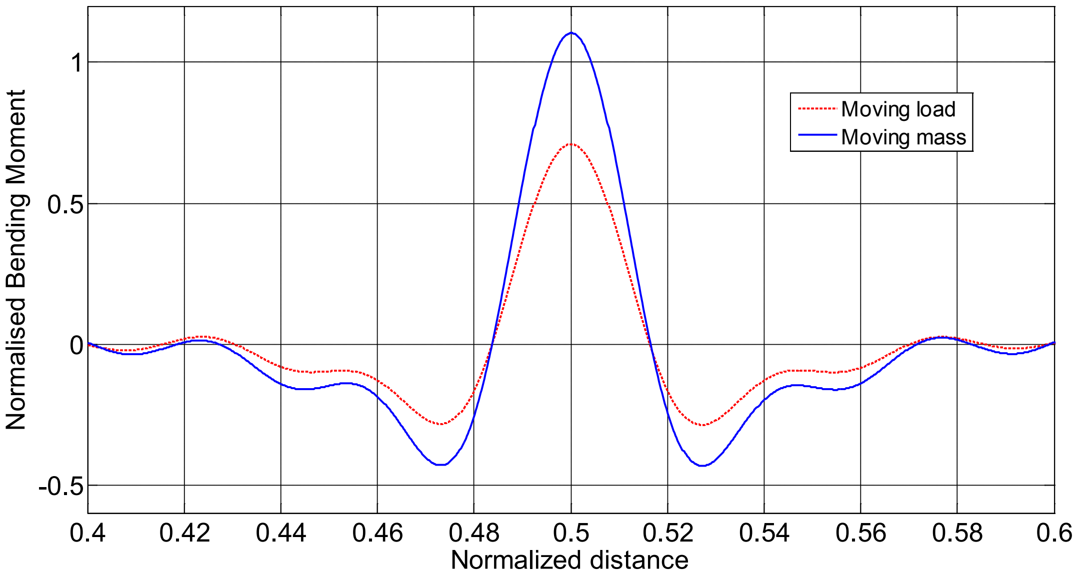
Normalised Bending Moment
1
0.5
0
-0.5
0.4
0.42
0.44
0.46
0.48
0.5
0.52
0.54
0.56
0.58
0.6
Normalized distance
Moving load
Moving mass

(b)

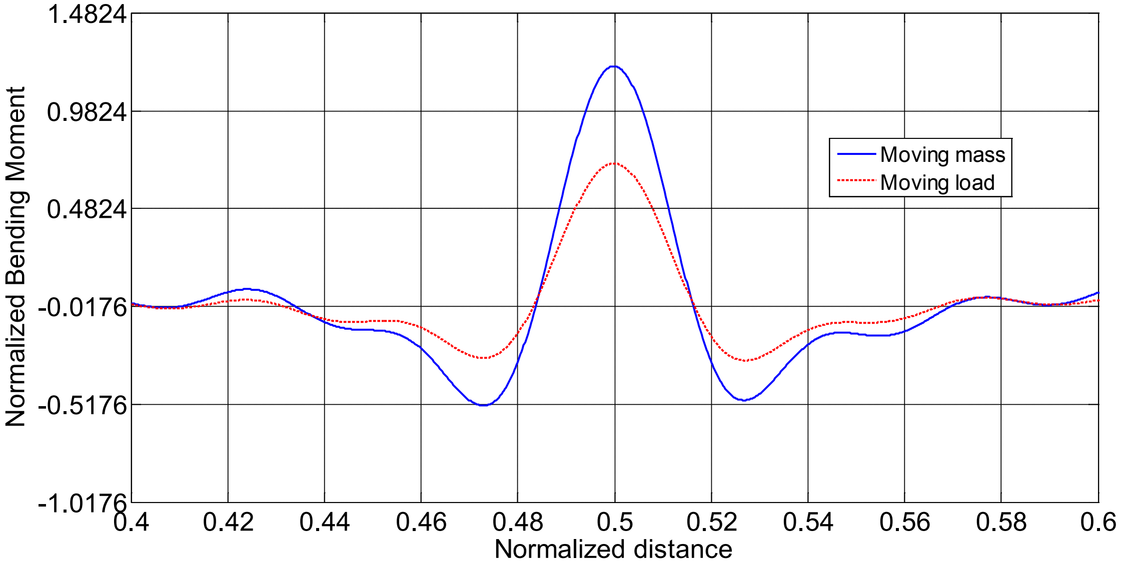
Normalized Bending Moment
1.4824
0.9824
0.4824
-0.0176
-0.5176
-1.0176
0.4
0.42
0.44
0.46
0.48
0.5
0.52
0.54
0.56
0.58
0.6
Normalized distance
Moving mass
Moving load

(c)

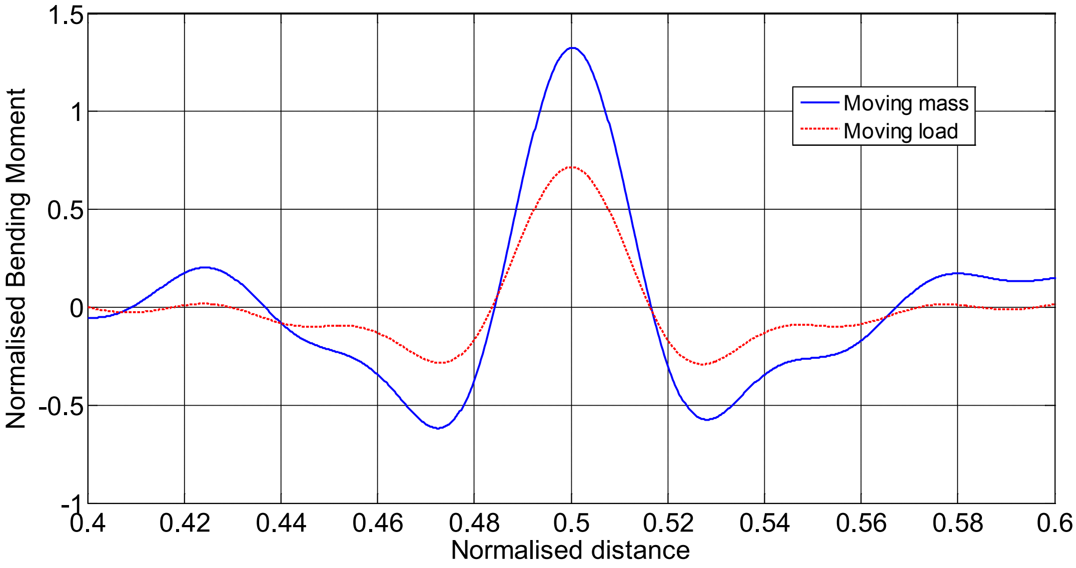

(d)

Fig. 2. 21**:** Normalized bending moment responses with different velocity ratios; (a) velocity ratio=0.025; (b) velocity ratio=0.05; (c) velocity ratio=0.075; (d) velocity ratio=0.1.

(ii) Effect of foundation stiffness

Foundation stiffness has significant influence on dynamic deflection response under both moving load and moving mass conditions, as shown in Fig. 2.22. For both cases, decreasing the foundation stiffness increases significantly the dimensionless peak deflections, while the speed is kept constant at 88.25 km/h. However, the rate of increment is slightly higher for moving load problem. When the value of the foundation stiffness decreases from 2.0 k_f to 0.5 k_f, the normalized maximum deflection increases from 0.607 to 1.667 for moving load, while it is 0.9298 to 2.493 for moving mass.

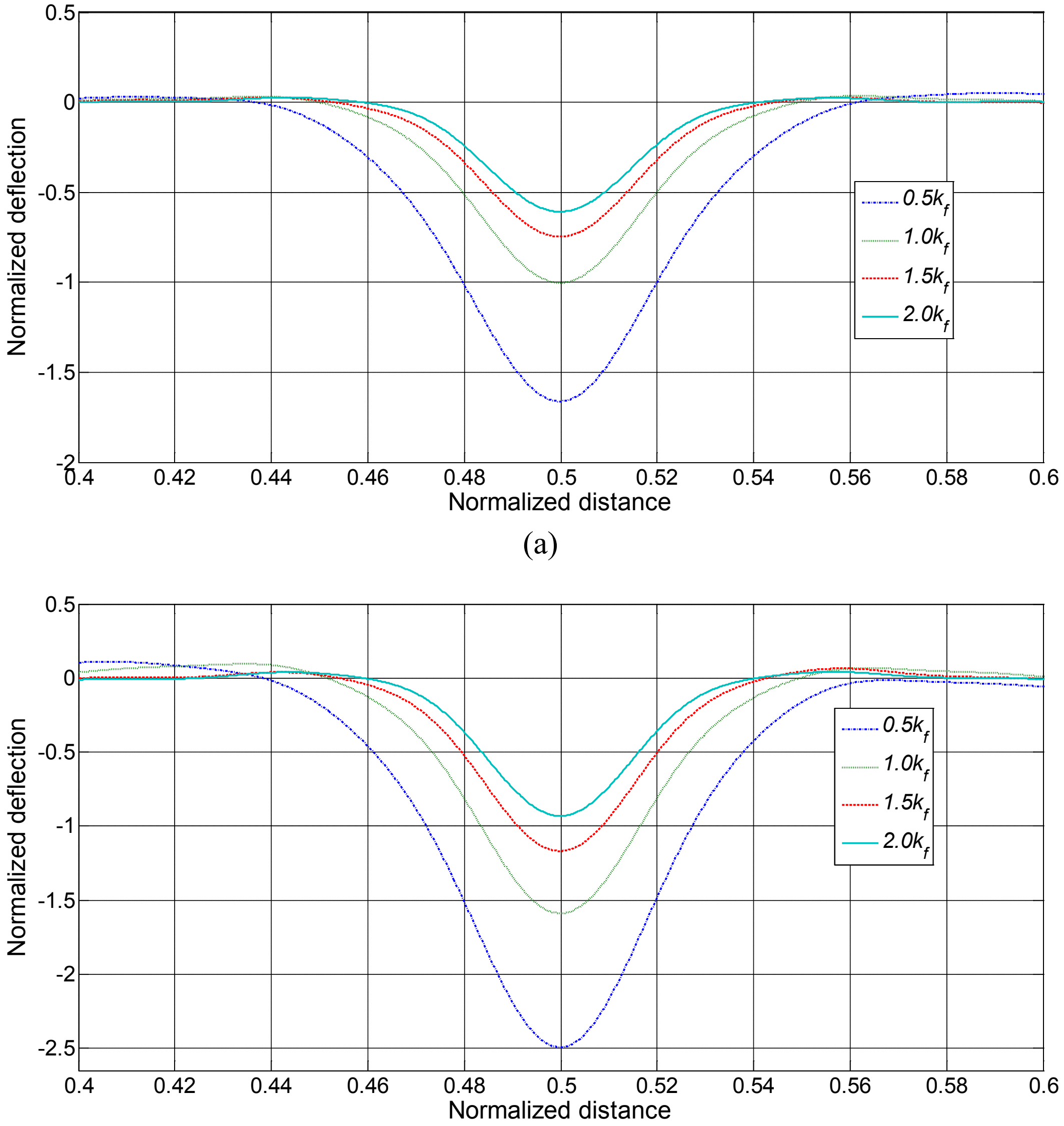

(a)

(b)

Fig. 2. 22: Effect of foundation stiffness on dynamic deflection responses at a constant speed of 88.25 km/h; (a) moving load (b) moving mass.

The effect of foundation stiffness on normalized dynamic bending moment response for both moving load and moving mass conditions is shown in Fig. 2.23. Similar to the deflection response, for a constant speed, decreasing the foundation stiffness increases the peak of the dimensionless bending moment. The rate of increment is slightly higher for moving load problem. In case of moving load, the maximum normalized bending moment increases from 0.5541 to 0.8907, while for moving mass it is 0.8545 to 1.362, when the value of the foundation stiffness decreases from 2.0 k_f to $0.5k_f$.

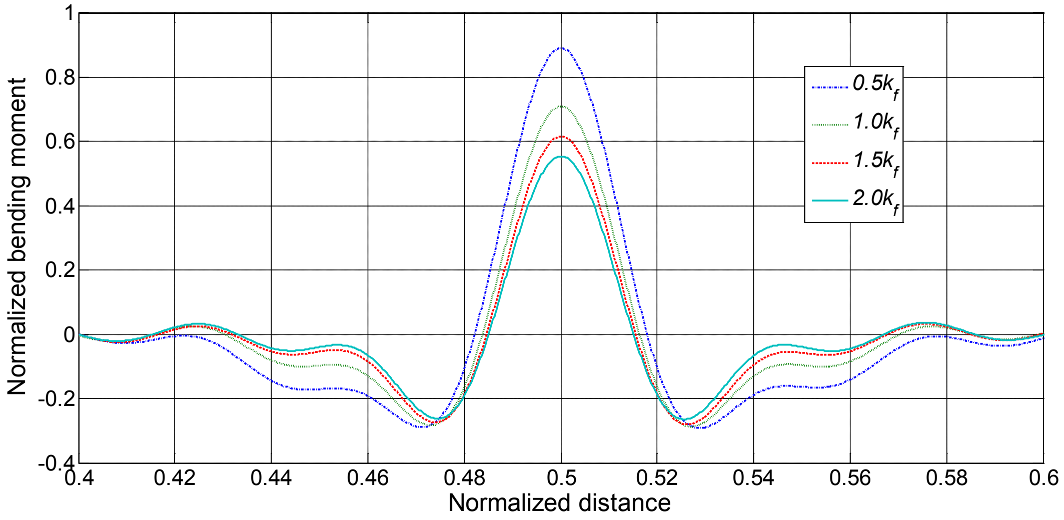

(a)

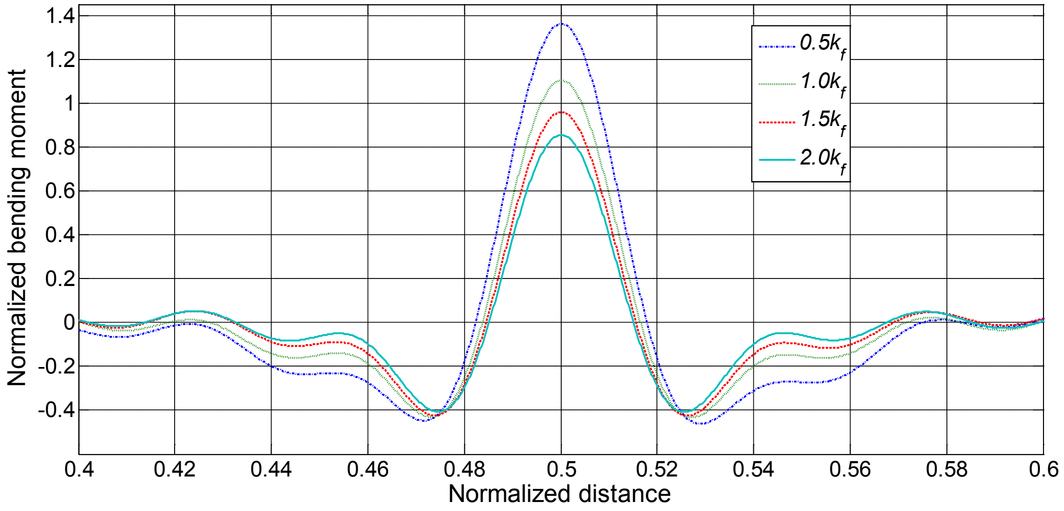

(b)

Fig. 2. 23: effect of foundation stiffness on dynamic bending moment responses at a constant speed of 88.25 km/h; (a) moving load (b) moving mass.

(iii)Effect of shear modulus

The effect of shear modulus on dynamic normalized deflection responses for both moving load and moving mass conditions is shown in Fig. 2.24. The figure shows that, for a constant speed, increasing the shear modulus decreases the peak of the dimensionless deflection. The rate of decrease is slightly higher for moving load problem. When the value of the shear modulus decreases from 3.0 k_1 to 0.1 k_1, the maximum normalized deflection increases about 17.71% and 15.22% for moving load and for moving mass, respectively.

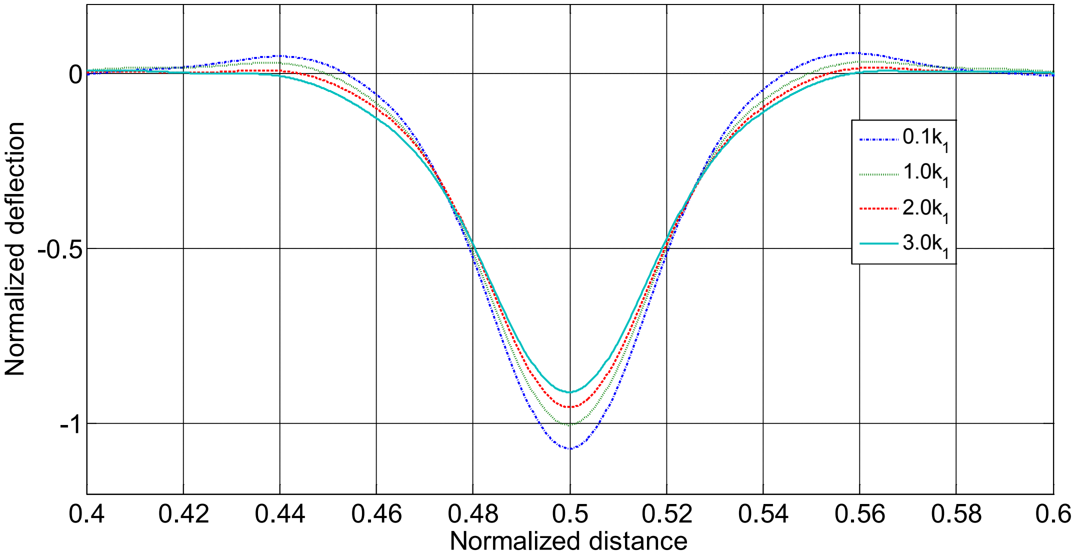

(a)

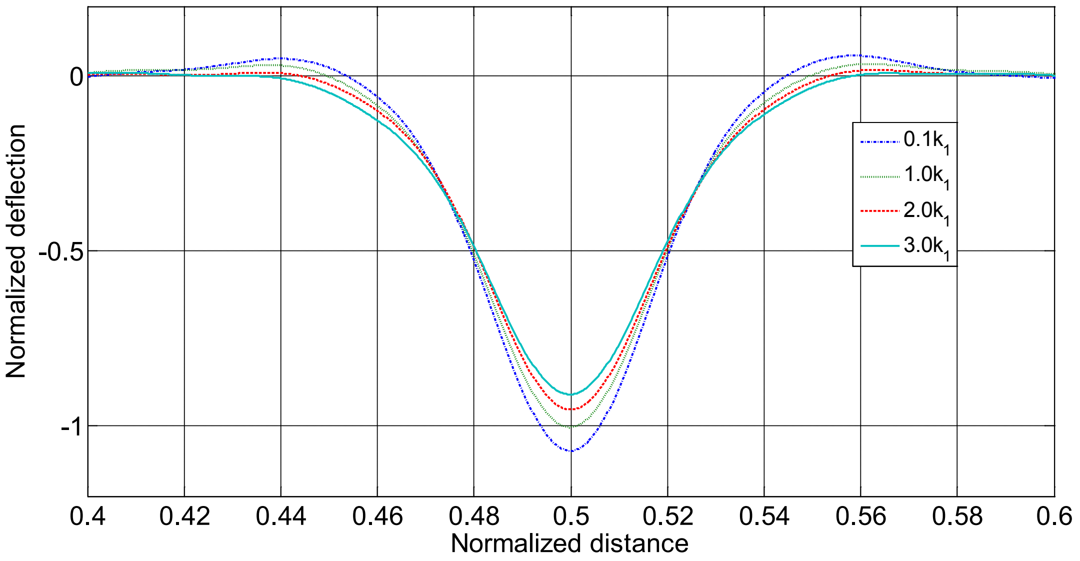

(b)

Fig. 2. 24: Effect of shear modulus on dynamic deflection responses at a constant speed of 88.25 km/h; (a) moving load (b) moving mass.

Figure 2.25 shows the effect of shear modulus on normalized bending moment responses for both moving load and moving mass conditions at a constant speed of 88.25 km/h. The figure clearly shows that decrease in shear modulus increases the normalized bending moment for given conditions. When the value of the shear modulus decreases from $3.0\,k_1$ to $0.1\,k_1$, the maximum normalized bending moment increases about 26.44% and 25.40% for moving load and for moving mass, respectively.

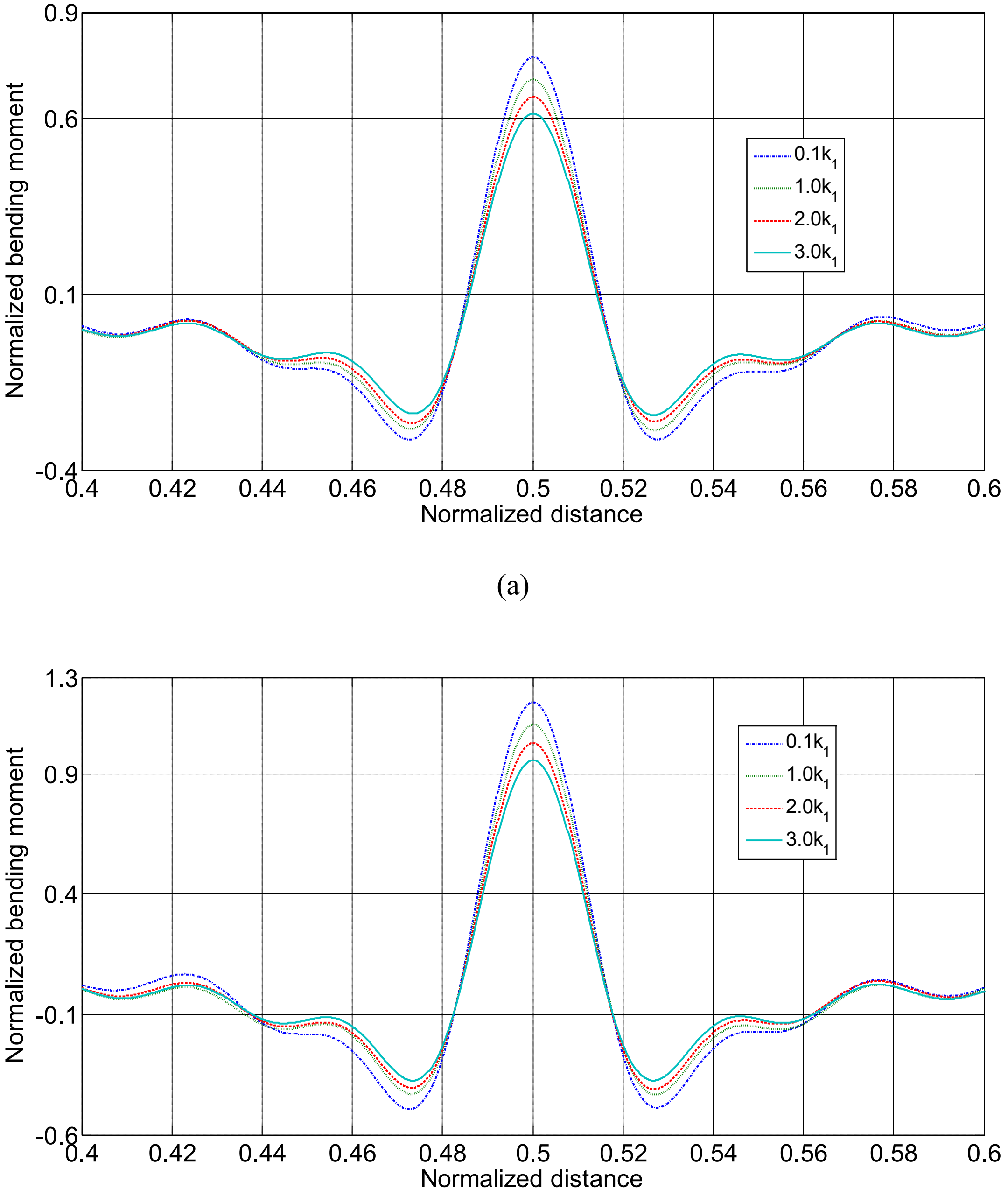

(a)

(b)

Fig. 2. 25: Effect of shear modulus on dynamic bending moment responses at a constant speed of 88.25 km/h; (a) moving load (b) moving mass.

2.7 SUMMARY

The dynamic response of an Euler-Bernoulli beam with both finite and infinite length supported on both one-parameter Winkler and two-parameter Pasternak foundation and subjected to a moving load as well as moving mass is investigated. Fourier transform technique is employed to find the exact analytical solution of the governing partial differential equation of an infinite beam subjected to a moving load. Modal analysis method is employed to convert the partial differential equation into a series of ordinary differential equations for both moving load and moving mass condition. Numerical calculations have been performed to analyze the displacement and bending moment responses of the beam on the Pasternak foundation subjected to both moving load and moving mass with different velocity ratios.

This study shows that for subcritical velocities of the moving load, the dynamic deflection and bending moment responses of the beam are symmetrical about the location of the moving load. In case of very low velocities ($v / v_{cr} \leq 0.5$), the maximum deflection, bending moment and shear force responses of the beam increases slightly with increase in speed and the responses approach those for the static one as the velocity decreases.

The study further shows that for supercritical velocities of the load, significant deflection occurs behind the load whereas bending moment and shear force are higher ahead of the load. The maximum values of the front and rear waves decrease with increase in damping ratio. The wavelengths of the rear waves are always higher than the front waves for deflection, bending moment and shear force response of the beam. For all speeds above the critical speed, the wavelengths of the front waves of deflection, bending moment and shear force decrease with increase in speed. These indicate that only a small amount of disturbance could propagate in front of a moving load when the load is moving at a very high speed. Furthermore, for supercritical velocities, the point of maximum deflection, bending moment and shear force behind the load shift farther behind with increase in speeds whereas the maximum positive peak of the front wave shift towards the location of the load. The variations in dynamic magnification factors with different velocities and damping ratios are analogous to the frequency response of the single degree-of-freedom system. All the curves show a peak value near the critical speeds. These peak values, however, increase with decrease in the damping ratios.

The study reveals that the results obtained from the modal analysis method are comparable to those obtained from exact analytical method. This study further reveals that moving mass has significantly higher effect on dynamic responses of the beam than that of the case of the moving load. Furthermore, increase in speed increases both displacements and bending moments of the beam. In case of moving load conditions, the deflections are symmetric about the contact point and maximum deflections occur beneath the load for all the selected velocity ratios. The deflection and bending moment responses are always higher for moving mass condition than those for the moving load. Detailed analyses are also performed to investigate the effect of various parameters such as foundation stiffness and shear modulus on dynamic deflection and bending moment responses under a moving load as well as moving mass. The study shows that the maximum deflection and bending moment of the beam increases significantly with the reduced shear modulus and stiffness of the foundation for a constant velocity. For a given velocity, this increment is always higher for moving load than the moving mass. For the given range of shear modulus, the normalized maximum deflection increases about 26.44% and 25.40% for moving load and moving mass, respectively.

CHAPTER 3

VEHICLE-TRACK SYSTEM MODEL AND ITS NATURAL FREQUENCIES

3.1 INTRODUCTION

The analysis of wheel-rail impact force or acceleration responses in the presence of wheel and/or rail defects requires development of a representative vehicle and track system models, wheel-rail contact model together with wheel and rail defects. The magnitudes of the impact forces and accelerations caused by the wheel and rail defects largely depend on interactions between these elements. This study is primarily concerned with vertical wheel-rail impact responses considering the contribution due to the pitch and roll motion of the car body and bogies in the presence of multiple wheel defects. This research further aims to analyze the dynamic interaction between the leading and trailing bogie, and two wheels within a wheelset in the presence of cross wheel defects. A comprehensive three-dimensional vehicle model incorporating a full car body, two bogies, and four wheelsets is thus required in order to investigate the wheel-rail impact responses in terms of both force and acceleration due to wheel defects. Since the impact magnitudes due to the presence of wheel flats are significantly influenced by the track properties, more effort has thus been made in order to develop an effective model of the track system [8]. Among these different types of railway track models, the most common approach is to model a rail beam based on Timoshenko or Euler-Bernoulli theory supported on discrete supports [2, 6, 13, 15].

This study describes the modeling of a three dimensional full car vehicle considering the roll and pitch motion of the car body and bogie. A three-dimensional track model is also developed using the discrete beam support. The rail beams are modeled as two parallel

Timoshenko beams periodically supporting lumped masses. The generalized coordinates method is used to convert the partial differential equations (PDE) describing the deflections of the continuous track to ordinary differential equations (ODE). In order to have practical representation of the track model, the nonlinear properties of the railpad and ballast are considered into the model. A shear parameter beneath the rail beams has also been considered into the model in order to facilitate interactions between the discrete railpads. The vehicle and track models are coupled through the nonlinear Hertzian contact spring. A MATLAB predefined function "ode 45" is employed in order to solve the coupled partial and ordinary differential equations of the vehicle-track system in presence of single wheel flat. The developed model is then employed to identify the natural frequencies of the vehicle and track system. Since the lateral and longitudinal relative motions between the wheel and rail are small, and creep forces at the wheel-rail contact interface have little effect on the dynamic vertical forces, the track is assumed as perfect and straight track. The forward speed of the vehicle is also assumed to be constant, while the contribution due to the track roughness is considered small in relation to forces that may be caused by wheel defects.

3.2 VEHICLE SYSTEM MODEL

The vehicle system model adopted in this study consists of a full car body, two bogie frames and four wheelsets. The car body is supported on two double-axle bogies at each end. The bogie frames are connected to the wheelsets through the primary suspensions and linked to the car body through the secondary suspensions. The primary and secondary suspensions are modeled as parallel combination of linear springs and viscous damping elements. The vehicle is assumed to move on the track with a constant travelling speed, v. The mass of the car body M_c, bogie mass M_b, and wheel mass M_w are coupled through the suspension elements, as shown in Fig.

3.1. The vehicle is modeled as a rigid body having a mass M_c and having second moments of area J_{cx} and J_{cy} about transverse and longitudinal horizontal centroidal axes, respectively. Each of the bogie frames is also modeled as a rigid body with a mass M_b (for two bogie frames M_{b1} and M_{b2}) with second moments of area J_{bx} and J_{by} about transverse and longitudinal horizontal centroidal axes, respectively. Each axle together with the wheels has a mass of M_w (for four axles M_{w1}, M_{w2}, M_{w3} and M_{w4}). The total vehicle system model is represented by a 17-DOF dynamic system that includes the car body vertical, pitch and roll motions, Z_c, θ_c, and ϕ_c, respectively, two bogies vertical, pitch and roll motions, Z_{b1} and Z_{b2}, θ_{b1} and θ_{b2}, and ϕ_{b1} and ϕ_{b2}, respectively, and four axles vertical and roll motions, Z_{w1}, Z_{w2}, Z_{w3} and Z_{w4}, and ϕ_{w1}, ϕ_{w2}, ϕ_{w3} and ϕ_{w4}, respectively. The primary suspension stiffness and damping elements are represented by K_p and C_p, respectively, while K_s and C_s represent the stiffness and viscous damping coefficient due to secondary suspension. Half of the bogie frame and wheelset distances in longitudinal direction, respectively, are l_c and l_b. Similarly, l_p and l_s are half of the primary and secondary suspension distance in lateral direction, respectively.

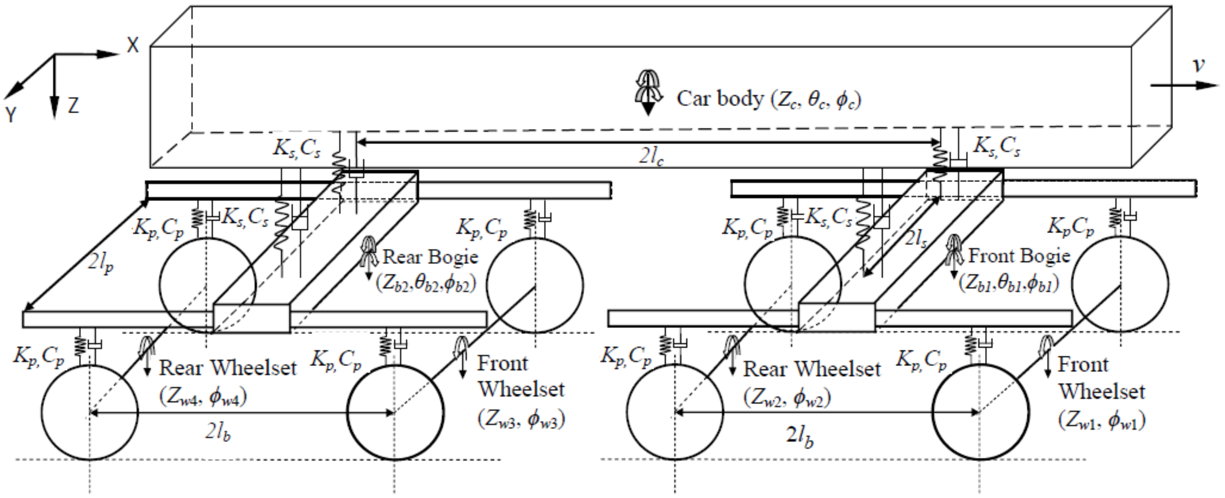

Fig. 3. 1: Three-dimensional railway vehicle model with one full car and two bogies.

The equations of motion of the vehicle model consisting of one car body, two bogie frames, and four wheelsets, are derived upon neglecting the contribution due to track roughness as follows:

Car body bounce motion:

$$M_c\ddot{Z}_c + 2C_s(\dot{Z}_c + l_c\dot{\theta}_c - \dot{Z}_{b1}) + 2C_s(\dot{Z}_c - l_c\dot{\theta}_c - \dot{Z}_{b2}) + 2K_s(Z_c + l_c\theta_c - Z_{b1}) \\ +2K_s(Z_c - l_c\theta_c - Z_{b2}) = 0 \tag{3.1}$$

$$\text{or, } M_c\ddot{Z}_c + 4C_s\dot{Z}_c + 4K_sZ_c - 2C_s\dot{Z}_{b1} - 2C_s\dot{Z}_{b2} - 2K_sZ_{b1} - 2K_sZ_{b2} = 0 \tag{3.2}$$

Car body pitch motion:

$$J_{cy}\ddot{\theta}_c + 2C_sl_c(\dot{Z}_c + l_c\dot{\theta}_c - \dot{Z}_{b1}) - 2C_sl_c(\dot{Z}_c - l_c\dot{\theta}_c - \dot{Z}_{b2}) + 2K_sl_c(Z_c + l_c\theta_c - Z_{b1}) \\ -2K_sl_c(Z_c - l_c\theta_c - Z_{b2}) = 0 \tag{3.3}$$

$$\text{or, } J_{cy}\ddot{\theta}_c + 4C_sl_c^2\dot{\theta}_c - 2C_sl_c\dot{Z}_{b1} + 2C_sl_c\dot{Z}_{b2} + 4K_sl_c^2\theta_c - 2K_sl_cZ_{b1} + 2K_sl_cZ_{b2} = 0 \tag{3.4}$$

Car body roll motion:

$$\begin{aligned}&J_{cx}\ddot{\phi}_c + C_s l_s\{\dot{Z}_c + l_s\dot{\phi}_c - (\dot{Z}_{b1} + l_p\dot{\phi}_{b1})\} - C_s l_s\{\dot{Z}_c - l_s\dot{\phi}_c - (\dot{Z}_{b1} - l_p\dot{\phi}_{b1})\}\\&+C_s l_s\{\dot{Z}_c + l_s\dot{\phi}_c - (\dot{Z}_{b2} + l_p\dot{\phi}_{b2})\} - C_s l_s\{\dot{Z}_c - l_s\dot{\phi}_c - (\dot{Z}_{b2} - l_p\dot{\phi}_{b2})\}\\&+K_s l_s\{Z_c + l_s\phi_c - (Z_{b1} + l_p\phi_{b1})\} - K_s l_s\{Z_c - l_s\phi_c - (Z_{b1} - l_p\phi_{b1})\}\\&+K_s l_s\{Z_c + l_s\phi_c - (Z_{b2} + l_p\phi_{b2})\} - K_s l_s\{Z_c - l_s\phi_c - (Z_{b2} - l_p\phi_{b2})\} = 0\end{aligned} \tag{3.5}$$

or, $$J_{cx}\ddot{\phi}_c + 4C_s l_s^2\dot{\phi}_c - 2C_s l_s^2\dot{\phi}_{b1} - 2C_s l_s^2\dot{\phi}_{b2} + 4K_s l_s^2\phi_c - 2K_s l_s^2\phi_{b1} - 2K_s l_s^2\phi_{b2} = 0 \tag{3.6}$$

Bogie bounce motion:

Front bogie bounce:

$$\begin{aligned}&M_{b1}\ddot{Z}_{b1} + K_s\{Z_{b1} + l_b\theta_{b1} - (Z_c + l_c\theta_c)\} + K_s\{Z_{b1} - l_b\theta_{b1} - (Z_c - l_c\theta_c)\} + 2K_p\\&(Z_{b1} + l_b\theta_{b1} - Z_{w1}) + 2K_p(Z_{b1} - l_b\dot{\theta}_{b1} - Z_{w2}) + C_s\{\dot{Z}_{b1} + l_b\dot{\theta}_{b1} - (\dot{Z}_c + l_c\dot{\theta}_c)\} +\\&C_s\{\dot{Z}_{b1} - l_b\dot{\theta}_{b1} - (\dot{Z}_c - l_c\dot{\theta}_c)\} + 2C_p(\dot{Z}_{b1} + l_b\dot{\theta}_{b1} - Z_{w1}) + 2C_p(\dot{Z}_{b1} - l_b\dot{\theta}_{b1} - \dot{Z}_{w2}) = 0\end{aligned} \tag{3.7}$$

or,

$$\begin{aligned}&M_{b1}\ddot{Z}_{b1} + 2K_s Z_{b1} - 2K_s Z_c + 4K_p Z_{b1} - 2K_p Z_{w1} - 2K_p Z_{w2} + 2C_s\dot{Z}_{b1}\\&-2C_s\dot{Z}_c + 4C_p\dot{Z}_{b1} - 2C_p\dot{Z}_{w1} - 2C_p\dot{Z}_{w2} = 0\end{aligned} \tag{3.8}$$

Rear bogie bounce:

$$\begin{aligned}&M_{b2}\ddot{Z}_{b2} + K_s\{Z_{b2} + l_b\theta_{b2} - (Z_c + l_c\theta_c)\} + K_s\{Z_{b2} - l_b\theta_{b2} - (Z_c - l_c\theta_c)\} + 2K_p\\&(Z_{b2} + l_b\theta_{b2} - Z_{w3}) + 2K_p(Z_{b2} - l_b\theta_{b2} - Z_{w4}) + C_s\{\dot{Z}_{b2} + l_b\dot{\theta}_{b2} - (\dot{Z}_c + l_c\dot{\theta}_c)\} +\\&C_s\{\dot{Z}_{b2} - l_b\dot{\theta}_{b2} - (\dot{Z}_c - l_c\dot{\theta}_c)\} + 2C_p(\dot{Z}_{b2} + l_b\dot{\theta}_{b2} - Z_{w3}) + 2C_p(\dot{Z}_{b2} - l_b\dot{\theta}_{b2} - \dot{Z}_{w4}) = 0\end{aligned} \tag{3.9}$$

or,

$$\begin{aligned}&M_{b2}\ddot{Z}_{b2} + 2K_s Z_{b2} - 2K_s Z_c + 4K_p Z_{b2} - 2K_p Z_{w3} - 2K_p Z_{w4} + 2C_s\dot{Z}_{b2} - 2C_s\dot{Z}_c\\&+4C_p\dot{Z}_{b2} - 2C_p\dot{Z}_{w3} - 2C_p\dot{Z}_{w4} = 0\end{aligned} \tag{3.10}$$

Bogie pitch motion:

Front bogie pitch:

$$
\begin{aligned}
&J_{by}\ddot{\theta}_{b1} + 2K_p l_b (Z_{b1} + l_b\theta_{b1} - Z_{w1}) - 2K_p l_b (Z_{b1} - l_b\theta_{b1} - Z_{w2}) \\
&+2C_p l_b (\dot{Z}_{b1} + l_b\dot{\theta}_{b1} - \dot{Z}_{w1}) - 2C_p l_b (\dot{Z}_{b1} - l_b\dot{\theta}_{b1} - \dot{Z}_{w2}) = 0
\end{aligned}
\qquad (3.11)
$$

or,

$$
J_{by}\ddot{\theta}_{b1} + 4C_p l_b^2 \dot{\theta}_{b1} - 2C_p l_b \dot{Z}_{w1} + 2C_p l_b \dot{Z}_{w2} + 4K_p l_b^2 \theta_{b1} - 2K_p l_b Z_{w1} + 2K_p l_b Z_{w2} = 0 \qquad (3.12)
$$

<u>Rear bogie pitch:</u>

$$
\begin{aligned}
&J_{by}\ddot{\theta}_{b2} + 2K_p l_b (Z_{b2} + l_b\theta_{b2} - Z_{w3}) - 2K_p l_b (Z_{b2} - l_b\theta_{b2} - Z_{w4}) \\
&+2C_p l_b (\dot{Z}_{b2} + l_b\dot{\theta}_{b2} - \dot{Z}_{w3}) - 2C_p l_b (\dot{Z}_{b2} - l_b\dot{\theta}_{b2} - \dot{Z}_{w4}) = 0
\end{aligned}
\qquad (3.13)
$$

or,

$$
J_{by}\ddot{\theta}_{b2} + 4C_p l_b^2 \dot{\theta}_{b2} - 2C_p l_b \dot{Z}_{w3} + 2C_p l_b \dot{Z}_{w4} + 4K_p l_b^2 \theta_{b2} - 2K_p l_b Z_{w3} + 2K_p l_b Z_{w4} = 0 \qquad (3.14)
$$

<u>Bogie roll motion:</u>

<u>Front bogie roll:</u>

$$
\begin{aligned}
&J_{bx}\ddot{\phi}_{b1} + K_p l_p \{Z_{b1} + l_p\phi_{b1} - (Z_{w1} + l_p\phi_{w1})\} - K_p l_p \{Z_{b1} - l_p\phi_{b1} - (Z_{w1} - l_p\phi_{w1})\} + K_p l_p \{Z_{b1} \\
&+l_p\phi_{b1} - (Z_{w2} + l_p\phi_{w2})\} - K_p l_p \{Z_{b1} - l_p\phi_{b1} - (Z_{w2} - l_p\phi_{w2})\} + K_s l_s \{Z_{b1} + l_s\phi_{b1} - (Z_c + l_s\phi_c \\
&-K_s l_s \{Z_{b1} - l_s\phi_{b1} - (Z_c - l_s\phi_c)\} + C_p l_p \{\dot{Z}_{b1} + l_p\dot{\phi}_{b1} - (\dot{Z}_{w1} + l_p\dot{\phi}_{w1})\} - C_p l_p \{\dot{Z}_{b1} - l_p\dot{\phi}_{b1} - \\
&(\dot{Z}_{w1} - l_p\dot{\phi}_{w1})\} + C_p l_p \{\dot{Z}_{b1} + l_p\dot{\phi}_{b1} - (\dot{Z}_{w2} + l_p\dot{\phi}_{w2})\} - C_p l_p \{\dot{Z}_{b1} - l_p\dot{\phi}_{b1} - (\dot{Z}_{w2} - l_p\dot{\phi}_{w2})\} + \\
&C_s l_s \{\dot{Z}_{b1} + l_s\dot{\phi}_{b1} - (\dot{Z}_c + l_s\dot{\phi}_c)\} - C_s l_s \{\dot{Z}_{b1} - l_s\dot{\phi}_{b1} - (\dot{Z}_c - l_s\dot{\phi}_c)\} = 0
\end{aligned}
\qquad (3.15)
$$

or,

$$
\begin{aligned}
&J_{bx}\ddot{\phi}_{b1} + 4K_p l_p^2 \phi_{b1} + 2K_s l_s^2 \phi_{b1} - 2K_p l_p^2 \phi_{w1} - 2K_p l_p^2 \phi_{w2} - 2K_s l_s^2 \phi_c \\
&+4C_p l_p^2 \dot{\phi}_{b1} + 2C_s l_s^2 \dot{\phi}_{b1} - 2C_p l_p^2 \dot{\phi}_{w1} - 2C_p l_p^2 \dot{\phi}_{w2} - 2C_s l_s^2 \dot{\phi}_c = 0
\end{aligned}
\qquad (3.16)
$$

<u>Rear bogie roll:</u>

$$\begin{aligned}&J_{bx}\ddot{\phi}_{b2}+K_pl_p\{Z_{b2}+l_p\phi_{b2}-(Z_{w3}+l_p\phi_{w3})\}-K_pl_p\{Z_{b2}-l_p\phi_{b2}-(Z_{w3}-l_p\phi_{w3})\}\\&+K_pl_p\{Z_{b2}+l_p\phi_{b2}-(Z_{w4}+l_p\phi_{w4})\}-K_pl_p\{Z_{b2}-l_p\phi_{b2}-(Z_{w4}-l_p\phi_{w4})\}+K_sl_s\\&\{Z_{b2}+l_s\phi_{b2}-(Z_c+l_s\phi_c)\}-K_sl_s\{Z_{b2}-l_s\phi_{b2}-(Z_c-l_s\phi_c)\}+C_pl_p\{\dot{Z}_{b2}+l_p\dot{\phi}_{b2}-\\&(\dot{Z}_{w3}+l_p\dot{\phi}_{w3})\}-C_pl_p\{\dot{Z}_{b2}-l_p\dot{\phi}_{b2}-(\dot{Z}_{w3}-l_p\dot{\phi}_{w3})\}+C_pl_p\{\dot{Z}_{b2}+l_p\dot{\phi}_{b2}-(\dot{Z}_{w4}+\\&l_p\dot{\phi}_{w4})\}-C_pl_p\{\dot{Z}_{b2}-l_p\dot{\phi}_{b2}-(\dot{Z}_{w4}-l_p\dot{\phi}_{w4})\}+C_sl_s\{\dot{Z}_{b2}+l_s\dot{\phi}_{b2}-(\dot{Z}_c+l_s\dot{\phi}_c)\}-\\&C_sl_s\{\dot{Z}_{b2}-l_s\dot{\phi}_{b2}-(\dot{Z}_c-l_s\dot{\phi}_c)\}=0\end{aligned}\tag{3.17}$$

or,

$$\begin{aligned}&J_{bx}\ddot{\phi}_{b2}+4K_pl_p^2\phi_{b2}+2K_sl_s^2\phi_{b2}-2K_pl_p^2\phi_{w3}-2K_pl_p^2\phi_{w4}-2K_sl_s^2\phi_c+4C_pl_p^2\dot{\phi}_{b2}\\&+2C_sl_s^2\dot{\phi}_{b2}-2C_pl_p^2\dot{\phi}_{w3}-2C_pl_p^2\dot{\phi}_{w4}-2C_sl_s^2\dot{\phi}_c=0\end{aligned}\tag{3.18}$$

Wheelset bounce motion:

1st Wheelset:

$$M_w\ddot{Z}_{w1}+2K_p\{Z_{w1}-(Z_{b1}+l_b\theta_{b1})\}+2C_p\{\dot{Z}_{w1}-(\dot{Z}_{b1}+l_b\dot{\theta}_{b1})\}+P_{WR1}=0\tag{3.19}$$

or,

$$M_w\ddot{Z}_{w1}+2K_pZ_{w1}-2K_pZ_{b1}+2K_pl_b\theta_{b1}+2C_p\dot{Z}_{w1}-2C_p\dot{Z}_{b1}+2C_pl_b\dot{\theta}_{b1}+P_{WR1}=0\tag{3.20}$$

2nd Wheelset:

$$M_w\ddot{Z}_{w2}+2K_p\{Z_{w2}-(Z_{b1}+l_b\theta_{b1})\}+2C_p\{\dot{Z}_{w2}-(\dot{Z}_{b1}+l_b\dot{\theta}_{b1})\}+P_{WR2}=0\tag{3.21}$$

or,

$$M_w\ddot{Z}_{w2}+2K_pZ_{w2}-2K_pZ_{b1}+2K_pl_b\theta_{b1}+2C_p\dot{Z}_{w2}-2C_p\dot{Z}_{b1}+2C_pl_b\dot{\theta}_{b1}+P_{WR2}=0\tag{3.22}$$

3rd Wheelset:

$$M_w\ddot{Z}_{w3}+2K_p\{Z_{w3}-(Z_{b2}+l_b\theta_{b2})\}+2C_p\{\dot{Z}_{w3}-(\dot{Z}_{b2}+l_b\dot{\theta}_{b2})\}+P_{WR3}=0\tag{3.23}$$

or,

$$M_w\ddot{Z}_{w3} + 2K_pZ_{w3} - 2K_pZ_{b2} + 2K_pl_b\theta_{b2} + 2C_p\dot{Z}_{w3} - 2C_p\dot{Z}_{b2} + 2C_pl_b\dot{\theta}_{b2} + P_{WR3} = 0 \tag{3.24}$$

4th Wheelset:

$$M_w\ddot{Z}_{w4} + 2K_p\{Z_{w4} - (Z_{b2} + l_b\theta_{b2})\} + 2C_p\{\dot{Z}_{w4} - (\dot{Z}_{b2} + l_b\dot{\theta}_{b2})\} + P_{WR4} = 0 \tag{3.25}$$

or,

$$M_w\ddot{Z}_{w4} + 2K_pZ_{w4} - 2K_pZ_{b2} + 2K_pl_b\theta_{b2} + 2C_p\dot{Z}_{w4} - 2C_p\dot{Z}_{b2} + 2C_pl_b\dot{\theta}_{b2} + P_{WR4} = 0 \tag{3.26}$$

Wheelset roll motion:

1st Wheelset:

$$\begin{aligned} &J_{wx}\ddot{\phi}_{w1} + K_pl_p\{Z_{w1} + l_p\phi_{w1} - (Z_{b1} + l_p\phi_{b1})\} - K_pl_p\{Z_{w1} - l_p\phi_{w1} - (Z_{b1} - l_p\phi_{b1})\} + \\ &C_pl_p\{\dot{Z}_{w1} + l_p\dot{\phi}_{w1} - (\dot{Z}_{b1} + l_p\dot{\phi}_{b1})\} - C_pl_p\{\dot{Z}_{w1} - l_p\dot{\phi}_{w1} - (\dot{Z}_{b1} - l_p\dot{\phi}_{b1})\} + P_{WR5} = 0 \end{aligned} \tag{3.27}$$

$$\text{or, } J_{wx}\ddot{\phi}_{w1} + 2K_pl_p^2\phi_{w1} - 2K_pl_p^2\phi_{b1} + 2C_pl_p^2\dot{\phi}_{w1} - 2C_pl_p^2\dot{\phi}_{b1} + P_{WR5} = 0 \tag{3.28}$$

2nd Wheelset:

$$\begin{aligned} &J_{wx}\ddot{\phi}_{w2} + K_pl_p\{Z_{w2} + l_p\phi_{w2} - (Z_{b1} + l_p\phi_{b1})\} - K_pl_p\{Z_{w2} - l_p\phi_{w2} - (Z_{b1} - l_p\phi_{b1})\} + \\ &C_pl_p\{\dot{Z}_{w2} + l_p\dot{\phi}_{w2} - (\dot{Z}_{b1} + l_p\dot{\phi}_{b1})\} - C_pl_p\{\dot{Z}_{w2} - l_p\dot{\phi}_{w2} - (\dot{Z}_{b1} - l_p\dot{\phi}_{b1})\} + P_{WR6} = 0 \end{aligned} \tag{3.29}$$

$$\text{or, } J_{wx}\ddot{\phi}_{w2} + 2K_pl_p^2\phi_{w2} - 2K_pl_p^2\phi_{b1} + 2C_pl_p^2\dot{\phi}_{w2} - 2C_pl_p^2\dot{\phi}_{b1} + P_{WR6} = 0 \tag{3.30}$$

3rd Wheelset:

$$\begin{aligned} &J_{wx}\ddot{\phi}_{w3} + K_pl_p\{Z_{w3} + l_p\phi_{w3} - (Z_{b2} + l_p\phi_{b2})\} - K_pl_p\{Z_{w3} - l_p\phi_{w3} - (Z_{b2} - l_p\phi_{b2})\} + \\ &C_pl_p\{\dot{Z}_{w3} + l_p\dot{\phi}_{w3} - (\dot{Z}_{b2} + l_p\dot{\phi}_{b2})\} - C_pl_p\{\dot{Z}_{w3} - l_p\dot{\phi}_{w3} - (\dot{Z}_{b2} - l_p\dot{\phi}_{b2})\} + P_{WR7} = 0 \end{aligned} \tag{3.31}$$

$$\text{or, } J_{wx}\ddot{\phi}_{w3} + 2K_pl_p^2\phi_{w3} - 2K_pl_p^2\phi_{b2} + 2C_pl_p^2\dot{\phi}_{w3} - 2C_pl_p^2\dot{\phi}_{b2} + P_{WR7} = 0 \tag{3.32}$$

4th Wheelset:

$$J_{wx}\ddot{\phi}_{w4} + K_p l_p\{Z_{w4} + l_p\phi_{w4} - (Z_{b2} + l_p\phi_{b2})\} - K_p l_p\{Z_{w4} - l_p\phi_{w4} - (Z_{b2} - l_p\phi_{b2})\} + \tag{3.33}$$
$$C_p l_p\{\dot{Z}_{w4} + l_p\dot{\phi}_{w4} - (\dot{Z}_{b2} + l_p\dot{\phi}_{b2})\} - C_p l_p\{\dot{Z}_{w4} - l_p\dot{\phi}_{w4} - (\dot{Z}_{b2} - l_p\dot{\phi}_{b2})\} + P_{WR8} = 0$$

$$\text{or, } J_{wx}\ddot{\phi}_{w4} + 2K_p l_p^2\phi_{w4} - 2K_p l_p^2\phi_{b2} + 2C_p l_p^2\dot{\phi}_{w4} - 2C_p l_p^2\dot{\phi}_{b2} + P_{WR8} = 0 \tag{3.34}$$

where, P_{WR1}, P_{WR2}, P_{WR3}, P_{WR4}, P_{WR5}, P_{WR6}, P_{WR7}, and P_{WR8} are the contact forces developed at the wheel-rail interfaces corresponding to the 8 degrees of freedom of the wheelsets obtained by algebraic summation of reactions from the left and right rails.

3.3 TRACK SYSTEM MODEL

The dynamic forces developed at the wheel-rail interface are derived upon development and analysis of the railway track. In this study, a three-dimensional model of the track system model consisting of rails, pads, sleepers and ballasts is developed upon consideration of two subsequent layers. Two rails modeled as Timoshenko beams are discretely supported on the sleepers through the railpads and fasteners that are modeled as combination of spring and damper elements, as shown in Fig. 3.2. The sleepers are modeled as lumped masses which are discretely supported on the ballasts. The ballasts are modeled as combination of spring and damper elements inserted between each discrete sleeper and subgrade with consideration of the elastic properties of the ballasts. The contribution due to the ballast mass to the wheel-rail contact forces is assumed to be negligible. Two rail beams are modeled as Timoshenko beams, where both rotary inertia of the beam cross section and beam deformations due to the shear force are taken into account. The track is assumed to be symmetric with respect to its centerline. Furthermore, the track system model is simplified to describe its dynamic motions in vertical plane only considering negligible contributions of the longitudinal and lateral deformations of the track system. Since the longitudinal and lateral motions have little effect on the vertical wheel-rail interactions, the longitudinal and lateral displacements of all the masses are neglected. A finite length of the track structure is considered by including a total of 100 sleepers/ballasts.

It has been suggested that a total of 50 to 60 sleepers/ballast elements would be sufficient for analysis of dynamic wheel-rail impact load due to a wheel/rail defects [80, 109]. However, 100 sleepers/ballasts are considered in this study in order to investigate the contribution due to pitch and roll dynamics of the car body and bogie, and various vehicle design parameters. The total length of the rail with 100 sleepers is about 59.4 m with 0.6 m of sleeper distance. This length is 4.6 times higher than the total length of a full length railway car with two bogies, which is about 12.86 m. This sufficiently long rail length will allow steady state simulated results when the system is stable. However, it will increase the simulation runtime of the total system. The vertical and rotational motions of the two rail beams (left and right beams) coupled with the sleepers are expressed as $Z_{rl}(x,t)$, $Z_{rr}(x,t)$ and $\psi_{rl}(x,t)$, $\psi_{rr}(x,t)$, respectively, while $Z_{si}(t)$ and $\phi_{si}(t)$ describe the vertical and roll motions of the i'th sleeper, respectively. K_{pri}, C_{pri}, K_{bi} and C_{bi} are the nonlinear railpad and ballast stiffness and damping coefficients, respectively. Further, k_1 is the shear viscosity coefficient of the foundation under the rail beam and L_s is the half of the lateral distance between left and right end railpads. The length of the track considered in simulation is sufficiently large to minimize the end effects. The infinite long track is modeled as a track of finite length, whose two ends are simply supported.

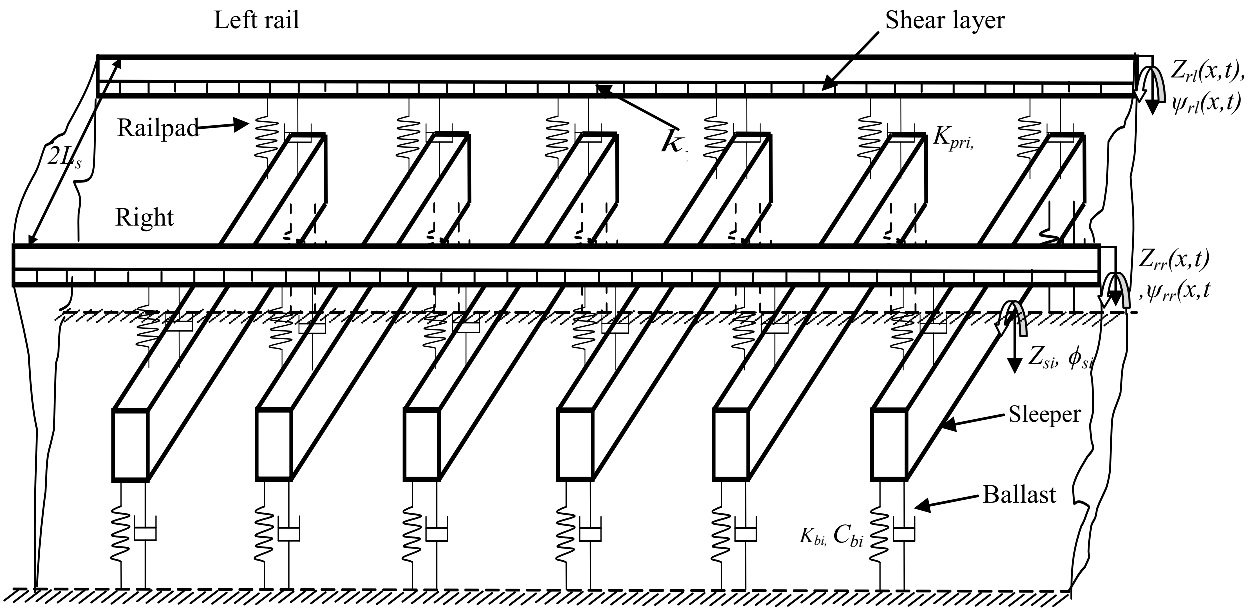

Fig. 3. 2: Three-dimensional two-layer railway track model.

The equations of motion of the entire track system are derived upon integrating the equation of motion for the two rails as Timoshenko beams with the differential equations of motion for the discrete sleepers. The deflection of the continuous rail can be derived from the partial differential equation for the Timoshenko beam as [17]:

For left rail:

$$\begin{aligned}&\rho A\frac{\partial^2 Z_{rl}(x,t)}{\partial t^2}-GAk_r\{\frac{\partial^2 Z_{rl}(x,t)}{\partial x^2}-\frac{\partial \psi_{rl}(x,t)}{\partial x}\}-k_1\frac{\partial^2 Z_{rl}(x,t)}{\partial x^2}\\&=-\sum_{i=1}^{N}F_{RSli\delta(x-x_i)}+\sum_{j=1}^{4}P_{WRlj\delta(x-x_{pj})}\end{aligned}\tag{3.35}$$

$$\rho A\frac{\partial^2 \psi_{rl}(x,t)}{\partial t^2}-GAk_r\{\frac{\partial Z_{rl}(x,t)}{\partial x}-\psi_{rl}(x,t)\}-EI\frac{\partial^2 \psi_{rl}(x,t)}{\partial x^2}=0\tag{3.36}$$

For right rail:

$$\rho A\frac{\partial^2 Z_{rr}(x,t)}{\partial t^2}-GAk_r\{\frac{\partial^2 Z_{rr}(x,t)}{\partial x^2}-\frac{\partial \psi_{rr}(x,t)}{\partial x}\}-k_1\frac{\partial^2 Z_{rr}(x,t)}{\partial x^2}$$
$$=-\sum_{i=1}^{N} F_{RSri\delta(x-x_i)}+\sum_{j=1}^{4} P_{WRrj\delta(x-x_{pj})} \tag{3.37}$$

$$\rho A\frac{\partial^2 \psi_{rr}(x,t)}{\partial t^2}-GAk_r\{\frac{\partial Z_{rr}(x,t)}{\partial x}-\psi_{rr}(x,t)\}-EI\frac{\partial^2 \psi_{rr}(x,t)}{\partial x^2}=0 \tag{3.38}$$

where, ρ is rail density, A is the rail cross sectional area, G is the shear modulus of rail, k_r is the Timoshenko shear coefficient, N is total number of the sleepers considered in the model, k is the number of deflection modes considered for the rail beam and j is the number of wheelsets incorporated in the vehicle model (j=1, 2,.., 4), which represent the number of moving point loads acting on the beam. E is the elastic modulus of rail beam materials and I is the second moment of area. The coordinate x represents the longitudinal position of the beam with respect to the left end support of the rail beam. x_i defines the position of the ith sleeper and $\delta(x)$ is the Dirac delta function. F_{RSri} and F_{RSli} are the forces developed at the ith right and left rail/sleeper interface, respectively (i=1,2,3,…N). P_{WRrj} is the contact force develop at the interface of the right side wheels of the vehicle and right rail, whereas P_{WRlj} is the contact force developed at the interface of the left side wheels of the vehicle and left rail.

The equation of motion for the sleeper can be written as:

Sleepers bounce motion:

$$M_{si}\ddot{Z}_{si}+2K_{bi}Z_{si}+2C_{bi}\dot{Z}_{si}+K_{pri}\left[Z_{sli}(t)-Z_{rl}(x_i,t)\right]+C_{pri}\left[\dot{Z}_{sli}(t)-\dot{Z}_{rl}(x_i,t)\right]+$$
$$K_{pri}\left[Z_{sri}(t)-Z_{rr}(x_i,t)\right]+C_{pri}\left[\dot{Z}_{sri}(t)-\dot{Z}_{rr}(x_i,t)\right]=0 \tag{3.39}$$

where, $Z_{sri}(t)$ and $Z_{sli}(t)$ are the vertical displacement of *i*'th sleeper at the right and left end pad location, respectively. K_{pri}, and C_{pri} are nonlinear dynamic stiffness and equivalent viscous damping of the railpad, which can be expressed for medium stiff pad as [105]:

$$K_{Pi} = k_0 e^{bZ_P} \text{ MN/m} \tag{3.40}$$

$$C_{Pi} = \eta_1 \sqrt{m_1 K_P} \text{ kN-s/m} \tag{3.41}$$

where, Z_P is the compression of the pad (in meter), η_1 is the loss factor of the hysteretic damping of the pad (η_1=0.25 [105]) and m_1 is the equivalent mass. Further, k_0 is the pad stiffness without load, and for a medium stiff pad k_0=115.2 MN/m and *b*=7.49/mm. Since at high frequency, the rail and sleepers vibrate separately on the pad and ballast stiffnesses, respectively. Thus, the equivalent mass (m_1) can be calculated as parallel combination of rail and sleeper masses, such as [105]:

$$m_1 = \frac{M_s M_r}{M_s + M_r} \tag{3.42}$$

where, M_r is the rail mass in a sleeper bay. Similarly, the nonlinear stiffness and equivalent viscous damping properties of the ballasts, K_{bi} and C_{bi}, can be expressed as [105]:

$$K_{bi} = 22.75 + 2.6 \times 10^8 Z_b^2 \text{ MN/m} \tag{3.43}$$

$$C_{bi} = \eta_2 \sqrt{m_2 K_b} \text{ kN-s/m} \tag{3.44}$$

where, Z_b is the compression of the pad (in meter), η_2 is the loss factor of the hysteretic damping of the ballast (η_2=1 [105]) and m_2 is the equivalent mass. In case of low frequency, the entire track (rail mass and sleeper mass) vibrates together on the ballast stiffness. Hence, the equivalent mass (m_2) can be calculated as series combination of rail and sleeper masses, such as [105]:

$$m_2 = M_s + M_r \tag{3.45}$$

Sleepers roll motion:

The equation for sleeper roll motion is given by:

$$\begin{aligned} & J_{si}\ddot{\phi}_{si} + K_{bi}L_s(Z_{si} + L_s\phi_{si}) - K_{bi}L_s(Z_{si} - L_s\phi_{si}) + C_{bi}L_s(\dot{Z}_{si} + L_s\dot{\phi}_{si}) - C_{bi}L_s \\ & (\dot{Z}_{si} - L_s\dot{\phi}_{si}) - K_{pri}L_s\left[Z_{sli}(t) - Z_{rl}(x_i,t)\right] - C_{pri}L_s\left[\dot{Z}_{sli}(t) - \dot{Z}_{rl}(x_i,t)\right] + \\ & K_{pri}L_s\left[Z_{sri}(t) - Z_{rr}(x_i,t)\right] + C_{pri}L_s\left[\dot{Z}_{sri}(t) - \dot{Z}_{rr}(x_i,t)\right] = 0 \end{aligned} \tag{3.46}$$

3.4 WHEEL-RAIL CONTACT MODEL

Wheel-rail interface distinguishes railways from other forms of land transports. In this study, the wheel-rail contact is established by the nonlinear Hertzian contact theory commonly used in the wheel-rail interaction problems [6, 4, 13, 14, 15, 87, 97, 105, 109, 113, 115, 119].

According to the Hertzian contact theory, the wheel-rail contact force is related to the rail deflection in a nonlinear manner, such as:

$$P(t) = C_H \Delta z(t)^{3/2} \tag{3.47}$$

where, $\Delta z(t)$ is the wheel-rail overlap in the vertical direction, C_H is the Hertzian contact stiffness coefficient. In the absence of a wheel defect, the overlap is defined by the relative motion of the wheel with respect to the rail:

$$\Delta z(t) = Z_w(t) - Z_r(x,t) \tag{3.48}$$

In the above equation, $Z_w(t)$ and $Z_r(x,t)$ are the wheel and rail deflections in vertical direction, respectively.

In the presence of a wheel defect, the instantaneous overlap $\Delta z(t)$ between the wheel and the rail can be expressed as:

$$\Delta z(t) = Z_w(t) - Z_r(x,t) - r(t) \tag{3.49}$$

where, $r(t)$ is the wheel flat function. In case of haversine flat, as shown in Fig. 3.3 (a), the function of the wheel flat geometry can be expressed as:

$$r(t) = \frac{1}{2} D_f [1 - \cos(2\pi x_f / L_f)] \tag{3.50}$$

where D_f is the flat depth that has been related to wheel radius R, in the following manner [8]:

$$D_f = L_f^2 / (16R) \tag{3.51}$$

where, L_f is the flat length, and x_f is the longitudinal coordinate of the instantaneous contact point within the flat. The origin of x_f lies at the vertical projection of the origin of the flat, as shown in Fig. 3.3 (a). The change in radius $r(t)$ diminishes when the wheel-rail contact lies outside the flat length.

In case of two flats within the same wheel, as shown in Fig. 3.3 (b), the variations in radius can be expressed in similar fashion:

$$r_i(t) = \frac{1}{2} D_{fi} [1 - \cos(2\pi x_{fi} / L_{fi})], \quad i=1,2 \tag{3.52}$$

where $r_i(t)$ define the change in radius of the wheel within the flat regions of lengths L_{fi}, and depths D_{fi}, respectively, and $x_{fi} = v\left(t - t_i\right)$, and t_i refer to the instants when leading and trailing flats come in contact with the rail, respectively. The relative position between the two flats, whether in a single wheel or in two wheels, is defined in terms of a phase angle φ (Fig. 3.3 (b)), which is expressed by the time lapse as a function of the forward velocity, such that:

$$t_2 - t_1 = R\varphi / v \tag{3.53}$$

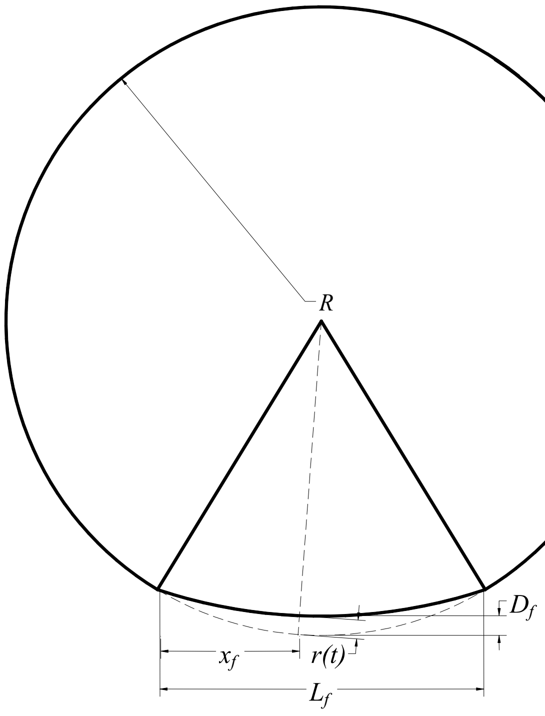

(a)

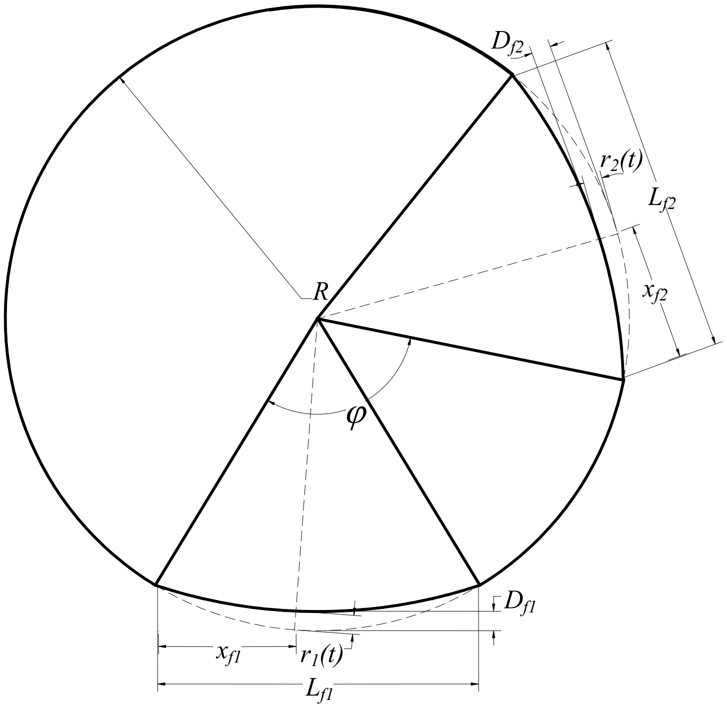

(b)

Fig. 3. 3: A railway wheel with (a) single and (b) double haversine type flats.

3.5 METHOD OF ANALYSIS

The linear equations of motion of the vehicle coupled with the nonlinear equations of motion of the track are solved in time domain considering the nonlinear contact between the wheel and rail. The presence of wheel defects as modeled in section 3.4 is also included in the resultant vehicle-track model. In this study, the nonlinear track system model formulation comprises both Ordinary Differential Equations (ODEs) and Partial Differential Equations (PDEs) describing the deflection of sleeper and the continuous rail, respectively, under moving contact forces. By applying Ritz's method, all the PDE's representing the continuous rail beam are converted in ODEs by assuming mode shape functions. The fourth order PDEs describing the motion of the continuous rail are expressed by a series of second order ordinary differential equations similar to the vehicle equations of motion in terms of the time coordinates. The resulting ODEs of the track and vehicle systems are then solved in time domain to obtain responses of individual components of the vehicle-track system model. As the vehicle moves along the track, the contact force and deflections of the rail and those of the lumped masses of vehicle and the track are calculated through numerical integration of the differential equations. It has been suggested that good convergence of solution can be obtained if the number of modes is equal to or more than 60. A total of 100 modes of a single rail beam are considered in this study for analysis of the coupled vehicle-track system model.

The vertical deflection $Z_{rl,r}(x,t)$ and rotation $\psi_{rl,r}(x,t)$ of the left and right rail are obtained using modal superposition method as:

$$Z_{rl,r}(x,t) = \sum_{k=1}^{K} N_z(k,x) Z_k(t) \tag{3.54}$$

and, $$\psi_{rl,r}(x,t) = \sum_{k=1}^{K} N_\psi(k,x) \Psi_k(t) \tag{3.55}$$

where, $N_z(k,x)$ and $N_\psi(k,x)$ are the kth mode shape functions of the vertical deflection and rotation of the rail, respectively. $Z_k(t)$ and $\Psi_k(t)$ are the kth mode time coefficients of the vertical deflection and rotation of the rail, respectively. Further, l,r denote either left or right side of the rail beam. K is the total number of modes considered into the simulation and x represents the linear coordinate along the length of the rail beam. $N_z(k,x)$ and $N_\psi(k,x)$ can be assumed as:

$$N_z(k,x) = N_\psi(k,x) = \sin\left(\frac{k\pi x}{L}\right) \tag{3.56}$$

where, L is the length of the beam considered into the simulation.

By substituting Eqns. (3.54) and (3.55) together with Eqn (3.56) into Eqns. (3.35) and (3.36) for left side rail beam, we get:

$$\frac{d^2 Z_{rl}(x,t)}{dt^2}+\frac{Gk_r}{\rho}\left(\frac{\pi k}{L}\right)^2 Z_k(t)-\frac{Gk_r}{\rho}\left(\frac{\pi k}{L}\right)\Psi_k(t)+\frac{k_1}{\rho A}\left(\frac{\pi k}{L}\right)^2 Z_k(t)= -\sum_{i=1}^{N} F_{RSli} N_z(k,x_i)+\sum_{j=1}^{4} P_{WRlj} N_z(k,x_j) \tag{3.57}$$

$$\frac{d^2\Psi_k(t)}{dt^2}+\left(\frac{GAk_r}{\rho I}+\frac{E}{\rho}\left(\frac{\pi k}{L}\right)^2\right)\Psi_k(t)-\frac{GAk_r}{\rho I}\left(\frac{\pi k}{L}\right)Z_k(t)=0 \tag{3.58}$$

The reaction force between the left rail and the i -th sleeper F_{RSli} is expressed as:

$$F_{RSli}(t)=K_{pri}\left[Z_{rl}(x_i,t)-Z_{sli}(t)\right]-C_{pri}\left[\dot{Z}_{rl}(x_i,t)-\dot{Z}_{sli}(t)\right] \tag{3.59}$$

where, $Z_{sli}(t)$ and $\dot{Z}_{sli}(t)$ are the vertical displacement and velocity of the i th sleeper at left end pad location as given by:

$$Z_{sli}(t)=Z_{si}(t)-L_s\phi_{si}(t) \text{ and } \dot{Z}_{sli}(t)=\dot{Z}_{si}(t)-L_s\dot{\phi}_{si}(t) \tag{3.60}$$

where, L_s is the lateral distance between two sleeper supports.

In Eqn. (3.57), the contact force P_{WRlj} between the j th wheel of the left side of the vehicle and rail is determined by non linear Hertz contact theory as given by:

$$P_{WRlj}(t)=\begin{Bmatrix} C_H\{Z_{wlj}(t)-Z_{rl}(x_j,t)-r(t)\}^{3/2} \\ 0 \end{Bmatrix} \quad \begin{matrix} Z_{wlj}(t)-Z_{rl}(x_j,t)-r(t)>0 \\ Z_{wlj}(t)-Z_{rl}(x_j,t)-r(t)\le 0 \end{matrix} \tag{3.61}$$

where, $Z_{wlj}(t)$ is the vertical displacement of the left wheel for a particular wheelset ($j=1,..,4$) and expressed as:

$$Z_{wlj}(t)=Z_{wj}(t)-l_p\phi_{wj}(t) \tag{3.62}$$

Similarly, for right side rail beam:

$$\frac{d^2 Z_{rr}(x,t)}{dt^2} + \frac{Gk_r}{\rho}\left(\frac{\pi k}{L}\right)^2 Z_k(t) - \frac{Gk_r}{\rho}\left(\frac{\pi k}{L}\right)\Psi_k(t) + \frac{k_1}{\rho A}\left(\frac{\pi k}{L}\right)^2 Z_k(t) = \tag{3.63}$$

$$-\sum_{i=1}^{N} F_{RSri} N_z(k, x_i) + \sum_{j=1}^{4} P_{WRrj} N_z(k, x_j)$$

$$\frac{d^2 \Psi_k(t)}{dt^2} + \left(\frac{GAk_r}{\rho I} + \frac{E}{\rho}\left(\frac{\pi k}{L}\right)^2\right)\Psi_k(t) - \frac{GAk_r}{\rho I}\left(\frac{\pi k}{L}\right) Z_k(t) = 0 \tag{3.64}$$

The reaction force between the right rail and the i th sleeper F_{RSri} is expressed as:

$$F_{RSri}(t) = K_{pri}\left[Z_{rr}(x_i, t) - Z_{sri}(t)\right] - C_{pri}\left[\dot{Z}_{rr}(x_i, t) - \dot{Z}_{sri}(t)\right] \tag{3.65}$$

where, $Z_{sri}(t)$ and $\dot{Z}_{sri}(t)$ are the vertical displacement and velocity of the i 'th sleeper at the right end pad location, and can be expressed as:

$$Z_{sri}(t) = Z_{si}(t) + L_s \phi_{si}(t) \text{ and } \dot{Z}_{sri}(t) = \dot{Z}_{si}(t) + L_s \dot{\phi}_{si}(t) \tag{3.66}$$

The contact force P_{WRrj} between the j th wheel and rail is determined by non-linear Hertz contact theory as given by:

$$P_{WRrj}(t) = \begin{cases} C_H \{Z_{wrj}(t) - Z_{rr}(x_j, t) - Z_0(t)\}^{3/2} & Z_{wrj}(t) - Z_{rr}(x_j, t) - r(t) > 0 \\ 0 & Z_{wrj}(t) - Z_{rr}(x_j, t) - r(t) \le 0 \end{cases} \tag{3.67}$$

where, $Z_{wrj}(t)$ is the vertical displacement of the right wheel for a particular wheelset ($j = 1,..,4$) and expressed as:

$$Z_{wrj}(t) = Z_{wj}(t) + l_p \phi_{wj}(t) \tag{3.68}$$

The equations of motion of the vehicle system described by Eqns. (3.1) to (3.34), and of the track system derived by Eqns. (3.35) to (3.46) together with the Hertzian nonlinear contact model in Eqn. (3.49) describe the vertical dynamics of the coupled vehicle-track system. These equations are solved simultaneously to obtain the wheel-rail interaction force or acceleration and the responses of the vehicle-track system components.

3.6 NATURAL VIBRATION ANALYSIS OF THE VEHICLE-TRACK SYSTEM

The natural vibration characteristics of the individual vehicle and track systems govern the overall wheel-rail interaction responses. Natural frequencies provide useful information to understand the basic behaviors of the vehicle-track system. In this section, the natural frequencies of the individual vehicle components, such as car body, bogies and wheelsets are investigated. The natural frequencies of the entire track system is also identified in order to compare these frequencies with those obtained from the individual vehicle components and the excitation frequencies obtained from the wheel-rail impact response analysis due to wheel flats.

3.6.1 Natural vibration of the vehicle components:

The dynamic behavior of the vehicle system components and structures largely depend upon the natural frequencies and deflection modes of the individual components. In this study, the vehicle system model consists of a car body, two bogies and four wheelsets. The car body and two bogies have vertical, pitch and roll motions, whereas the four wheelsets have vertical and roll motions only. The total vehicle system model is represented by 17-DOF system. This system, thus, has a number of different natural frequencies and these frequencies can be separated. An eigenvalue problem is formulated to derive the natural frequencies and deflection modes of the vehicle, which is discussed below:

The equation of free vibration of linear vehicle can be written in matrix form as:

$$M_v\left[\ddot{z}\right]+C_v\left[\dot{z}\right]+K_v\left[z\right]=\left[0\right] \tag{3.69}$$

where, M_v, C_v and K_v are (17×17) mass, damping and stiffness matrices, respectively. These matrices are shown below:

$$M_v = \begin{bmatrix} M_c & 0 & 0 & 0 & 0 & 0 & 0 & 0 & 0 & 0 & 0 & 0 & 0 & 0 & 0 & 0 & 0 \\ 0 & J_{cy} & 0 & 0 & 0 & 0 & 0 & 0 & 0 & 0 & 0 & 0 & 0 & 0 & 0 & 0 & 0 \\ 0 & 0 & J_{cx} & 0 & 0 & 0 & 0 & 0 & 0 & 0 & 0 & 0 & 0 & 0 & 0 & 0 & 0 \\ 0 & 0 & 0 & M_{b1} & 0 & 0 & 0 & 0 & 0 & 0 & 0 & 0 & 0 & 0 & 0 & 0 & 0 \\ 0 & 0 & 0 & 0 & M_{b2} & 0 & 0 & 0 & 0 & 0 & 0 & 0 & 0 & 0 & 0 & 0 & 0 \\ 0 & 0 & 0 & 0 & 0 & J_{by1} & 0 & 0 & 0 & 0 & 0 & 0 & 0 & 0 & 0 & 0 & 0 \\ 0 & 0 & 0 & 0 & 0 & 0 & J_{by2} & 0 & 0 & 0 & 0 & 0 & 0 & 0 & 0 & 0 & 0 \\ 0 & 0 & 0 & 0 & 0 & 0 & 0 & J_{bx1} & 0 & 0 & 0 & 0 & 0 & 0 & 0 & 0 & 0 \\ 0 & 0 & 0 & 0 & 0 & 0 & 0 & 0 & J_{bx2} & 0 & 0 & 0 & 0 & 0 & 0 & 0 & 0 \\ 0 & 0 & 0 & 0 & 0 & 0 & 0 & 0 & 0 & M_{w1} & 0 & 0 & 0 & 0 & 0 & 0 & 0 \\ 0 & 0 & 0 & 0 & 0 & 0 & 0 & 0 & 0 & 0 & M_{w2} & 0 & 0 & 0 & 0 & 0 & 0 \\ 0 & 0 & 0 & 0 & 0 & 0 & 0 & 0 & 0 & 0 & 0 & M_{w3} & 0 & 0 & 0 & 0 & 0 \\ 0 & 0 & 0 & 0 & 0 & 0 & 0 & 0 & 0 & 0 & 0 & 0 & M_{w4} & 0 & 0 & 0 & 0 \\ 0 & 0 & 0 & 0 & 0 & 0 & 0 & 0 & 0 & 0 & 0 & 0 & 0 & J_{wx1} & 0 & 0 & 0 \\ 0 & 0 & 0 & 0 & 0 & 0 & 0 & 0 & 0 & 0 & 0 & 0 & 0 & 0 & J_{wx2} & 0 & 0 \\ 0 & 0 & 0 & 0 & 0 & 0 & 0 & 0 & 0 & 0 & 0 & 0 & 0 & 0 & 0 & J_{wx3} & 0 \\ 0 & 0 & 0 & 0 & 0 & 0 & 0 & 0 & 0 & 0 & 0 & 0 & 0 & 0 & 0 & 0 & J_{wx4} \end{bmatrix}$$

$$K_v = \left[\begin{array}{cccccccc}
-4K_s & 0 & 0 & 2K_s & 2K_s & 0 & 0 & 0 \\
0 & -4K_s l_c^2 & 0 & 2K_s l_c & -2K_s l_c & 0 & 0 & 0 \\
0 & 0 & -4K_s l_s^2 & 0 & 0 & 0 & 0 & 2K_s l_s^2 \\
2K_s & 0 & 0 & -2K_s - 4K_p & 0 & 0 & 0 & 0 \\
2K_s & 0 & 0 & 0 & -2K_s - 4K_p & 0 & 0 & 0 \\
0 & 0 & 0 & 0 & 0 & -4K_p l_b^2 & 0 & 0 \\
0 & 0 & 0 & 0 & 0 & 0 & -4K_p l_b^2 & 0 \\
0 & 0 & 2K_s l_s^2 & 0 & 0 & 0 & 0 & -4K_p l_p^2 - 2K_s l_s^2 \\
0 & 0 & 2K_s l_s^2 & 0 & 0 & 0 & 0 & 0 \\
0 & 0 & 0 & 2K_p & 0 & -2K_p l_b & 0 & 0 \\
0 & 0 & 0 & 2K_p & 0 & -2K_p l_b & 0 & 0 \\
0 & 0 & 0 & 0 & 2K_p & 0 & -2K_p l_b & 0 \\
0 & 0 & 0 & 0 & 2K_p & 0 & -2K_p l_b & 0 \\
0 & 0 & 0 & 0 & 0 & 0 & 0 & 2K_p l_p^2 \\
0 & 0 & 0 & 0 & 0 & 0 & 0 & 2K_p l_p^2 \\
0 & 0 & 0 & 0 & 0 & 0 & 0 & 0 \\
0 & 0 & 0 & 0 & 0 & 0 & 0 & 0
\end{array}\right. \quad \ldots\ldots$$

$$\left.\begin{array}{ccccccccc}
0 & 0 & 0 & 0 & 0 & 0 & 0 & 0 & 0 \\
0 & 0 & 0 & 0 & 0 & 0 & 0 & 0 & 0 \\
2K_s l_s^2 & 0 & 0 & 0 & 0 & 0 & 0 & 0 & 0 \\
0 & 2K_p & 2K_p & 0 & 0 & 0 & 0 & 0 & 0 \\
0 & 0 & 0 & 2K_p & 2K_p & 0 & 0 & 0 & 0 \\
0 & 2K_p l_b & -2K_p l_b & 0 & 0 & 0 & 0 & 0 & 0 \\
0 & 0 & 0 & 2K_p l_b & -2K_p l_b & 0 & 0 & 0 & 0 \\
0 & 0 & 0 & 0 & 0 & 2K_p l_p^2 & 2K_p l_p^2 & 0 & 0 \\
-4K_p l_p^2 - 2K_s l_s^2 & 0 & 0 & 0 & 0 & 0 & 0 & 2K_p l_p^2 & 2K_p l_p^2 \\
0 & -2(K_p + K_H) & 0 & 0 & 0 & 0 & 0 & 0 & 0 \\
0 & 0 & -2(K_p + K_H) & 0 & 0 & 0 & 0 & 0 & 0 \\
0 & 0 & 0 & -2(K_p + K_H) & 0 & 0 & 0 & 0 & 0 \\
0 & 0 & 0 & 0 & -2(K_p + K_H) & 0 & 0 & 0 & 0 \\
0 & 0 & 0 & 0 & 0 & -2l_p^2(K_p + K_H) & 0 & 0 & 0 \\
0 & 0 & 0 & 0 & 0 & 0 & -2l_p^2(K_p + K_H) & 0 & 0 \\
2K_p l_p^2 & 0 & 0 & 0 & 0 & 0 & 0 & -2l_p^2(K_p + K_H) & 0 \\
2K_p l_p^2 & 0 & 0 & 0 & 0 & 0 & 0 & 0 & -2l_p^2(K_p + K_H)
\end{array}\right]$$

$$
C_v = \left[\begin{matrix}
-4C_s & 0 & 0 & 2C_s & 2C_s & 0 & 0 & 0 \\
0 & -4C_s l_c^2 & 0 & 2C_s l_c & -2C_s l_c & 0 & 0 & 0 \\
0 & 0 & -4C_s l_s^2 & 0 & 0 & 0 & 0 & 2C_s l_s^2 \\
2C_s & 0 & 0 & -2C_s - 4C_p & 0 & 0 & 0 & 0 \\
2C_s & 0 & 0 & 0 & -2C_s - 4C_p & 0 & 0 & 0 \\
0 & 0 & 0 & 0 & 0 & -4C_p l_b^2 & 0 & 0 \\
0 & 0 & 0 & 0 & 0 & 0 & -4C_p l_b^2 & 0 \\
0 & 0 & 2C_s l_s^2 & 0 & 0 & 0 & 0 & -4C_p l_p^2 - 2C_s l_s^2 \\
0 & 0 & 2C_s l_s^2 & 0 & 0 & 0 & 0 & 0 \\
0 & 0 & 0 & 2C_p & 0 & -2C_p l_b & 0 & 0 \\
0 & 0 & 0 & 2C_p & 0 & -2C_p l_b & 0 & 0 \\
0 & 0 & 0 & 0 & 2C_p & 0 & -2C_p l_b & 0 \\
0 & 0 & 0 & 0 & 2C_p & 0 & -2C_p l_b & 0 \\
0 & 0 & 0 & 0 & 0 & 0 & 0 & 2C_p l_p^2 \\
0 & 0 & 0 & 0 & 0 & 0 & 0 & 2C_p l_p^2 \\
0 & 0 & 0 & 0 & 0 & 0 & 0 & 0 \\
0 & 0 & 0 & 0 & 0 & 0 & 0 & 0
\end{matrix} \right. \cdots
$$

$$
\left. \begin{matrix}
0 & 0 & 0 & 0 & 0 & 0 & 0 & 0 & 0 \\
0 & 0 & 0 & 0 & 0 & 0 & 0 & 0 & 0 \\
2C_s l_s^2 & 0 & 0 & 0 & 0 & 0 & 0 & 0 & 0 \\
0 & 2C_p & 2C_p & 0 & 0 & 0 & 0 & 0 & 0 \\
0 & 0 & 0 & 2C_p & 2C_p & 0 & 0 & 0 & 0 \\
0 & 2C_p l_b & -2C_p l_b & 0 & 0 & 0 & 0 & 0 & 0 \\
0 & 0 & 0 & 2C_p l_b & -2C_p l_b & 0 & 0 & 0 & 0 \\
0 & 0 & 0 & 0 & 0 & 2C_p l_p^2 & 2C_p l_p^2 & 0 & 0 \\
-4C_p l_p^2 - 2C_s l_s^2 & 0 & 0 & 0 & 0 & 0 & 0 & 2C_p l_p^2 & 2C_p l_p^2 \\
0 & -2C_p & 0 & 0 & 0 & 0 & 0 & 0 & 0 \\
0 & 0 & -2C_p & 0 & 0 & 0 & 0 & 0 & 0 \\
0 & 0 & 0 & -2C_p & 0 & 0 & 0 & 0 & 0 \\
0 & 0 & 0 & 0 & -2C_p & 0 & 0 & 0 & 0 \\
0 & 0 & 0 & 0 & 0 & -2l_p^2 C_p & 0 & 0 & 0 \\
0 & 0 & 0 & 0 & 0 & 0 & -2l_p^2 C_p & 0 & 0 \\
2C_p l_p^2 & 0 & 0 & 0 & 0 & 0 & 0 & -2l_p^2 C_p & 0 \\
2C_p l_p^2 & 0 & 0 & 0 & 0 & 0 & 0 & 0 & -2l_p^2 C_p
\end{matrix} \right]
$$

$$[z]=[Z_c,\theta_c,\phi_c,Z_{b1},Z_{b2},\theta_{b1},\theta_{b2},\phi_{b1},\phi_{b2},Z_{w1},Z_{w2},Z_{w3},Z_{w4},\phi_{w1},\phi_{w2},\phi_{w3},\phi_{w4}]^T$$

$$\begin{Bmatrix}\ddot{z}\\ \dot{z}\end{Bmatrix}=\begin{bmatrix}-M_v^{-1}C_v & -M_v^{-1}K_v\\ I & 0\end{bmatrix}\begin{Bmatrix}\dot{z}\\ z\end{Bmatrix} \tag{3.70}$$

where, I is an identity matrix, K_H is linearized Hertzian contact stiffness that can be obtained from Eqn. (3.47). If we consider the overlap between the wheel and rail (Δz) in Eqn. (3.47) is constant and can be evaluated by the static wheel load P_0. The linear contact stiffness can be expressed as:

$$K_H=\frac{\partial P}{\partial \Delta z} \tag{3.71}$$

or, $K_H=1.5C_H(P_0/C_H)^{\frac{1}{3}}$ (3.72)

where, C_H is the nonlinear Hertzian contact coefficient.

The eigenvalue solution of the dynamic matrix of Eqn. (3.70) will generally yield 17 pairs of complex conjugate eigenvalues of form:

$$D_i=\alpha_i+j\beta_i \tag{3.73}$$

Natural frequency of ith mode is given by:

$$\omega_{ni}=\sqrt{\alpha_i^2+\beta_i^2} \tag{3.74}$$

The damped natural frequency of ith mode is:

$$\omega_{di}=|\beta_i| \tag{3.75}$$

In order to identify the mode associated with the *i*'th natural frequency, the eigenvector for the *i*'th eigenvalue may be examined. The maximum absolute value in a column of the eigenvector will identify the corresponding eigenvalue and the corresponding 17 motions associated with the natural modes. The eigenvalues and eigenvectors are obtained by using MATLAB. The eigenvalue problem is solved using the model parameters summarized in Table 3.1.

Table 3.1: Vehicle model parameters [8].

Notation	Parameter	Value
M_c	Car body mass	76150 kg
M_t	Bogie mass	1700 kg
M_w	Wheelset mass	1120 kg
J_{cx}	Mass moment of inertia of the car body about X axis	95576 kg-m^2
J_{cy}	Mass moment of inertia of the car body about Y axis	726462 kg-m^2
J_{bx}	Mass moment of inertia of the bogie about X axis	1600 kg-m^2
J_{by}	Mass moment of inertia of the bogie about Y axis	760 kg-m^2
J_{wx}	Mass moment of inertia of the wheelset about X axis	420.1 kg-m^2
K_P	Primary suspension stiffness	7.88×10^5 kN/m
C_P	Primary suspension damping	3.5 kN-s/m
K_S	Secondary suspension stiffness	5.32×10^3 kN/m
C_S	Secondary suspension damping	70 kN-s/m
l_c	Semi-longitudinal distance between bogies	5.18 m
l_b	Semi-longitudinal distance between wheelsets in bogie	1.25 m
l_s	Semi-lateral distance between secondary suspensions	0.80 m
l_p	Semi-lateral distance between primary suspensions	0.80 m
R	Wheel radius	0.475 m

The natural frequencies, damped natural frequencies and their corresponding deflection modes for fully loaded conditions (103 kN of static wheel load) are shown in Table 3.2. It can be seen from Table 3.2 that the natural frequencies of the car body are very small compared to the wheelset natural frequencies. This is because of the very high primary stiffness considered in modeling to ensure the isolation of the vibration from the exciting source. Furthermore, this also indicates that the properties of the wheel-track system have little effect on fundamental frequency of the vehicle system.

Table 3. 2: Natural frequencies, damped natural frequencies and corresponding deflection modes

Natural frequency (Hz)	Damped natural frequency (Hz)	Dominant modes
2.0308	2.0301	Car body roll
2.7544	2.7528	Car body bounce
4.7818	4.7818	Car body pitch
137.4785	137.3983	Front bogie roll
137.5231	137.3984	Rear bogie roll
156.1791	155.7443	Front bogie bounce
156.0906	155.7442	Rear bogie bounce
312.0656	312.0656	Axle bounce (j = 1, 2)
346.8085	345.8302	Axle bounce (j = 3, 4)
405.1506	405.1506	Front bogie pitch
405.1506	405.1506	Rear bogie pitch
407.6833	407.6833	Axle roll (j = 1, 2)
423.5512	423.1655	Axle roll (j = 3, 4)

3.6.2 Natural vibration of the track structure

The natural frequencies and different associated modes of the vibrating systems have significant importance in railway engineering. The natural frequency of the railroad track has been investigated in different studies for many years [9, 180, 181, 182]. Most of these reported studies considered the railway track model as continuous Euler-Bernoulli or Timoshenko beam resting on elastic layers to find out the natural frequencies of the track. These layers are modeled as either one-parameter Winkler or two-parameter Pasternak foundation model. Cai [9] reported a three-dimensional railway track model with discrete elastic supports representing the railpads and ballasts. The entire track model was simplified to a generalized track element in order to investigate the natural frequencies of the track. In this section, the natural frequencies of the railway track model developed in section 3.3 will be identified. In order to facilitate the analysis, the complex three-dimensional track model is simplified into a two-dimensional generalized track model with linear railpad and ballast stiffness.

Equations of motion of Timoshenko beam under general condition:

Let us consider a free-body diagram of a differential element dx of an arbitrary beam. As shown in Fig. 3.4, the beam is acted upon by general distributed force $p(x,t)$, and a constant axial force P_a. U and $U+\frac{\partial U}{\partial x}dx$ are the sectional shear forces, M and $M+\frac{\partial M}{\partial x}dx$ are the sectional bending moments, F is the inertial force and $\overline{R}$ is the rotary inertial moment. Since the beam is considered as Timoshenko beam, the effects of the shear distortion and rotary inertia of the beam mass has been taken into account. The rotational angle and shear distortion are denoted by ψ and η, respectively.

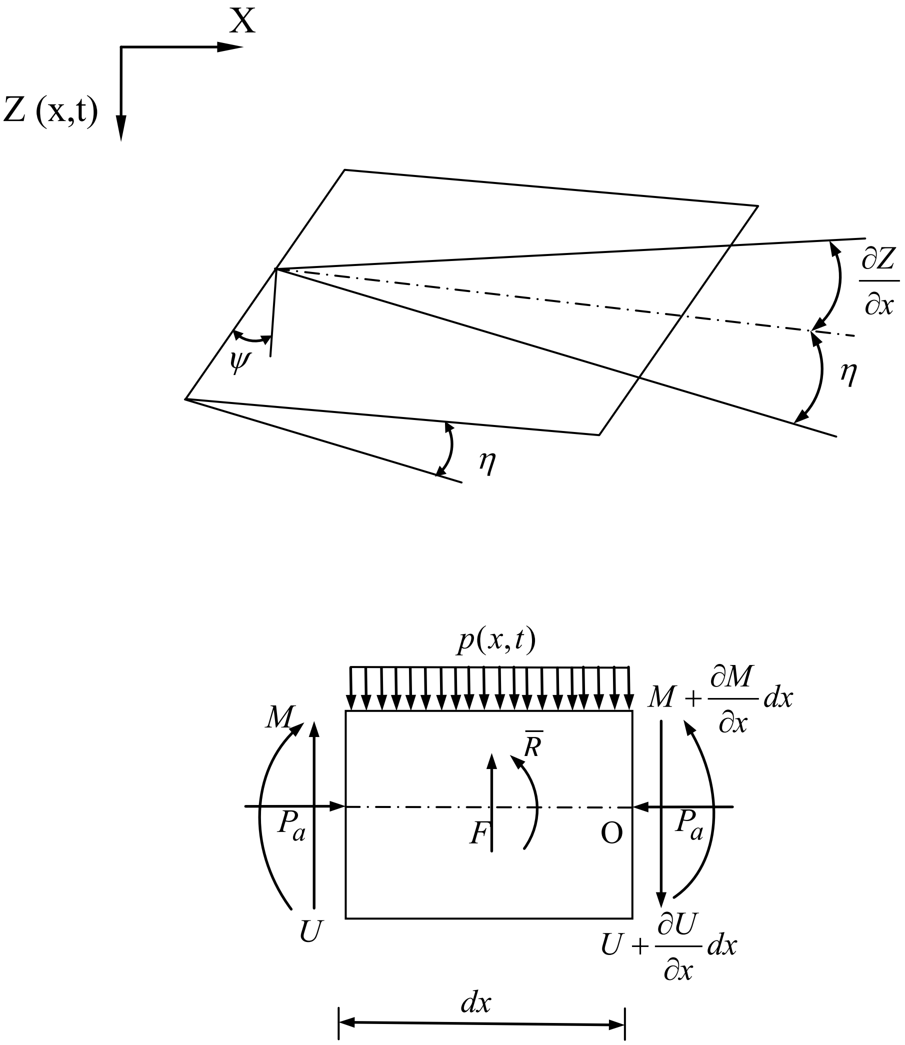

Fig. 3. 4: Flexural vibration of Timoshenko beam

The vibrational equilibrium of the differential element can be established by summing up the forces and moments equal to zero, as:

Summing all the forces in vertical direction:

$$-U+p(x,t)dx+(U+\frac{\partial U}{\partial x}dx)-F=0 \tag{3.76}$$

which can be shown upon reduction as:

$$-\frac{\partial U}{\partial x}+F=p(x,t) \tag{3.77}$$

Summing all the moments about point O gives:

$$M+Udx-(M+\frac{\partial M}{\partial x}dx)-p(x,t)dx\frac{dx}{2}+\overline{R}+P_a\psi dx=0 \tag{3.78}$$

Neglecting the higher order terms in dx yields:

$$M+Udx-(M+\frac{\partial M}{\partial x}dx)+\overline{R}+P_a\psi dx=0 \tag{3.79}$$

where the rotary inertia $\overline{R}$ is given by:

$$\overline{R}=\overline{m}\overline{r}^2dx\frac{\partial^2\psi}{\partial t^2} \tag{3.80}$$

where, $\overline{m}$ is the unit mass of the beam, and $\overline{r}$ is the radius of gyration of the beam cross-section. Rearranging Equation 3.78 leads to:

$$U=-P_a\psi+\overline{m}\overline{r}^2\frac{\partial^2\psi}{\partial t^2}+\frac{\partial M}{\partial x} \tag{3.81}$$

The relationships between the shear force and shear distortion, and between the moment and the curvature can be expressed as:

$$U=-k_rAG\eta(x,t) \tag{3.82}$$

$$M=-EI\frac{\partial\psi(x,t)}{\partial x} \tag{3.83}$$

where, k_r and A are the shear coefficient and area of the beam cross section, respectively, and G is the shear modulus of the beam material.

Substituting Equations (3.82) and (3.83) into Equations (3.77) and (3.81), the following relations can be obtained:

$$\frac{\partial}{\partial x}(k_r AG\eta)+\bar{m}\frac{\partial^2 z}{\partial t^2}=p(x,t) \tag{3.84}$$

$$-k_r AG\eta=-P_a\psi+\overline{mr}^2\frac{\partial^2\psi}{\partial t^2}-\frac{\partial}{\partial x}\left[EI\frac{\partial\psi}{\partial x}\right] \tag{3.85}$$

the shear distortion η can be replaced as:

$$\psi=\eta+\frac{\partial z}{\partial x} \tag{3.86}$$

The final form of Timoshenko beam can be written in terms of vertical deflection and rotation angle as:

$$\frac{\partial}{\partial x}\left[k_r AG(\psi-\frac{\partial z}{\partial x})\right]+\bar{m}\frac{\partial^2 z}{\partial t^2}=p(x,t) \tag{3.87}$$

$$\frac{\partial}{\partial x}\left[EI\frac{\partial\psi}{\partial x}\right]-k_r AG(\psi-\frac{\partial z}{\partial x})-\overline{mr}^2\frac{\partial^2\psi}{\partial t^2}+P_a\psi=0 \tag{3.88}$$

For free vibration case, setting $p(x,t)$=0 and with added foundation stiffness term $k_s z(x,t)$, Equation (3.87) and (3.88) can be written as:

$$\frac{\partial}{\partial x}\left[k_r AG(\psi-\frac{\partial z}{\partial x})\right]+k_s z(x,t)+\bar{m}\frac{\partial^2 z}{\partial t^2}=0 \tag{3.89}$$

$$\frac{\partial}{\partial x}\left[EI\frac{\partial\psi}{\partial x}\right]-k_r AG(\psi-\frac{\partial z}{\partial x})-\overline{mr}^2\frac{\partial^2\psi}{\partial t^2}+P_a\psi=0 \tag{3.90}$$

Dynamic stiffness matrix of a Timoshenko beam:

For a steady-state harmonic motion, displacement z and rotation ψ may be expressed by:

$$z(x,t) = Z(x)e^{i\omega t} \tag{3.91}$$

$$\psi(x,t) = \Psi(x)e^{i\omega t}$$

where, ω represents the frequency, and Z and Ψ represent the amplitude functions.

Therefore, Equations (3.89) and (3.90) can be rewritten as:

$$Z'' + q_1 Z - \Psi' = 0 \tag{3.92}$$

$$EI\Psi'' + (\overline{mr}^2\omega^2 - k_r AG + P_a)\Psi + k_r AGZ' = 0 \tag{3.93}$$

where, $q_1 = \frac{1}{k_r AG}(\overline{m}\omega^2 - k_s)$

Eliminating Z and Ψ from Equations (3.92) and (3.93) yields the following results:

$$Z'''' + \alpha Z'' + \beta = 0 \tag{3.94}$$

$$\Psi'''' + \alpha\Psi'' + \beta = 0 \tag{3.95}$$

$$\text{where, } \alpha = q_1 + \frac{1}{EI}(\overline{mr}^2\omega^2 + P_a); \quad \beta = \frac{q_1}{EI}(\overline{mr}^2\omega^2 - k_r AG + P_a) \tag{3.96}$$

Equations (3.94) and (3.95) represent the same form of 4th order ordinary differential equations for the complex variables $Z(x)$ and $\Psi(x)$.

The solutions of the amplitude functions $Z(x)$ and $\Psi(x)$ can be assumed in the form:

$$Z(x) = \sum_{j=1}^{4} C_j e^{\lambda_j x} \tag{3.97}$$

$$\Psi(x) = \sum_{j=1}^{4} D_j e^{\lambda_j x} \tag{3.98}$$

where, C_j and D_j represent integration coefficients, and λ_j represents solution of the characteristic equations.

Substituting Equations (3.97) and (3.98) into Equations (3.94) and (3.95) gives the solution of λ_j as:

$$\lambda_j = \pm\frac{1}{\sqrt{2}}\left(-\alpha \pm \sqrt{\alpha^2 - 4\beta}\right)^{1/2} \tag{3.99}$$

Substituting Equations (3.97) and (3.98) into Equations (3.92) and (3.93) yields the relationship between the complex coefficients C_j and D_j as:

$$D_j = s_j C_j \tag{3.100}$$

where, $s_j = \lambda_j\left(1+\frac{q_1}{\lambda_j^2}\right) \quad j = 1,2,3,4$ (3.101)

The four unknown complex coefficients C_j's or D_j's can be determined by four boundary conditions at the beam ends.

The nodal displacement amplitudes at the beam ends can be expressed by the four complex coefficients $C_j\,(j = 1,2,3,4)$ such that:

$$\begin{Bmatrix} Z(0) \\ \Psi(0) \\ Z(l) \\ \Psi(l) \end{Bmatrix} = \begin{Bmatrix} 1 & 1 & 1 & 1 \\ s_1 & -s_1 & s_3 & -s_3 \\ e^{\lambda_1 l} & -e^{\lambda_1 l} & e^{\lambda_3 l} & -e^{-\lambda_3 l} \\ s_1 e^{\lambda_1 l} & -s_1 e^{\lambda_1 l} & s_3 e^{\lambda_3 l} & -s_3 e^{-\lambda_3 l} \end{Bmatrix} \tag{3.102}$$

or, $\{\Delta\} = [P]\{C\}$ (3.103)

Similarly, the nodal forces at the beam ends can be expressed by the corresponding displacements by Equations (3.82) and (3.83) such that:

$$\{F\} = \begin{Bmatrix} U(0) \\ -M(0) \\ -U(l) \\ M(l) \end{Bmatrix} = \begin{Bmatrix} k_r AG[\Psi(0) - Z^{'}(0)] \\ -EI\Psi^{'}(0) \\ -k_r AG[\Psi(l) - Z^{'}(l)] \\ EI\Psi^{'}(l) \end{Bmatrix} \tag{3.104}$$

Substituting Equations (3.97) and (3.98) into Equation (3.104) gives:

$$\{F\} = [L]\{C\} \tag{3.105}$$

where, the matrix $[L]$ is given as:

$$[L] = \begin{bmatrix} s_k(s_1 - \lambda_1) & -s_k(s_1 - \lambda_1) & s_k(s_3 - \lambda_3) & -s_k(s_3 - \lambda_3) \\ -fs_1\lambda_1 & -fs_1\lambda_1 & -fs_3\lambda_3 & -fs_3\lambda_3 \\ -s_k e^{\lambda_1 l}(s_1 - \lambda_1) & s_k e^{\lambda_1 l}(s_1 - \lambda_1) & -s_k e^{\lambda_3 l}(s_3 - \lambda_3) & s_k e^{\lambda_3 l}(s_3 - \lambda_3) \\ fe^{\lambda_1 l}s_1\lambda_1 & fe^{-\lambda_1 l}s_1\lambda_1 & fe^{\lambda_3 l}s_3\lambda_3 & fe^{-\lambda_3 l}s_3\lambda_3 \end{bmatrix} \tag{3.106}$$

where, $f = EI$ and $s_k = k_r AG$.

From Equations (3.105) and (3.106), the dynamic stiffness matrix of a beam can be written as:

$$\{F\} = [K]\{\Delta\} \tag{3.107}$$

where, $[K] = [L][P]^{-1}$ (3.108)

since above discussions involve manipulation of complex numbers depending upon the relative values of α and $\sqrt{\alpha^2 - 4\beta}$ of Equation (3.99), which in turn depend upon the magnitude of frequency ω.

Considering the values of α and $\sqrt{\alpha^2 - 4\beta}$, following two different cases with respect to the value of ω_c (known as cut-off frequency) are dealt individually. Cut-off frequency can be defined as:

$$\omega_c = \left(\frac{k_r AG - P_a}{\bar{m} r^2} \right)^{1/2} \tag{3.109}$$

Case 1: if the frequency satisfies the condition $\omega \le \omega_c$,

The values of λ_j 's are two imaginaries and two reals, and assumed as:

$$\lambda_{1,2} = \pm i\rho_1 \text{ and } \lambda_{3,4} = \pm\rho_2 \tag{3.110}$$

where, ρ_1 and ρ_2 are given as follows:

$$\rho_1 = \frac{1}{\sqrt{2}} \left(\alpha + \sqrt{\alpha^2 - 4\beta} \right)^{1/2} \tag{3.111}$$

$$\rho_2 = \frac{1}{\sqrt{2}} \left(-\alpha + \sqrt{\alpha^2 - 4\beta} \right)^{1/2} \tag{3.112}$$

The corresponding s_j values those relate the coefficients C_j and D_j are given by:

$$s_{1,2} = \pm iu_1 \text{ and } s_{3,4} = \pm u_2 \tag{3.113}$$

$$\text{where, } u_1 = \rho_1 \left(1 - \frac{q_1}{\rho_1^2} \right) \text{ and } u_2 = \rho_2 \left(1 - \frac{q_1}{\rho_2^2} \right) \tag{3.114}$$

The corresponding amplitude functions $Z(x)$ and $\Psi(x)$ given by the Equations (3.97) and (3.98) can be reduced to the following form as:

$$Z(x) = C_1^{'} \cos \rho_1 x + C_2^{'} \sin \rho_1 x + C_3^{'} \cosh \rho_2 x + C_4^{'} \sinh \rho_2 x \tag{3.115}$$

$$\Psi(x) = D_1^{'} \sin \rho_1 x + D_2^{'} \cos \rho_1 x + D_3^{'} \sinh \rho_2 x + D_4^{'} \cosh \rho_2 x \tag{3.116}$$

where, $C_1^{'}$'s and $D_1^{'}$'s are all real, and their relationships can be expressed as:

$$D_1^{'} = -u_1 C_1^{'},\ D_2^{'} = u_1 C_2^{'},\ D_3^{'} = -u_2 C_3^{'},\ D_4^{'} = u_2 C_4^{'} \tag{3.117}$$

Finally, the general dynamic stiffness matrix for a Timoshenko beam for $\omega \le \omega_c$ is then given as follows:

$$[K]=\begin{bmatrix} K_{11} & K_{12} & K_{13} & K_{14} \\ K_{21} & K_{22} & K_{23} & K_{24} \\ K_{31} & K_{32} & K_{33} & K_{34} \\ K_{41} & K_{42} & K_{43} & K_{44} \end{bmatrix} \tag{3.118}$$

where,

$$K_{11}=K_{33}=B_k u_1 u_2 (u_1\rho_1+\rho_2 u_2)(u_1 s_k C_k + u_2 S_k c_k) \tag{3.119}$$

$$K_{12}=K_{21}=-K_{34}=-K_{43}=$$

$$B_k u_1 u_2 \left[(u_2\rho_1-\rho_2 u_1)\left(1-c_k C_k\right)+(u_2\rho_1-\rho_2 u_1) s_k S_k\right]$$

$$K_{22}=K_{44}=-B_k u_1 u_2 (u_1\rho_1+\rho_2 u_2)(u_1 S_k c_k - u_2 s_k C_k)$$

$$K_{13}=K_{31}=-B_k u_1 u_2 (u_1\rho_1+\rho_2 u_2)(u_1 s_k + u_2 S_k)$$

$$K_{23}=K_{32}=-K_{14}=-K_{41}=B_k u_1 u_2 (u_1\rho_1+\rho_2 u_2)(c_k - C_k)$$

$$K_{24}=K_{42}=B_k (u_1\rho_1+\rho_2 u_2)(u_1 S_k - u_2 s_k)$$

where, $s_k=\sin(\rho_1 l)$, $c_k=\cos(\rho_1 l)$, $S_k=\sinh(\rho_2 l)$, $C_k=\cosh(\rho_2 l)$, and

$$B_k=\frac{EI}{\left(u_2^2-u_1^2\right)s_k S_k+2u_1u_2(c_k C_k-1)}$$

Case 2: if the frequency satisfies the condition $\omega>\omega_c$,

The values of λ_j's and s_j's are all imaginaries, and assumed as:

$$\lambda_{1,2}=\pm i\rho_1 \text{ and } \lambda_{3,4}=\pm i\rho_2 \tag{3.120}$$

$$s_{1,2}=\pm iu_1 \text{ and } s_{3,4}=\pm iu_2 \tag{3.121}$$

where, ρ_1 and ρ_2 are given as follows:

$$\rho_1 = \frac{1}{\sqrt{2}}\left(\alpha + \sqrt{\alpha^2 - 4\beta}\right)^{1/2} \tag{3.122}$$

$$\rho_2 = \frac{1}{\sqrt{2}}\left(\alpha - \sqrt{\alpha^2 - 4\beta}\right)^{1/2} \tag{3.123}$$

and, $u_1 = \rho_1\left(1 - \frac{q_1}{\rho_1^2}\right)$ and $u_2 = \rho_2\left(1 - \frac{q_1}{\rho_2^2}\right)$ (3.124)

The corresponding amplitude functions $Z(x)$ and $\Psi(x)$ given by the Equations (3.97) and (3.98) can be reduced to the following form as:

$$Z(x) = C_1^{'}\cos\rho_1 x + C_2^{'}\sin\rho_1 x + C_3^{'}\cos\rho_2 x + C_4^{'}\sin\rho_2 x \tag{3.125}$$

$$\Psi(x) = D_1^{'}\sin\rho_1 x + D_2^{'}\cos\rho_1 x + D_3^{'}\sin\rho_2 x + D_4^{'}\cos\rho_2 x \tag{3.126}$$

where, $D_1^{'} = -u_1 C_1^{'}$, $D_2^{'} = u_1 C_2^{'}$, $D_3^{'} = -u_2 C_3^{'}$, $D_4^{'} = u_2 C_4^{'}$ (3.127)

The general dynamic stiffness matrix for a Timoshenko beam for $\omega > \omega_c$ is then exactly same as Equation (3.118) with different values of elements, such as:

$$K_{11} = K_{33} = B_k u_1 u_2 (u_1\rho_1 - \rho_2 u_2)(-u_1 s_k C_k + u_2 S_k c_k) \tag{3.128}$$

$$K_{12} = K_{21} = -K_{34} = -K_{43} =$$

$$-B_k u_1 u_2 \left[(u_2\rho_1 + \rho_2 u_1)\left(1 - c_k C_k\right) - (u_2\rho_1 + \rho_2 u_1) s_k S_k\right]$$

$$K_{22} = K_{44} = B_k u_1 u_2 (u_1\rho_1 - \rho_2 u_2)(u_1 S_k c_k - u_2 s_k C_k)$$

$$K_{13} = K_{31} = B_k u_1 u_2 (u_1\rho_1 - \rho_2 u_2)(u_1 s_k - u_2 S_k)$$

$$K_{23} = K_{32} = -K_{14} = -K_{41} = -B_k u_1 u_2 (u_1\rho_1 - \rho_2 u_2)(c_k - C_k)$$

$$K_{24} = K_{42} = B_k (u_1\rho_1 - \rho_2 u_2)(-u_1 S_k + u_2 s_k)$$

where, $s_k = \sin(\rho_1 l)$, $c_k = \cos(\rho_1 l)$, $S_k = \sin(\rho_2 l)$, $C_k = \cos(\rho_2 l)$,and

$$B_k = \frac{EI}{\left(u_2^2 + u_1^2\right) s_k S_k + 2u_1 u_2 (c_k C_k - 1)}$$

Natural frequencies of the railway track:

The railway track model developed in section 3.3, as shown in Fig 3.2, has periodic, chain type structure composed of two parallel rails and equally spaced sleepers. In order to obtain the fundamental vibration characteristics of the railway track model, a generalized track element model is developed, as described in [9]. The simplified model is shown in Fig. 3.5. The entire three-dimensional track model is simplified to an assembly which consists of one rail span, two adjacent sleepers and the contact stiffness between the rail and sleepers, as shown in Fig. 3.5 (a). The rail beam is continuous and modeled by Timoshenko theory, whereas the sleepers are considered as rigid masses. The stiffness and damping properties of the individual railpad and ballast, rail sleeper mass are further represented by equivalent linear spring stiffness at each end of the rail span, as shown in Fig. 3.5 (b). This equivalent spring stiffness depends upon the inertial and elastic properties of the rail components as well as the vibration frequency of the track, which can be expressed as [9]:

$$\bar{K}_e = K_p \left(1 - \frac{K_p}{K_p + K_s - M_t \omega^2} \right) \tag{3.129}$$

where, $\bar{K}_e$ represents the equivalent frequency-dependent spring stiffness, K_p represents the linear stiffness of the rail pad, M_t is the total tie mass with respect to one rail, ω is the vibrational frequency of the entire track system and K_s is the total foundation stiffness that can be expressed as:

$$K_s = \frac{K_p K_b}{K_p + K_b} \tag{3.130}$$

where, K_b is the linear stiffness of the rail ballast.

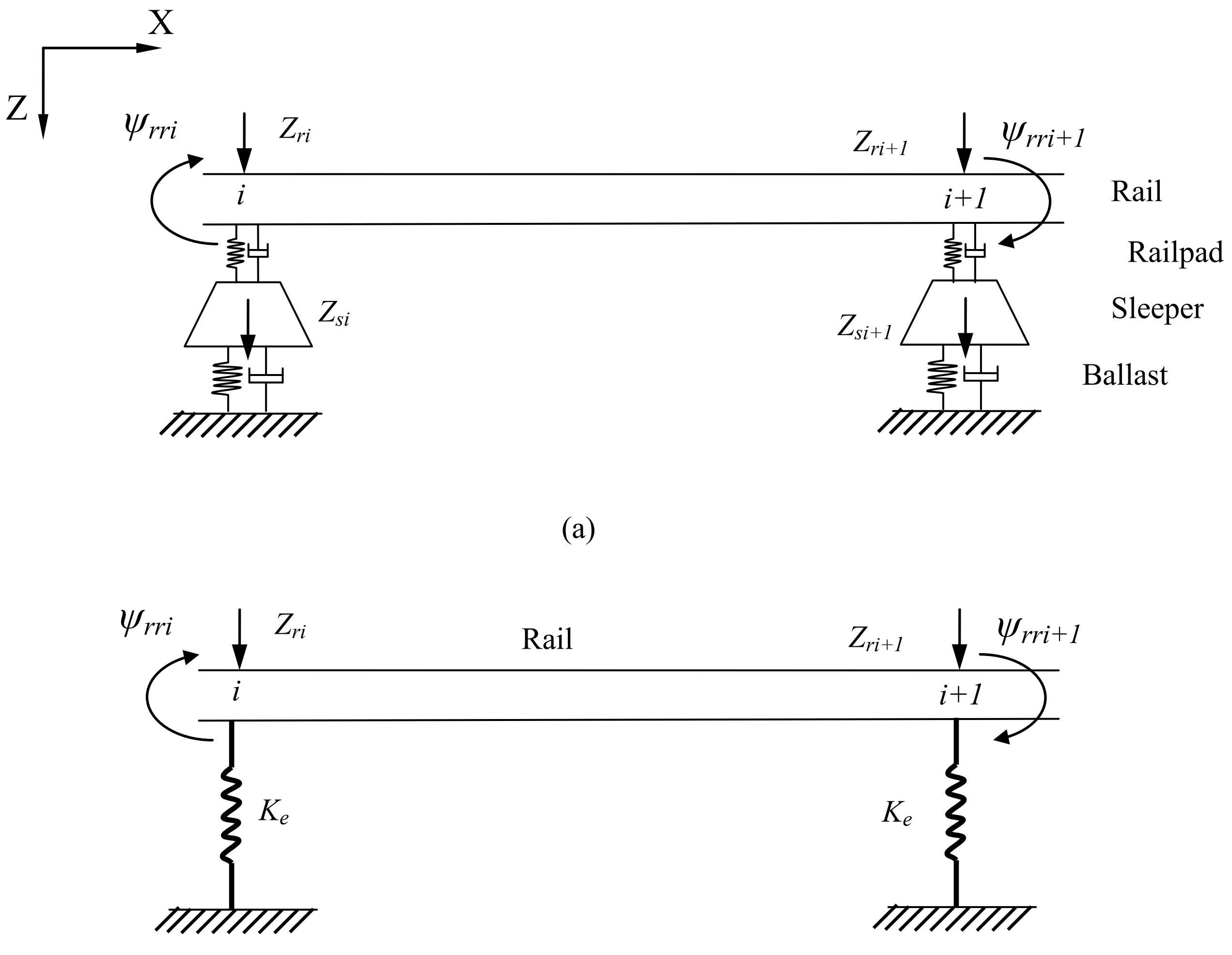

(a)

(b)

Fig. 3. 5: Formulation of the track element for eigenvalue analysis (a) generalized track element (b) simplified track element.

This equivalent spring stiffness significantly simplifies the analysis while preserving the characteristics of the underlying rail supports. However, the damping properties of the railpad and ballast are ignored in natural frequency analysis. The dynamic stiffness matrix of the rail span as described in Eqn. (3.118) can be combined with the equivalent spring stiffness as described in Eqn. (3.129) in order to formulate the generalized dynamic stiffness matrix of the track element as:

$$[K_r]=\begin{bmatrix} K_{11}+\overline{K}_e & K_{12} & K_{13} & K_{14} \\ K_{21} & K_{22} & K_{23} & K_{24} \\ K_{31} & K_{32} & K_{33}+\overline{K}_e & K_{34} \\ K_{41} & K_{42} & K_{43} & K_{44} \end{bmatrix} \tag{3.131}$$

where, K_{ij} 's are the elements of the dynamic stiffness matrix as described by Eqns. (3.119) and (3.128). The relationship between the modal forces and corresponding displacements, as shown in Fig. 3.5, can be expressed as:

$$\{F_r\}=[K_r(\omega)]\{\delta_r\} \tag{3.132}$$

where,

$$\{F_r\}=[F_i,M_i,F_{i+1},M_{i+1}]^T \tag{3.133}$$

and, $\{\delta_r\}=[Z_{ri},\psi_{rri},Z_{ri+1},\psi_{rri+1}]^T$ (3.134)

where, i refers to the ith rail/sleeper connection point, F,M denote the modal force and moment, respectively; Z_r,ψ_{rr} denote the modal deflection and rotation angle of the rail, respectively.

The natural frequencies of the entire track are determined by formulating the overall dynamic stiffness matrix of the track. The resulting set of simultaneous equations can be written as:

$$[K_R(\omega)]\{\Delta_R\}=0 \tag{3.135}$$

where, $[K_R(\omega)]$ represents the global dynamic stiffness matrix, and

$\{\Delta_R\}=\left[Z_{r1},\psi_{rr1},Z_{r2},\psi_{rr2},........,Z_{rN},\psi_{rrN}\right]^T$ represents the displacements of the rail. Here, N is the total number of sleepers included into the track model. The determinant of the overall dynamic stiffness matrix needs to be set to zero in order to obtain non-trivial solutions of $\{\Delta_R\}$ in Eqn. (3.135), such as:

$$|K_R(\omega)| = 0 \tag{3.136}$$

which forms the characteristic frequency function of the track system.

The undamped natural frequencies of the track system are obtained from Eqn. 3.136, while the parameters used to solve the equation are summarized in Table 3.3.

Table 3. 3: Track model parameters [8, 17].

Notation	Parameter	Value
m_r	Rail mass per unit length	60.64 kg/m
E	Elastic modulus of the rail	207×10^{9} N/m^2
I	Rail second moment of area	2.94×10^{-5} m^4
A	Rail cross sectional area	7.77×10^{-3} m^2
G	Shear modulus of the rail	8.1×10^{9} N/m^2
k_r	Timoshenko shear coefficient of the rail	0.34
M_s	Sleeper mass	250 kg
K_p	Railpad stiffness (linear)	140 MN/m
C_p	Railpad damping (linear)	45 kN-s/m
K_b	Ballast stiffness (linear)	40 MN/m
C_b	Ballast damping (linear)	50 kN-s/m
L	Length of the rail beam	60 m

Figure 3.6 shows the first 10 natural frequencies of the railway track numerically, 161.54 Hz, 165.68 Hz, 175.86 Hz, 179.84 Hz, 187.80 Hz, 193.53 Hz, 201.49 Hz, 206.10 Hz, 213.26 Hz and 218.52 Hz. Cai [9] published natural frequencies of railway track model for 1st and 10th modes as 158.3 Hz and 176.0 Hz, respectively. The track model developed by Cai for natural frequency study was similar to the model presented in this study. The track model was a two-layer three dimensional Timoshenko beam model with linear railpad and ballast properties. However, the parameters used for track model were different from the present model.

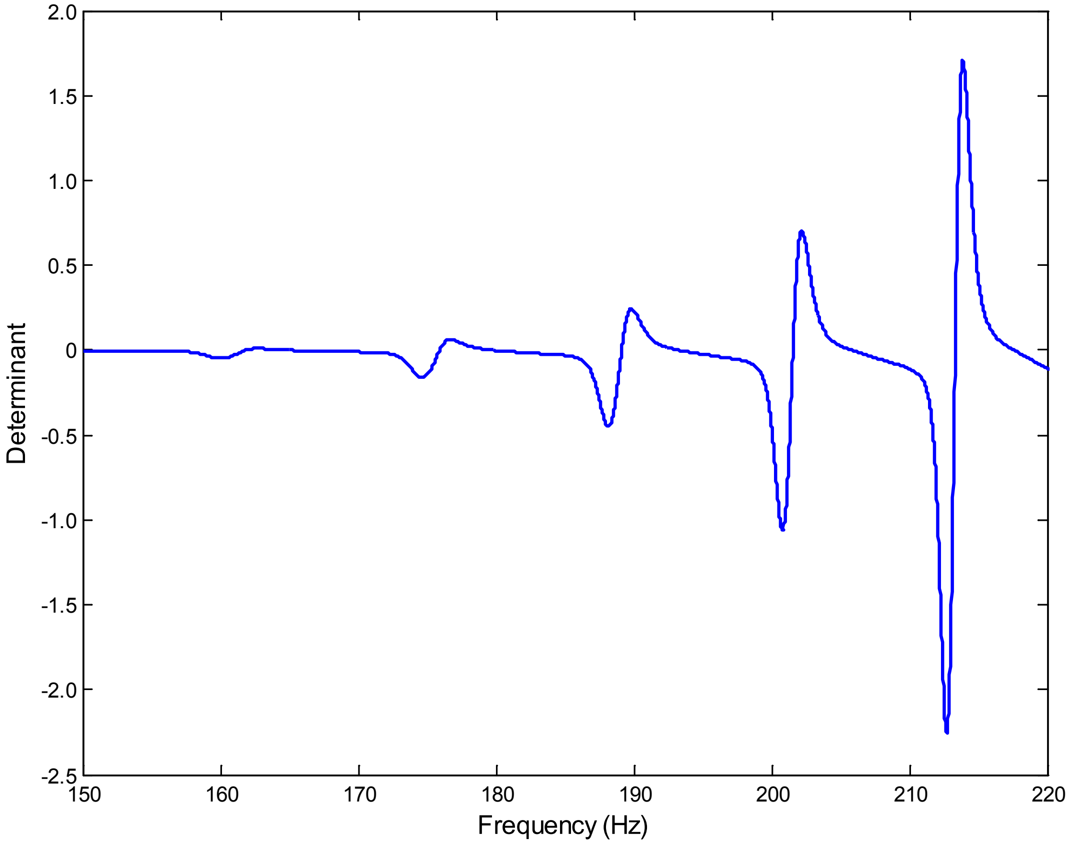

Fig. 3. 6: First 10 natural frequencies of the railway track

3.7 SUMMARY

This chapter presents modeling of a comprehensive three-dimensional railway vehicle-track in presence of wheel flat. The vehicle system model consists of a full car body, two bogies and four wheelsets, whereas the railway track model consists of two parallel Timoshenko beams periodically supported by lumped masses representing the sleepers. The equations of motion for the lumped mass vehicle model and Timoshenko beam theory based continuous track model have been formulated. Both the linear and nonlinear properties of the railpads and ballasts are considered in the model in terms of nonlinear stiffness and damping elements.

In order to ensure the interactions between the railpads, a shear parameter beneath the rail beams has also been considered into the model. A nonlinear Hertzian contact model is considered for deriving the dynamic wheel-rail contact force. Wheel flats have been modeled for both single and multiple flats. The solution method for the three dimensional vehicle and track system has been presented. The PDEs representing the motion of the continuous rail beam is converted to a set of ODEs by using generalized coordinate method.

The natural frequencies of the individual components of the railway vehicle and entire track system have been obtained through eigenvalue analysis. In order to identify the natural frequencies of the track, the three-dimensional railway track model has been simplified to a generalized track element with equivalent stiffness representing the railpad and ballast stiffness and sleeper mass. The nonlinear Hertzian contact stiffness has been converted in linear contact stiffness in order to facilitate the eigenvalue analysis of the vehicle. Linear parameters of the railpad and ballast stiffness have also been considered for eigenvalue analysis of the track model. Damping properties of the railpads and ballasts are ignored in eigenvalue analysis of the track model. The study shows that natural frequencies of the car body are far less than the natural frequencies of the wheelsets, which in turn shows that the influence of primary suspension is negligible due to relatively large wheelset stiffness. The fundamental natural frequency of the track is found as 161.54 Hz, which is slightly higher than the reported study with different parameters.

CHAPTER 4

MODEL VALIDATION AND DYNAMIC RESPONSE OF VEHICLE-TRACK SYSTEM DUE TO WHEEL FLAT

4.1 INTRODUCTION

The primary objective in developing the three-dimensional railway vehicle-track model is to examine the wheel-rail impact force and acceleration response of the wheel in the presence of single and multiple wheel defects such as wheel flats. In order to examine the effect of relative position of the wheel flats within the wheelsets or bogie on pitch and roll motion of the vehicle necessitates a three-dimensional coupled railway vehicle-track model. Furthermore, in order to find out the effect of presence of nonlinearity in the track model requires a nonlinear railpad and ballast model. However, such a complex railway vehicle-track model together with the nonlinear wheel-rail contact model must be first examined using the test data and analytical results that deal with impact response due to wheel flats available in literature. Due to the lack of available data for wide range of operating conditions and vehicle-track system design parameters in addition to wheel defects, only a limited validation is possible for a study of this scope. Thus, the present model parameters are assembled from different sources in order to represent the vehicle-track system presented for the purpose of examining the model validity.

This chapter is devoted to the validation of the developed vehicle-track model where simulations are carried out in order to examine quantitative and qualitative responses of the wheel-rail impact responses. The wheel-rail contact model together with the coupled vehicle-track model developed in chapter 3 is applied to obtain the vehicle-track interaction responses in terms of impact forces and accelerations. Since the wheel-rail contact, the railpad and ballast properties are nonlinear the proposed model is validated in time domain. The validated model is utilized to investigate the responses in terms of impact forces or accelerations in the presence of either single or multiple wheel flats. The purpose of this chapter is to carry out a thorough investigation of wheel-rail impact load and acceleration responses in the presence of a single wheel flat. The analyses are performed with different position of the wheel flats such as in front or rear wheelsets within a front or rear bogie. The response characteristics are also obtained with different flat sizes and vehicle speeds.

4.2 VALIDATION OF THE DEVELOPED MODEL

In an attempt to validate the present model in the presence of a wheel flat, the equations of motion of vehicle and track system described in Eqns. (3.1) to (3.46) are combined with wheel-rail interface and wheel defect models presented in Eqns. (3.49) and (3.50), respectively. The developed model has been validated using the experimental data reported by Newton and Clark [4], and the analytical data presented by Sun and Dhanasekar [17]. The study reported by Sun and Dhanasekar [17] has presented and compared both the analytical and experimental data. In this reported study, a 10-DOF pitch-plane model of the full car was considered with a four-layer track model. The rail was modeled as a Timoshenko beam. The parameters employed in the simulation are obtained from reported studies [4, 17] and listed in Table 4.1. The nonlinear parameters of the railway track model such as railpad and ballast stiffness and damping are obtained from Eqns. (3.40), (3.41) and Eqns. (3.43) , (3.44), respectively. The listed parameters resulted in the total track length of 59.4 m and a total of 617 coupled ordinary differential equations for the vehicle and track system model. A MATLAB predefined function “ode 45” has been applied to solve the coupled partial and ordinary differential equations.

Table 4. 1: Parameters used for model validation [4, 17]

Notation	Parameter	Value
M_c	Car body mass	58400 kg
M_b	Bogie mass	3600 kg
M_w	Wheelset mass	1900 kg
J_{cx}	Mass moment of inertia of the car body about X axis	95576 kg-m^2
J_{cy}	Mass moment of inertia of the car body about Y axis	726462 kg-m^2
J_{bx}	Mass moment of inertia of the bogie about X axis	1600 kg-m^2
J_{by}	Mass moment of inertia of the bogie about Y axis	1801 kg-m^2
J_{wx}	Mass moment of inertia of the wheelset about X axis	420.1 kg-m^2
K_P	Primary suspension stiffness	7.88×10^5 kN/m
C_P	Primary suspension damping	3.5 kN-s/m
K_S	Secondary suspension stiffness	5.32×10^3 kN/m
C_S	Secondary suspension damping	70 kN-s/m
l_c	Semi-longitudinal distance between bogies	5.18 m
l_b	Semi-longitudinal distance between wheelsets in bogie	1.25 m
l_s	Semi-lateral distance between secondary suspensions	0.80 m
l_p	Semi-lateral distance between primary suspensions	0.80 m
R	Wheel radius	0.475 m
L_f	Flat length	150 mm
D_f	Flat depth	2.15 mm
C_H	Hertz spring constant	87×10^9 N/m$^{3/2}$
m_r	Rail mass per unit length	60.64 kg/m
E	Elastic modulus of the rail	207×10^9 N/m^2
I	Rail second moment of area	2.94×10^{-5} m^4
A	Rail cross sectional area	7.77×10^{-3} m^2
G	Shear modulus of the rail	8.1×10^9 N/m^2
k_r	Timoshenko shear coefficient of the rail	0.34
k_1	Shear viscosity coefficient of the foundation	666870 N
M_s	Sleeper mass	270 kg
J_s	Roll moment of inertia of the sleeper	90 kg-m^2
K_p	Railpad stiffness (linear)	140 MN/m
C_p	Railpad damping (linear)	45 kN-s/m
K_b	Ballast stiffness (linear)	40 MN/m
C_b	Ballast damping (linear)	50 kN-s/m
L	Length of the rail beam	60 m
L_S	Semi-lateral distance between left and right side railpads	0.80 m
S_l	Sleeper spacing	0.6 m
N	No. of sleepers	100

The dynamic response of the entire vehicle-track system is evaluated under a constant speed of 117 km/h and static wheel load of 82 kN in the presence of a 150 mm long and 2.15 mm deep flat on the left side wheel of the leading wheelset of the front bogie, as reported by Sun and Dhanasekar [17]. The comparisons between the responses obtained by the developed model with that of the reported study are shown in Fig. 4.1. In order to have in-depth investigation of the developed model, validation has been carried out in four steps, namely (a) with linear railpad and ballast; (b) with linear railpad and nonlinear ballast; (c) with nonlinear railpad and linear ballast; and (d) with nonlinear railpad and ballast. However, the wheel-rail contact is always nonlinear for all the simulations carried out in this study. The variation in the dynamic contact force obtained at the interface of the defective wheel and rail is evaluated when the effect of the end conditions diminishes. The simulations under selected excitations are performed with a time step of 4.615e-5 s, which is significantly smaller than the time required for the selected flat size to overcome the contact with rail in order to obtain accurate prediction of the contact force.

Figure 4.1 shows that the contact force response predicted by the current model with nonlinear railpad and ballast properties agrees reasonably well with the experimental data reported by Newton and Clark [4]. The ratio of the dynamic wheel-rail contact force to the static wheel load can be defined as peak impact force factor. The value of peak impact force factor and period of vibration due to excitation predicted by the current model and experimental data are in very good agreement. The dominant period of oscillation of the contact force is approximately 4.1 ms for both experimental data and current model. The peak contact force factor predicted by the current model with nonlinear railpad and ballast is about 3.9, whereas for linear railpad and ballast it is about 4.5. In the case of nonlinear railpad and linear ballast the peak contact force factor is about 4.12, whereas for linear railpad and nonlinear ballast it is about

4.18. It can be seen from Fig. 4.1 that as the model moves from nonlinear to linear railpad and ballast properties (Figs. 4.1 (a) to 4.1 (d)), the peak impact force factor increases slowly. It can be seen from Fig. 4.1 that the impact force reaches a peak value of about 4.8 after followed by a loss of contact between the wheel and rail. This loss of contact occurs in the time histories of the impact force for about 2.7 ms as the wheel comes in contact with the rail. This loss of contact time period predicted by the current model is almost same as the analytical study reported in [17]. The figure further suggests that for a static load of 82 kN and a vehicle speed of 117 km/h, the peak impact force could increase by 56.86% due to the consideration of the linear properties of the railpad and ballast into the track model for the selected wheel flat parameter. This could be attributed to the lower deflection of the relatively stiffer rail beam in the case of linear railpad.

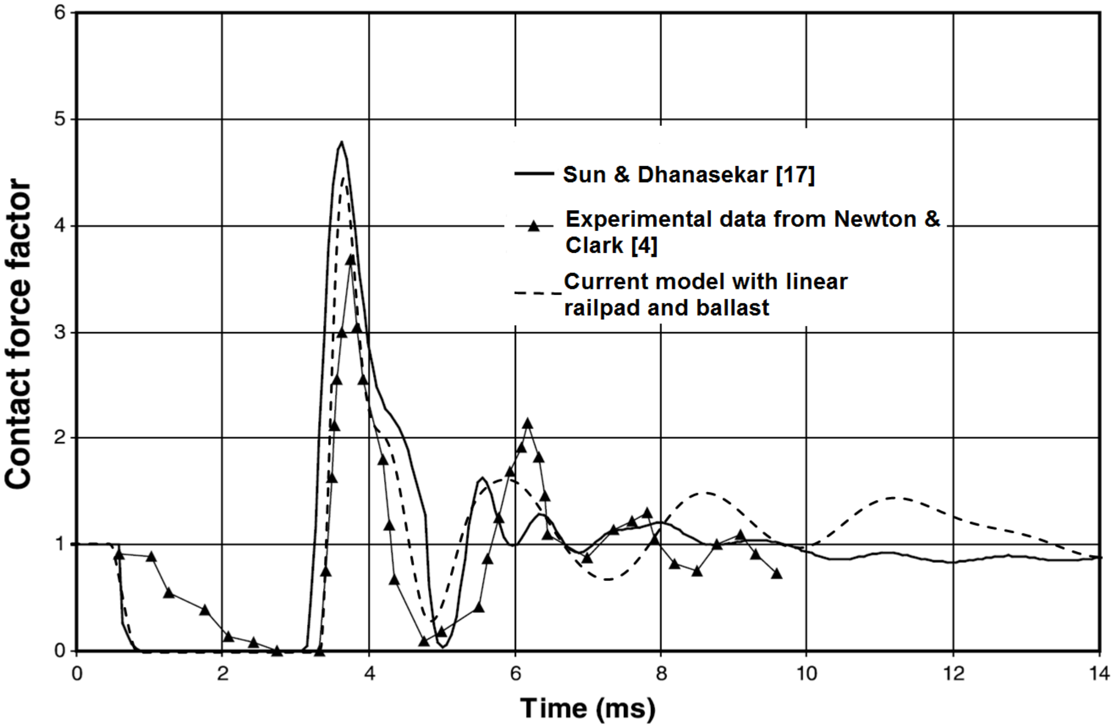

(a)

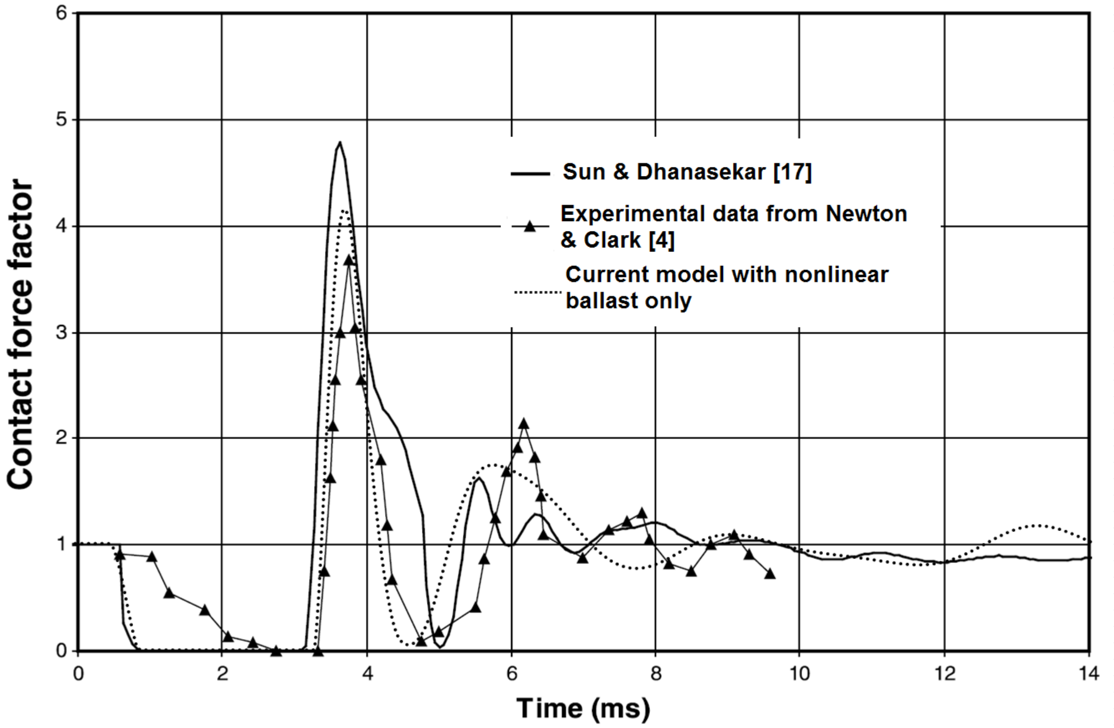

6
5
4
3
2
1
0
0
2
4
6
8
10
12
14
Contact force factor
Time (ms)
Sun & Dhanasekar [17]
Experimental data from Newton & Clark [4]
Current model with nonlinear ballast only

(b)

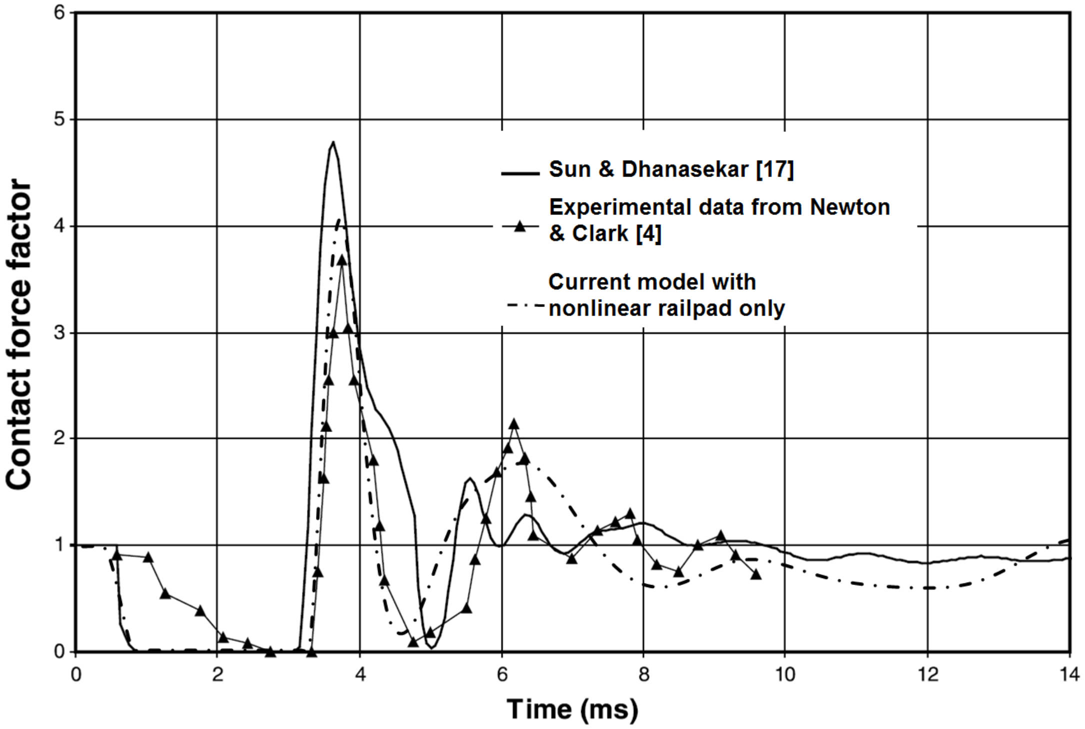

6
5
4
3
2
1
0
0
2
4
6
8
10
12
14
Contact force factor
Time (ms)
Sun & Dhanasekar [17]
Experimental data from Newton & Clark [4]
Current model with nonlinear railpad only

(c)

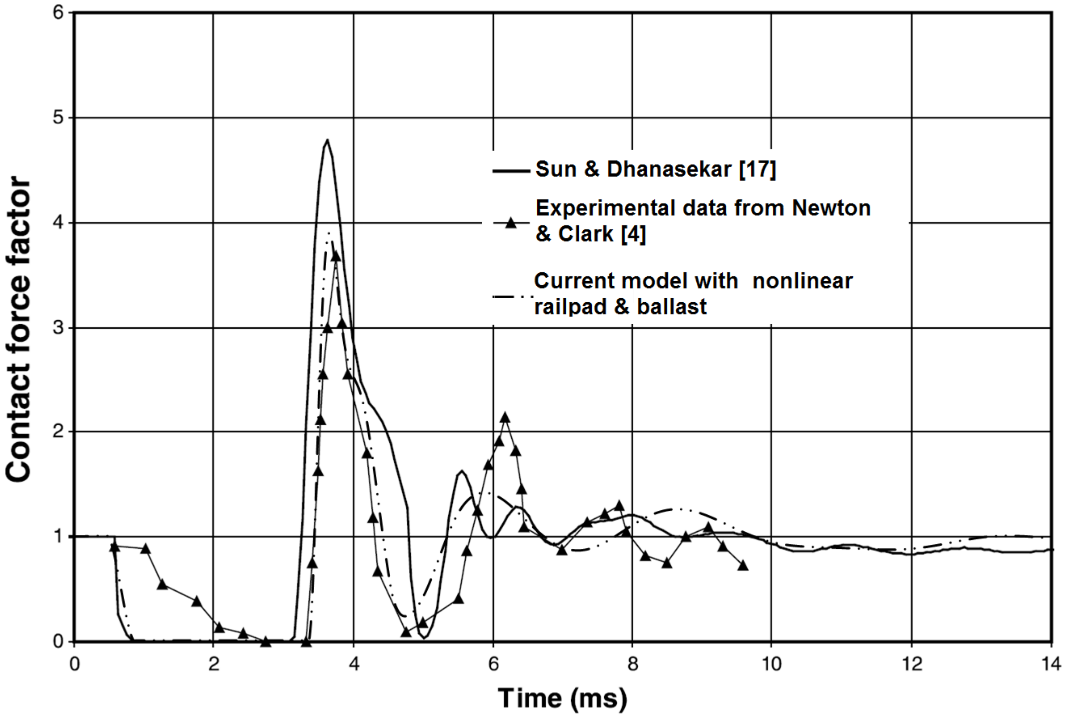

(d)

Fig. 4. 1: Comparison of the wheel-rail impact force factor predicted by the current model with experimental data [4] and analytical study [17]; (a) both railpad and ballast are linear; (b) linear railpad and nonlinear ballast; (c) nonlinear railpad and linear ballast; and (d) both railpad and ballast are nonlinear.

The effect of speed on peak wheel-rail impact force for both linear and nonlinear railpad and ballast stiffness and damping properties are shown in Figs. 4.2 (a) to 4.2 (d). The results are shown for three different sizes of flats ranging from small to relatively large flat. For all these simulations, a single flat is assigned to the left wheel of the front wheelset of the front bogie with same size as considered for validation. It can be seen from Figs. 4.2 (a) to 4.2 (d) that speed has significant influence on peak wheel-rail impact force in the presence of wheel flat for both linear and nonlinear railpad and ballast.

Figures 4.2 (a) to 4.2 (c) further show that the results of peak wheel-rail impact forces have a small peak in low speed range (30-50 km/h) and rise gradually with increase in speed. However, the rate of increase in peak impact load is lower in low speed range (up to 60 km/h) and higher at high speed range. When the speed reaches over 80 km/h, the rate of increase of impact force is very significant, which is due to the separation of the wheel, rail, and tie during the impact process. The figure further shows that linear railpad and ballast model predicts higher wheel-rail impact force than the nonlinear railpad and ballast model for the selected speed range and flat sizes. These differences in peak impact forces are, however, more at high speeds and large size flat and less at low speeds and small size flat. The comparison between the experimental data reported by Johansson and Nielson [2] and the current model with linear and nonlinear railpad and ballast properties is shown in Fig. 4.2 (b). It can be seen that the current model with linear and nonlinear railpad and ballast underestimate the peak wheel-rail impact force at low speed range (up to 60 km/h) and overestimate at high speed range. These discrepancies in the peak impact forces can be attributed to the inclusion of nonlinear single point Hertzian contact spring into the wheel-rail contact model.

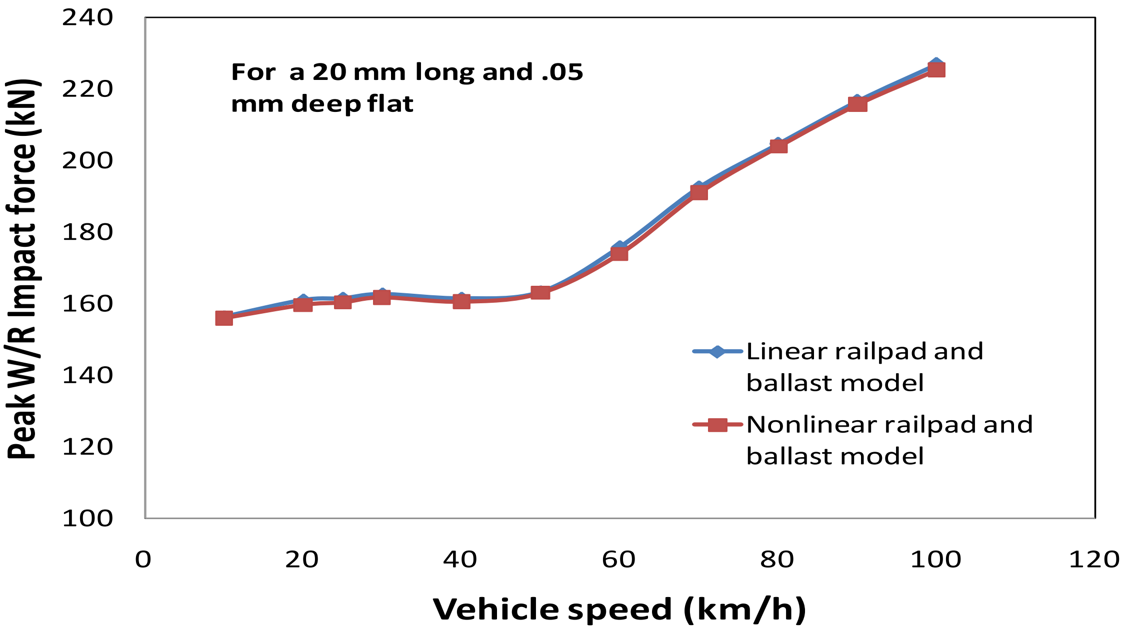

240
220
200
180
160
140
120
100
0
20
40
60
80
100
120
Peak W/R Impact force (kN)
Vehicle speed (km/h)
For a 20 mm long and .05 mm deep flat
Linear railpad and ballast model
Nonlinear railpad and ballast model

(a)

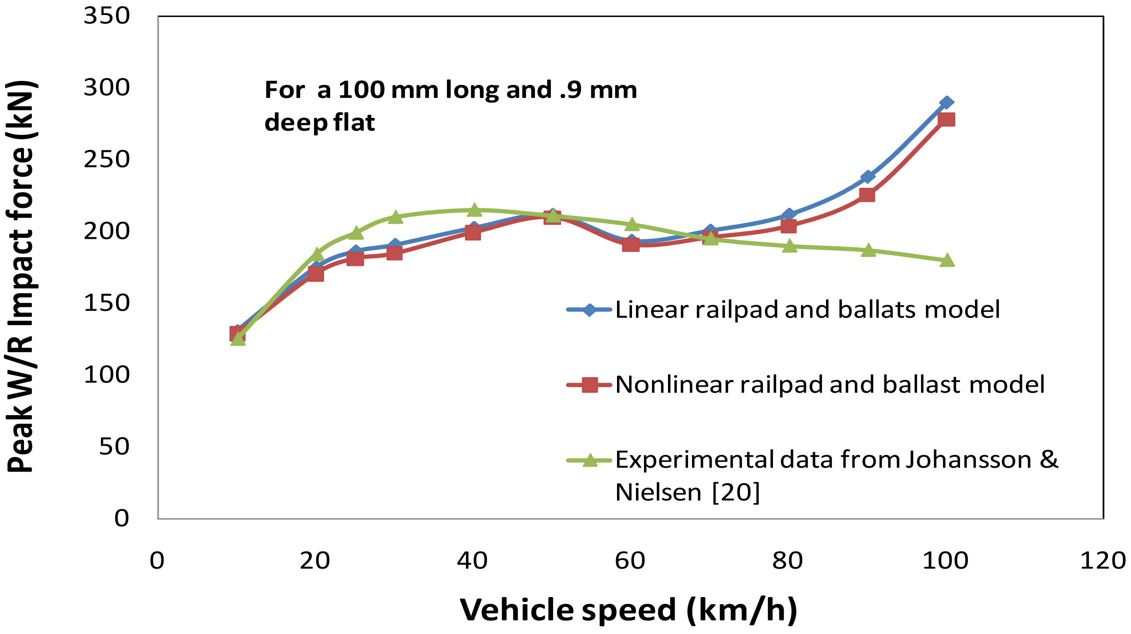

350
300
250
200
150
100
50
0
0
20
40
60
80
100
120
Peak W/R Impact force (kN)
Vehicle speed (km/h)
For a 100 mm long and .9 mm deep flat
Linear railpad and ballats model
Nonlinear railpad and ballast model
Experimental data from Johansson & Nielsen [20]

(b)

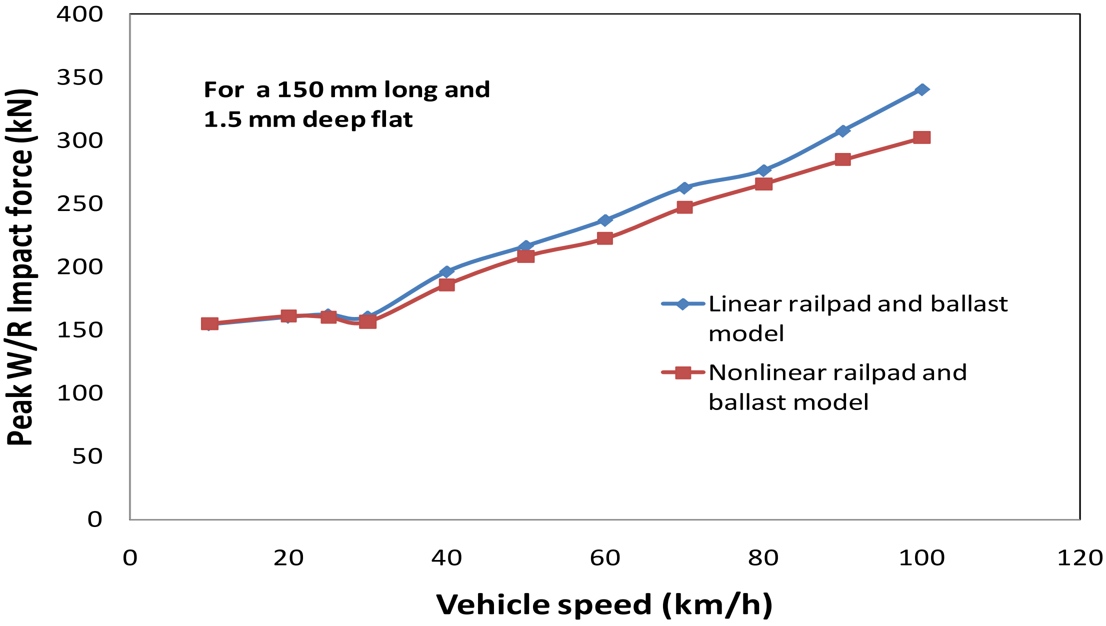

(c)

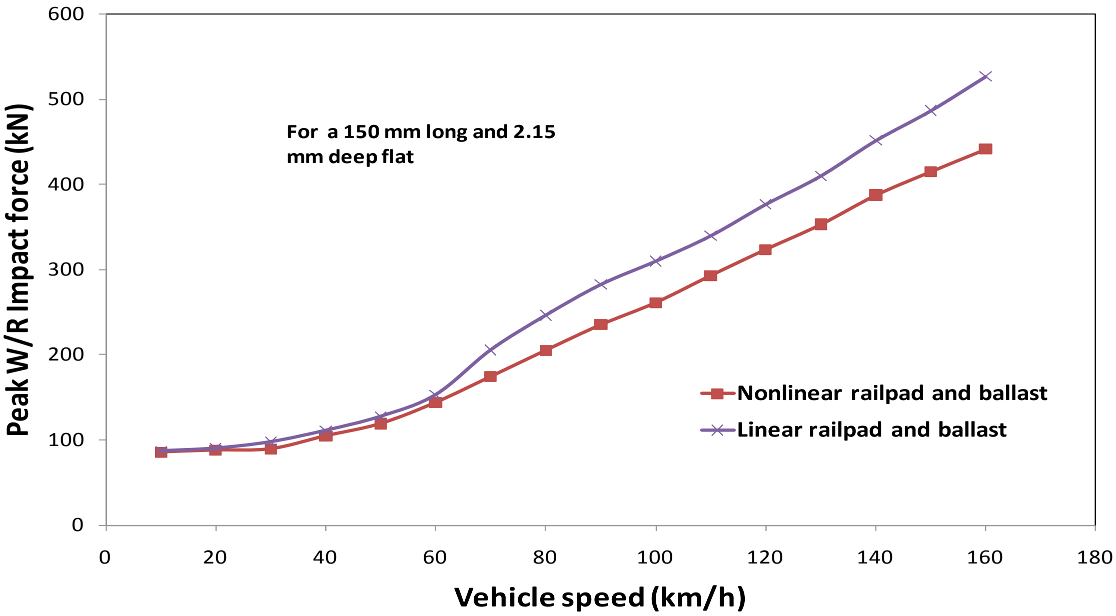

(d)

Fig. 4. 2: Effect of speed on peak wheel-rail impact force with linear and nonlinear railpad and ballast; (a) small flat (D_f=.05 mm, L_f=20 mm); (b) medium flat (D_f=.9 mm, L_f=100 mm); (c) large flat (D_f=1.5 mm, L_f=150 mm); and (d) very large flat (D_f=2.15 mm, L_f=150 mm)

4.3 IMPACT RESPONSE DUE TO A SINGLE WHEEL FLAT

Wheel flat is the most common type of wheel defects encountered by the railway industry. This defect causes significant wheel-rail impact loads, which can be as high as 2-3 times the static wheel load. The peak dynamic impact loads produced by the wheel flats can be further intensified by the flat sizes and speeds of the vehicle. The high magnitude impact loads create high magnitude impact acceleration at both the defective and flat free wheels, which may cause final fracture in vehicle and track components level such as bearings, axles and rails. Although the impact accelerations produced at the flat free surface due to the adjacent wheel flat is small in magnitude, they may contribute to the fatigue damage of the track and increase the maintenance cost.

In this section, studies on impact acceleration response are carried out due to a single wheel flat of 50 mm long and 0.35 mm deep. This size of the wheel flat is within the limit of the wheel removal criteria set by AAR, Transport Canada and UK Rail safety and standard board [1, 139, 145]. The flat is only introduced to the left wheel of the first wheelset of the front bogie, while all other wheels within the front and rear bogies of the car body are assumed to have perfect profiles. The variations in radius of a wheel with a 50 mm long and 0.35 mm deep flat is shown in Fig. 4.3 as a function of wheel angular position. The analytical method presented in chapter 3 is utilized here to generate time domain solutions. The vehicle and track parameters used for simulations are presented in Tables 4.2 and 4.3, respectively. The simulations have been carried out for a constant vehicle speed of 100 km/h and static wheel load of 103 kN.

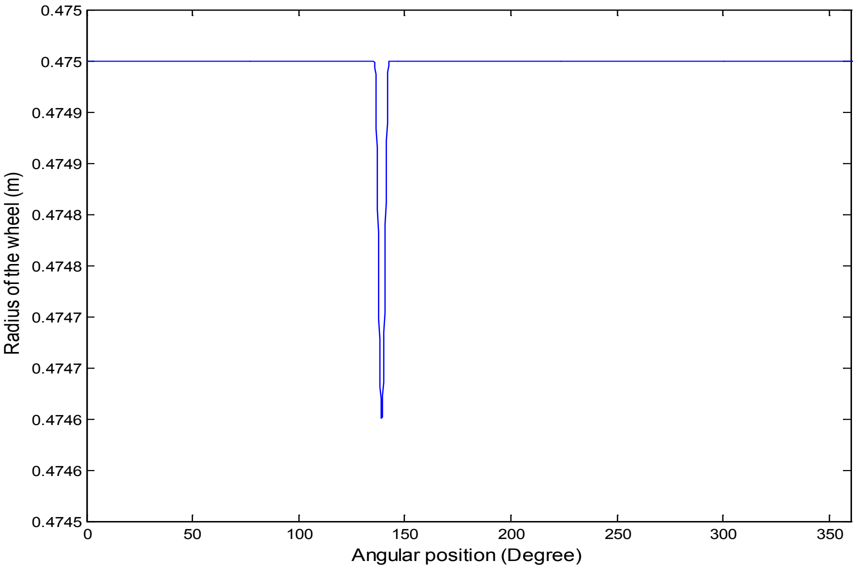

Fig. 4. 3: Variations in radius of a wheel with single flat (L_f = 50 mm and D_f = 0.35 mm) as a function of angular position of the contact.

Figure 4.4 shows the variations in the vertical displacement responses of the left wheel with haversine flat and flat-free right wheel within first wheelset, while the vehicle is moving with a constant velocity of 100 km/h. Figure 4.4 illustrates the displacement responses over two consecutive cycles, while the static load per wheel is 103 kN. It can be seen from Fig. 4.4 (a) that the left wheel with flat moves downwards due to its flat geometry as the flat approaches the contact region. This is followed by a relaxation of the wheel prior to further compressions. The maximum downward displacement of the left wheel with flat is 1.24 mm, while the steady deflection of the wheel is 1.15 mm.

Table 4. 2: Vehicle parameters for analysis of system response [4, 17]

Notation	Parameter	Value
M_c	Car body mass	76150 kg
M_t	Bogie mass	1700 kg
M_w	Wheelset mass	1120 kg
J_{cx}	Mass moment of inertia of the car body about X axis	95576 kg-m^2
J_{cy}	Mass moment of inertia of the car body about Y axis	726462 kg-m^2
J_{bx}	Mass moment of inertia of the bogie about X axis	1600 kg-m^2
J_{by}	Mass moment of inertia of the bogie about Y axis	760 kg-m^2
J_{wx}	Mass moment of inertia of the wheelset about X axis	420.1 kg-m^2
K_P	Primary suspension stiffness	7.88×10^5 kN/m
C_P	Primary suspension damping	3.5 kN-s/m
K_S	Secondary suspension stiffness	5.32×10^3 kN/m
C_S	Secondary suspension damping	70 kN-s/m
l_c	Semi-longitudinal distance between bogies	5.18 m
l_b	Semi-longitudinal distance between wheelsets in bogie	1.25 m
l_s	Semi-lateral distance between secondary suspensions	0.80 m
l_p	Semi-lateral distance between primary suspensions	0.80 m
R	Wheel radius	0.475 m
C_H	Nonlinear Hertzian spring constant	87×10^9 N/m$^{3/2}$
L_f	Flat length	50 mm
D_f	Flat depth	0.35 mm

Table 4. 3: Track parameters for analysis of system response [4, 17, 105]

Notation	Parameter	Value
m_r	Rail mass per unit length	60.64 kg/m
E	Elastic modulus of the rail	207×10^9 N/m^2
I	Rail second moment of area	2.94×10^{-5} m^4
A	Rail cross sectional area	7.77×10^{-3} m^2
G	Shear modulus of the rail	8.1×10^9 N/m^2
k_r	Timoshenko shear coefficient of the rail	0.34
k_1	Shear viscosity coefficient of the foundation	666870 N
M_s	Sleeper mass	250 kg
K_p	Railpad stiffness (nonlinear)	$*\,k_0 e^{bZ_P}$ MN/m
C_p	Railpad damping (nonlinear)	$*\,\eta_1\sqrt{m_1 K_P}$ kN-s/m
K_b	Ballast stiffness (nonlinear)	$*\,22.75 + 2.6\times10^8 Z_b^2$ MN/m
C_b	Ballast damping (nonlinear)	$*\,\eta_2\sqrt{m_2 K_b}$ kN-s/m
L	Length of the rail beam	60 m
S_l	Sleeper spacing	0.6 m
N	No. of sleepers	100

* Z_P and Z_b are the compression of the pad and ballast, respectively (in meter), η_1=.25 and η_2=1, $m_1 = \dfrac{M_s M_r}{M_s + M_r}$ and $m_2 = M_s + M_r$, k_0=115.2 MN/m and b=7.49/mm. [105]

The impact caused by the left wheel flat also yields deflections of flat free right wheel, as shown in Fig. 4.4 (b), although the peak displacement is relatively small. This is attributed to the cross wheel impact force generated at the left wheel-rail contact point. Figure 4.4 (b) further shows that as the left wheel flat comes into the contact point, the right wheel moves upward at the same time. Both Figs. 4.4 (a) and 4.4 (b) show that the variations in wheel displacement tend to recover its static value in 15.5 ms, while the displacement responses exhibit oscillations near 45.6 Hz, which has been referred to as coupled vehicle-track system resonance [8, 17, 97].

The variations in the vertical velocity responses of the left wheel with flat and rear wheel without flat within the first wheelset are shown in Fig. 4.5 for a constant vehicle speed of 100 km/h. Figure 4.5 (a) shows the velocity response for defective left wheel whereas Fig. 4.5 (b) shows the velocity response for the flat-free right wheel. It can be seen from Fig. 4.5 that as the wheel flat comes in contact with the rail, the velocity response of the left wheel goes downward first before it reaches its maximum peak value, while the velocity of the flat free right wheel goes upward at the same instant. For the given flat size and vehicle speed, the maximum peak vertical velocity for the left wheel with flat is 0.128 m/s, whereas for flat-free right wheel it is 0.046 m/s. Figures 4.5 (a) and 4.5 (b) further illustrate that the oscillations of the vertical velocity response due to the excitation by the wheel flat comes into steady value (almost zero) after approximately 28.3 ms for both the defective left wheel and flat-free right wheels.

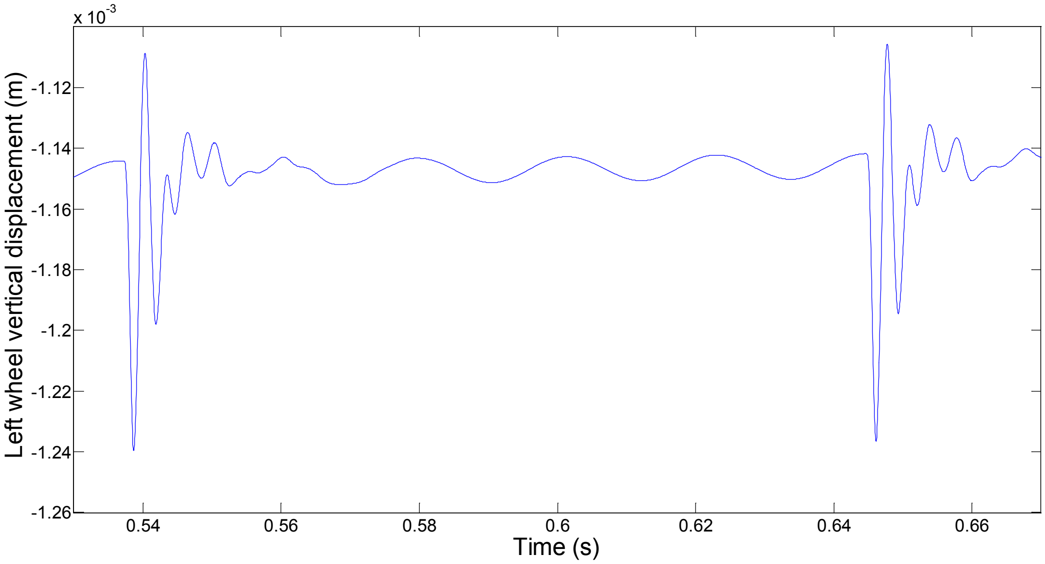

(a)

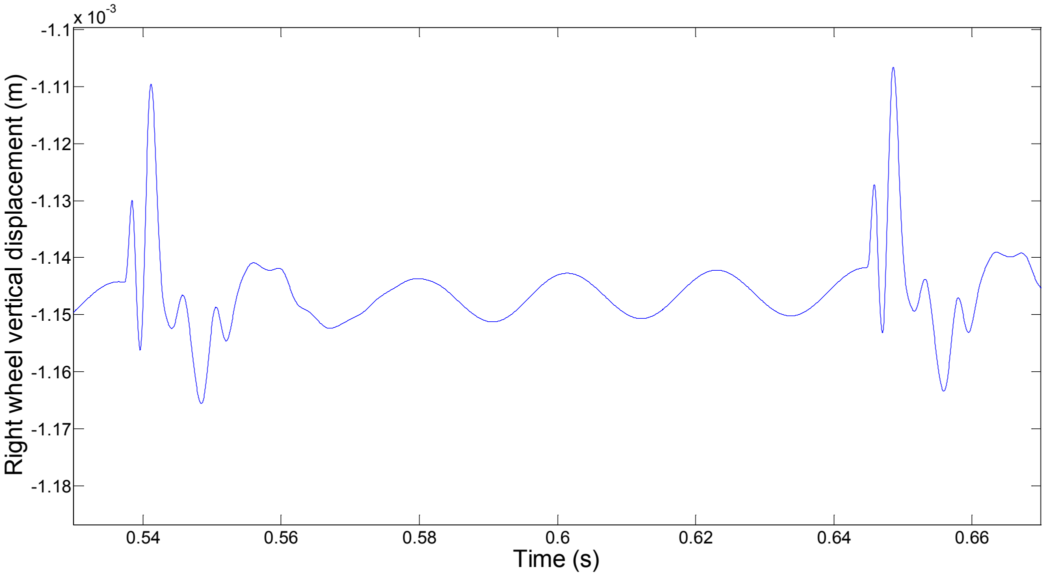

(b)

Fig. 4. 4: Time histories of vertical displacement responses of the wheels in first wheelset (v = 100 km/h; $L_f = 50$ mm; $D_f = 0.35$ mm): (a) left wheel with flat; (b) right wheel without flat

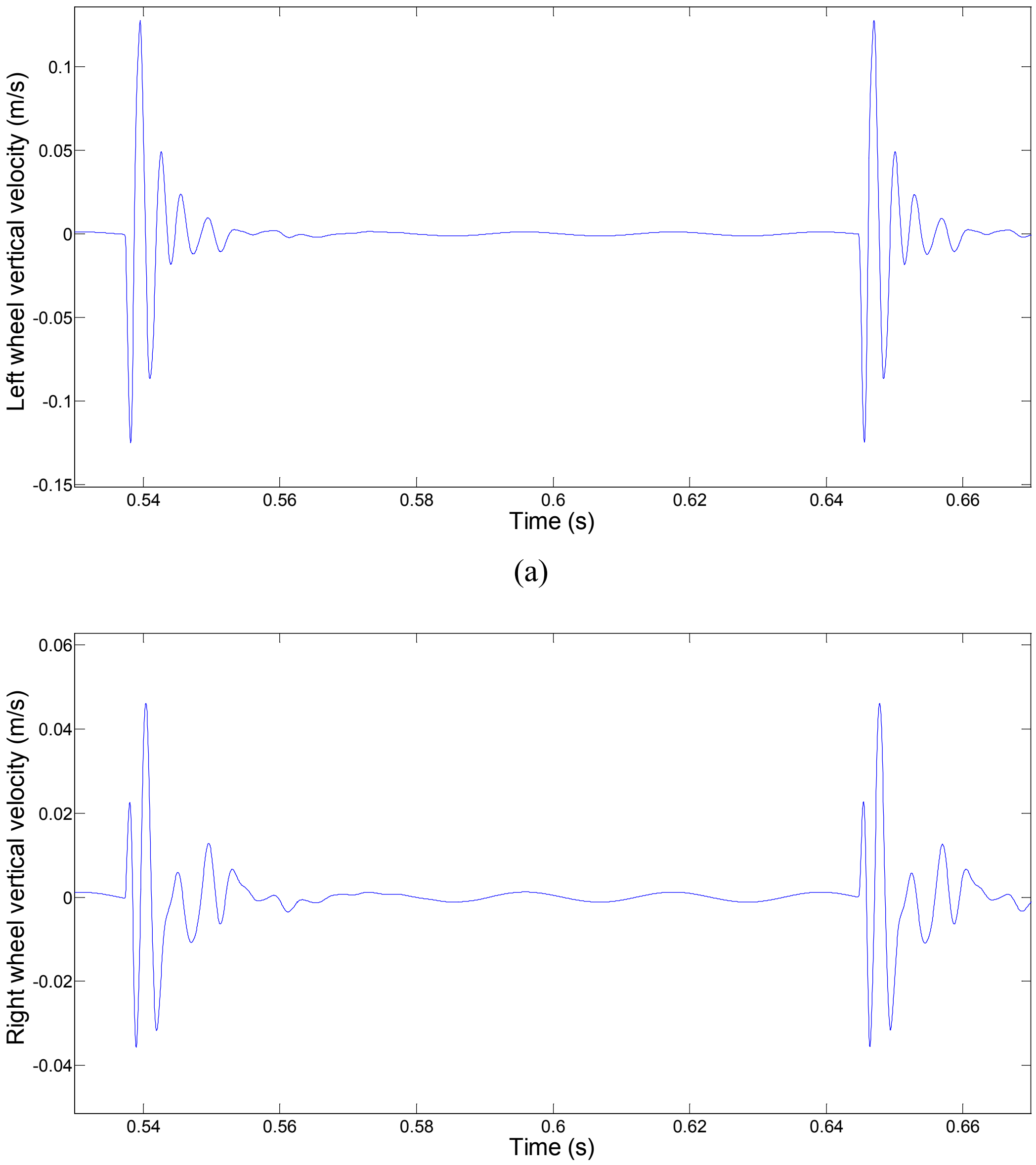

(a)

(b)

Fig. 4. 5: Time histories of vertical velocity responses of the wheels in first wheelset (v = 100 km/h; L_f = 50 mm; D_f = 0.35 mm): (a) left wheel with flat; (b) right wheel without flat

The time histories of the vertical acceleration response for the both left wheel with flat and flat- free right wheel within the first wheelset are shown in Fig. 4.6 for a constant vehicle speed of 100 km/h. Figure 4.6 illustrates the acceleration responses over two consecutive cycles, while the static load per wheel is 103 kN. It can be seen from Fig. 4.6 that the nature of oscillations is similar to those obtained for displacement and velocity responses for both the defective left wheel and flat-free right wheel. Figure 4.6 shows that as the vertical acceleration response at the left wheel due to the flat goes down, the right wheel vertical acceleration response goes up at the same instant. For the given parameters as listed in Tables 4.2 and 4.3, the maximum vertical acceleration of the left wheel with flat is 33.32 g, whereas for the flat-free right wheel it is 10.24 g. It can also be seen from Fig. 4.6 that the excitation frequency due to the wheel flat of the given size is approximately 588.2 Hz. Figure 4.6 further illustrates that the oscillations of the vertical acceleration response due to the excitation by the wheel flat comes into steady value after approximately16.9 ms for both the defective left wheel and flat-free right wheels.

The time histories of the roll displacement, velocity and acceleration responses of the first wheelset with left wheel flat are shown in Figs. 4.7, 4.8 and 4.9, respectively. These figures show that presence of flat, either in right or left wheel, has significant effect on roll displacement, velocity and acceleration response of a wheelset. Figure 4.9 shows that for the given parameters and flat size, the maximum roll acceleration of the wheelset with a medium size flat can be as high as 250 rad/s^2.

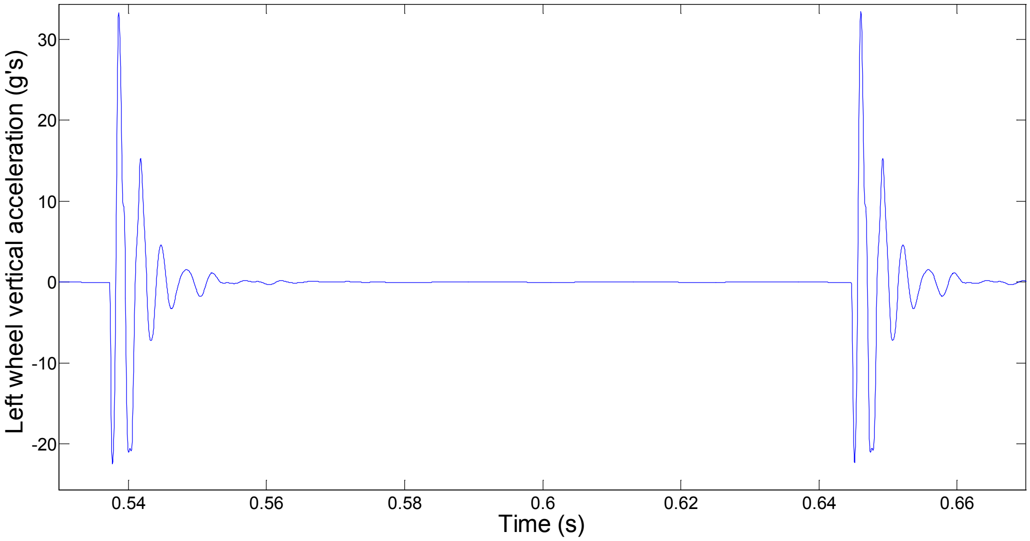

(a)

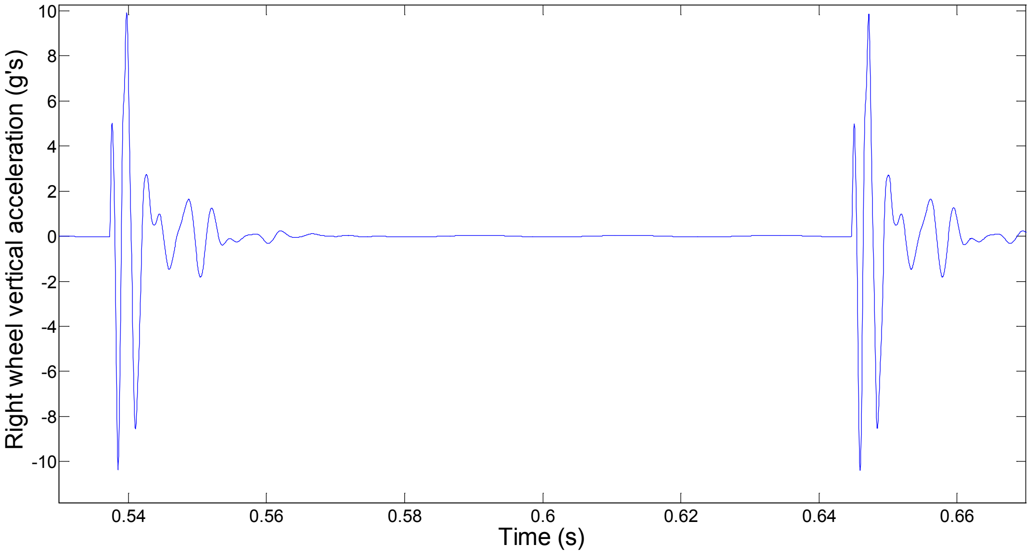

(b)

Fig. 4. 6**:** Time histories of vertical acceleration responses of the wheels in first wheelset (v = 100 km/h; L_f = 50 mm; D_f = 0.35 mm): (a) left wheel with flat; (b) right wheel without flat

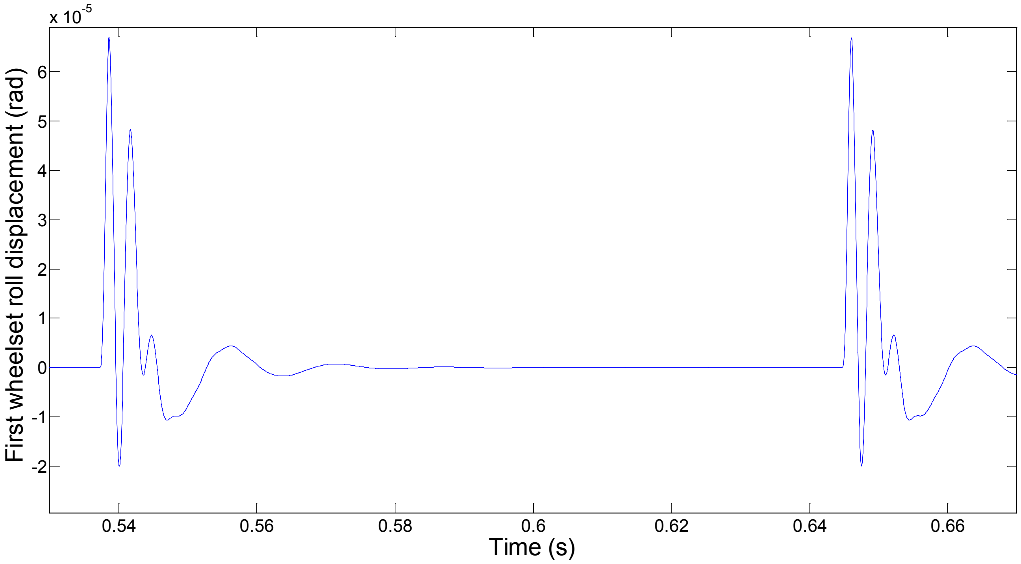

Fig. 4. 7**:** Time histories of first wheelset with one wheel flat roll displacement response (v = 100 km/h; $L_f = 50$ mm; $D_f = 0.35$ mm).

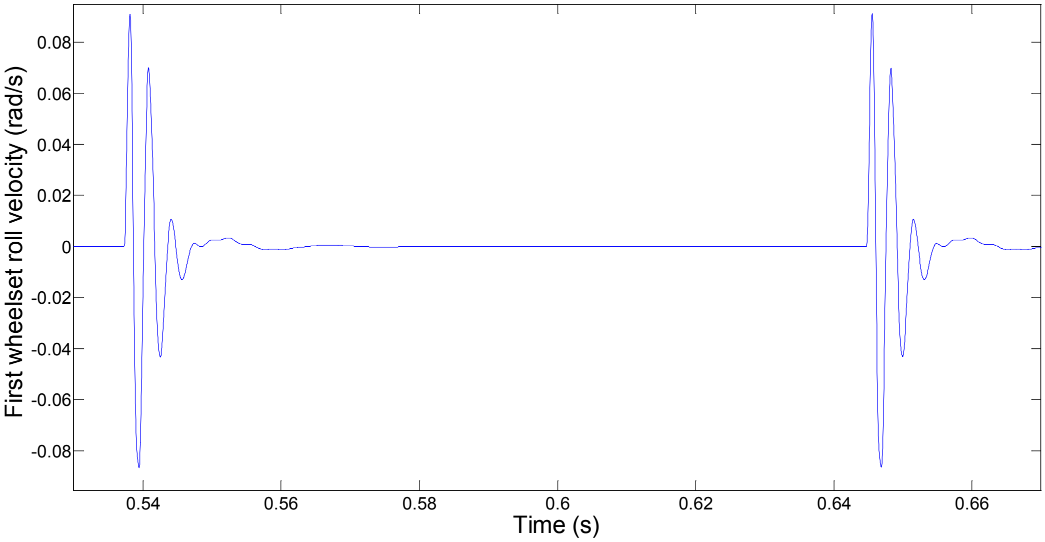

Fig. 4. 8**:** Time histories of first wheelset with one wheel flat roll velocity response (v = 100 km/h; L_f = 50 mm; D_f = 0.35 mm).

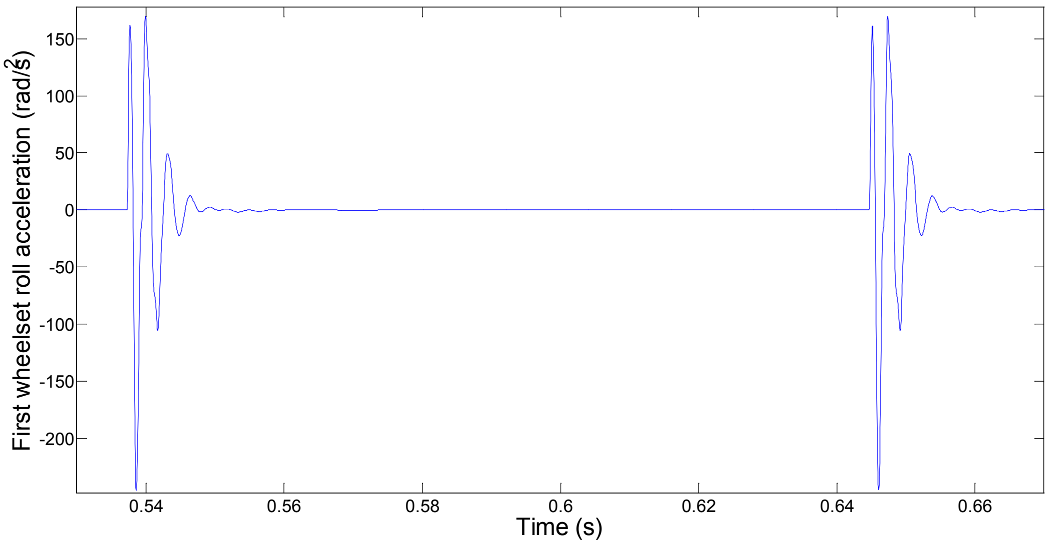

Fig. 4. 9: Time histories of first wheelset with one wheel flat roll acceleration response (v = 100 km/h; L_f = 50 mm; D_f = 0.35 mm).

Figure 4.10 illustrates the variations in displacement responses of all the four wheelsets of the vehicle, while the left wheel of the first wheelset has flat only. The displacement responses are evaluated under constant static load of 103 kN, while the speed of the vehicle is 100 km/h. Figure 4.10 clearly shows the difference in peak displacement responses due to the presence of wheel flat. The maximum displacement of the first wheelset with a left wheel flat is 1.18 mm, whereas the peak displacement of the second wheelset without any flat is in the order of 1.17 mm. The static displacements of all the wheelsets are in the order of 1.14 mm. The results clearly show a considerable phase difference between the peak displacement responses developed at the leading wheelset with a flat and the flat-free trailing wheelset, which is mainly due to the transmission delay of the impact associated with the deflection of the continuous rail. It can be further seen that the presence of flat within the first wheelset does not have any effect on displacement responses of the third and fourth wheelsets of the rear bogie, which is mainly due to the location of the flat being far away.

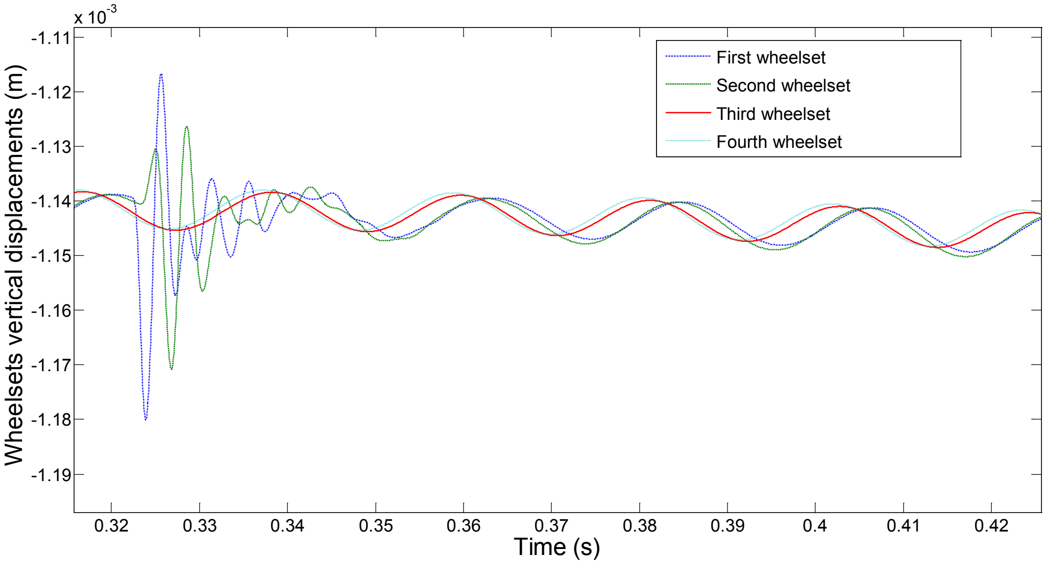

Fig. 4. 10: Time histories of all four wheelsets vertical displacement response with left wheel flat in first wheelset (v = 100 km/h; L_f = 50 mm; D_f = 0.35 mm).

The variations in all four wheelsets roll motions due to a single wheel flat within first wheelset are shown in Fig. 4.11. It can be seen that the peak value of roll motion is higher for first wheelset, which is due to the presence of the flat within first wheelset. It can be also seen that presence of wheel flat within first wheelset has also effect on roll motion of the second wheelset although it does not have any effect on third and fourth wheelsets roll motions. Figure 4.11 further shows that the magnitudes of oscillations due to the impact come to zero after 45.8 ms. The magnitude of the first wheelset peak roll motion is in the order of 6.32×10^{-5} rad, while for second wheelset it is in the order of 3.95×10^{-5} rad. When the wheelset with flat reaches the wheel-rail contact point, the wheel axle starts to oscillate. This explains why the impact load at left wheel-rail contact point is transmitted to the right rail as it will be shown in Fig. 4.15.

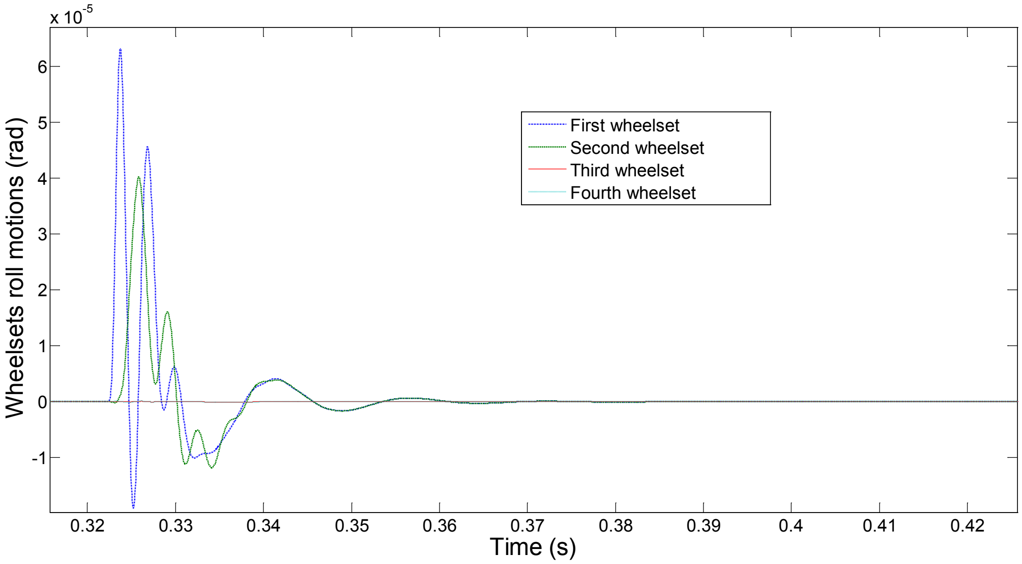

Fig. 4. 11: Time histories of all four wheelsets roll motions with left wheel flat in first wheelset (v = 100 km/h; L_f = 50 mm; D_f = 0.35 mm).

The time histories of the front and rear bogie bounce, pitch and roll motions are shown in Figs. 4.12, 4.13 and 4.14, respectively. It can be seen from all these three figures that the presence of a single wheel flat within first wheelset largely affect the front bogie bounce, pitch and roll motions, which is primarily due to the location of the flat within the front bogie. Since the location of the flat is not within the rear bogie the presence of flat within front wheelset has little or no effect on bounce, pitch and roll motions of the rear bogie, as it can be seen from Figs. 4.12, 4.13 and 4.14. This can be attributed to the low secondary suspension spring stiffness. Figure 4.12 shows that the maximum vertical displacement of the front bogie can reach up to 1.305 mm from a static value of 1.275 mm, for the given flat size and vehicle speed. This figure further shows that the bounce motion of the front bogie is almost stabilized after 25.5 ms, as the wheel with flat leaves the wheel-rail contact point by this time period as shown in Fig. 4.4. For the given parameters, as shown by Figs. 4.13 and 4.14, the maximum pitch and roll motions of the front bogie are 2.61×10^{-5} rad and 3.56×10^{-5} rad, respectively.

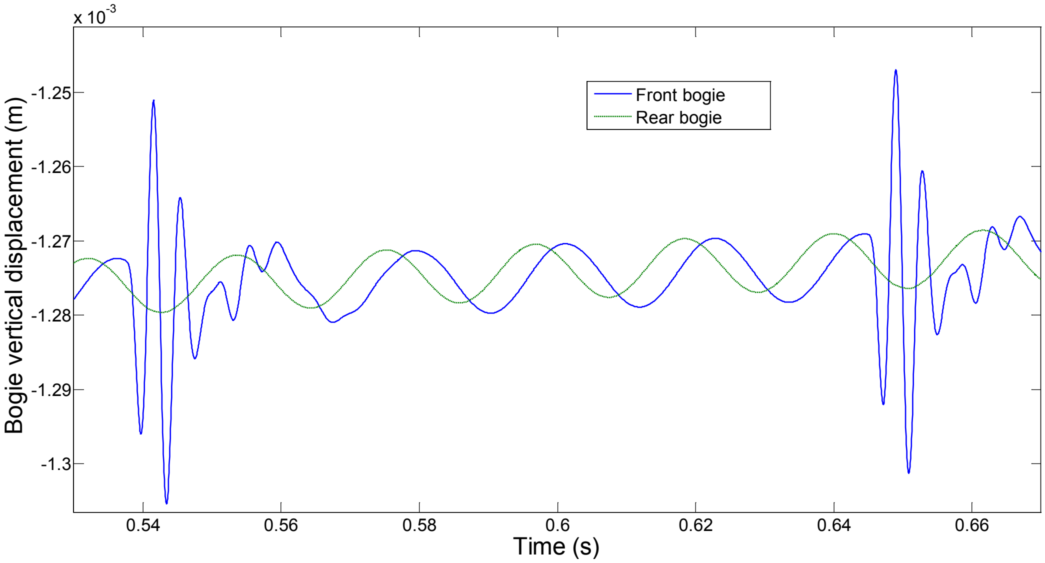

Fig. 4. 12: Time histories of bogie vertical displacement response with left wheel flat in first wheelset (v = 100 km/h; $L_f = 50$ mm; $D_f = 0.35$ mm).

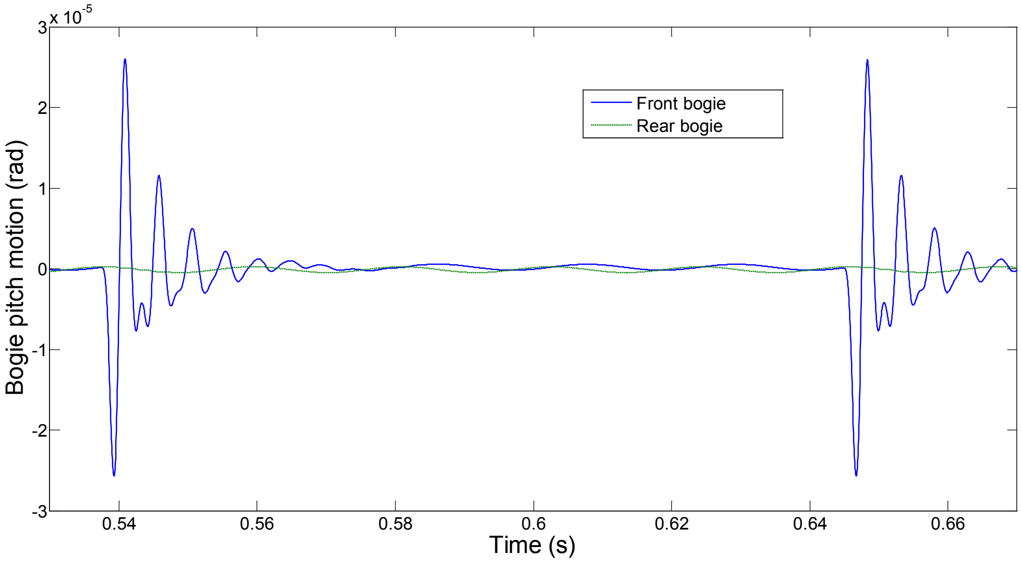

Fig. 4. 13: Time histories of bogie pitch motion with left wheel flat in first wheelset (v = 100 km/h; $L_f = 50$ mm; $D_f = 0.35$ mm).

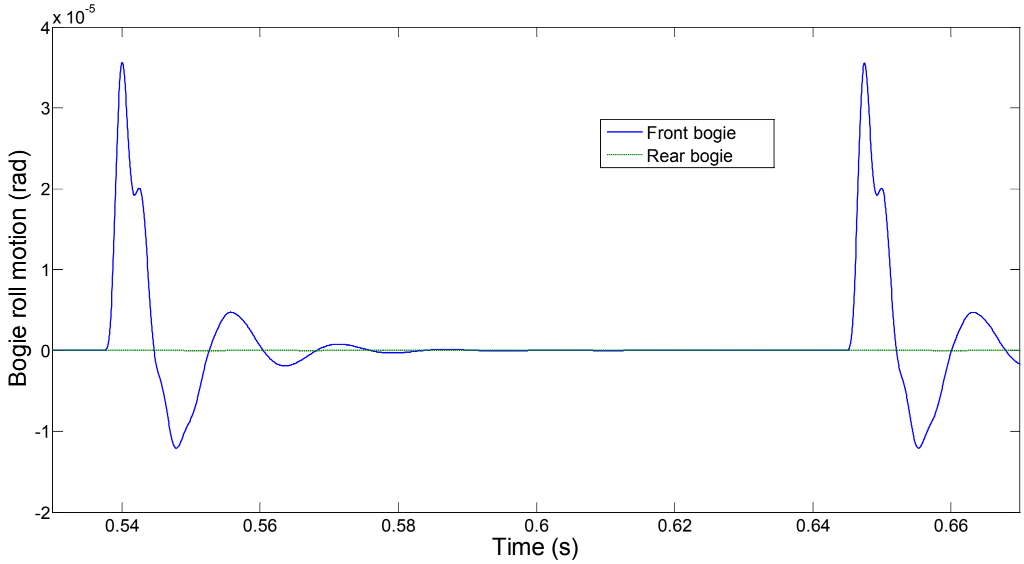

Fig. 4. 14: Time histories of bogie roll motion with left wheel flat in first wheelset (v = 100 km/h; $L_f = 50$ mm; $D_f = 0.35$ mm).

The deflection and acceleration responses of the left and right rail due to a single wheel flat are also evaluated, as shown in Fig. 4.15 for the rail deflection and Fig 4.16 for rail acceleration response. The left and right rail deflection response, as shown in Fig. 4.15, reveals that presence of wheel flat in left wheel-rail contact point affects not only the left rail but also the right rail deflection. However, the magnitude of the maximum amount of deflection is less for right rail. Figure 4.15 further shows that as the flat approaches the contact region, the rail moves up prior to the impact at the contact point followed by the downward deformation of the rail due to the impact force developed at the wheel-rail interface, as seen in Fig. 4.4 (a). Subsequently, the rail profile tends to recover its steady value after approximately 25 ms of the impact. The acceleration response of the left rail with a single wheel flat shows that the impact acceleration can be as high as 219 g, as it can be seen in Fig. 4.16, for the given parameters as listed in Tables 4.2 and 4.3. The figure further shows that the acceleration response comes to steady value after 9.5 ms of the impact for both left and right rails.

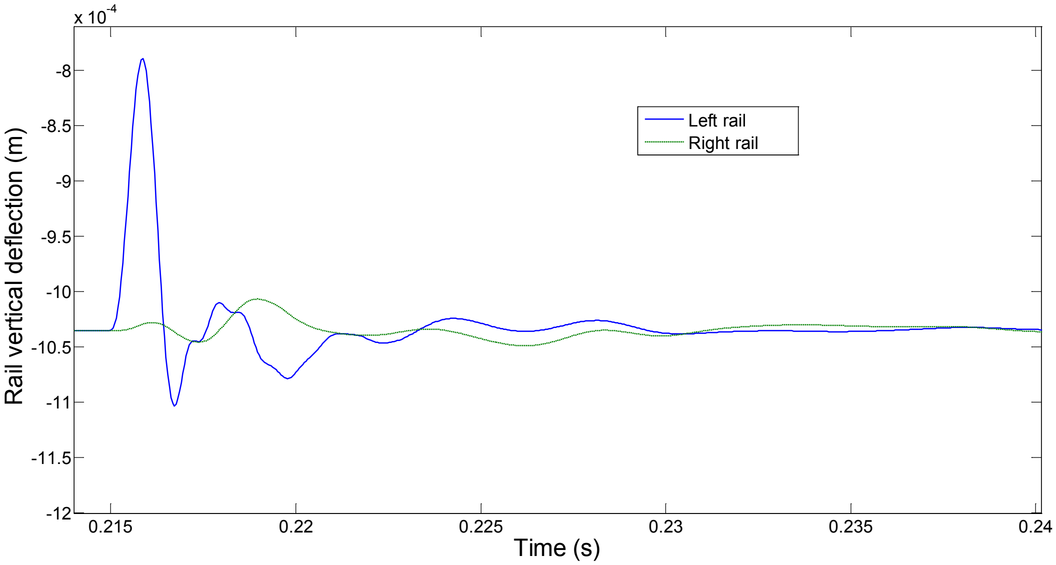

Fig. 4. 15: Time histories of rail vertical deflection with left wheel flat in first wheelset (v = 100 km/h; L_f = 50 mm; D_f = 0.35 mm).

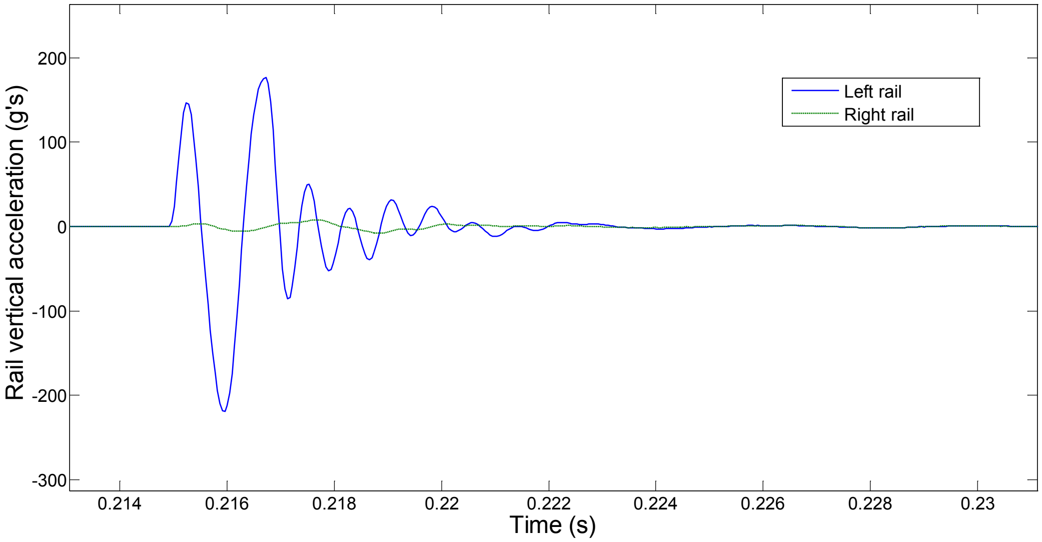

Fig. 4. 16: Time histories of rail vertical acceleration with left wheel flat in first wheelset (v = 100 km/h; L_f = 50 mm; D_f = 0.35 mm).

The effects of wheel flat on peak wheel acceleration due to different vehicle speeds in the range of 20-140 km/h are further investigated and the results obtained are shown in Fig. 4.17. The results are presented for both left wheel with flat and flat-free right wheel accelerations under the influence of five different sizes of wheel flats, while the static wheel load of 103 kN is considered. Here, the depth of the flat is varied during the simulation and the length of the flat is automatically changed following the relation between the length and the depth of the flat as stated by Eqn. 3.51 in chapter 3. The figure illustrates that peak wheel acceleration increases with increasing the speed of the vehicle for both defective and flat-free wheels. The rate of increment, however, is considerably larger in the defective left wheel acceleration responses.

The left wheel acceleration response shows that the impact response exhibits higher magnitude in the medium speed range (70-90 km/h) for low flat sizes (D_f=0.2-.04 mm), and tends to increase rapidly at speeds above 100 km/h. However, this higher magnitudes in the peak acceleration response of the left wheel is not profound for higher flat sizes, which can be attributed to the matching in excitation frequency due to the wheel flat (approximately 330 Hz) with the natural bounce frequency of the first wheelset (312 Hz). The right wheel peak acceleration responses due to the presence of left wheel flat within same wheelset also shows the increase in peak acceleration with speeds and flat sizes as well. However, the magnitudes of the right wheel peak impact accelerations are less than that of the left wheel. Furthermore, the cross-wheel impact acceleration developed at the right wheel increases slightly with vehicle speed for low flat sizes, while the effect of left wheel flat becomes evident at speeds above 90 km/h.

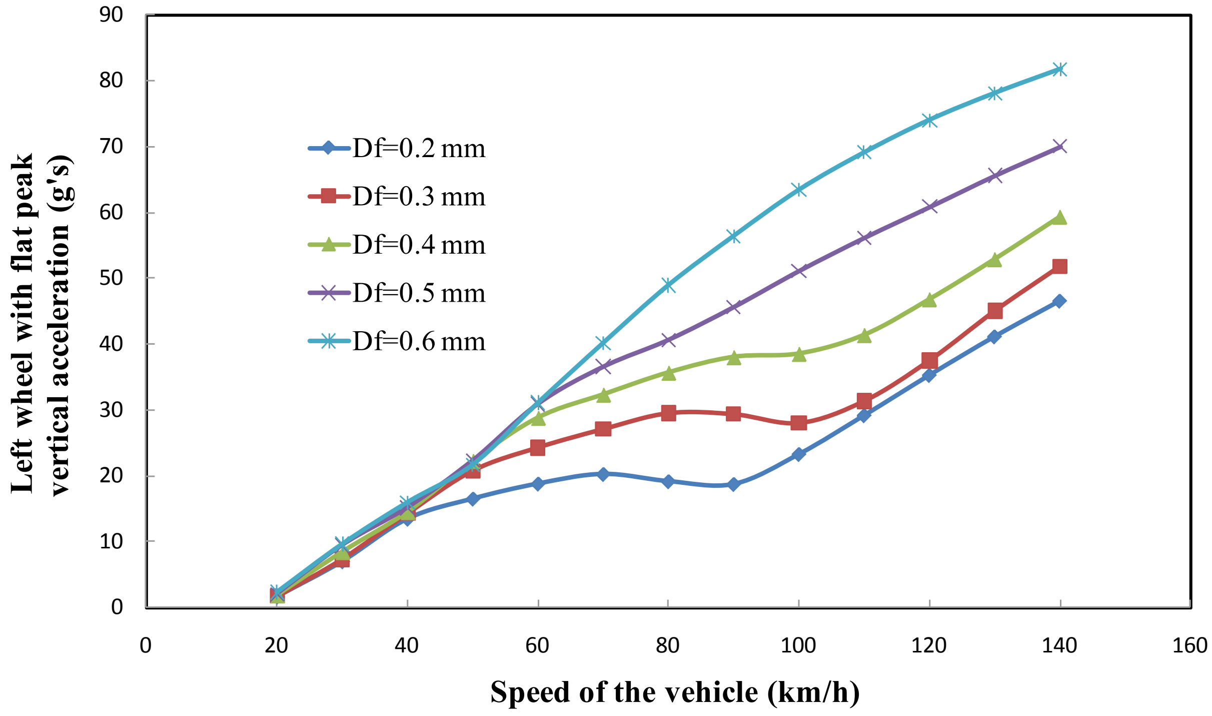

(a)

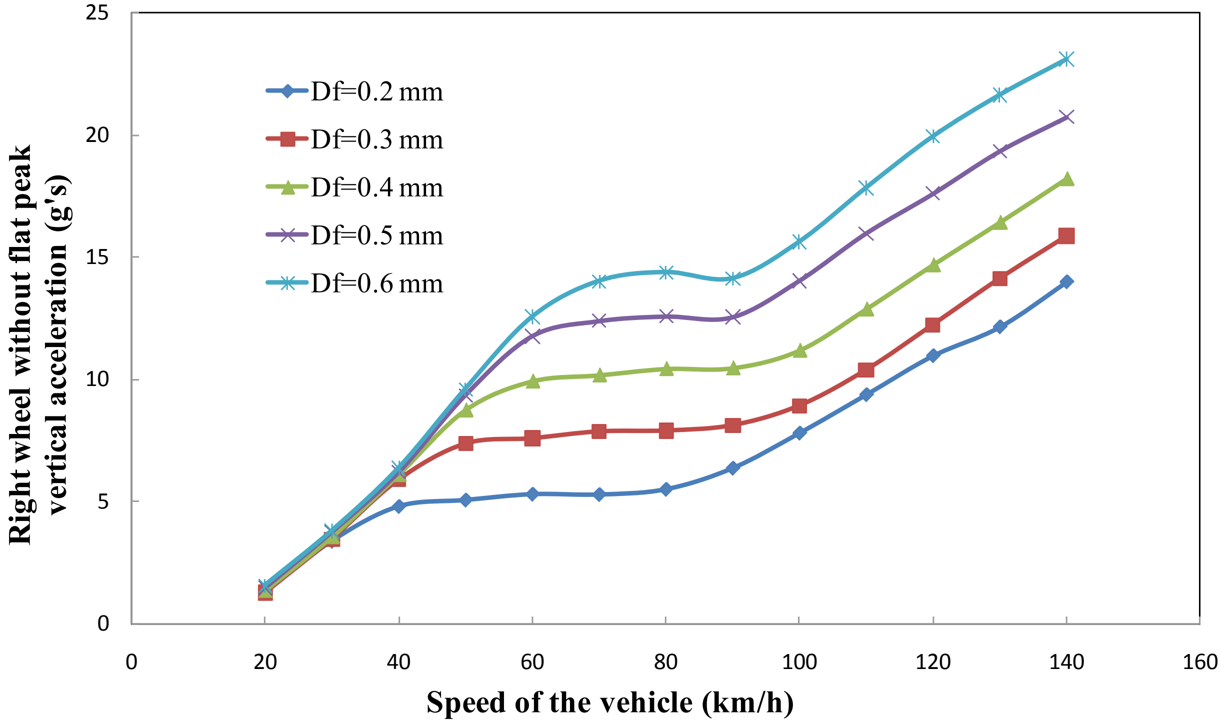

(b)

Fig. 4. 17: Effect of vehicle speed on peak wheel acceleration: (a) with flat; (b) without flat.

The size of the wheel flat has significant effect on excitation frequency due to the presence of the wheel flat. The effects of speed on excitation frequency for different flat lengths are shown in Fig. 4.18. It can be seen that increase in speed always increases the frequency of excitation. However, for a constant speed, increase in wheel flat length decreases the frequency of excitation.

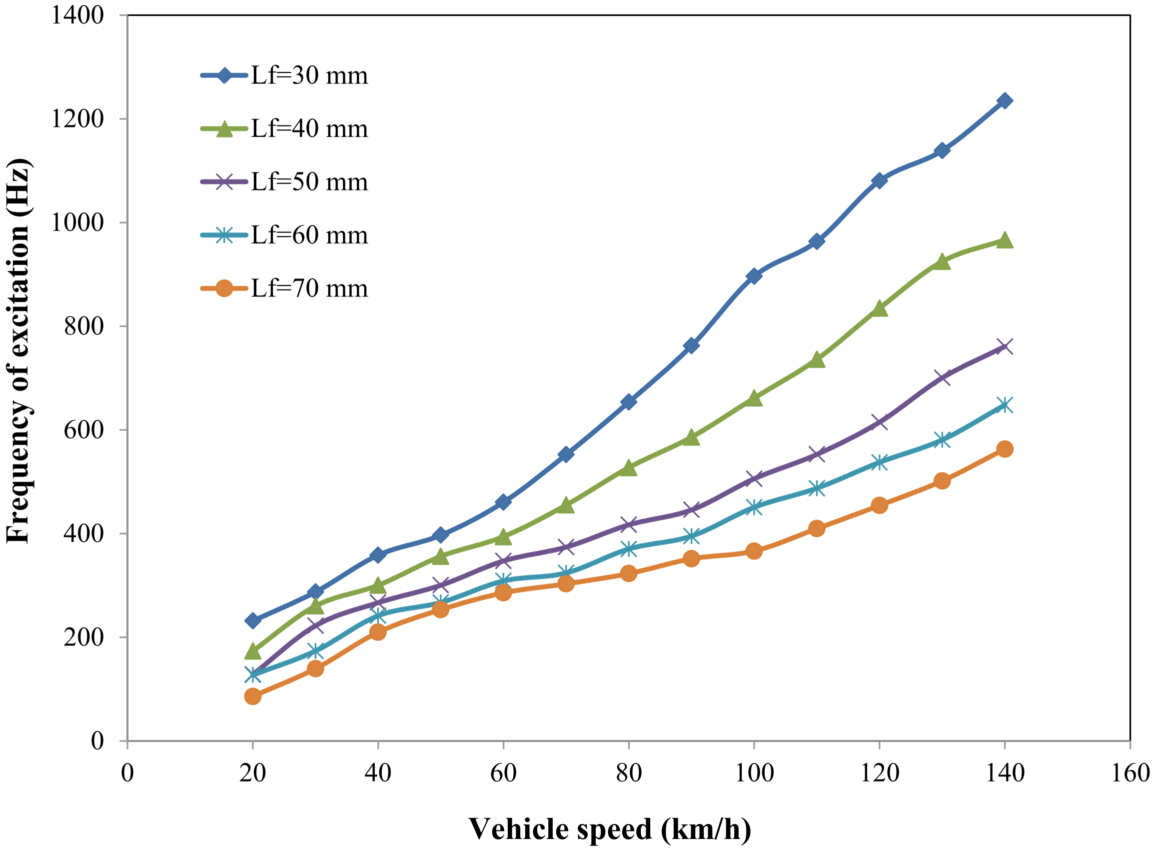

Fig. 4.18: Effect of vehicle speed and flat size on frequency of excitation due to a flat.

4.4 SUMMARY

The coupled three-dimensional vehicle-track model developed in this dissertation has been validated with both experimental and analytical data from the reported studies on the resulting impact force. The validation has been carried out with both linear and nonlinear railpad and ballast properties. The study shows that nonlinear railpad and ballast model gives better prediction of the wheel-rail impact force than that of the linear model when compared with the experimental data. The study shows that speed has significant effect on peak wheel-rail impact force for both linear and nonlinear railpad and ballast models. However, linear railpad and ballast predict higher peak wheel-rail impact forces in the selected speed range. This study shows that for the selected parameter the consideration of the linear properties of the railpad and ballast into the track model could increase the peak impact force up to 56.86%.

The validated model is then applied to obtain the response of individual vehicle and track components. The effects of a single wheel flat on the responses of vehicle and track components in terms of displacements and accelerations responses are investigated for both defective wheel and the flat-free wheel. The characteristics of the bounce, pitch and roll motions of the bogie due to a single wheel flat are also investigated. The results clearly show that presence of wheel flat within the same wheelset has significant effect on the impact force, displacement and acceleration responses of that wheelset. The results further show that although the effect of cross wheel impact on responses of the neighborhood wheelset or bogie displacements and accelerations responses are not so significant, this low magnitude impact may cause rapid fatigue damage of the vehicle and track components. However, this study shows that the effect of the transmitted force on the rear bogie due to the presence of the wheel flat within the front bogie is little and negligible which can be attributed to the low suspension spring stiffness. The study further shows that increase in vehicle speed and flat sizes always increases the wheel peak accelerations for both defective and flat-free wheels.

CHAPTER 5

IMPACT RESPONSE DUE TO MULTIPLE WHEEL FLATS

5.1 INTRODUCTION

The presence of wheel flats can cause high magnitude impact excitations on both wheel and rail eliciting large responses. This high frequency vibration in the vehicle track system affects the track maintenance and reliability of the vehicle's rolling elements. The presence of multiple wheel flats within a wheel or axle of a car is not very uncommon in practice. Multiple flats can be developed at the same locations of both wheels within a wheelset due to the locking of the brake system. The presence of multiple flats on same wheel or wheelsets causes multiple impacts in every revolutions of the wheel or wheelset. Furthermore, the number of flats, their sizes and their location with respect to each other may play an important role on the peak wheel-rail impact responses.

Various railroad organizations have been trying to set a threshold of flat size as an indication for replacement of the wheel with flat. The American Association of Railroad (AAR) has set the criteria to replace the wheel from the service for 50.8 mm long single flat or 38.1mm long two adjoining flats [139]. According to Transport Canada safety regulations, a railway car may not continue in service if one of its wheels has a flat of more than 63.50 mm in length or two adjoining flats each of which is more than 50.80 mm [1]. Swedish Railway sets the condemning limit for a wheel flat based on a flat length of 40 mm and flat depth of 0.35 mm [17]. According to UK Rail safety and standard board [146], a wheel with flat length exceeding 70 mm must be taken out of service. Most of these wheel removal criteria are based on single or multiple adjoining flats within a wheel. The possible existence of flats on both wheels within same wheelsets or bogies is not dealt by any of the requirements.

Although the presence of multiple wheel flats within a wheel or wheelset is common in practice, the vast majority of the studies dealing with wheel flat utilizes simple vehicle-track model and considers single wheel flat only. Presence of multiple defects within the contact point would further enhance the complexity of the analytical model. The nonlinear contact of the wheel and rail makes it more complex for analysis. Furthermore, the contributions due to roll and pitch dynamics of the car and relative positions of different wheel flats with wide variations in relative positions between the flats on the wheel-rail impact forces were not investigated. A detailed study on dynamic wheel-rail interactions with 3-dimensional car and track model is thus required in order to characterize the contact impact responses due to the presence of multiple wheel flats.

In this chapter, the three-dimensional railway vehicle-track model developed in chapter 3 and validated in chapter 4 is employed to study the effect of multiple wheel flats on wheel acceleration response. Studies are carried out for different types of wheel flats and their relative positions. The effect of multiple wheel flats on both direct and cross wheels within same or different wheelsets are also investigated. The effects of vehicle speed on peak wheel acceleration in presence of multiple wheel flats are further investigated for both left and right wheel within same wheelset. Finally, the effect of bogie pitch and roll motion on overall peak acceleration of the wheel is also investigated in presence of two in-phase flats.

5.2 MULTIPLE WHEEL FLATS MODEL

A single flat in one wheel may be followed by another flat of same or different size in the adjacent wheel. Their relative positions can also be different. As discussed in chapter 1, although the presence of multiple wheel flats in a single wheel or within same wheelsets are widely observed the resulting impact response in terms of accelerations have not been reported. In this section, the developed three-dimensional vehicle-track model is applied to study the influences of multiple flats. In this study, similar to the single wheel flat model as described before, commonly used haversine wheel flat model is utilized to study the effect of multiple flats. The studies s are performed for two different cases: (i) two identical size flats on the same wheel located at different angular positions (phase angle) (ii) two same size flats on the different wheels either in phase or out-of-phase. Descriptions of two flats in same wheel with different angular positions are already given in chapter 3. The positions of two similar or different flats in same wheel or two different wheels within same wheelset are shown in Fig. 5.1. The flats are defined such that the leading flat comes into contact with the rail first followed by trailing flat, which enters the contact with a defined phase angle. The variations in radius of a wheel with two flats each with 60 mm length and 0.45 mm depth that are 45^0 apart are illustrated in Fig. 5.2, as a function of the wheel position.

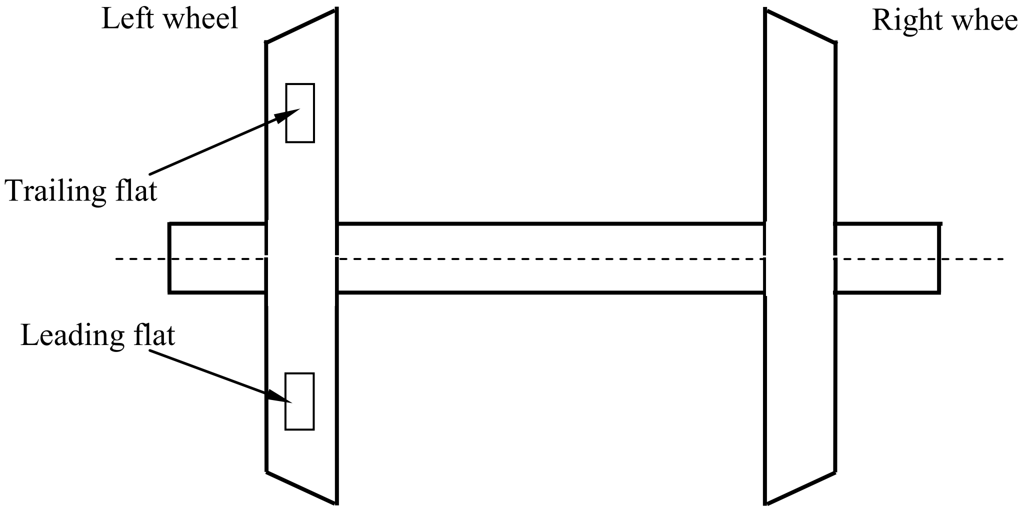

(a)

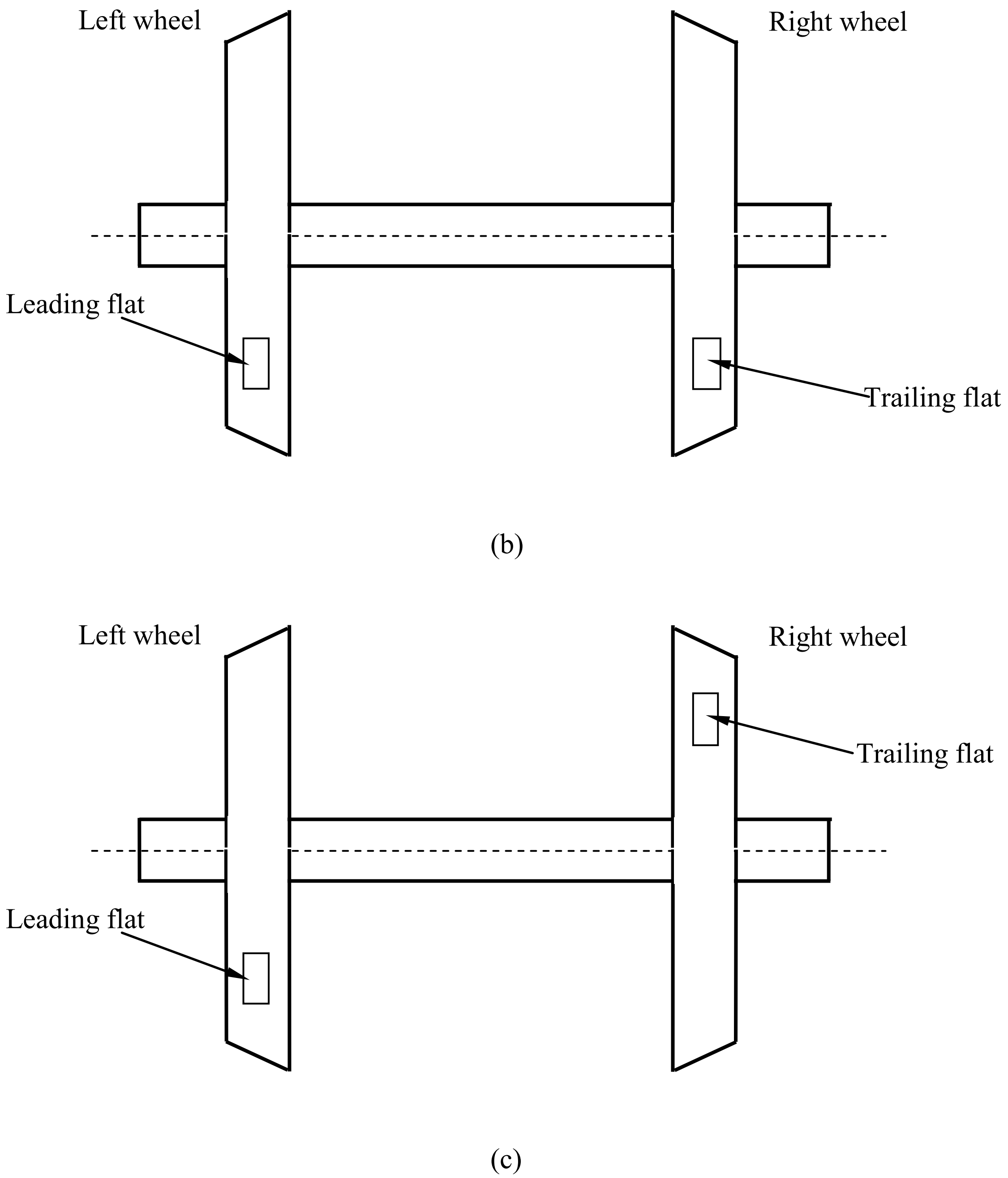

Fig. 5. 1: Location of same or different size flats (a) two flats within same wheel out-of-phase; (b) two flats in different wheels within same wheelset in-phase; (c) two flats in different wheels within same wheelset out-of- phase.

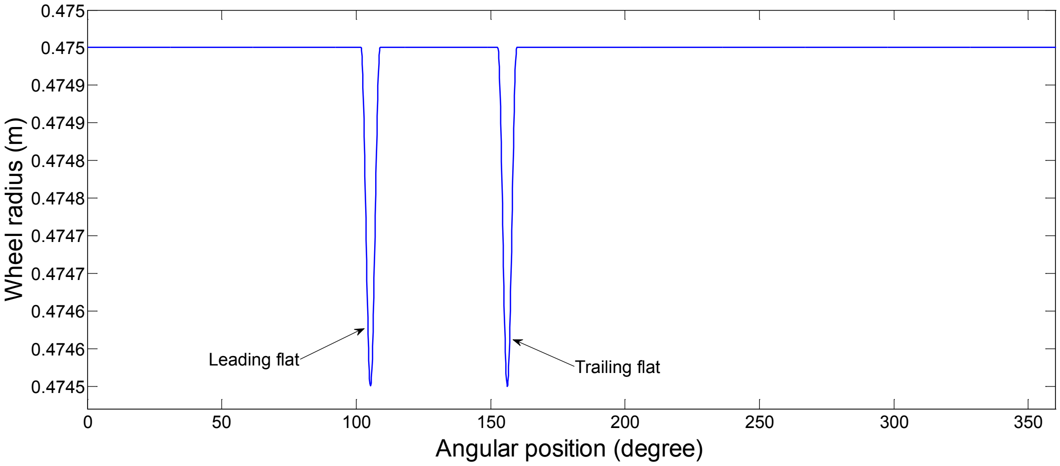

Fig. 5. 2: Variations in radius of a wheel with two same size flats (L_f = 60 mm and D_f = 0.45 mm), which are 45^0 apart.

5.3 DYNAMIC RESPONSE DUE TO TWO FLATS ON SINGLE WHEEL

In order to analyze the effect of multiple wheel flats in same wheel on wheel acceleration response, two same size flats with different specified phase angles are considered. The simulations are carried out for multiple flats within the left wheel of first wheelset at a forward speed of 100 km/h. Both flats are 60 mm long and the depths of the flats are determined by the relationship between them as shown by Eqn. (3.51). Studies are carried out by considering the fact that all wheels except the left wheel of front wheelset are perfect. The variations in the wheel impact acceleration due to the presence of multiple flats are evaluated by considering different phase angles between the two flats, namely, 5^0, 15^0, 30^0 and 45^0.

Figures 5.3 to 5.6 illustrate the variations in wheel acceleration response at the left and right wheels for different phase angles between the flats, while the flats are within left wheel only and the right wheel is assumed as perfect. The results clearly show two distinct peaks in the impact acceleration response of both left and right wheel due to the presence of two flats in two different locations. However, as expected, the peak impact accelerations for right wheel without flats are much less than that for the left wheel with flats. The figures further show that although two flats are identical in size, the magnitudes of the peak impact accelerations induced by the two flats differ. The peak impact acceleration induced by the leading flat is in the order of ±45.6 g at the left wheel and approximately ±13.5 g at the right wheel irrespective of the position of the trailing flat. In case of left wheel acceleration, the magnitude of the peak impact acceleration induced by the trailing flat tends to increase with increase in phase angles between the flats. The figures further show that the difference between the peak acceleration induced by the leading and trailing flats are insignificant when the flats are 30^0 and 45^0 apart, while the time lapse between the two peak accelerations directly related to the vehicle speed and the phase difference between the two flats.

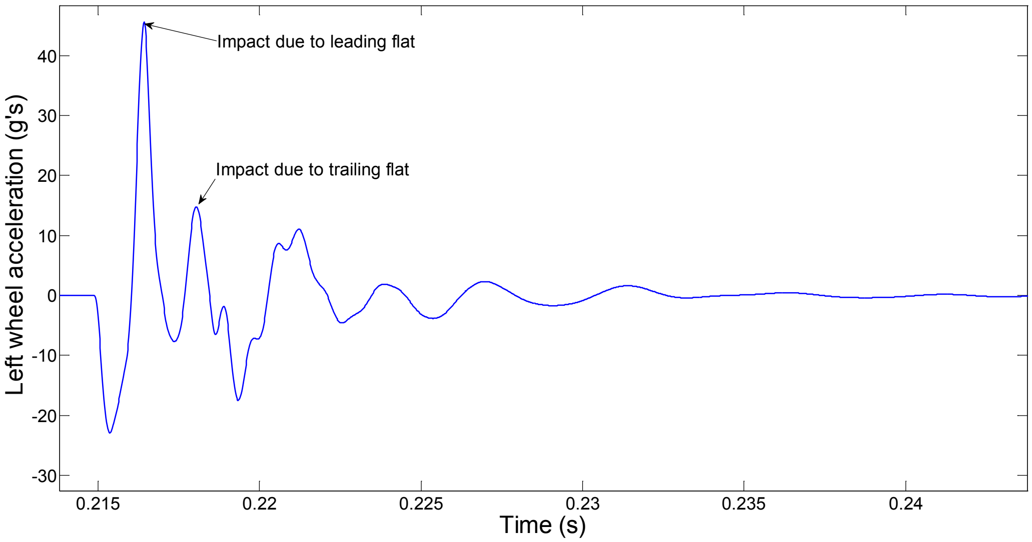

(a)

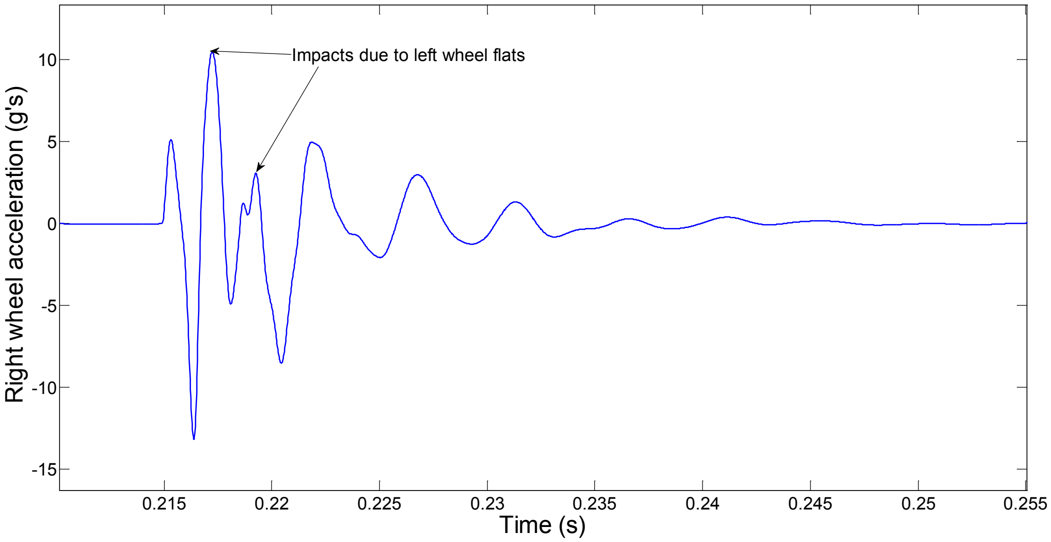

(b)

Fig. 5. 3: Wheel impact acceleration responses due to two flats on left wheel at 5^0 out-of-phase (v=100 km/h and $L_f = 60$ mm): (a) left wheel; (b) right wheel.

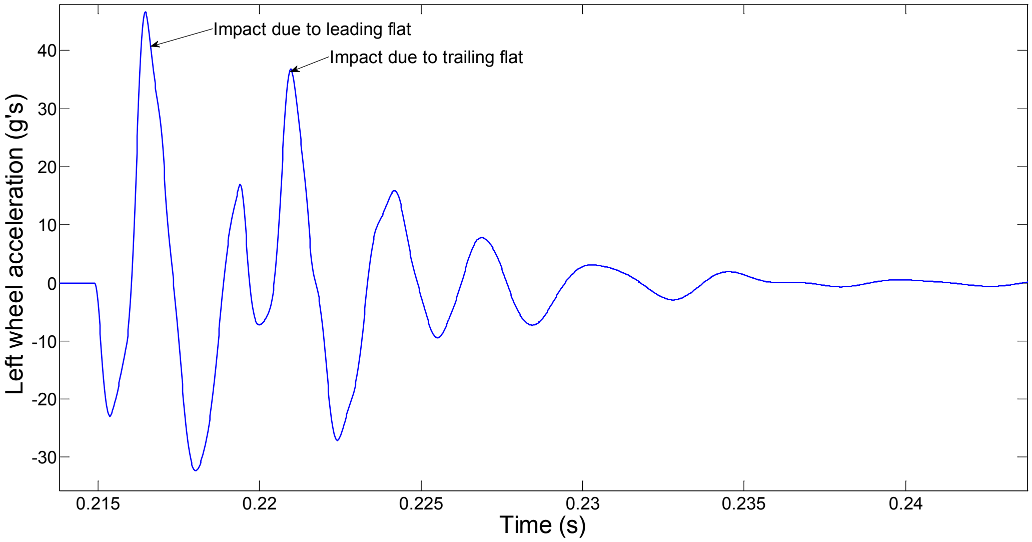

(a)

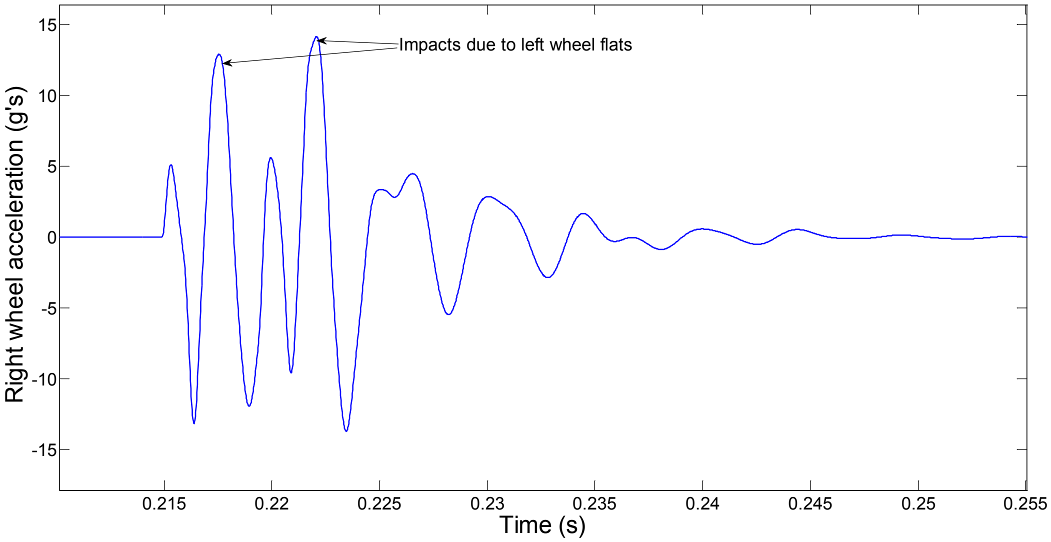

(b)

Fig. 5. 4: Wheel impact acceleration responses due to two flats on left wheel at 15^0 out-of-phase (v=100 km/h and L_f = 60 mm): (a) left wheel; (b) right wheel.

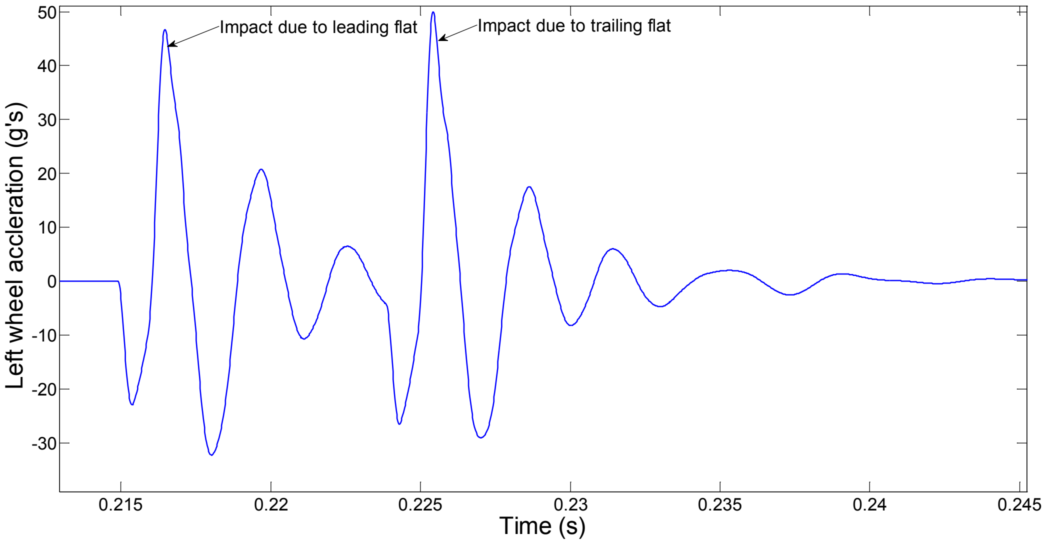

(a)

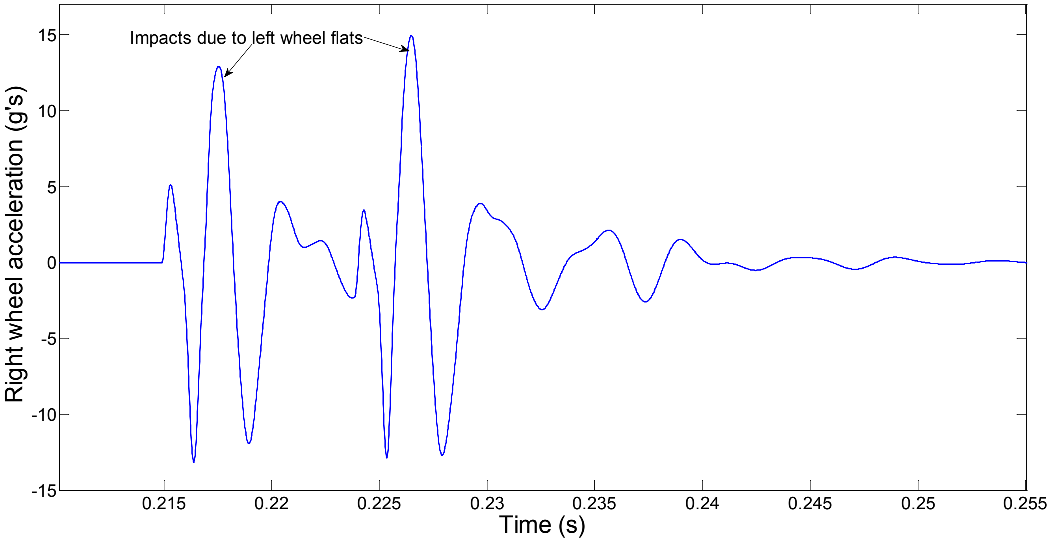

(b)

Fig. 5. 5: Wheel impact acceleration responses due two flats on left wheel at 30^0 out-of-phase (v=100 km/h and L_f = 60 mm): (a) left wheel; (b) right wheel.

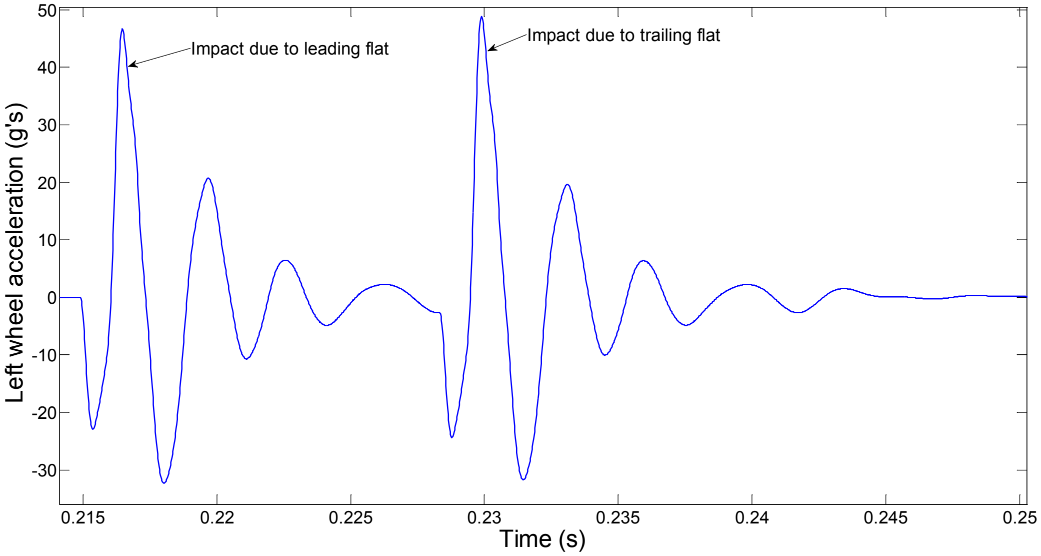

(a)

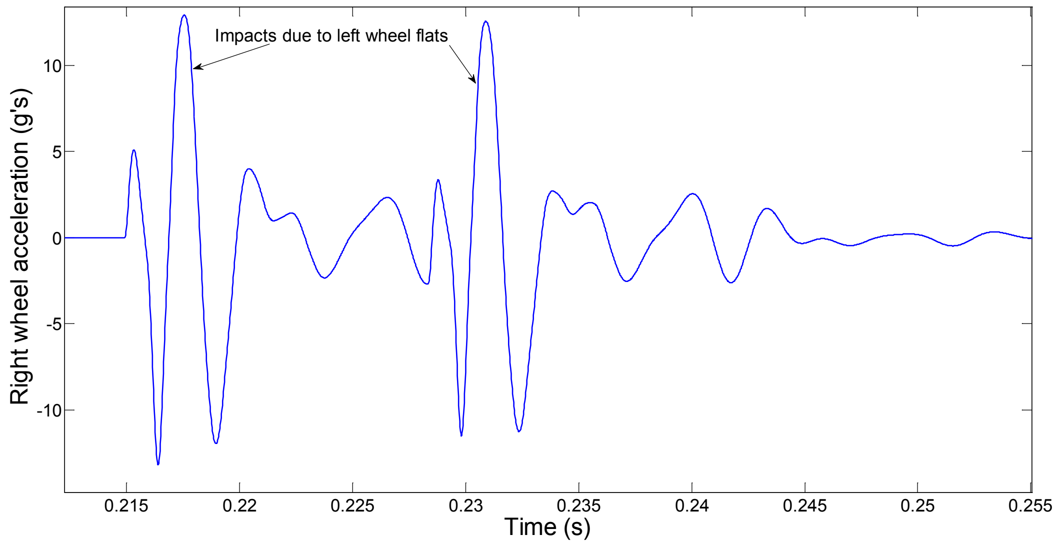

(b)

Fig. 5. 6: Wheel impact acceleration responses due to two flats on left wheel at 45^0 out-of-phase (v=100 km/h and $L_f = 60$ mm): (a) left wheel; (b) right wheel.

In case of right wheel acceleration, the figures show that the peak impact acceleration induced by the trailing flat can be slightly higher than the peak impact acceleration induced by the leading flat for some phase angles, as it is evident in Figs. 5.4 and 5.5, for 30^0 and 45^0 phase angles. The results further suggest that the magnitudes of impact accelerations induced by two flats are similar to that caused by a single flat, if they are apart from each other by 30^0 phase angle or more. The frequency of the impact, however, increases with increase in number of flats, which could yield rapid fatigue damage of the vehicle and track components.

The second flat in a wheel of multiple flats may generate different impact acceleration from those of a single flat case under certain condition, as it is shown in Figs. 5.3 to 5.6. Speed of the vehicle also strongly affects the variations in impact accelerations responses induced by the multiple flats. Increase in vehicle speed will particularly decrease the time lapse between the two peak impacts caused by two flats. The effect of speed on the peak wheel accelerations due to multiple wheel flats within left wheel under certain phase angles is therefore examined in the speed range of 20-140 km/h. Figures 5.7 to 5.9 show the effect of speed on peak left wheel acceleration responses caused by the presence of two flats within left wheel only and with phase angles of 15^0, 30^0 and 45^0, respectively. The results show that, similar to single wheel flat, increase in speed and flat size always increases the left wheel impact acceleration caused by the leading flat irrespective of the phase angles between the two flats.

In case of left wheel acceleration caused by the trailing flat, the results show complex relationship between the vehicle speed, flat size and the peak acceleration responses. It can be seen from Figs. 5.7 to 5.9 that the peak impact acceleration due to the trailing flat on the multiple-flat left wheel is significantly affected by the phase angles, when the phase angle is small and the flat size is large. The results further show that the difference in impact accelerations due to the leading and trailing flats on left wheel is not significant, when the phase angle between the flats is more than 45^0 and the flat length is equal to or less than 60 mm, irrespective of the vehicle speed. Beyond this value of phase angle and within this flat size, the impact acceleration caused by the trailing flat is same as that predicted by the simulation of single flat of same size.

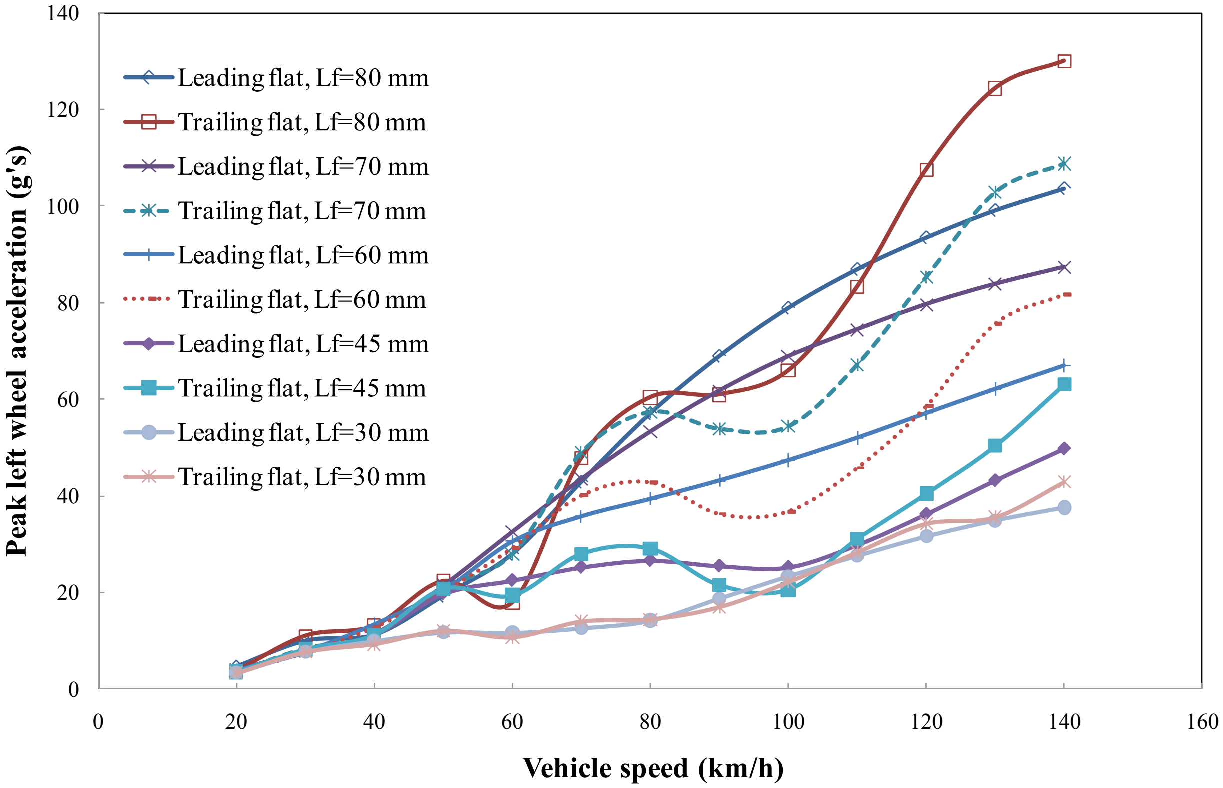

Fig. 5. 7: Effect of speed on peak wheel acceleration response for different sizes of flats with two flats on left wheel at 15^0 of phase angle.

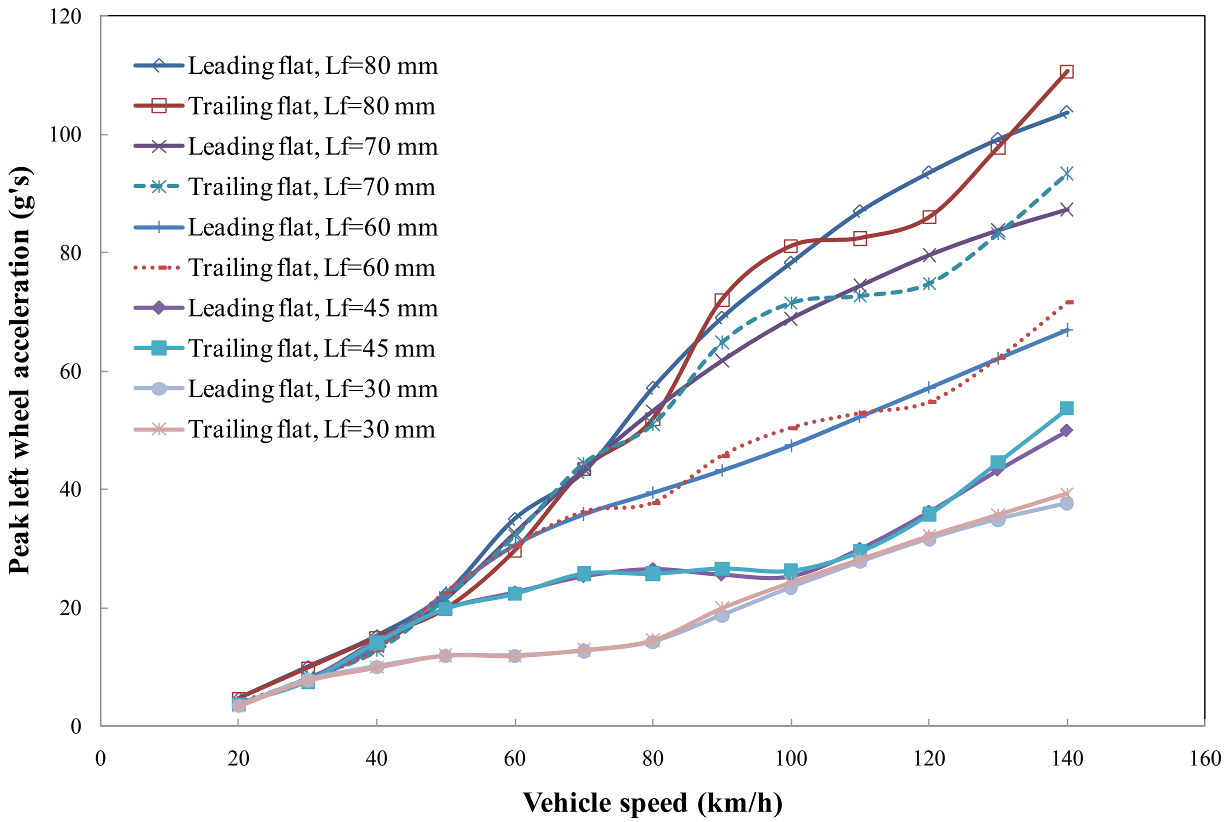

Fig. 5. 8: Effect of speed on peak wheel acceleration response for different sizes of flats with two flats on left wheel at 30^0 of phase angle.

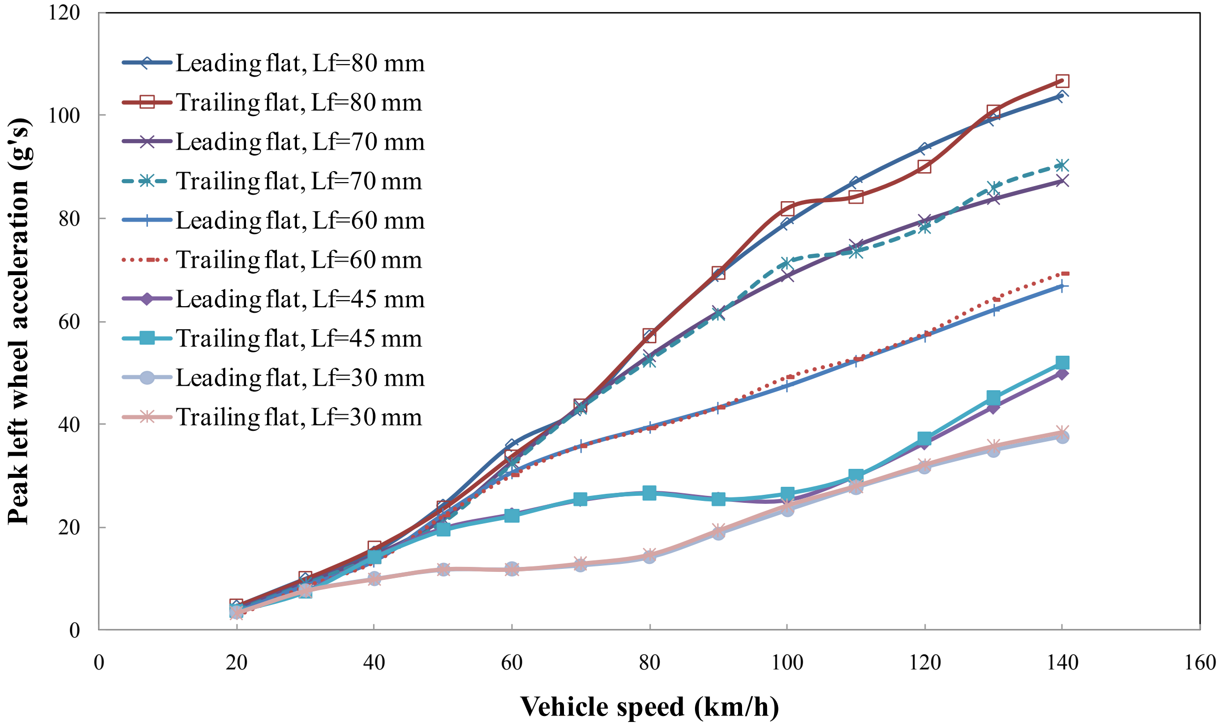

Fig. 5. 9: Effect of speed on peak wheel acceleration response for different sizes of flats with two flats on left wheel at 45^0 of phase angle.

5.4 DYNAMIC RESPONSE DUE TO SINGLE FLAT ON TWO WHEELS OF SAME WHEELSET OUT-OF-PHASE

The effect of multiple wheel flats on wheel acceleration response is further investigated with two same size flats on both left and right wheels of the first wheelset with different specified phase angles, while all other wheels of the vehicle are assumed as perfect. The simulations are carried out for multiple flats of 60 mm length and a forward vehicle speed of 100 km/h. The depths of the flats are determined by the relationship between the wheel flat length and depth as shown by Eqn. (3.51). The left wheel flat is assigned ahead of the right wheel flat with a specific phase angle. The variations in the both left and right wheel impact acceleration due to the presence of multiple flats within a same wheelset are evaluated by considering different phase angles between the two flats, namely, 15^0, 30^0 and 45^0.

The time histories of left and right wheel impact acceleration due to a single flat on both the left and right wheels at 15^0, 30^0, and 45^0 out-of-phase are shown in Figs. 5.10 to 5.12, respectively. The results clearly show two distinct peaks in both left and right wheel acceleration responses corresponding to their respective flats, when the phase angle is more than 15^0. The difference in magnitudes of the peak acceleration due to the direct and cross wheel flat is also pronounced for all three phase angles considered. The magnitudes of the peak acceleration due to the direct wheel flat are same as those obtained for a single wheel flat earlier.

Figures 5.10 to 5.12 illustrate that the impact acceleration due to the flat on left wheel which enters into the contact first is unaffected by the flat on the right wheel, which enters the contact region after the defined phase angle. This is consistent with the right wheel impact acceleration responses too. The results further illustrate that the cross wheel flat effect is more pronounced primarily for low phase angles. However, the extent of the effect is dependent on speed, flat size and phase angles between the flats. For the given speed and flat size, the magnitude of the left or right wheel acceleration due to direct wheel flat is in the order of 47.5 g irrespective of the phase angle. However, the magnitudes of the left wheel acceleration due to the right wheel flat (cross wheel flat effect) are 12.9, 14.6 and 16.4 g for phase angles of 15^0, 30^0 and 45^0, respectively. On the other hand, the magnitude of the right wheel acceleration due to cross wheel flat is in the order of 12.85 g irrespective of the phase angle.

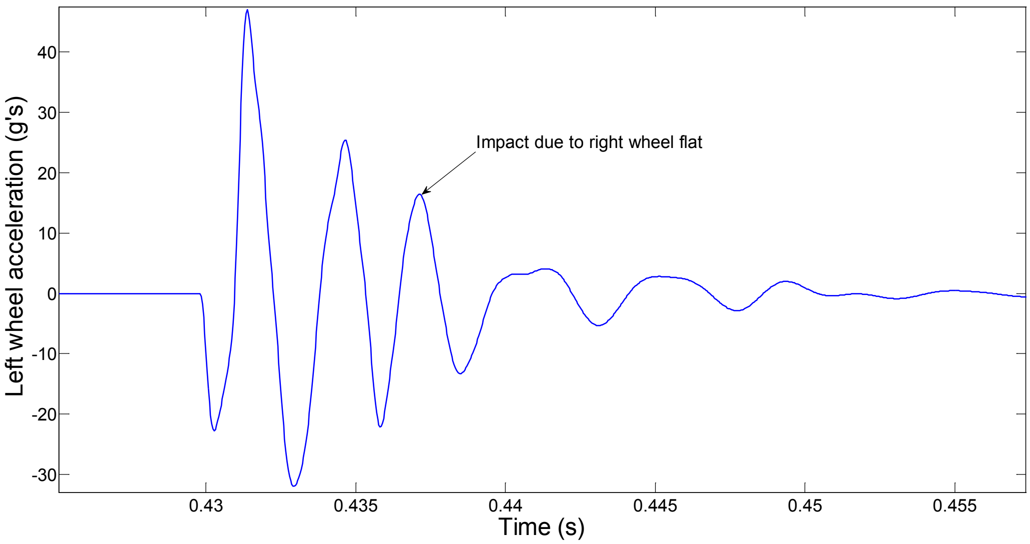

(a)

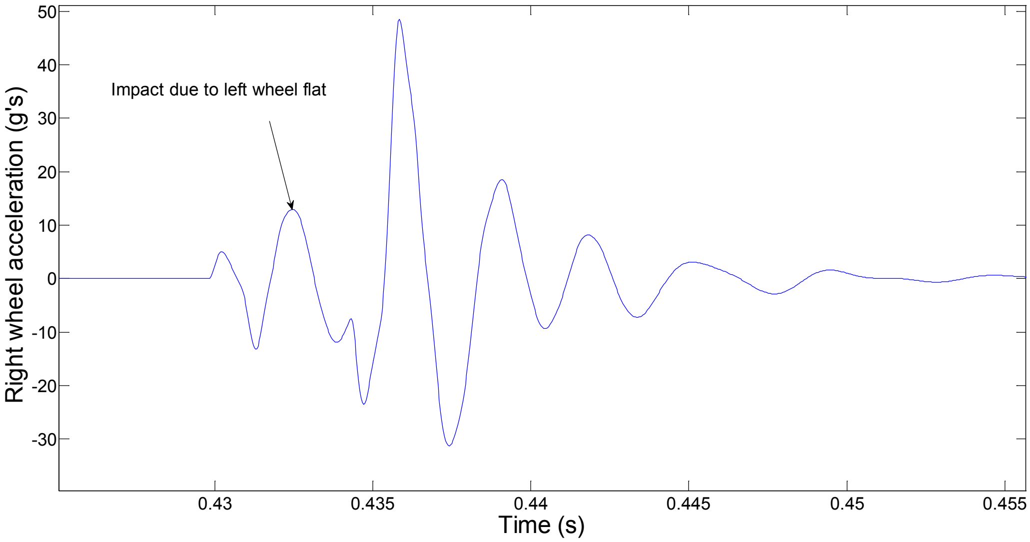

(b)

Fig. 5. 10: Left and right wheel impact acceleration responses due to a single flat on both wheels of a wheelset at 15^0 out-of-phase (left wheel flat ahead by 15^0)

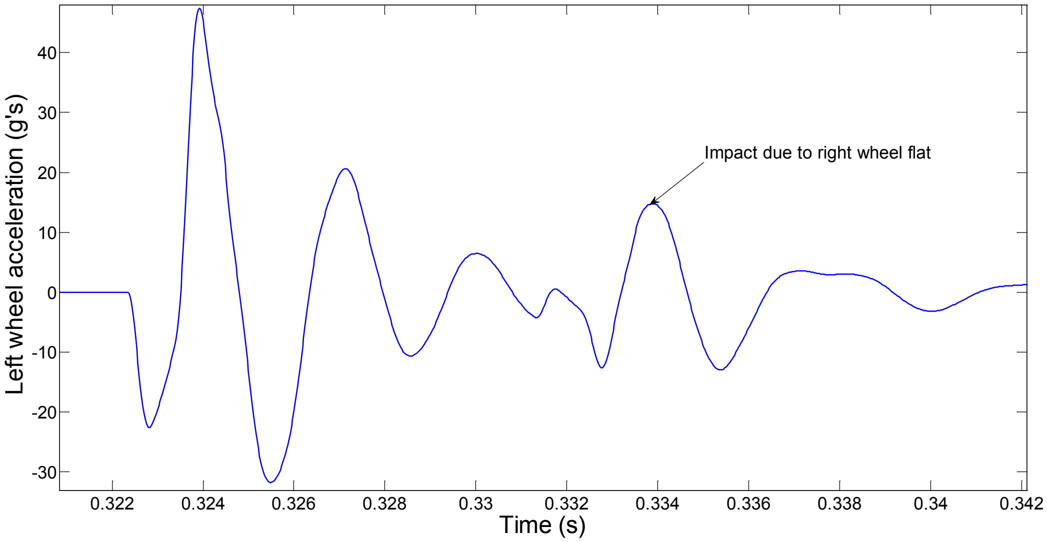

(a)

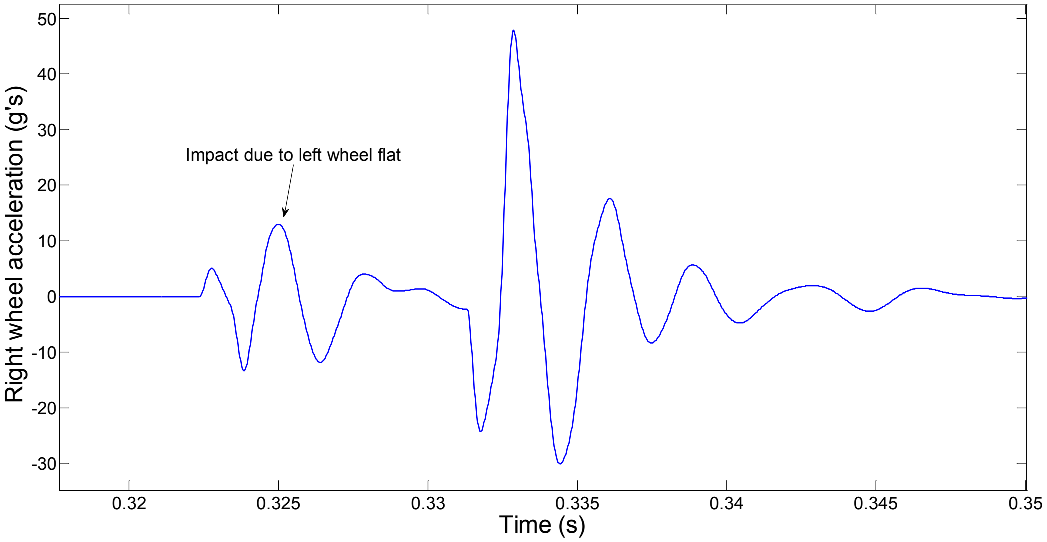

(b)

Fig. 5. 11: Left and right wheel impact acceleration responses due to a single flat on both wheels of a wheelset at 30^0 out-of-phase (left wheel flat ahead by 30^0)

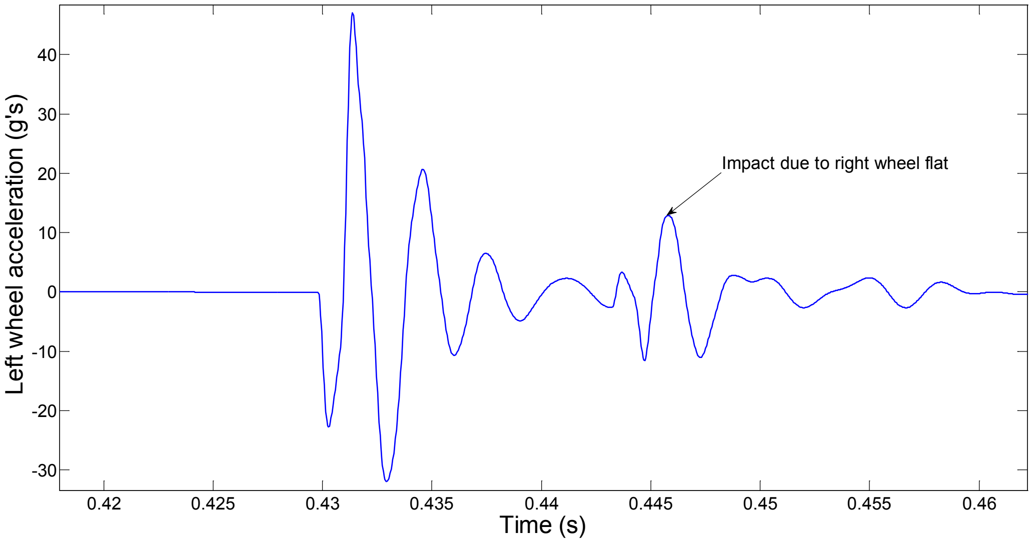

(a)

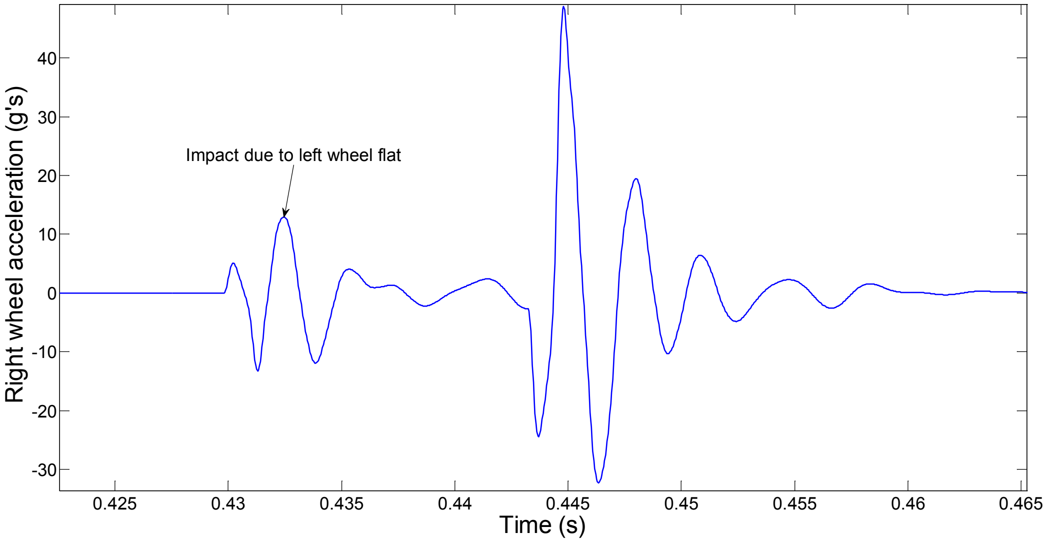

(b)

Fig. 5. 12: Left and right wheel impact acceleration responses due to a single flat on both wheels of a wheelset at 45^0 out-of-phase (left wheel flat ahead by 45^0)

The effect of speed on peak left and right wheel acceleration due to a single flat on both wheels at particular phase angles is further investigated in speed range of 20-140 km/h. Two identical flats are assumed to be present on both left and right wheels of first wheelset of the front bogie at 15^0, 30^0 and 45^0 phase difference. The peak magnitudes of the left and right wheel acceleration due to the direct wheel flat with 30, 45, 60, 70 and 80 mm of lengths as a function of speed were investigated. The depths of the flats are calculated by the relation as stated in Eqn. (3.51). The simulations are carried out with static load per wheel of 103 kN, and the results obtained are shown in Figs. 5.13 to 5.15 with different flat sizes and phase angles.

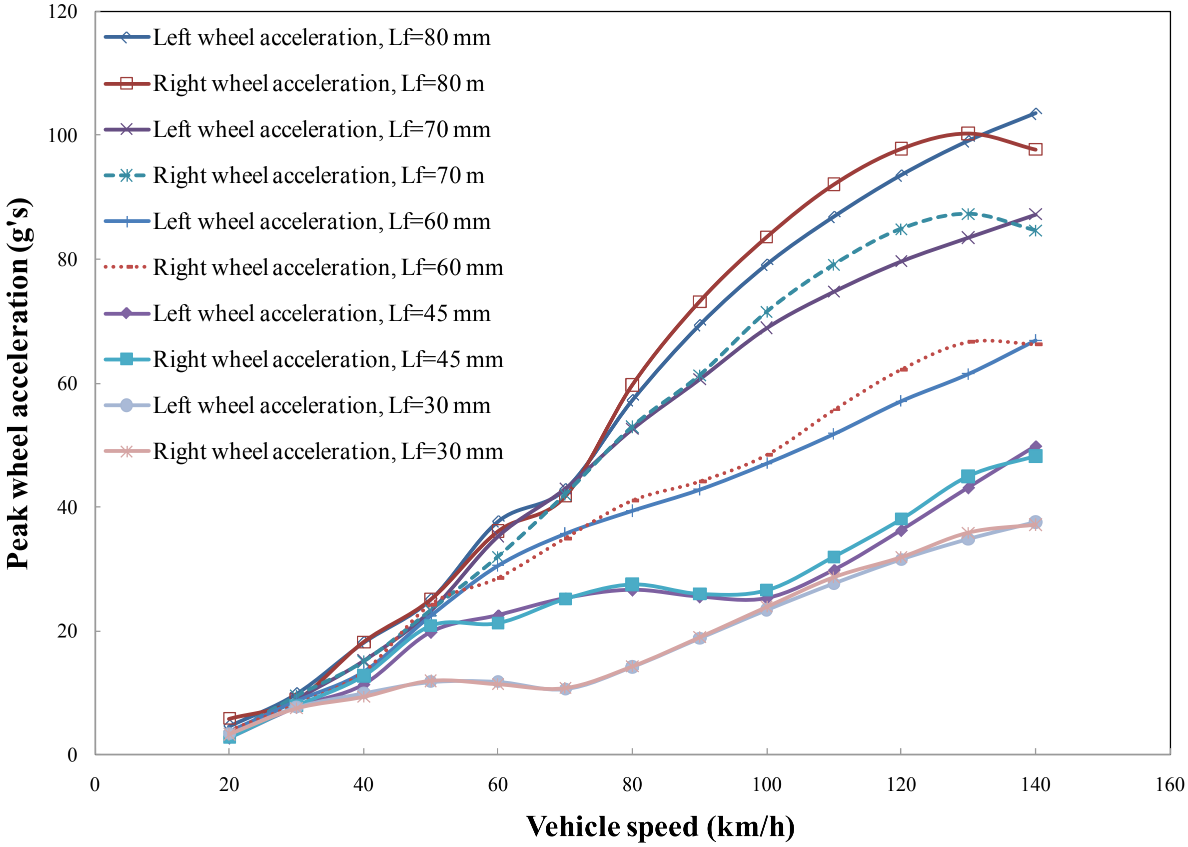

Fig. 5. 13: Effect of speed on peak wheel impact acceleration due to a single flat on both wheels of a wheelset at 15^0 out-of-phase.

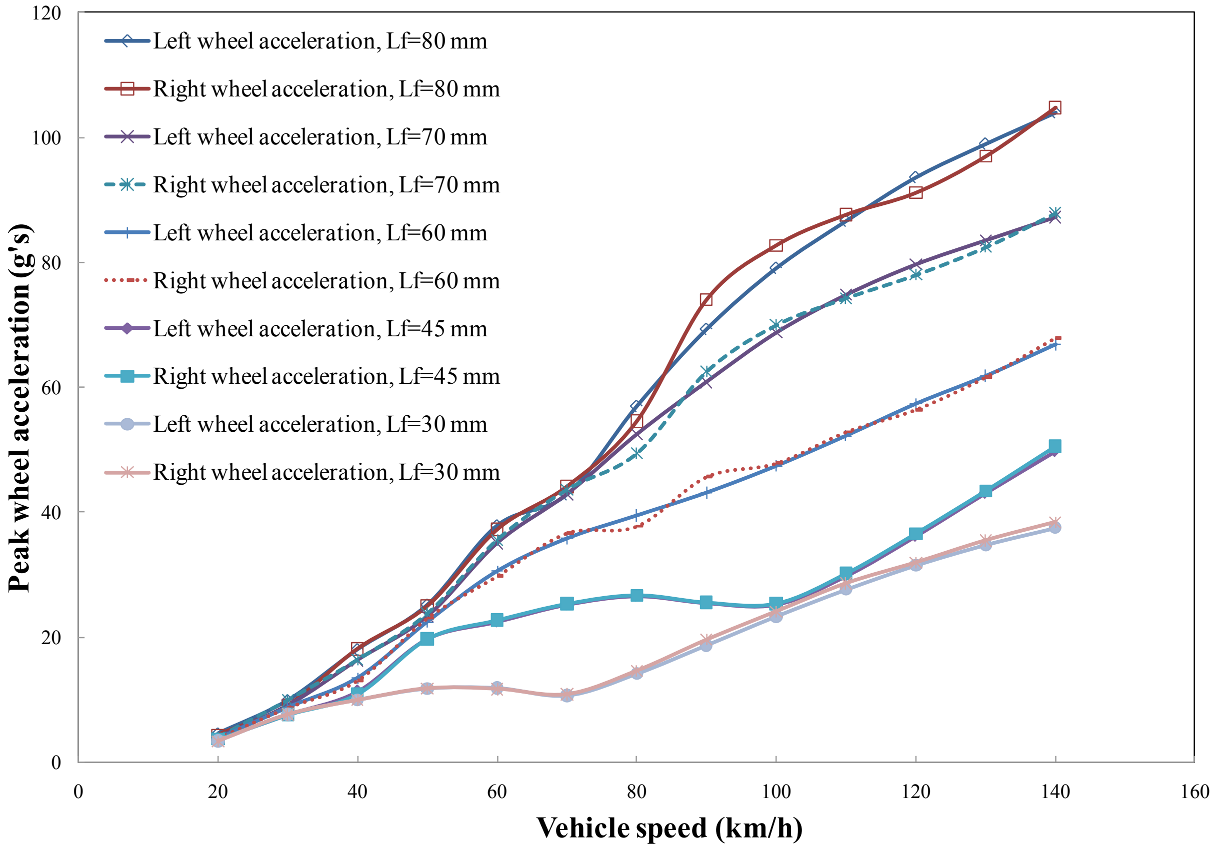

Fig. 5. 14: Effect of speed on peak wheel impact acceleration due to a single flat on both wheels of a wheelset at 30^0 out-of-phase.

Similar to the peak impact acceleration response due to single wheel flat, figures 5.13 to 5.15 clearly show that increase in vehicle speed and flat length always increases the peak acceleration responses for both the left and right wheel peak acceleration responses irrespective of phase angles between the two flats. The right wheel peak impact acceleration increases in sinusoidal motion which is mainly due to the sinusoidal motion of the left wheel acceleration response after the impact. The results clearly demonstrate that the right wheel peak acceleration experienced larger magnitudes of impact acceleration than that of the left wheel, when the speed is higher and flat size is larger. This indicates the possibility of significantly larger impact acceleration due to a direct wheel flat if the other wheel has experienced a flat prior to it. This study shows that for a speed of 110 km/h, the left wheel with single flat of 60 mm length that comes into wheel-rail contact first will generate a peak acceleration of 51.81g for a 15^0 phase angle between the flats. However, the right wheel that experiences an impact due to a similar flat on left wheel 15^0 prior to the direct wheel flat will generate a peak acceleration of 55.69 g.

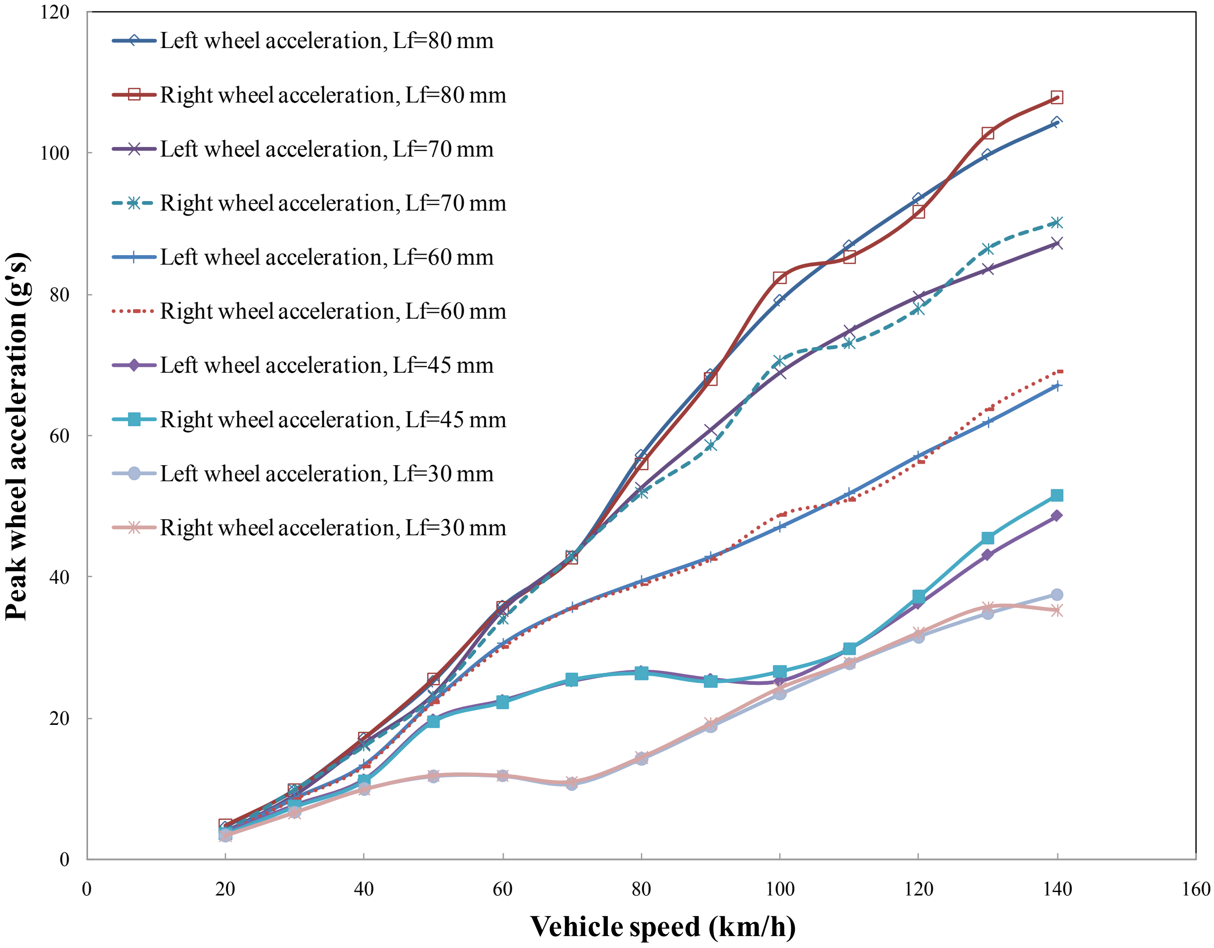

Fig. 5. 15: Effect of speed on peak wheel impact acceleration due to a single flat on both wheels of a wheelset at 45^0 out-of-phase.

5.5 DYNAMIC RESPONSE DUE TO A SINGLE FLAT ON ALL WHEELS OF FRONT BOGIE AND ENTIRE VEHICLE

In an attempt to investigate the effect of car body pitch and roll motion on peak wheel acceleration response, the developed three-dimensional vehicle-track model is applied to study the influence of multiple flats. Studies are carried out for two different cases: (i) four identical wheel flats on four wheels within the front bogie only at same angular position; (ii) eight same size flats on eight wheels of both front and rear bogies of the entire vehicle at same angular position. Simulations are carried out with 60 mm flat length and for a vehicle speed of 100 km/h. The entire parameters are same as for single wheel flat used before. The results obtain from simulations are shown in Fig. 5.16 for both cases.

Figure 5.16 shows the time histories of left or right wheel acceleration response for the first wheelset in presence of single flats on four wheels or eight wheels of the vehicle. However, it is expected that all other wheels of the same bogie or entire car would show similar responses. Hence, they are not shown here. It can be seen that time histories of impact acceleration for multiple flats in phase within the front bogie and entire vehicle are same as the time history of impact acceleration due to single wheel flat. However, there is a difference in peak magnitude and frequency of oscillations after impact between the impact acceleration response due to single and multiple wheel flats. This difference in peak magnitude of the impact acceleration is in the order of 21 g.

Peak impact acceleration due to single flat on four wheels is 21 g less than the peak impact acceleration due to single wheel flat of same size. This difference can be attributed to the symmetry of the bogie about the central lateral axis due to the presence of flats on all four wheels at same location. In the presence of flats on four wheels, both front and rear wheelsets of the front bogie move together while the pitch and roll motions of the bogie are not excited. On the other hand, in case of single wheel flat, owing to the pitch and roll motion of the front bogie together with the roll motion of the wheelset, the deflections of wheel is more which ultimately increases the wheel acceleration.

Fig. 5.16 further shows that there is no difference in peak magnitude and frequency of oscillation of the impact acceleration due to four wheel flats within front bogie and eight wheel flats within the entire vehicle. For both of these cases, the peak magnitude of the impact acceleration is 26.7 g. This shows that car body pitch and roll motion have no effect on peak acceleration response due to wheel flats. This can be attributed to the high suspension stiffness of the primary and secondary suspension that isolates the car body from impact that occurs in wheel-rail contact region.

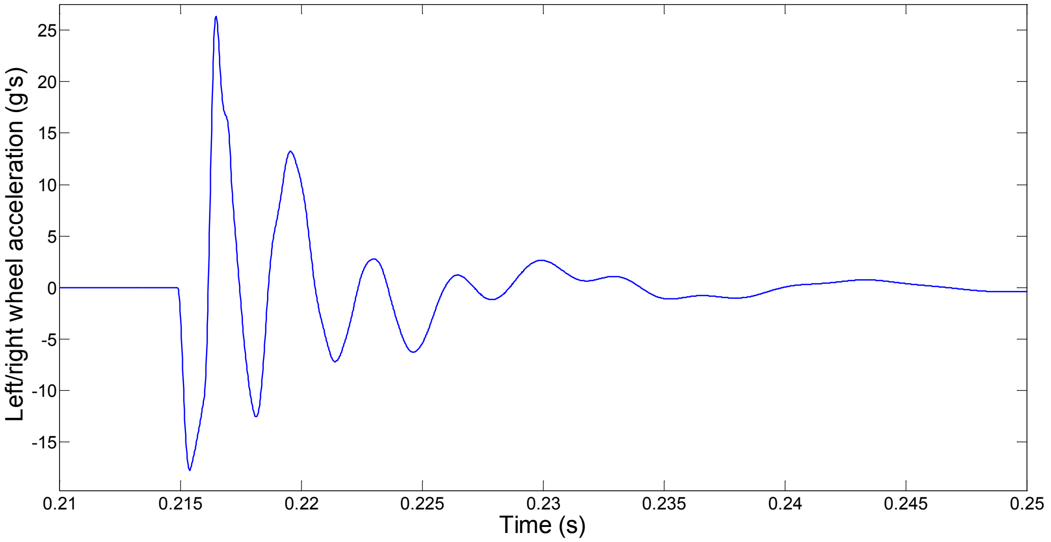

(a)

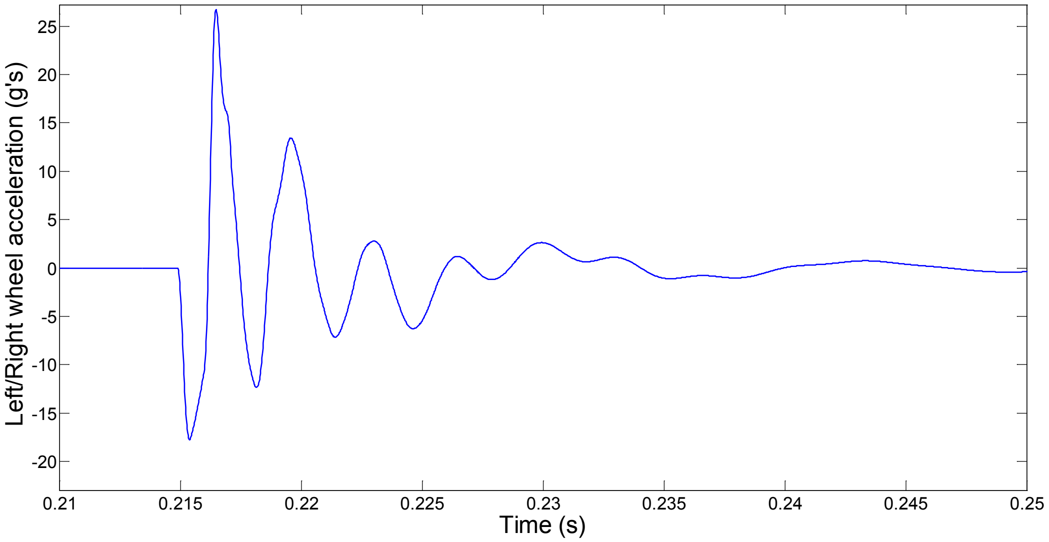

(b)

Fig. 5. 16: Time history of left or right wheel impact acceleration responses due to a single flat on (a) all four wheels of the front bogie; (b) all eight wheels of the entire vehicle, in phase.

5.6 DYNAMIC RESPONSE DUE TO TWO FLATS ON OPPOSITE WHEELS OF SAME WHEELSET IN PHASE

The presence of two flats in two wheels of same wheelset is very common in practice due to the sliding of the locked wheelset. These flats may be same or different in size and their effects on impact acceleration response can be different too. In this subsection, the wheel impact acceleration responses and effect of speed on peak impact accelerations are investigated. Two flats of same size are assigned to left and right wheels of the first wheelset at same position, i.e. 0^0 phase angle.

Figure 5.17 illustrates the time history of left or right wheel impact acceleration due to a 60 mm long flat on both left and right wheels in same location within the first wheelset of the front bogie. As the result shows, with two similar flats on both wheels in phase, the left or right wheel impact acceleration develops response identical to the single wheel flat acceleration response.

However, the magnitude of the peak acceleration for two flats in opposite wheels in phase is less than the impact acceleration due to single wheel flat. It can be seen that the magnitude of the peak left or right wheel acceleration is in the order of 37.64 g. This peak is approximately 11 g more than the peak magnitude of impact acceleration in the presence of single flat of same size on all four wheels of the front bogie as shown in Fig. 5.16 (a). This difference can be attributed to the excitation of the bogie pitch motion, in case of single flat on two wheels of first wheelset of the front bogie. In case of flats on both wheels of the first wheelset, the displacement of the first wheelset of the front bogie is more while the second wheelset without any flats remains same. This motion of the first wheelset increases the peak wheel acceleration in case of single flat on both wheels in phase.

The effect of speed on peak wheel acceleration due to a single flat on left wheel and two in-phase flats on both wheels of a wheelset is shown in Fig. 5.18. The results are shown for speed range of 20-140 km/h, where the flat length is varied from 30-80 mm. The figure clearly shows that the peak impact acceleration due to a single wheel flat is higher than the peak wheel acceleration due to the two in-phase flats on both wheels of same wheelset. This result is consistent for the selected speed range and the flat sizes. For a vehicle speed of 140 km/h and flat length of 80 mm, the difference can be as high as 27.3 g.

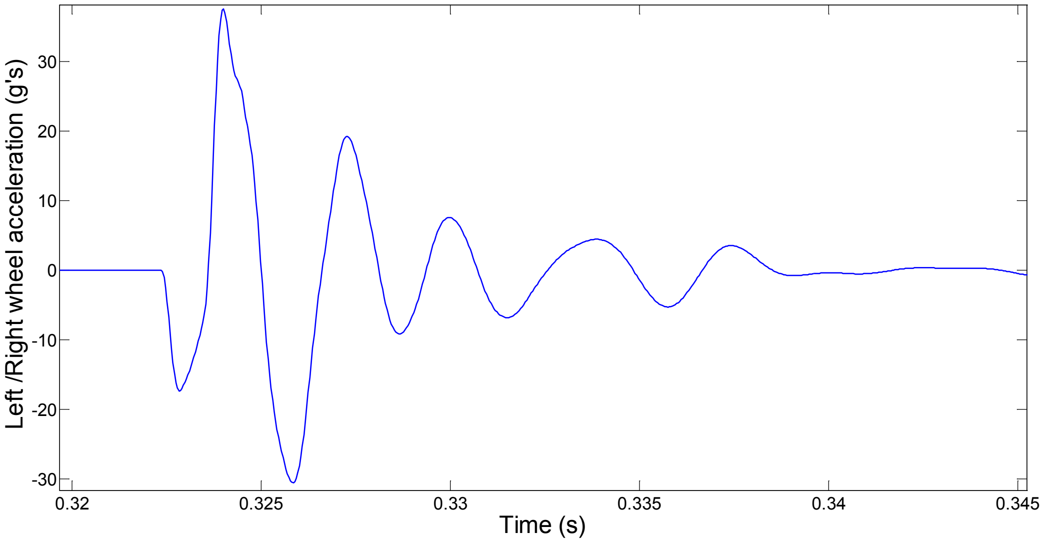

Fig. 5. 17: Time history of left and right wheel impact acceleration responses due to a single flat on both wheels in phase (bogie pitch effect).

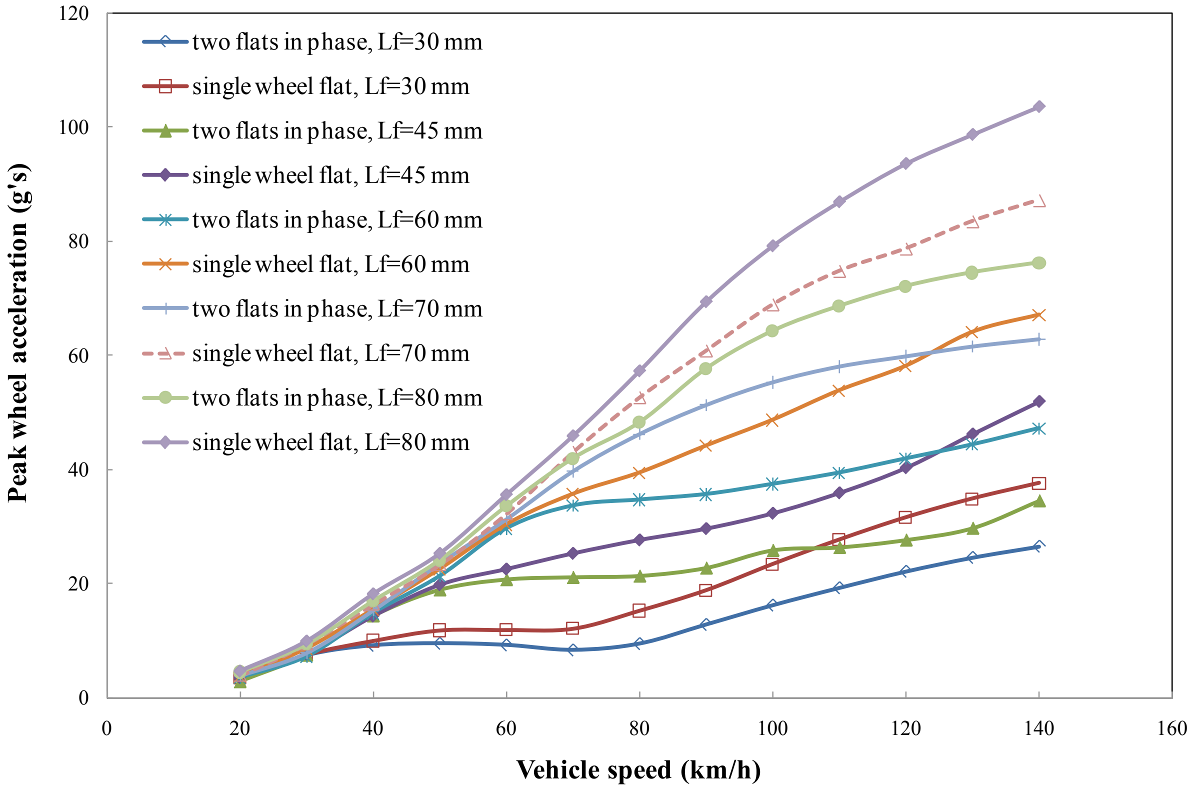

Fig. 5. 18: Effect of speed on peak wheel impact acceleration due to a single flat on left wheel and two flats on both wheels of a wheelset in phase.

5.7 DYNAMIC RESPONSE DUE TO TWO FLATS ON LEFT WHEELS OF TWO WHEELSETS AT SAME POSITION

The effect of presence of multiple wheel flats on two different wheelsets within the same bogie is further investigated for a vehicle speed of 100 km/h. Two flats of identical size are assigned to left wheels of the first and second wheelsets at same location. Figure 5.19 illustrates the time history of left wheel impact acceleration due to a 60 mm long flat on left wheels of first and second wheelsets within the front bogie in same location. As the result shows, the left wheel impact acceleration response follows similar trend as the single wheel flat acceleration response. However, similar to the multiple flats on both wheels within the same wheelset in phase condition, the magnitude of the peak acceleration for two flats in left wheel of opposite wheelsets in phase is less than the impact acceleration due to a single wheel flat.

The magnitude of the peak left wheel acceleration is in the order of 38.80 g, which is approximately 12.2 g more than the peak magnitude of impact acceleration in the presence of single flat of same size on all four wheels of the front bogie as shown in Fig. 5.16 (a). This difference can be attributed to the excitation of the bogie roll motion. In case of flats on left wheels of the first and second wheelset, the displacement of the left wheels of both first and second wheelsets are more while the flat-free right wheels of first and second wheelsets remains same. These motions of the left wheels increase the peak wheel acceleration in case of single flat on left wheels of first and second wheelsets in phase. Furthermore, due to the presence of the flats on left wheels only the roll motion of the wheel is also excited, which contributes in increasing the magnitude of the peak wheel acceleration.

Figure 5.20 shows the effect of speed on peak wheel acceleration due to a single flat on left wheel and two in-phase flats on left wheels of first and second wheelsets. The results are shown for speed range of 20-140 km/h, where the flat length is varied from 30-80 mm. The figure clearly shows that the peak impact acceleration due to a single wheel flat is higher than the peak wheel acceleration due to the two in-phase flats on left wheels of first and second wheelset. This result is consistent for the selected speed range and the flat sizes. For a vehicle speed of 100 km/h and flat length of 70 mm, the difference in magnitude of peak acceleration can be as high as 13.25 g.

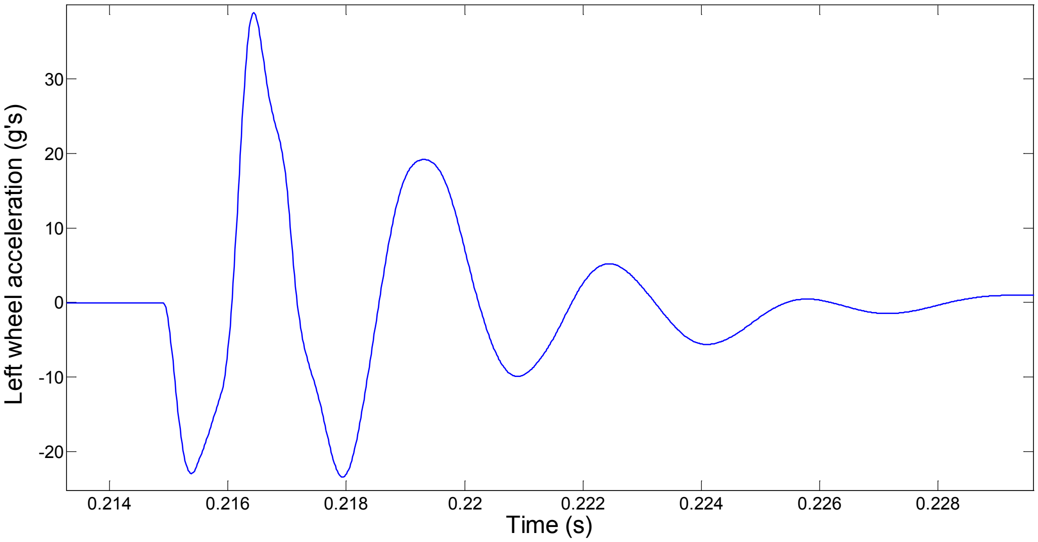

Fig. 5. 19: Time history of left wheel impact acceleration responses due to a single flat on left wheels of first and second wheelset of the front bogie in phase (bogie roll effect).

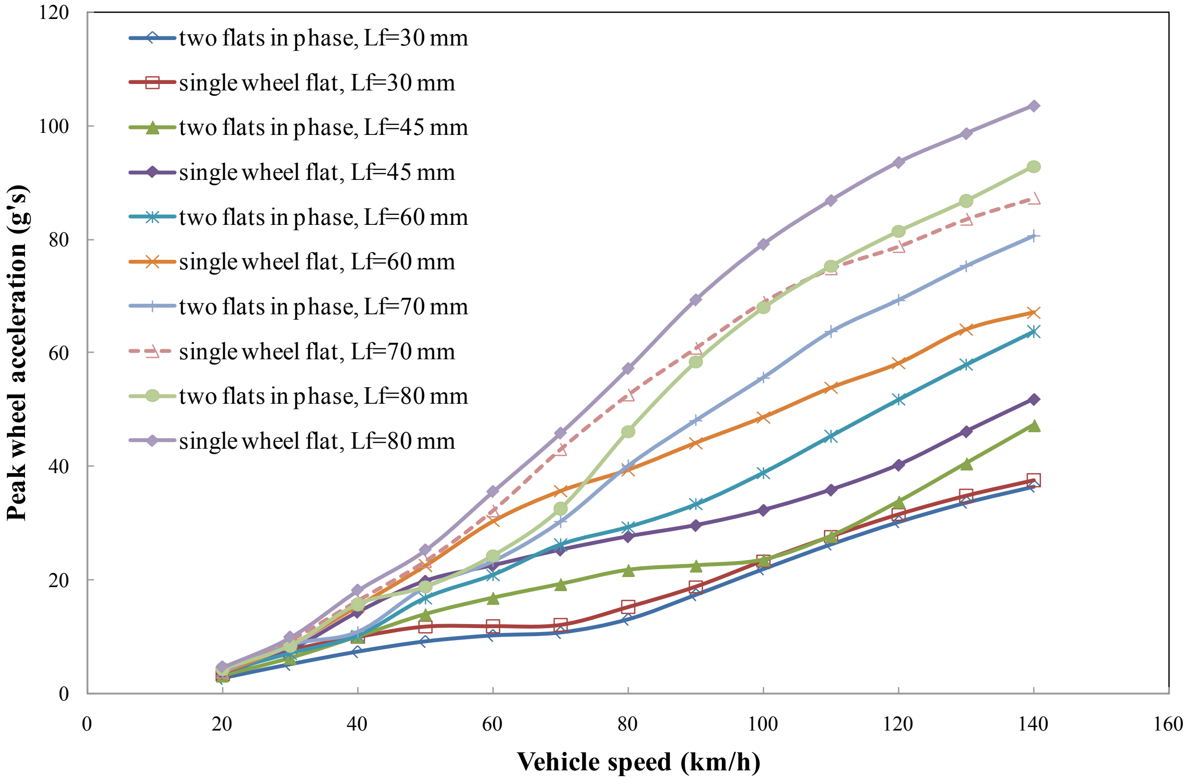

Fig. 5. 20: Effect of speed on peak wheel impact acceleration due to a single flat on left wheel and two flats on left wheels of first and second wheelset in phase.

5.8 SUMMARY

In this chapter, the developed coupled vehicle-track model is employed to study the wheel impact acceleration responses caused by multiple wheel flats. Effect of multiple wheel flats on peak wheel acceleration is investigated with different sizes and relative positions of the flats. In case of two out-of-phase flats, the study shows that there are two distinct peaks in acceleration responses of both left and right wheel due to the presence of two flats. However, the peak magnitudes of the acceleration differ due to direct and cross wheel flats. This study shows that although this cross wheel impact acceleration is considerably less than that of the direct wheel impact acceleration, its effect can be significant in high-speed condition.

In investigations of impact acceleration due to multiple flats with the three-dimensional vehicle-track model, it is observed that the presence of two flats on same location of different wheels within same or different wheelsets has considerable effect on peak wheel-rail impact load. This study shows that the presence of a single flat in all four wheels of front bogie in phase induces impact acceleration less than the impact acceleration induces by a single wheel flat of same size, which can be attributed to the symmetry of the bogie about the central lateral axis due to the presence of flats on all four wheels at same location.

This study further shows that the magnitudes of the peak wheel impact accelerations produced by two in-phase flats within same wheelset are lower than the impact acceleration produced by a single flat of same size on one wheel for all vehicle speeds. This can be attributed to the bogie pitch motion effect, which is excited due to the presence of two in-phase flats. It is also obvious from this study that due to the excitation of bogie roll motion, the impact acceleration produced by two in-phase flats on different wheels of opposite wheelset is lower than the impact acceleration produced by a single flat of same size on one wheel for all vehicle speeds. The study further illustrates that the magnitudes of the direct wheel impact acceleration generated due to multiple flats either in the same or different wheels are same to that generated by single wheel flat when the flats are far away from each other.

CHAPTER 6

DEVELOPMENT OF A SMART WHEELSET

6.1. INTRODUCTION

Formation of wheel flats on railway wheel profile is a major concern for railway industry because of its effect on safe, secure and efficient operation of the railway. Due to the increases in speed and axle load of the modern railway vehicle, presence of these defects either in wheel or in rail can lead to excessive impact force leading to an accelerated deterioration of the vehicle or track structure components, such as wheelsets, bearings, rails, and sleepers. It is estimated that the railway industry in North America is currently spending nearly $90 millions annually to replace 125,000 wheels due to wheel defects [8]. When a wheel flat exceeds a certain length and depth, their impact forces become unacceptably high to keep operating in that condition. Presence of undetected wheel flats can thus cause untimely on service failure of the railway vehicle, requiring suspension of the operation and on-site replacement of wheelsets which is very costly. Many defects worsen gradually and can be repaired or replaced before they reach unacceptable level. In order to facilitate in-time maintenance of the vehicle, it is thus necessary to detect and monitor the development of wheel defects so that its replacement or repair can be properly scheduled. An automatic wheel defect detection system will allow for train maintenance schedule to be done as indicated by the condition of the wheels, rather than just based on past experience or regulations.

Industries have been looking for improved means to identify defective wheels for several decades. The most primitive way to detect the wheel defects is by physical inspection of the train by inspectors. Over the years, numerous techniques and tools have been developed to automate the detection of wheel defects. Some of these include, acoustic, optical and laser-based detection technology [161, 162, 168, 169]. In these detection systems, the variations of the signals in the form of sound, light, or laser beam are detected through the detectors. In case of acoustical detection system, the sound signal can be influenced by surrounding noise and therefore is not considered as accurate as necessary in railway operation. Wheel flat detections can also be carried out by measuring the dynamic force or acceleration of the track under the wheel. Belotti et al. [156] and Yue et al. [157] have presented a wheel-flat diagnostic tool by using wavelet transform method. In these studies, the detection of the wheel flats is carried out through the measurement of peak acceleration by the use of several accelerometers placed in the fixed position of the rail. These along with other measurement techniques are referred to as way-side measurements, where the measurements are taken at a fixed instrumented location of the track as the train passes over the section. Some of the drawbacks of such system include the fact that the instrumented section can be far away from the maintenance facility. The detection system may not accurately identify the wheel with the defect. The measurement may miss the wheel defect as the impact due to defect may occur at different location with respect to the instrument. In general way-side detection systems are known to exhibit poor repeatability and unreliable as they often generate false warning or miss the defect. Most of these limitations of way-side detection system based on instrumented track can be overcome by developing an instrumented smart wheelset that will have an on-board measurement system, capable of monitoring its health in real time.

A smart wheelset is an instrumented wheelset that continuously monitors its dynamic response and uses it to identify if and when a defect is developed on the wheel profile. It also has the capability to establish the length and depth of the defect or a flat under all operation conditions. The methodology for the smart wheelset is developed based on the extensive study carried out in this investigation examining the responses of railway vehicle system due to existence of wheel flats. Response acceleration of wheelsets being the most convenient variable is selected for measurements. In this technique, two bearings of the wheelset will be fitted with low cost accelerometers that does not require the wheel to be machined, thus the structural integrity will not be altered. The major challenge in developing the smart wheelset is in formulating the methodology in using the acceleration signals in real time to establish the existence of a defect, the type of defect and the extent of the defect at all operating conditions. The operating condition of a railway vehicle can vary widely as they carry wide range of loads at a wide range of speeds. Since many factors strongly influence the response of railway wheelset depending on the flat size, the system must predict the flat size using acceleration signal under all conditions. It is, thus, required to establish, examine and incorporate the relationships between all the operating parameters that are related to the change in acceleration of the defective wheel.

In this chapter, development of a smart wheelset for continuous in-time automatic detection of wheel defects is developed and described that can be realized through the use of an on-board measurement technique. The effects of wheel flat size on peak wheel acceleration at different vehicle speeds are identified. Simulations are carried out for different axle loads including empty and fully loaded car conditions. Finally, the relation between the peak wheel acceleration, vehicle speed and the wheel flat size is formulated for selected axle loads that can be readily applied towards the development of a smart wheelset. The objective in this formulation for smart wheelset is to measure the peak acceleration signal that should be an indicator for flat size regardless of vehicle speed and axle weight.

6.2. FORMULATION OF INDICATOR AS A FUNCTION OF SPEED

Throughout the present investigation it has been shown that speed has a very significant effect on the peak impact force and acceleration generated due to a flat within a wheel profile. The effect of speed must therefore be an integral part in the formulation of a smart wheelset. The maximum allowable speed of a freight car in Canada is 108 km/h [9]. Thus, for this investigation, the influences of selected parameters on the nature of impact accelerations are evaluated in 0-140 km/h speed range in order to ensure that the study is valid for future trends. The range of flat is chosen in accordance with the threshold values for wheel removal by different railway organizations. The American Association of Railroad (AAR) [144] criteria for removal of wheel from service requires that a railway car wheel with a 50.8 mm long single flat or two 38.1mm long adjoining flats cannot continue to be in service. According to Swedish Railway, the condemning limit for single wheel flat is 40 mm long and 0.35 mm deep [17]. Transport Canada safety regulations [145] require that a railway company do not keep a car in service if a wheel has a slid flat spot that is more than 63.50 mm in length or two adjoining flat spots each of which is more than 50.80 mm.

In order to incorporate the stipulated guidelines, this study considers the flat length size in the range of 30-80 mm, while the flat depths are changed automatically by following the relation between the flat length and depth given by Eqn. 3.51. Simulations are carried out for a single wheel flat assigned at the left side of the first wheelset. The parameters used for the simulations are same as those presented in Tables 4.2 and 4.3. In Parametric studies, only one parameter and its effects are varied while the other parameters are kept same as their nominal value. All the results presented in this section correspond to the peak value of the acceleration level at the bearing location of the wheel with defect predicted by a simulation.

Figure 6.1 shows the trend for peak wheel acceleration with vehicle speed due to a single wheel flat on left wheel of first wheelset for different flat lengths and full load. A fully loaded vehicle corresponds to a wheel load of 103 kN. As the results show, the relationships between the vehicle speed and peak wheel acceleration for a given flat are similar to those obtained as peak impact force presented in chapter 4. From these results it is observed that there is a clear trend for increase in the peak acceleration as the speed is increased while the sensitivity to flat size increases with increase in speed. It is further observed that the relationship between the peak wheel acceleration and vehicle speed can be effectively expressed by a third order polynomial function with real coefficients. For example, the third order polynomial function for a flat length of 60 mm, can be expressed as:

$$Y = -1.98e\text{-}5*v^3 + 0.0039*v^2 + 0.324*v \qquad (6.1)$$

where, Y is the peak wheel acceleration in g's and v is the vehicle speed in km/h. These polynomial functions for each of the flat sizes are also presented in Figure 6.1 for comparison.

A close examination of all the polynomials obtained for different flat size in Figure 6.1 further reveals that there exist a trend for the coefficients of v^3, v^2 and v as a function of flat size. These coefficients of v^3, v^2 and v as a function of flat lengths are shown in Fig. 6.2. Figures 6.2 (a) to (c) show each of these coefficients along with a third order polynomials that can represent the trend for the change in each of the coefficients as a function of flat size (L_f). In order to incorporate the effect of flat size within the expression for acceleration as a function of speed, the fist, second and third coefficients in Equation 6.1 are replaced by the polynomials of L_f obtained from Figures 6.2 (a), (b) and (c), respectively. In doing so, the final expression for the peak acceleration as a function of velocity, v for different flat size can be predicted using:

$$A_{peak}=(2.60e\text{-}9*L_f^3-4.62e\text{-}7*L_f^2+2.42e\text{-}5*L_f-3.7e\text{-}4)*v^3+(-5.25e\text{-}7*L_f^3+9.60e\text{-}5*L_f^2-0.005*L_f+0.081)*v^2+(2.34e\text{-}5*L_f^3-0.0044*L_f^2+0.25*L_f-3.98)*v \quad (6.2)$$

where, A_{peak} is the peak acceleration due to a wheel flat in g's, L_f is the wheel flat length in mm, and v is the vehicle speed in km/h.

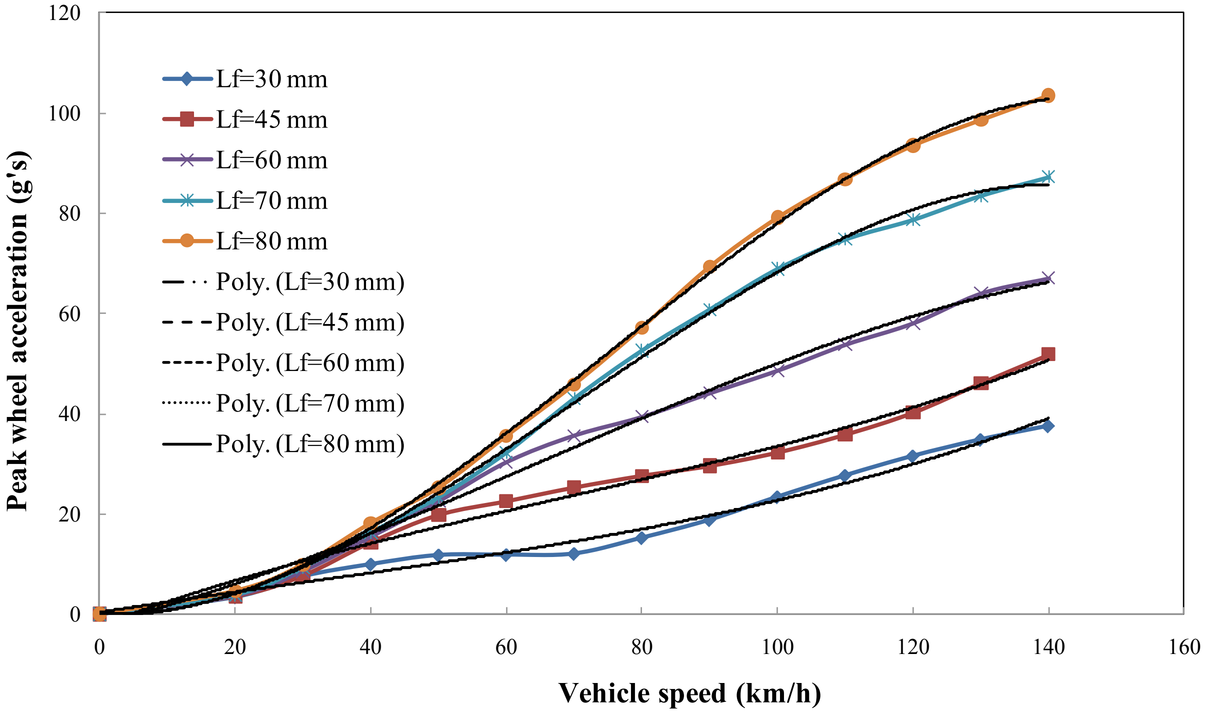

Fig. 6. 1: Relationship between the speed of the vehicle, peak wheel acceleration and their corresponding third order polynomials for different flat lengths for fully loaded condition.

In order to examine the effectiveness of Equation (6.2) obtained using compound polynomials, it is utilized to obtain the peak acceleration as a function of speed for different flat sizes and compared with the best fit lines derived from simulations in Figure 6.1. These results presented in Figure 6.3 show that although there is slight difference for some flat sizes, the percentage difference is negligibly small. In order to improve the results, further attempts were made using higher order polynomials. The results, however, showed that improvement is negligible for the complexity added by introducing higher order polynomials.

The Equation (6.2) thus established above can be readily used to estimate the flat length L_f, knowing the vehicle forward speed, v, for a fully loaded freight train. When the flat length is known, the flat depth can be easily identified by their relationship as given by Eqn. (3.51).

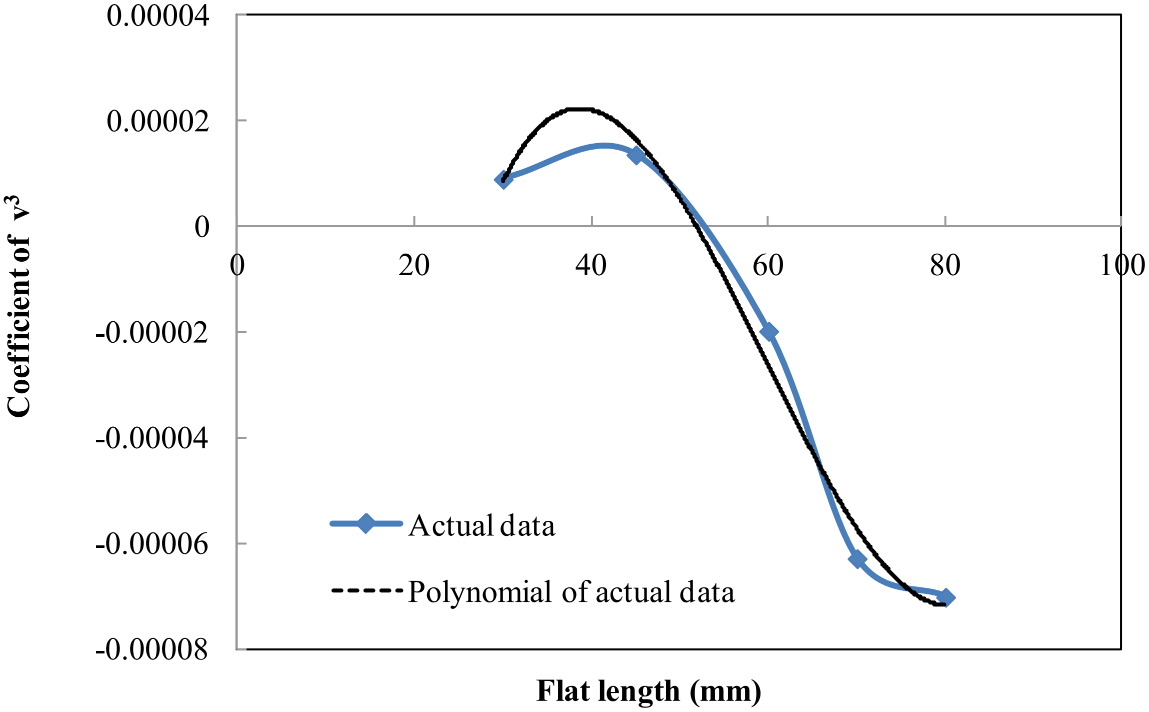

(a)

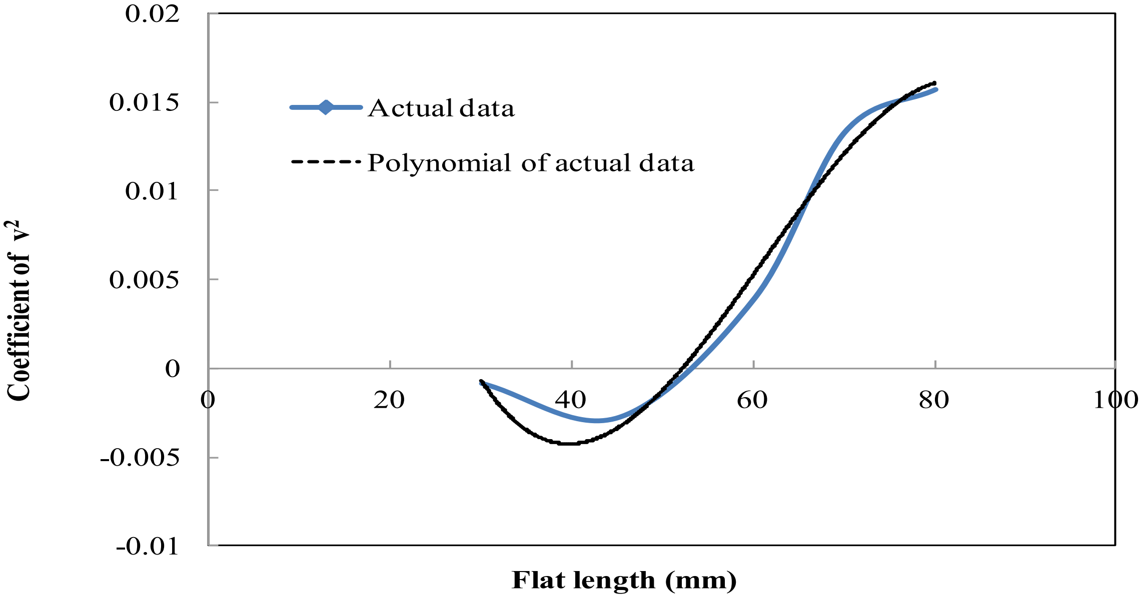

(b)

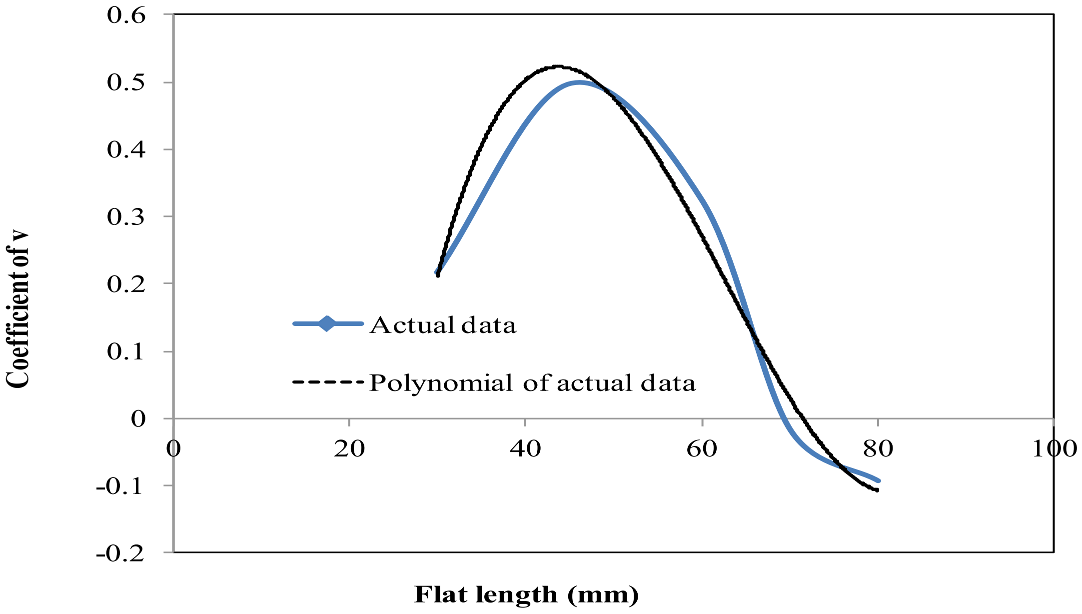

(c)

Fig. 6. 2: The relationships between the coefficients of the polynomials obtained from best fit lines in Figure 6.1 as a function of flat length along with their representation by a third order polynomial, (a) coefficient of v^3; (b) coefficient of v^2; (c) coefficient of v.

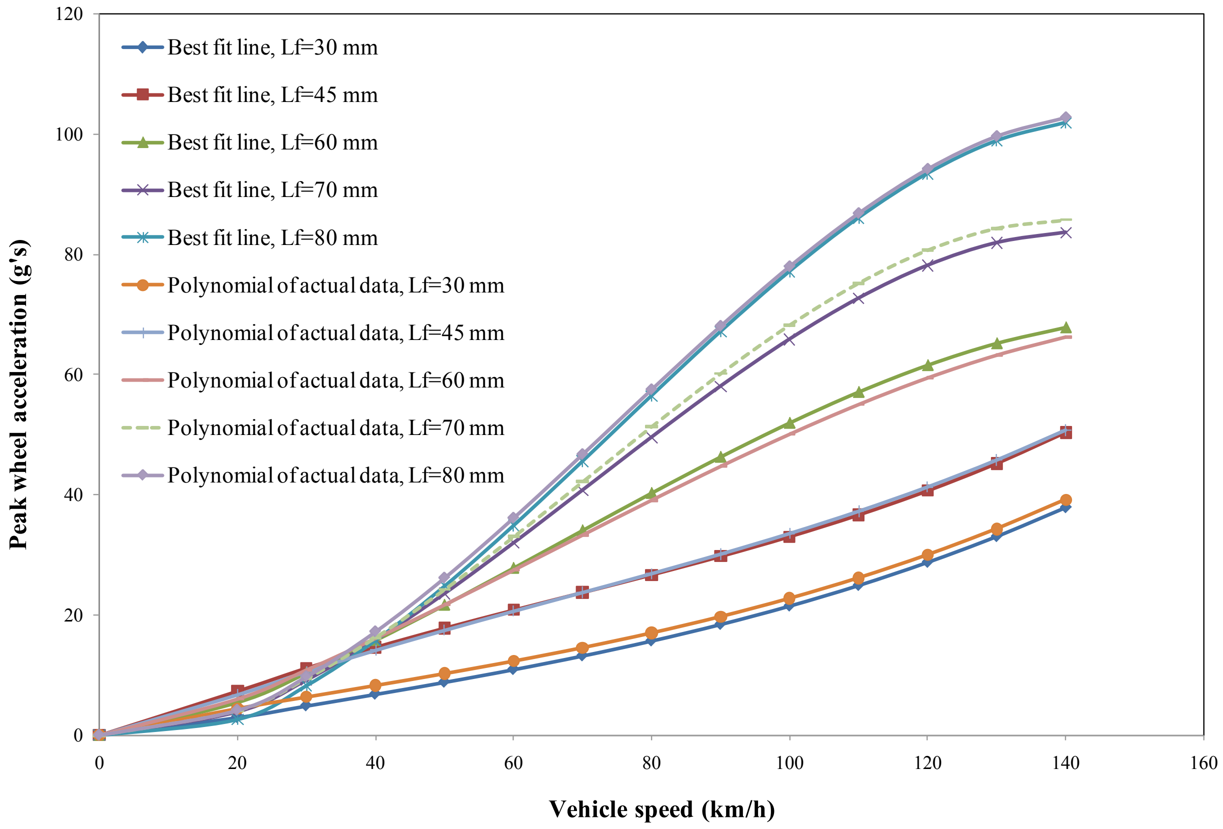

Fig. 6. 3: Comparison of best fit peak acceleration generated by simulation (Figure 6.1) with those predicted using Equation (6.2) as a function of speed for different flat lengths.

A modern railway freight train typically may consist of over 100 cars, each with four wheelsets. Such a train will require 800 sensors or accelerometers simultaneously being monitored. It is therefore desirable to minimize the costs of sensors and processors. One further attempt is thus made to simplify the Equation (6.2) by reducing the number of coefficients for the flat size. For this the results in Figure 6.2 are repeated using a second order polynomial rather than the third order used earlier. These results showing comparison of the coefficients as function of flat length with approximation by a second order polynomial are presented in Figure 6.4. Similar to Equation (6.2), replacing the three coefficients in Equation (6.1) by flat size polynomial of Figure 6.4 (a) to (c), a simplified equation for acceleration can be established as:

$$A_{peak} = (-3.37e\text{-}8 \cdot L_f^2 + 1.857e\text{-}6 \cdot L_f - 1.184e\text{-}6) \cdot v^3 + (9.055e\text{-}6 \cdot L_f^2 - 6.112e\text{-}4 \cdot L_f + 8.437e\text{-}3) \cdot v^2 + (-5.198e\text{-}4 \cdot L_f^2 + 0.0486 \cdot L_f - 0.732) \cdot v \tag{6.3}$$

where, A_{peak} is the peak acceleration due to a wheel flat in g's, L_f is the wheel flat length in mm, and v is the vehicle speed in km/h.

The simulated relationships between the vehicle speed and the peak wheel acceleration expressed by the best fit line as shown in Figure 6.1 and those predicted using Equations (6.3) are shown in Figure 6.5 for a wheel load of 103 kN. These results when compared to those presented in Figure 6.3 reveal noticeable superiority of Equation (6.2) over that of (6.3) and thus use of Equation (6.2) is recommended for the development of smart wheelset concept.

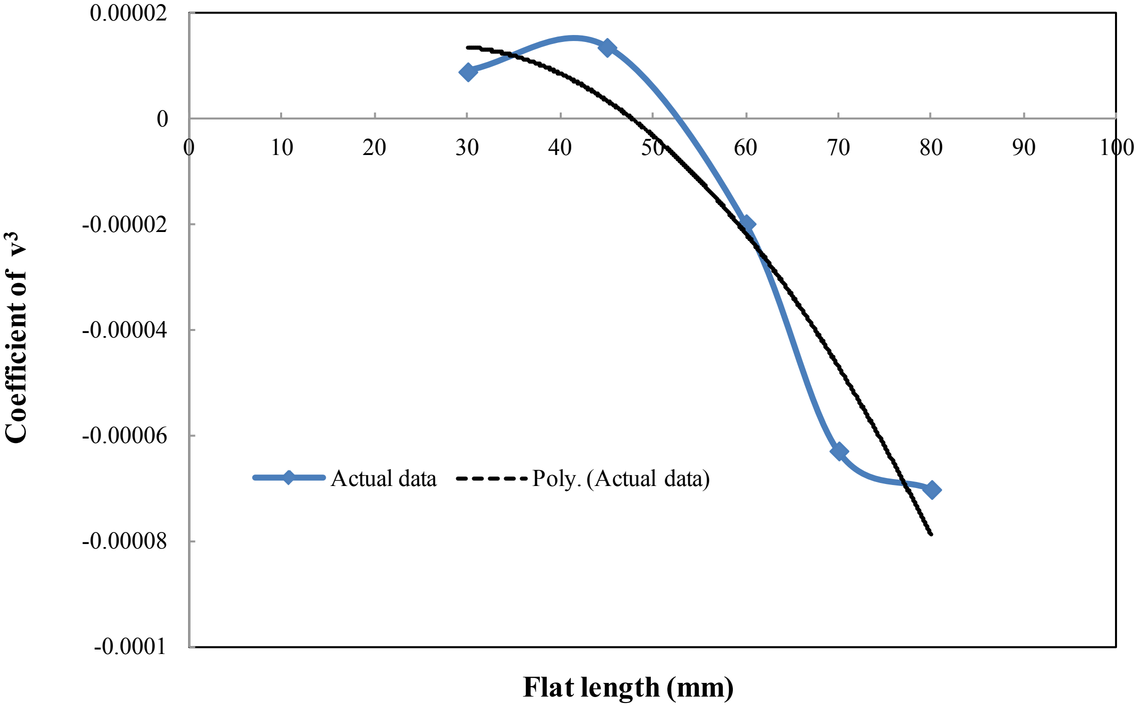

(a)

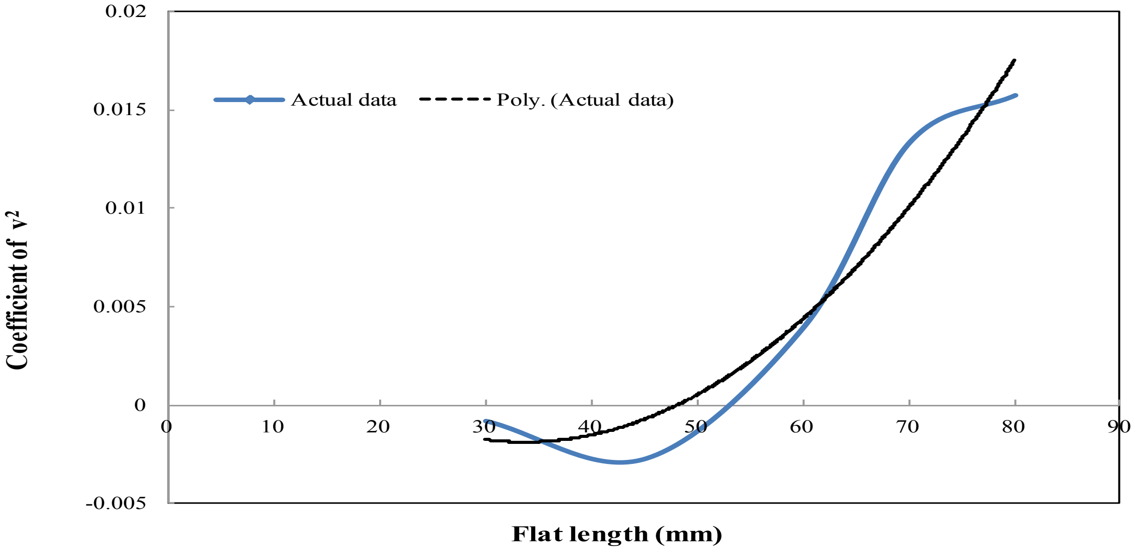

(b)

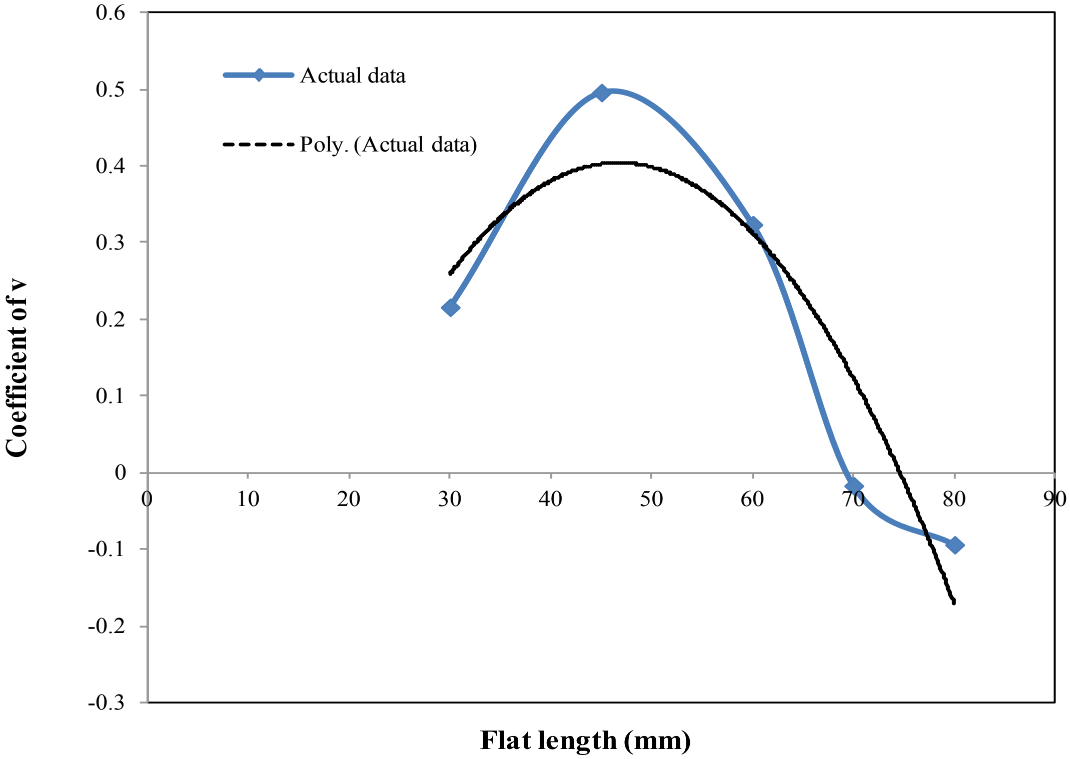

(c)

Fig. 6. 4: The relationships between the coefficients of the polynomials obtained from best fit lines in Figure 6.1 as a function of flat length along with their representation by a second order polynomial, (a) coefficient of v^3; (b) coefficient of v^2; (c) coefficient of v.

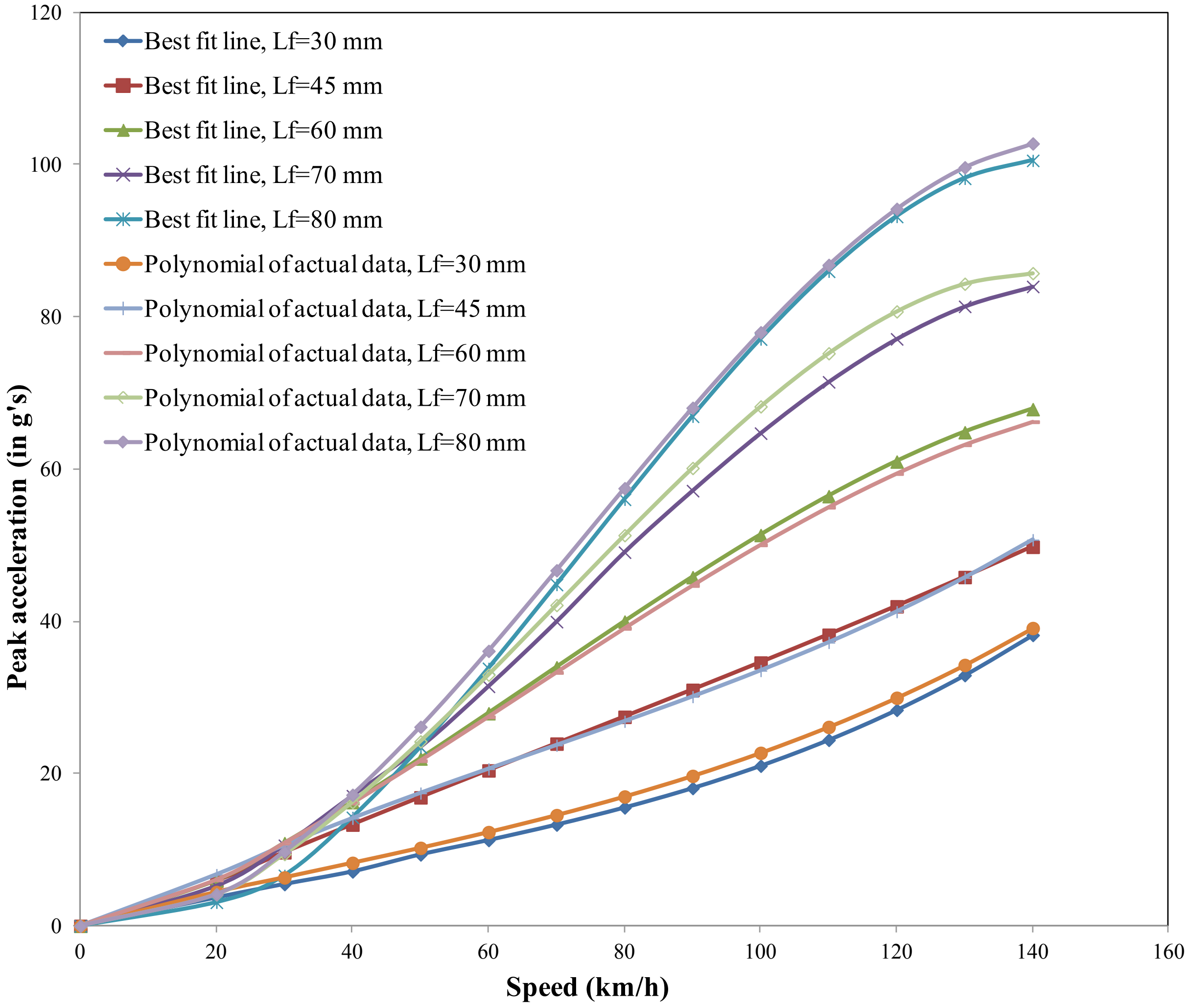

Fig. 6. 5: Comparison of best fit peak acceleration generated by simulation (Figure 6.1) with those predicted using Equation (6.3) as a function of speed for different flat lengths.

The results presented thus far in this section towards the development of smart wheelset for freight trains consider response acceleration as vehicle speed is changed while the vehicle weight represent a fully load car. It is, however, known that the axle load also plays a very significant role on the magnitude of impact loads generated due to wheel flats. It is thus expected that the load will also strongly influence the acceleration responses. For a smart wheelset to be useful, it must also be effective at all wheel loads. This will introduce additional challenge in the development of smart wheelset not only because of the effect of load but also due to difficulty in determining the static axle load at each wheel. The following section examines the issues of wheel loads.

6.3. FORMULATION OF INDICATOR AS A FUNCTION OF LOAD

During the operation of a freight car, its load can fluctuate from empty car to the fully loaded condition. For a given freight car, the axle or wheel loads corresponding to empty as well as when fully loaded condition are well defined or can be assumed to be a known parameter. Since the axle load must be taken into account in the formulation of model for smart wheelset, it is suggested that the model only consider either empty or fully loaded scenario. This will simplify the design of the processor significantly while limiting the capability of smart wheelset to detect defects only when operating under those conditions. Such approach is reasonable since determination of wheel load at other loading conditions will be difficult. It is also reasonable to assume that a freight train will operate more frequently when either empty or fully loaded.

Similar to the smart wheelset developed in section 6.2 for fully loaded condition, the procedure is repeated here in order to develop a new relationship for an empty car. Literature review shows that the variation in wheel load is in the range of 34.325-117.68 kN in Sweden [17], and 3.11-146.8 kN in Canada [8]. In this study, a fully loaded car is assigned a static wheel load of 103 kN and was the parameter used in section 6.2. For an empty car, a static load of 5 kN will be assigned for each wheel. These are in line with load parameters commonly used in the literature [8, 9, 17].

Similar to section 6.2, simulations are further carried out, for an empty car load in order to establish the relationship between the peak wheel acceleration, vehicle speed and wheel flat length. Figure 6.6 shows the simulated relationship between the vehicle speed and peak acceleration at the wheel bearing location of the wheel with a flat for different flat sizes. These results show that for very low static wheel loads, the dynamic response is significantly more complex than those predicted for very high loads. In these cases, there is more than one peak that can be attributed to natural frequencies of the vehicle and vehicle–track systems when the loads are low. These cases further show that the peak acceleration has a decreasing tendency at very high speeds, which is lower and more significant for smaller flat lengths.

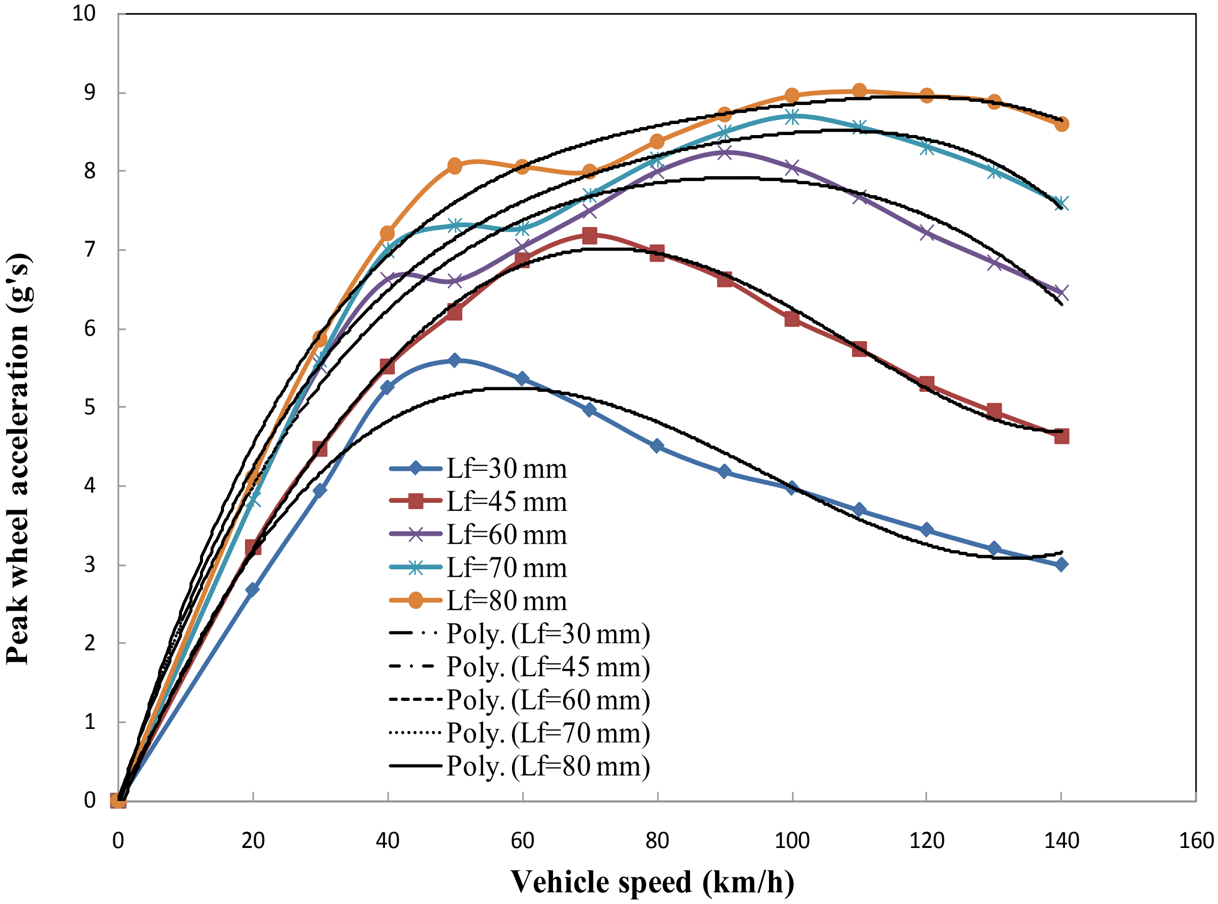

Fig. 6.6: Relationship between the speed of the vehicle, peak wheel acceleration and their corresponding fourth order polynomials for different flat lengths for empty car.

In order to account for such variations, the best fit of these trends are obtained using a fourth order polynomials instead of third order used for fully loaded cars in Section 6.2. These best fit lines are also presented in Figure 6.6 for direct comparison with the simulated results. As an example, the polynomial generated for flat length of 60 mm, the fourth order polynomial function for empty car wheel can be expressed as:

$$Y = -5.68e\text{-}8*v^4 + 2.03e\text{-}5*v^3 - 0.003*v^2 + 0.25*v \qquad (6.4)$$

where, Y is the peak wheel acceleration in g's and v is the vehicle speed in km/h.

The coefficients of v^4, v^3, v^2 and v in the best fit line for each of the curves representing a flat size in Figure 6.6 are next examined in order to establish a trend. For this the coefficients are plotted as a function of flat size in Figure 6.7. The best fit lines for each of these coefficients are next expressed using four different third order polynomials. These results are shown in Figures 6.7 (a) to (d). The third order polynomials are finally used to replace the coefficients in Equation (6.4) which yields a relationship between the peak wheel acceleration, vehicle speed and wheel flat length for empty car and is expressed as:

$$A_{peak}=(1.02e\text{-}11*L_f^3 - 1.72e\text{-}9*L_f^2 + 8.91e\text{-}8*L_f - 1.38e\text{-}6)*v^4 +(-2.84e\text{-}9*L_f^3 + 4.87e\text{-}7*L_f^2 - 2.56e\text{-}5*L_f + 4.13e\text{-}3)*v^3 +(2.38e\text{-}7*L_f^3 -4.2e\text{-}5*L_f^2 + 2.22e\text{-}3*L_f - 0.038)*v^2 + (-5.64e\text{-}6*L_f^3 + 9.93e\text{-}4*L_f^2 - 0.053*L_f + 1.05)*v \qquad (6.5)$$

where, A_{peak} is the peak acceleration due to a wheel flat in g's, L_f is the wheel flat length in mm, and v is the vehicle speed in km/h.

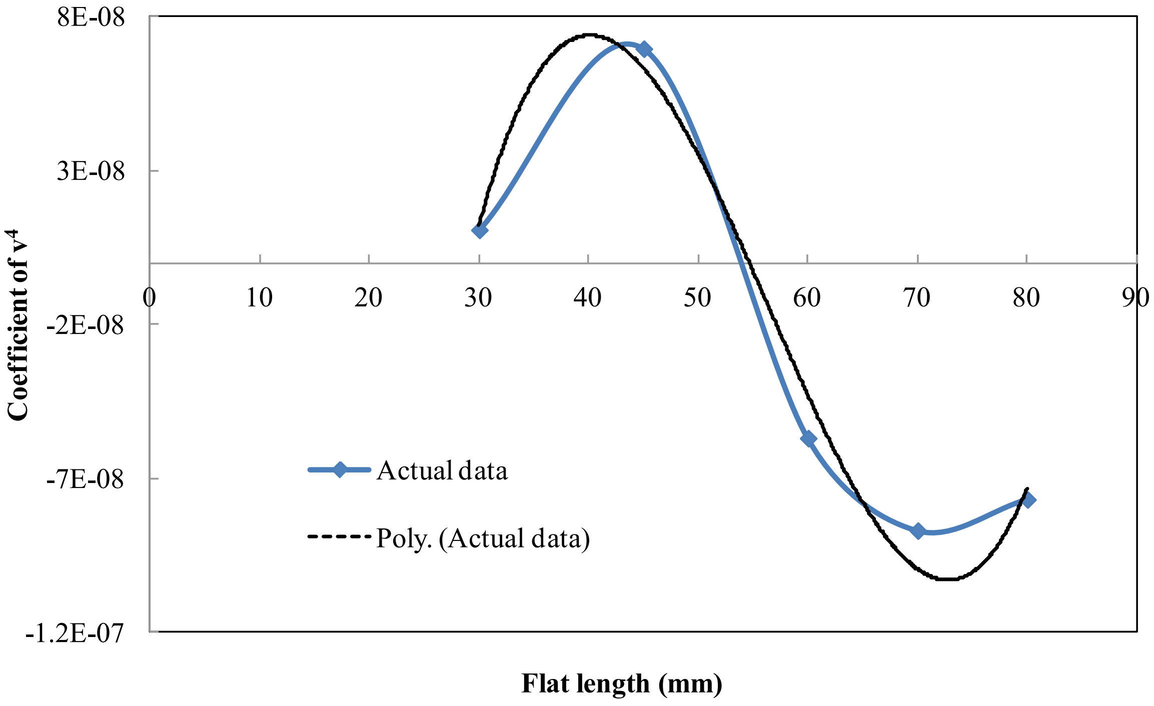
8E-08
3E-08
-2E-08
-7E-08
-1.2E-07
0
10
20
30
40
50
60
70
80
90
Coefficient of v^4
Flat length (mm)
Actual data
Poly. (Actual data)

(a)

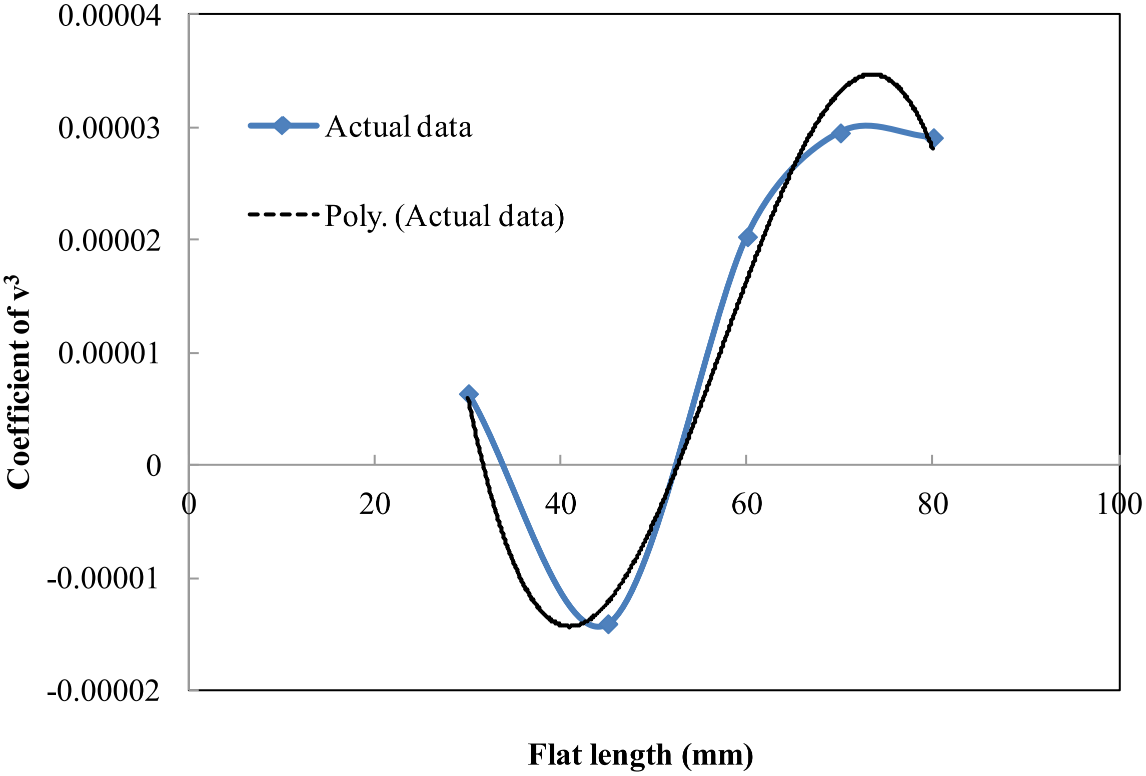
0.00004
0.00003
0.00002
0.00001
0
-0.00001
-0.00002
0
20
40
60
80
100
Coefficient of v^3
Flat length (mm)
Actual data
Poly. (Actual data)

(b)

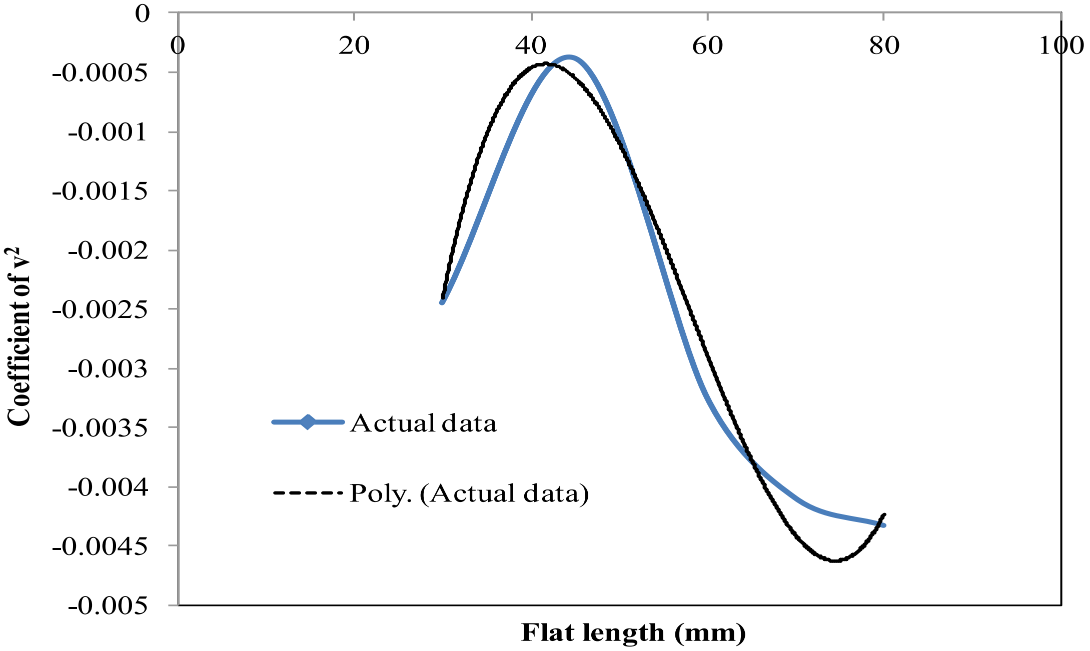

(c)

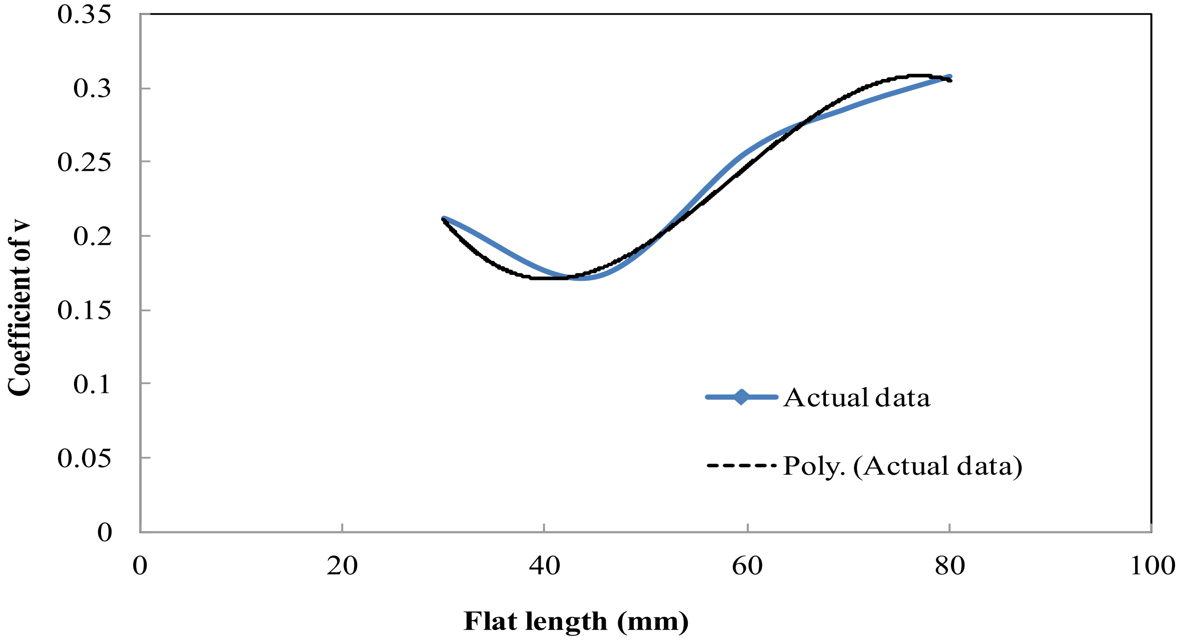

(d)

Fig. 6. 7: The relationships between the coefficients of the polynomials obtained from best fit lines in Figure 6.6 as a function of flat length along with their representation by a fourth order polynomial: (a) coefficient of v^4; (b) coefficient of v^3; (c) coefficient of v^2; (d) coefficient of v.

Similar to the fully loaded condition of the vehicle, if the peak wheel acceleration and vehicle speed are known, we can easily find the wheel flat length from Eqn. (6.5) for operation of an unloaded car. Figure 6.8 shows the relationships between the vehicle speed and the peak wheel acceleration obtained by the best fit line of simulations as shown in Figure 6.6, and the compound polynomial derived in Equation (6.5). The results show the effectiveness of the compound equation in predicting the peak acceleration for variation of speeds and flat sizes for empty operation. It is, however, easy to foresee that the effectiveness of Equation (6.2) to predict flat size of a fully loaded car will be superior to that of Equation (6.5) for prediction of flat size on an unloaded wheel. This is due to the fact that multiple peaks are generated for empty cars which will require higher order polynomial for generating better best fit lines. The results generated using Equation (6.5) presented in Figure 6.8 clearly cannot predict these peaks and may not be accurate in predicting flat size from the peak acceleration levels.

In order to overcome this limitation, polynomials with sixth order are considered in order to represent the relationship between the peak wheel acceleration and vehicle speed. The results obtained with sixth order polynomials are shown in Fig. 6.9. It can be seen that sixth order polynomials can more accurately represent the actual peak wheel acceleration as a function of velocity for only low flat sizes. On the other hand, it fails to predict the peaks accurately for larger flats when multiple peaks are generated. It is, thus, logical to consider fourth degree polynomials to represent actual relationship between the peak wheel acceleration and vehicle speed, as it is shown in Fig. 6.8.

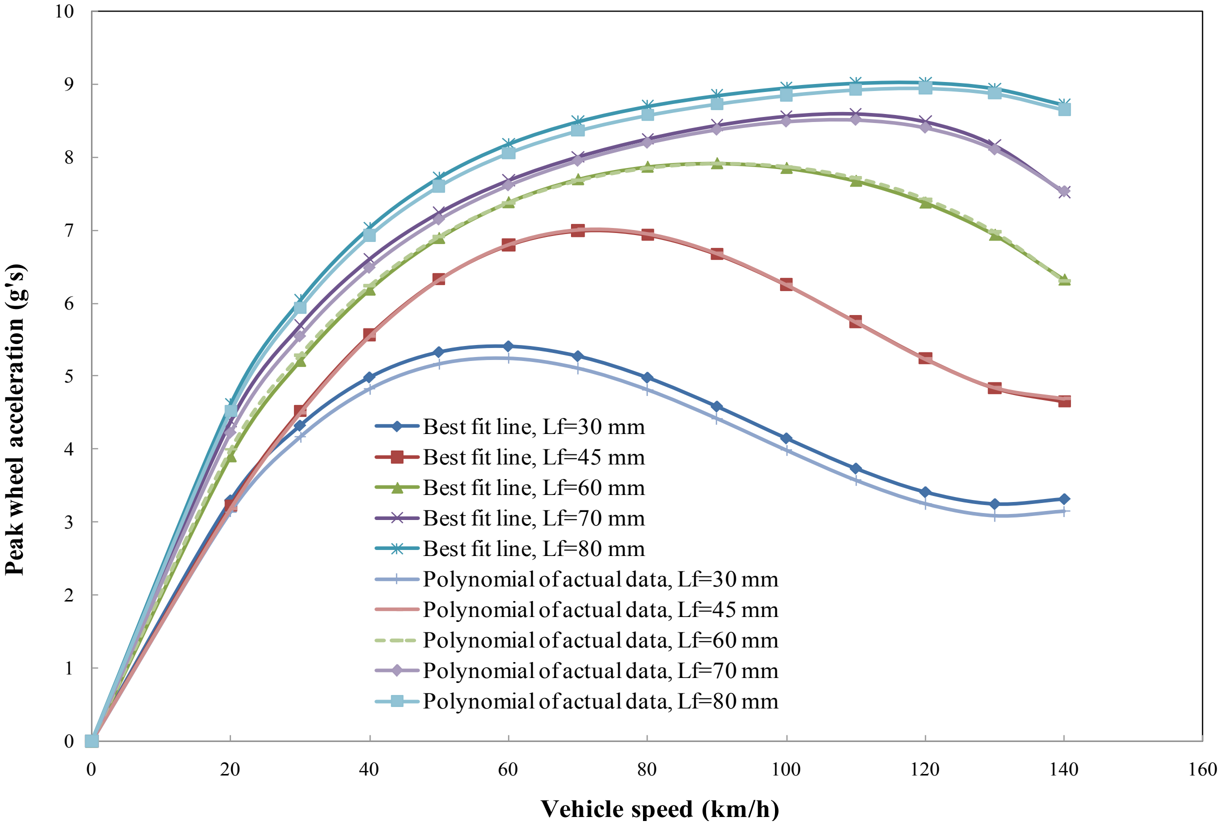

Fig. 6. 8: Comparison of best fit peak acceleration generated by simulation (Figure 6.6) with those predicted using Equation (6.5) as a function of speed for different flat lengths.

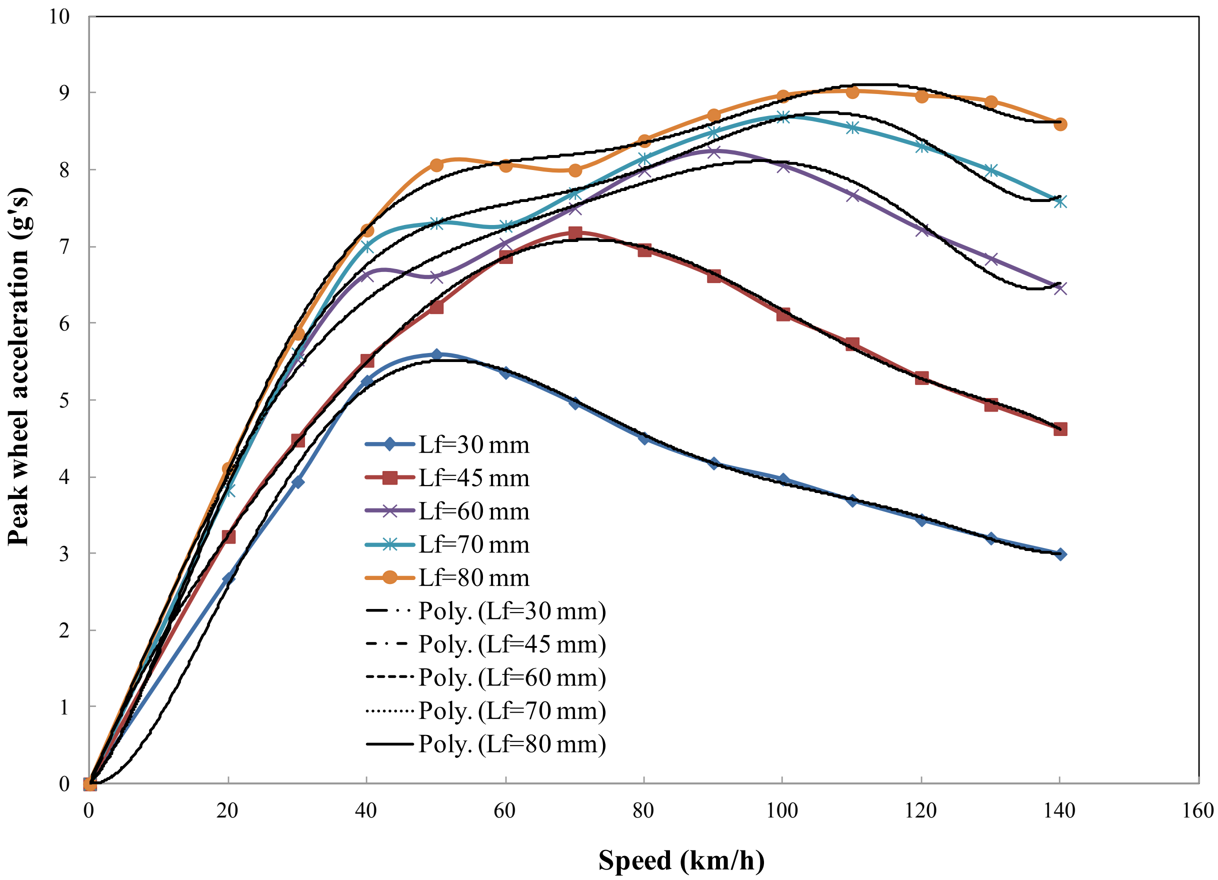

Fig. 6. 9: Relationship between the speed of the vehicle, peak wheel acceleration and their corresponding sixth order polynomials for different flat lengths for empty car.

6.4. FINAL PROPOSED MODEL FOR SMART WHEELSET

As presented in the previous sections, acceleration responses are the simplest among the different response variable that can be used for detecting wheel defects. It is also reasonable to assume that a freight train will operate either empty or fully loaded conditions at most of the times. Therefore the smart wheelset formulations presented in the previous sections can be practically implemented for detection of wheel flats. The procedure will involve selecting the appropriate equation based on the loading condition being either empty or fully loaded. Based on the present investigation and parameters used for the vehicle, the proposed prediction models are:

For empty condition:

$$A_{peak}=(1.02e\text{-}11*L_f^3 - 1.72e\text{-}9*L_f^2 + 8.91e\text{-}8*L_f - 1.38e\text{-}6)*v^4 +(-2.84e\text{-}9*L_f^3 + 4.87e\text{-}7*L_f^2 - 2.56e\text{-}5*L_f + 4.13e\text{-}3)*v^3 +(2.38e\text{-}7*L_f^3 -4.2e\text{-}5*L_f^2 + 2.22e\text{-}3*L_f - 0.038)*v^2 + (-5.64e\text{-}6*L_f^3 + 9.93e\text{-}4*L_f^2 - 0.053*L_f+ 1.05)*v \tag{6.6}$$

and,

For fully loaded condition:

$$A_{peak}= (2.60e\text{-}9*L_f^3- 4.62e\text{-}7*L_f^2 + 2.42e\text{-}5*L_f - 3.7e\text{-}4)*v^3 + (-5.25e\text{-}7*L_f^3+9.60e\text{-}5*L_f^2 - 0.005*L_f + 0.081)*v^2 + (2.34e\text{-}5*L_f^3 -0.0044*L_f^2 + 0.25*L_f - 3.98)*v \tag{6.7}$$

where, A_{peak} is the peak acceleration due to a wheel flat in g's, L_f is the wheel flat length in mm, and v is the vehicle speed in km/h.

In the above equation, if we know the peak wheel acceleration due to a flat that can be measured by an accelerometer we can easily obtain the wheel flat length knowing the velocity of the vehicle. For example, if an empty train is moving at a speed of 80 km/h and the repeated peak acceleration measured by an accelerometer on a wheel bearing is 7.9 g, the length of the flat can be obtained from Eqn. (6.6) as 60 mm.

Similarly, if a fully loaded train is moving at a speed of 80 km/h and the repeated peak acceleration measured by an accelerometer on a wheel bearing is 40.3 g, the length of the flat can be obtained from Eqn. (6.7) as 60 mm. It should be noted that for each peak acceleration value, Eqns. (6.6) and (6.7) will give three flat lengths out of which one will be positive and two other will be negative. As wheel flat length cannot be negative, the positive value will be used as the predicted flat size. Once the flat size is determined, the processor can be designed to further determine if and when the wheel should be maintained or replaced based on existing guidelines.

6.5. SUMMARY

This chapter is devoted for development of a smart wheelset for detection of wheel flats from the relationship between the peak wheel acceleration, vehicle speed and flat sizes. Two different load conditions are considered assuming that the vehicle will operate on either empty or fully loaded conditions. The influences of vehicle speeds on the nature of peak impact accelerations are evaluated in 0-140 km/h speed range, which covers the maximum allowable speed of a freight car in Canada. The range of flat is chosen in accordance with the threshold values for wheel removal by different railway organizations, such as American Association of Railroad (AAR), Transport Canada, and Swedish Railway.

In this chapter, the effects of speed on peak wheel acceleration due to different flat sizes have been investigated for two common vehicle loading conditions. The models for smart wheelset are based on curve fitting of simulated results as a function of vehicle speed. A further curve fitting for the coefficients lead to a single compound equation that relates peak acceleration, velocity and flat length for either empty or a fully loaded condition of the vehicle. By using these relations, it is easy to identify the flat size developed at the wheel surface by knowing the peak wheel acceleration developed at the wheel with defects. Two numerical examples are given in order to show how to find the flat size from a knowledge of the peak wheel acceleration for a given vehicle speed. The effects of using different order polynomials for generating the final equation are also presented and discuss in this chapter. The development of a MEMS based accelerometer in order to detect the wheel flat automatically is further presented in next chapter.

CHAPTER 7

MODELING OF A MEMS BASED ACCELEROMETER FOR AUTOMATIC DETECTION OF WHEEL FLAT

7.1 INTRODUCTION

As described in chapter 1, wheel flat is the most common type of wheel defect encountered by railway industry. During sliding of the wheel on the rail, the part of the wheel tread could be removed causing a flat surface to form on the wheel profile. This surface irregularity causes impact loads on the rail and track structure as the wheel rolls. A damaged bearing that seizes can also cause skidding. Extreme flat wheels produce an audible "clank-clank" noise, due to the flat surface impacting the rail with each turn. This impact load induces high frequency vibration of the track and the vehicle components [183]. It has been suggested that excessive magnitude of the impact load may even shear the rail [7].

With continuing increases in the in the axle loads and operating speed, the wheel flats are becoming increasingly common. The high magnitude of impacts due to wheel flats, whether single or multiple, not only induce high magnitude impact force and stress on vehicle components but also to the rails and the sleepers [13, 15]. Wheel flats thus affect track maintenance and the reliability of the vehicle's rolling elements [130]. In addition to safety and economic considerations, these defects reduce passenger comfort and significantly increase the intensity of noise [120]. The high impact forces from a flat wheel cause stress in the rail, and in extreme cases can break the track or cause the wheel to jump off the track, resulting in a derailment. The contact forces are quite high; therefore, damage and wear are consistently relevant, mainly due to the great weights involved in the rail traffic and to the hardness of rail and wheel materials.

It is also clear that the continuous repetitions of impacts on rail, together with the high forces involved, cause rapid deterioration of both rolling and fixed railway equipments. If ignored or underestimated, the defects will wear out materials up to the breakdown. Various methods have been proposed for detecting flat wheels. One method is to employ inspectors to listen to the trains as they move through a particular location. Some flat wheels are found through routine inspections when the cars are being serviced. A wide range of sensors has been proposed for detecting flat wheels. These employ a range of technologies from optical systems that gauge the wheels in real time to sensors that look for vibrations and stress.

From the review of the relevant literature as discussed in chapter 1, it is evident that considerable efforts have been made to detect the presence of flats in the wheel. However, all these detection techniques utilize the railway track to mount the sensors, which requires the train to pass through that particular section of the rail in order to investigate the wheel flat. A train in operation that needs prompt investigation may not be possible by the present techniques i.e. continuous monitoring of all the wheels for detection of the flat is not possible. Furthermore, the present techniques require huge connections of wires to transfer the data from the test section to analysis center. One of the challenges for sensors is the need to operate remotely in harsh environments with exposure to wide temperature ranges as well as rain, snow, slush, dirt and grime.

The aim of this study is to design a MEMS based sensor that can be placed on a wheel bearing that will enable to detect the wheel defect continuously. This MEMS based accelerometer can sense and transmit the peak acceleration due to wheel flat automatically in terms of electrical signal for further analytical study. The three-dimensional coupled railway vehicle-track developed in chapter 3 is employed in this section in order to investigate the acceleration level at the wheel in presence of a single wheel flat. An idealized haversine wheel flat with the rounded corner is included in the wheel-rail contact model. A commercially available software COMSOL Multiphysics is employed in order to validate the developed accelerometer model. The simulated responses are compared with the results obtained from the calculation. Finally, the stability and maximum stress level of the accelerometer is estimated in order to ensure the safe operation of the sensor.

7.2 MODELING OF THE VEHICLE, TRACK, AND WHEEL FLAT

In order to design a MEMS based sensor to detect the acceleration caused by the presence of wheel flat, it is required to know first the acceleration level that the sensor should able to detect. The three-dimensional coupled vehicle-track model developed earlier in chapter 3 together with wheel flat model and nonlinear Hertzian contact model are employed here. The dynamic model used in this study to investigate the vehicle-track response in vertical direction consists of a 17-DOF vehicle model coupled with a 2-layer three-dimensional track system.

The detailed descriptions of the mathematical model combined with the equations of motion for vehicle and track system are given in chapter 3. The final forms of the equations for vehicle and track subsystem are as follows:

Vehicle subsystem: $\mathrm{M_V}\ddot{\mathrm{d}}_\mathrm{V} + \mathrm{C_V}\dot{\mathrm{d}}_\mathrm{V} + \mathrm{K_V}\mathrm{d}_\mathrm{V} = \mathrm{F_{VT}}$ (7.1)

Track subsystem: $\mathrm{M_T}\ddot{\mathrm{d}}_\mathrm{T} + \mathrm{C_T}\dot{\mathrm{d}}_\mathrm{T} + \mathrm{K_T}\mathrm{d}_\mathrm{T} = \mathrm{F_{VT}}$ (7.2)

Wheel-rail interface subsystem: $\mathrm{F_{VT}} = C_H(\Delta Z)^{3/2}$ (7.3) where, $\mathrm{M_V}$, $\mathrm{C_V}$ and $\mathrm{K_V}$ are mass, damping and stiffness matrices of the vehicle subsystem, respectively. $\mathrm{d_V}$, $\mathrm{\dot{d}_V}$, $\mathrm{\ddot{d}_V}$ are displacement, velocity and acceleration vectors of the vehicle subsystem, respectively. $\mathrm{F_{VT}}$ is the interface force vector between the vehicle and track subsystem. $\mathrm{M_T}$, $\mathrm{C_T}$ and $\mathrm{K_T}$ are mass, damping and stiffness matrices of the track subsystem respectively. $\mathrm{d_T}$, $\mathrm{\dot{d}_T}$ and $\mathrm{\ddot{d}_T}$ are displacement, velocity and acceleration vectors of the track subsystem respectively. ΔZ is the wheel-rail overlap in the vertical direction and C_H is the Hertzian constant.

The equations of motion of the vehicle system described by Eqn. (7.1) and of the track system shown by Eqn. (7.2) together with the Hertzian nonlinear contact model in Eqn. (7.3) describe the vertical dynamics of the coupled vehicle-track system. All these equations of motion are simultaneously solved together in order to obtained the acceleration level of the wheel in the presence of a flat.

7.3 DYNAMIC ANALYSIS OF WHEEL IN THE PRESENCE OF A FLAT

In order to design of an accelerometer, the peak acceleration of the wheel in the presence of a flat is required to be known for selection of the operating range of the accelerometer. Thus, the coupled vehicle-track system developed at the previous is simulated for a set of given parameters. In the simulation of the wheel-rail interaction, the contact is modeled with the consideration of the wheel lift-off from the rail. The nominal vehicle, track and flat parameters used for the simulations are presented in Tables 7.1 and 7.2.

Table 7. 1: Vehicle model parameters [8].

Notation	Parameter	Value
M_c	Car body mass	76150 kg
M_t	Bogie mass	1700 kg
M_w	Wheelset mass	1120 kg
J_{cx}	Mass moment of inertia of the car body about X axis	95576 kg-m^2
J_{cy}	Mass moment of inertia of the car body about Y axis	726462 kg-m^2
J_{bx}	Mass moment of inertia of the bogie about X axis	1600 kg-m^2
J_{by}	Mass moment of inertia of the bogie about Y axis	760 kg-m^2
J_{wx}	Mass moment of inertia of the wheelset about X axis	420.1 kg-m^2
K_P	Primary suspension stiffness	7.88×10^5 kN/m
C_P	Primary suspension damping	3.5 kN-s/m
K_S	Secondary suspension stiffness	5.32×10^3 kN/m
C_S	Secondary suspension damping	70 kN-s/m
l_c	Semi-longitudinal distance between bogies	5.18 m
l_b	Semi-longitudinal distance between wheelsets in bogie	1.25 m
l_s	Semi-lateral distance between secondary suspensions	0.80 m
l_p	Semi-lateral distance between primary suspensions	0.80 m
R	Wheel radius	0.475 m
C_H	Nonlinear Hertzian spring constant	87×10^9 N/m$^{3/2}$

Table 7. 2: Track model parameters [4, 17, 105]

Notation	Parameter	Value
m_r	Rail mass per unit length	60.64 kg/m
E	Elastic modulus of the rail	207×10^{9} N/m^2
I	Rail second moment of area	2.94×10^{-5} m^4
A	Rail cross sectional area	7.77×10^{-3} m^2
G	Shear modulus of the rail	8.1×10^{9} N/m^2
k_r	Timoshenko shear coefficient of the rail	0.34
k_1	Shear viscosity coefficient of the foundation	666870 N
M_s	Sleeper mass	250 kg
K_p	Railpad stiffness (nonlinear)	$* \, k_0 e^{bZ_P}$ MN/m
C_p	Railpad damping (nonlinear)	$* \, \eta_1\sqrt{m_1 K_P}$ kN-s/m
K_b	Ballast stiffness (nonlinear)	$* \, 22.75 + 2.6\times10^{8} Z_b^2$ MN/m
C_b	Ballast damping (nonlinear)	$* \, \eta_2\sqrt{m_2 K_b}$ kN-s/m
L	Length of the rail beam	60 m
S_l	Sleeper spacing	0.6 m
N	No. of sleepers	100

* Z_P and Z_b are the compression of the pad and ballast, respectively (in meter), η_1=.25 and η_2=1, $m_1 = \dfrac{M_s M_r}{M_s + M_r}$ and $m_2 = M_s + M_r$, k_0=115.2 MN/m and b=7.49/mm. [105],

The time histories of the acceleration of the front wheel of the vehicle obtained from the simulation are shown in Fig. 7.1 for three different vehicle forward speeds (v = 50, 90 and 130 km/h), which covers the speed range of a freight car in Canada [9]. A wheel flat of 50 mm length and 0.35 mm depth is considered that meets the wheel replacement criteria set by Association of American Railway (AAR) [139] and Transport Canada [1]. The static load acting on the wheel is 103 kN, which is the nominal load for a freight car system in North America [120]. The figure shows that the peak acceleration of the wheel can be reached as high as 46.86 g in the presence of a single haversine wheel flat, when the speed of the vehicle is 130 km/h. After the first peak, the time history of acceleration shows several peaks which die out after about 17.1 ms at a vehicle speed of 130 km/h. Thus, an accelerometer capable of receiving this peak acceleration within the fraction of a second should be designed.

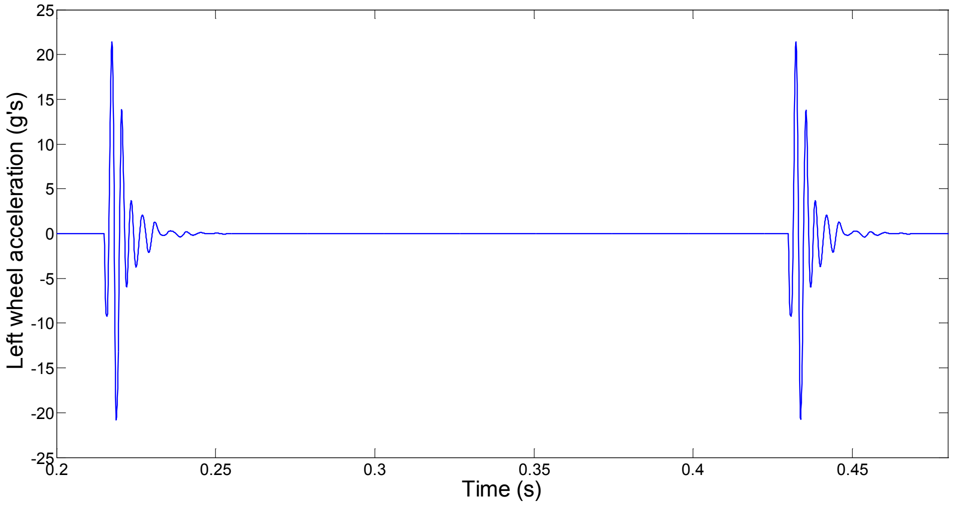

(a)

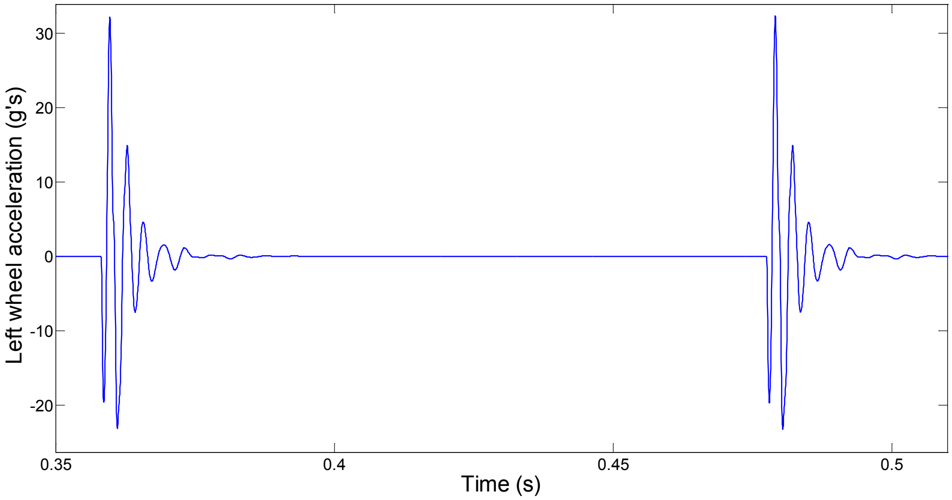

(b)

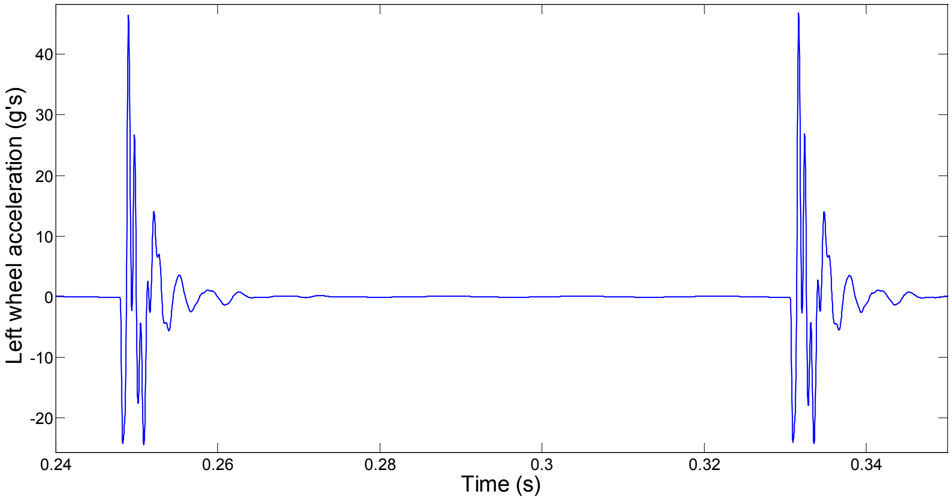

(c)

Fig. 7. 1: Acceleration time history of left wheel in the presence of a single wheel flat ($L_f = 50$ mm; $D_f = 0.35$ mm) at a speed of (a) 50 km/h; (b) 90 km/h and (c) 130 km/h.

7.4 DESIGN OF THE ACCELEROMETER

It is apparent from the above section that the proposed accelerometer needs to sense the acceleration in the range of ±50 g in vertical direction while able to maintain a 10 kHz frequency response. The accelerometer should also able to survive a maximum shock of ±150 g in case of extreme condition. The design's layout should fit within an area of 1 cm^2. In order to achieve the desired output, accurate design of the each elements of the accelerometer is required. In this, the analyses of the design of the various components are presented in order to satisfy the design requirements. The design presented in this project geared towards the use of a multi-user microfabrication facility/process known as PolyMUMPS. The decision to design the accelerometer with this predefined process in mind was tied down to the low costs involved when using such multi-user facilities and also due to the very high reliability of this microfabrication process, which has turned out over 69 different fabrication runs with outstanding success [184].

The PolyMUMPs process, started in 1992, is a surface micromachining process containing a series of coating and etching procedures [184]. It contains three-layers of doped polysilicon, which work as both structural and conducting layers. The anchor polysilicon layers are separated by silicon dioxide layers that acted as sacrificial layers. In addition, there is a silicon nitride layer at the bottom for isolation and metal on the top for making electrical contacts. This is the most popular process that can be used for fabricating variety of MEMS designs. Other more complex processes involving up-to 5 structural layers are also available (such as the SUMMiT IV process from SANDIA National labs). However, the extra layers are not necessary for this accelerometer design.

7.4.1 Spring

In an accelerometer, the displacement of the proof mass is restricted by the spring force. The displacement of the proof mass will compress one spring and stretch the other until the spring forces cancel the force due to acceleration. Thus, the combined spring constant of the springs will determine the amount of proof mass displacement and hence the signal generated by the sensing capacitors. Therefore, a suitable spring parameter is required to choose for accurate prediction of the accelerometer output. In MEMS, the most convenient way to make a spring is to use a folded structure as shown in Fig. 7.2 [185].

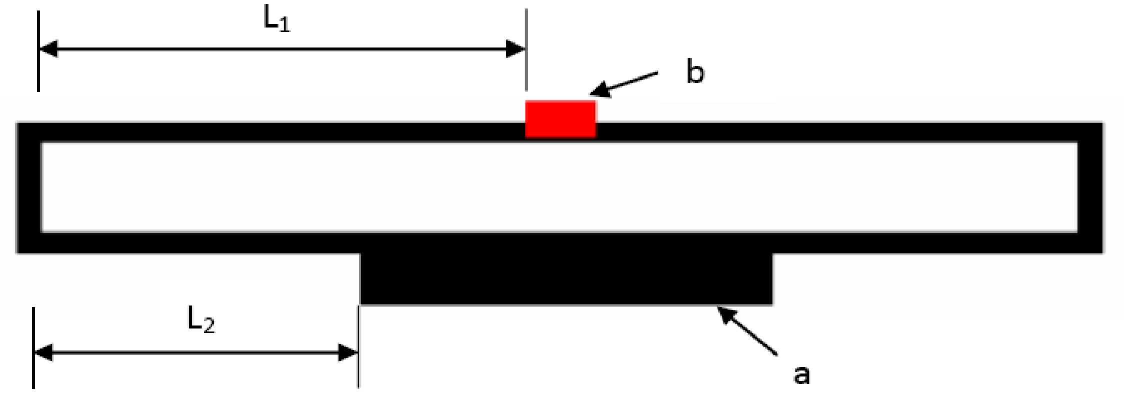

Fig. 7. 2: Schematic diagram of a folded spring made of polysilicon.

The spring is composed of four beams made of polysilicon layers. The "b" marked area in Fig. 7.2 is the anchor, which fixes the spring on to the substrate. The central plate (proof mass) is connected from the "a" marked area to the other symmetrical spring. The spring constant (K_C) determined the extent of displacement of the proof mass and can be calculated by the formula in Equation (7.4) as given in [185].

$$K_C = (\frac{\pi^4}{6})[\frac{E_P W H^3}{(2L_1)^3 + (2L_2)^3}] \tag{7.4}$$

where, E_P is the Young's modulus of polysilicon, W is the beam width, H is the beam thickness and L_1, L_2 are the beam lengths as shown in Fig. 7.2. From the above formula, it can be seen that the spring constant is strongly dependent on the lengths (L_1 and L_2), if H and W are fixed. Other important parameter in the design of an accelerometer is the proof mass (m) since the spring constant and proof mass determine the resonant frequency (ω_0) as given in Equation (7.5):

$$\omega_0 = 2\pi f = \sqrt{\frac{K_C}{m}} \text{ or, } m = \frac{K_C}{\omega_0^2} \tag{7.5}$$

The resonant frequency determines how fast the accelerometer can responds to a changing acceleration or the bandwidth of operation. This study required the bandwidth to be approximately 700 Hz and it is necessary to set the resonant frequency to be higher than the bandwidth to avoid unstable operation [186]. In the present design, the resonant frequency was set to be about 15 times the bandwidth or 10 kHz. For simplicity, lengths L_1 and L_2 are assumed to be the same and the dimensions of W and H are also taken to be the same as the polysilicon layer thickness (2 μm). In order to estimate the proof mass that gives the resonant frequency of about 10 kHz, the total spring constant due to the two springs ($2K_C$) using Eqn. (7.4) is first calculated. Thereafter, using the resonant frequency and the calculated spring constants, the mass of the proof mass are determined for different sets of L_1 and L_2. Several iterations are carried out in order to find out the mass of the proof mass. The analysis showed that in order to achieve 10 kHz resonant frequency, it is necessary to have $L_1 = L_2 = 150$ μm and proof mass of 2.924×10^{-10} kg. The total stiffness of the accelerometer ($2K_C$) is obtained as 1.1545 N/m.

7.4.2 Proof mass and electrodes

The proof mass included the masses of the central plate and all the moving electrodes as illustrated in Fig. 7.3. In order to perform the self-test function, the whole structure is separated into two parts, the sensing region, and the self-test region.

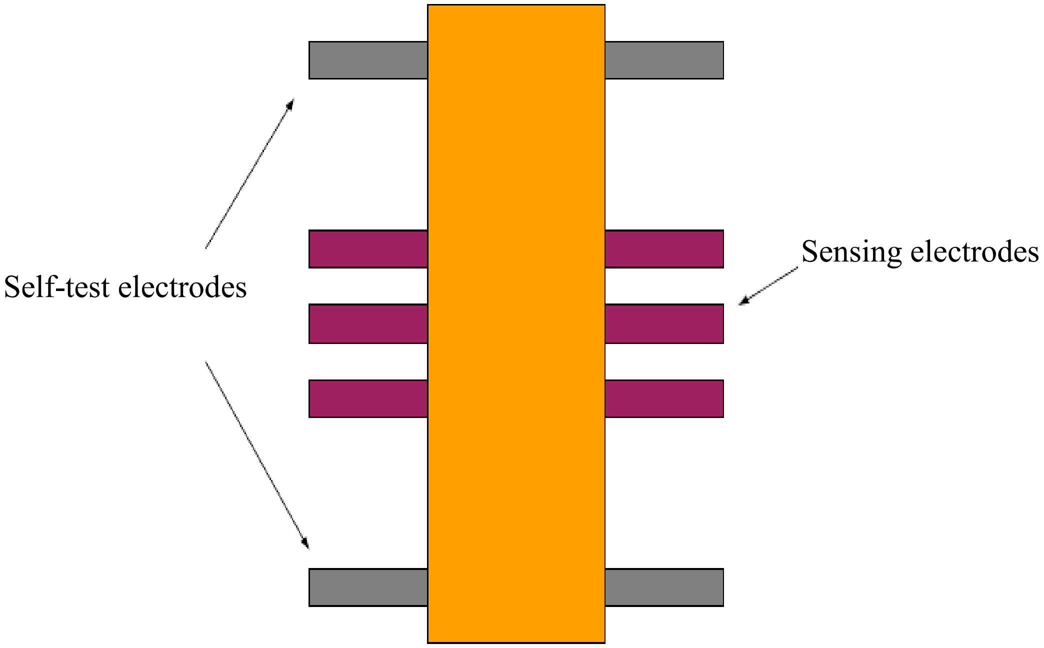

Fig. 7. 3: Schematic diagram of proof mass with sensing and self-test electrodes.

(i)Design of the electrodes

Sensing region is responsible for detecting motion when the acceleration is applied. According to the previous calculation, the proof mass including the central plate and all of the connected electrodes should be limited to about 2.924×10^{-10} kg. The attached finger-like polysilicon structure in the central plate is the sensing element. The moving and fixed fingers formed a parallel plate capacitor and the capacitance (*C*) can be estimated using Eqn. (7.6).

$$C = \frac{\varepsilon_0 A_0}{g_{ap}} \tag{7.6}$$

where, ε_0 is the permittivity, A_0 is the total overlap area between all the fingers in the sensing region, and g_{ap} is the separation between adjacent fingers. Since the changing capacitance is proportional to the area (A_0), in order to achieve higher signal it is necessary to increase the area or number of fingers. By setting the value of the capacitance to be about 100 fF, the number of fingers required is found to be about 80. The parameters used in this estimation are summarized in Table 7.3. These electrodes can be placed on either side of the proof mass as illustrated in Fig. 7.3.

Table 7. 3: Parameters of electrodes attached to the center plate

Parameters	**Electrodes design data**
Total length	176 μm
Overlap length	141 μm
Width	2 μm
Depth	2 μm
Gap between fingers	2 μm
Permittivity	8.854×10^{-12} F/m
Density of the polysilicon	2330 kg/m^3

In the self-test region, the design considerations are the same as that in the sensing region except for the applied voltages and number of electrodes. Approximately, 30% of the sensing electrodes (24) are selected for generating an internal electrostatic force for self-testing. These are located on both sides of the central plate and separated into 4 regions. Each region is made of 6 electrodes and the dimensions are all the same as those found in Table 7.3.

(ii)Design of the proof mass

In order to achieve the required total mass (*m*), the dimensions of the central plate is determined by subtracting the mass of all the fingers (including the ones used for testing) and found to be 624 μm for length and 42.11 μm for width. The calculations of mass of the central plate and 104 electrodes are shown below.

$$m_{central} = \rho_C V_C = 624\mu m \times 42.11\mu m \times 2\mu m \times 2330kg/m^3 = \ \ 1.2167 \times 10^{-10} kg$$

$$m_{fingers} = 104 \times 2\mu m \times 176\mu m \times 2\mu m \times 2330kg/m^3 = \ \ 1.7077 \times 10^{-10} kg$$

$$m = m_{central} + m_{fingers} = 2.9243 \times 10^{-10} kg$$

where, ρ_C and V_C are the density and volume of the central plate, respectively.

Force on the proof mass is achieved by applying a DC voltage to the self-test capacitor. The amount of force as a function of DC voltage can be estimated using the stored energy (W_C) on the capacitor as followed:

$$W_C = \frac{1}{2} C V^2 \tag{7.7}$$

where, V is the potential difference in Voltage .Using Eqn. (7.7), the electrostatic force F can be found as:

$$F = \frac{\partial W_C}{\partial g_{ap}} = \frac{\varepsilon_0 A_0 V^2}{2 g_{ap}^2} \tag{7.8}$$

If one plate is free and the other one is fixed in the parallel capacitor, it would mean that the free plate could be driven by electrostatic force. The force controlled by voltage is inversely proportional to g_{ap} and directly proportional to V^2. The force between each pair of movable and fixed electrodes is given by:

$$F = \frac{\varepsilon_0 A_0 V^2}{2 g_{ap}^2} \tag{7.9}$$

Combining Hook's law and Newton's second law as well as the effective spring constant, one could compute the displacement of the proof mass under the conditions of self-test, and under 50 g and 150 g of acceleration.

$$F = K_C x = ma \tag{7.10}$$

Using the total mass of the proof mass of 2.924×10^{-10} kg, the deflections under 50 g and 150 g are found to be 1.242×10^{-7} m and 3.73×10^{-7} m, respectively. The corresponding voltages required for achieving above displacements using the self-test capacitor can be estimated using Eqn. (7.8) and found to be about 4.37 V and 7.58 V, respectively.

At this point, the preliminary design and operating parameters are set. These design parameters of the accelerometer are used to layout the design using COMSOL Multiphysics software as shown in Fig. 7.4. In addition to layout, COMSOL software is also used for finite element modeling of the designed software. COMSOL is then used to run simulations that took into account all the nonlinearities of the design and the results are used to perform analysis of the designed accelerometer. The 3-D views of the various components of the accelerometer are shown below in Figs. 7.5 to 7.7.

7.5 SIMULATIONS AND RESULTS

In order to perform a realistic simulation of the performance of the accelerometer, the boundary conditions of the 3-D model with the points of acting load are set up in COMSOL, where the COMSOL would perform the simulation depending on the various forces applied by the user. Since the proof mass activates the movement due to acceleration, the supplied force was also put on the central plate body and denoted as a force point in COMSOL. The simulated results would show displacements and stresses in vertical axis. According to the requirements described in section 7.4, the device should survive 150 g of acceleration. Although it is desired that measurements at this high acceleration level are not required, but it should survive such shocks. The easiest way to make sure that it works is to check whether the structure exceeds its stress limits under 150 g of acceleration.

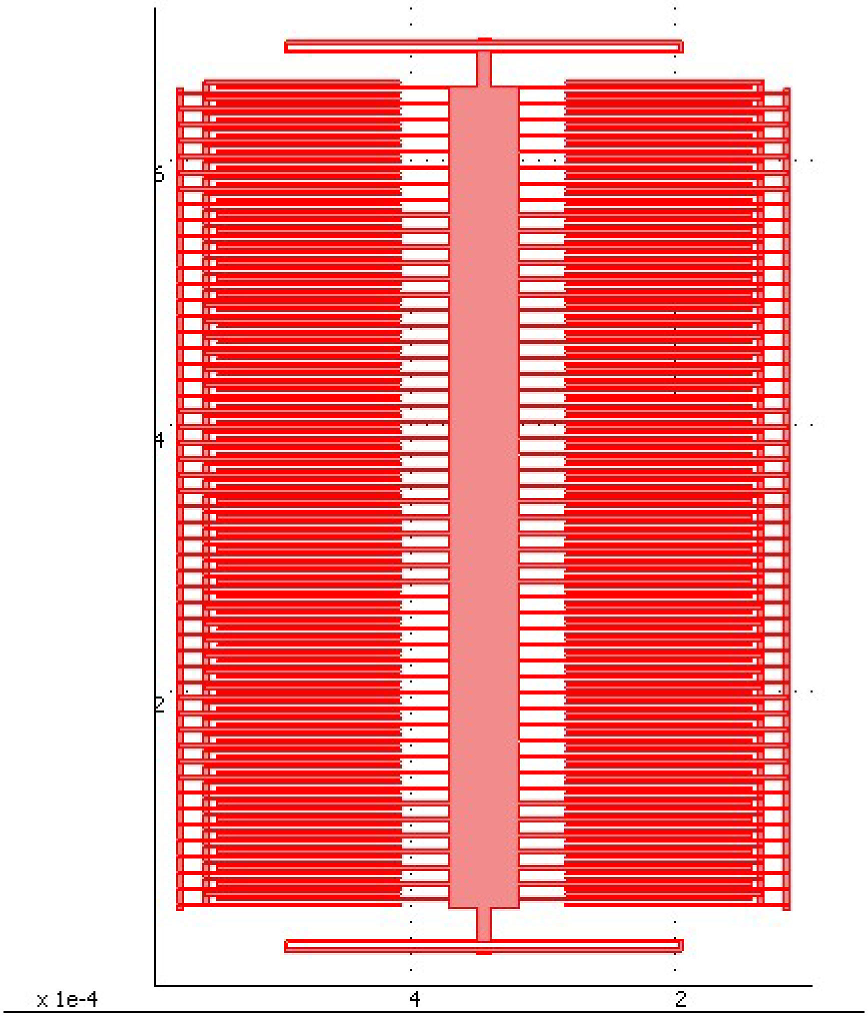

Fig. 7. 4: Schematic view of the proposed accelerometer in COMSOL

7.5.1 50 g Force

The designed accelerometer is first analyzed under the force of 50 g acceleration applied on the proof mass. The simulations were carried out in COMSOL software. The simulated results are shown in Figs. 7.8-7.9. In Figs. 7.8-7.9, the amount of deflection is color coded with maroon being the highest deflection. The maximum deflection is found to be about 1.26×10^{-7} m. The highlighted view of the local area of the springs shows that the deflection is minimum near the anchors and increased gradually towards the center of the spring where the proof mass is connected. This response is similar to the preliminary calculated result as presented in the previous. The difference between the preliminary calculations and the COMSOL simulations is about 1.5%.

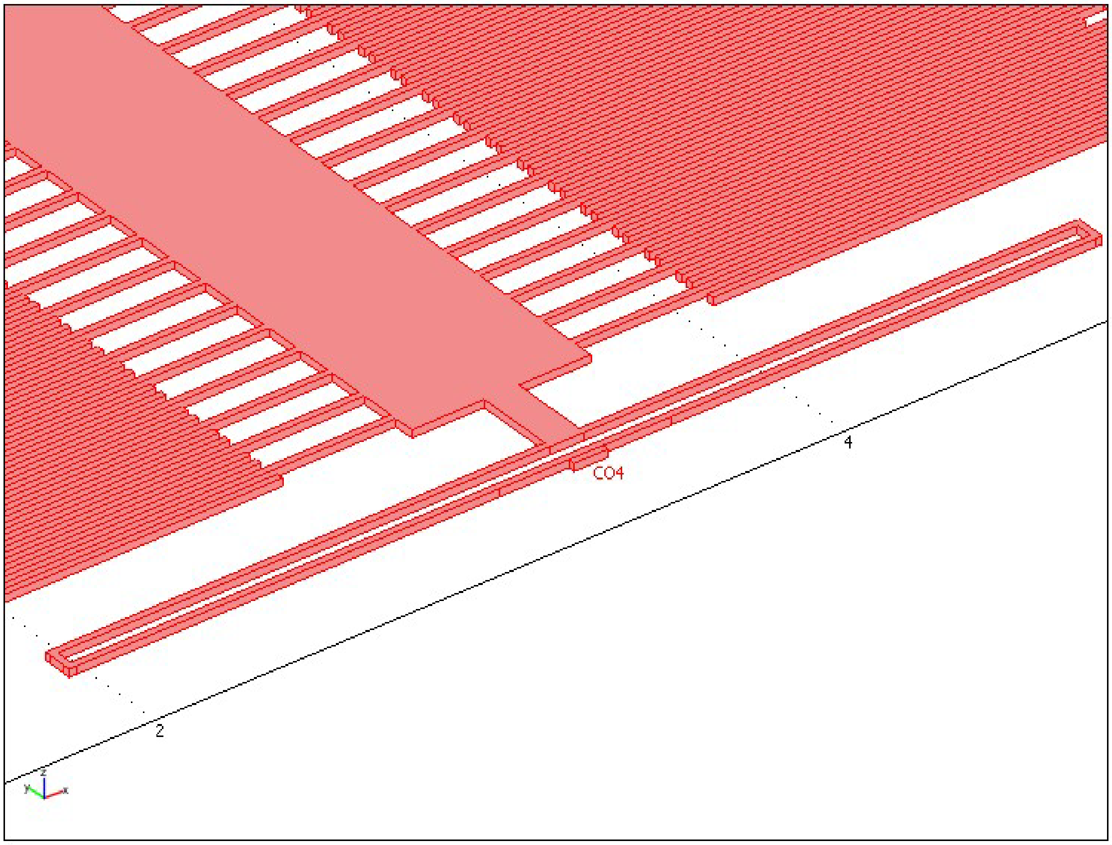

Fig. 7. 5: 3-D highlighted view of the folded spring of the accelerometer

7.5.2 150 g Force

Similar to the 50 g simulation, one could put the force of 150 g on the central plate. In this simulation, it is necessary to pay attention to stresses in the beams of the springs in addition to displacements. Because the connecting region of springs to proof mass displayed the maximum displacement, the COMSOL simulations were carried out highlighting these sections as shown in Figs. 7.10-7.11. The simulated results yielded displacement of about 3.76×10^{-7} m along the direction of the force (y direction). This is about 3 times larger than the displacement under 50 g force. The calculated value is lower than the simulation by almost 1%. The maximum stress in the anchor is found as 9.87 MPa as shown in Fig. 7.12. This stress level is, however, far smaller than the material elastic limit of 130 GPa.

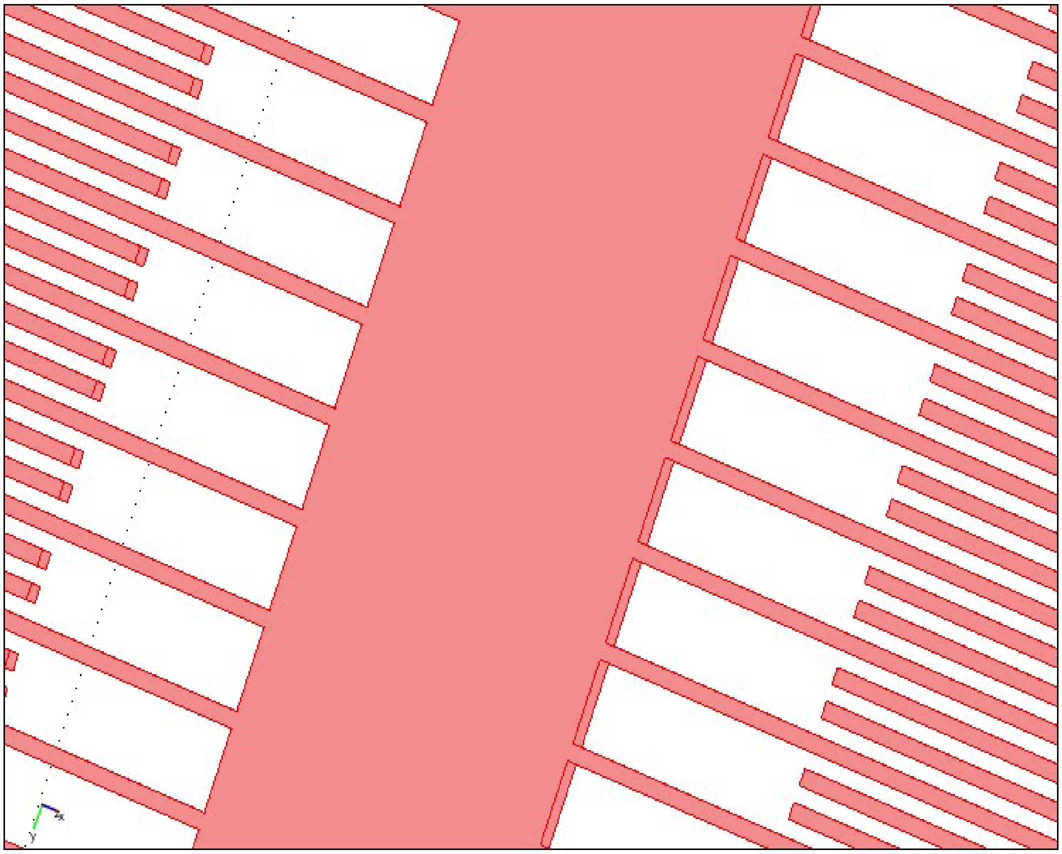

Fig. 7. 6: 3-D highlighted view of the moveable electrodes attached to the center plate

7.6 FUNCTIONAL ANALYSIS

7.6.1 Output voltage and displacement:

The basic working principle of the accelerometer is based on the fact that under an external acceleration a proof mass is displaced a small distance, which changed the gap between the electrodes that behave as varying capacitors. The moveable electrodes are located between two fixed electrodes, which are biased using two voltage supplies with equal magnitudes and opposite in direction. The device can be described by the following equivalent electrical circuit [185], as shown in Fig. 7.13, where the C_1 and C_2 are variable capacitors.

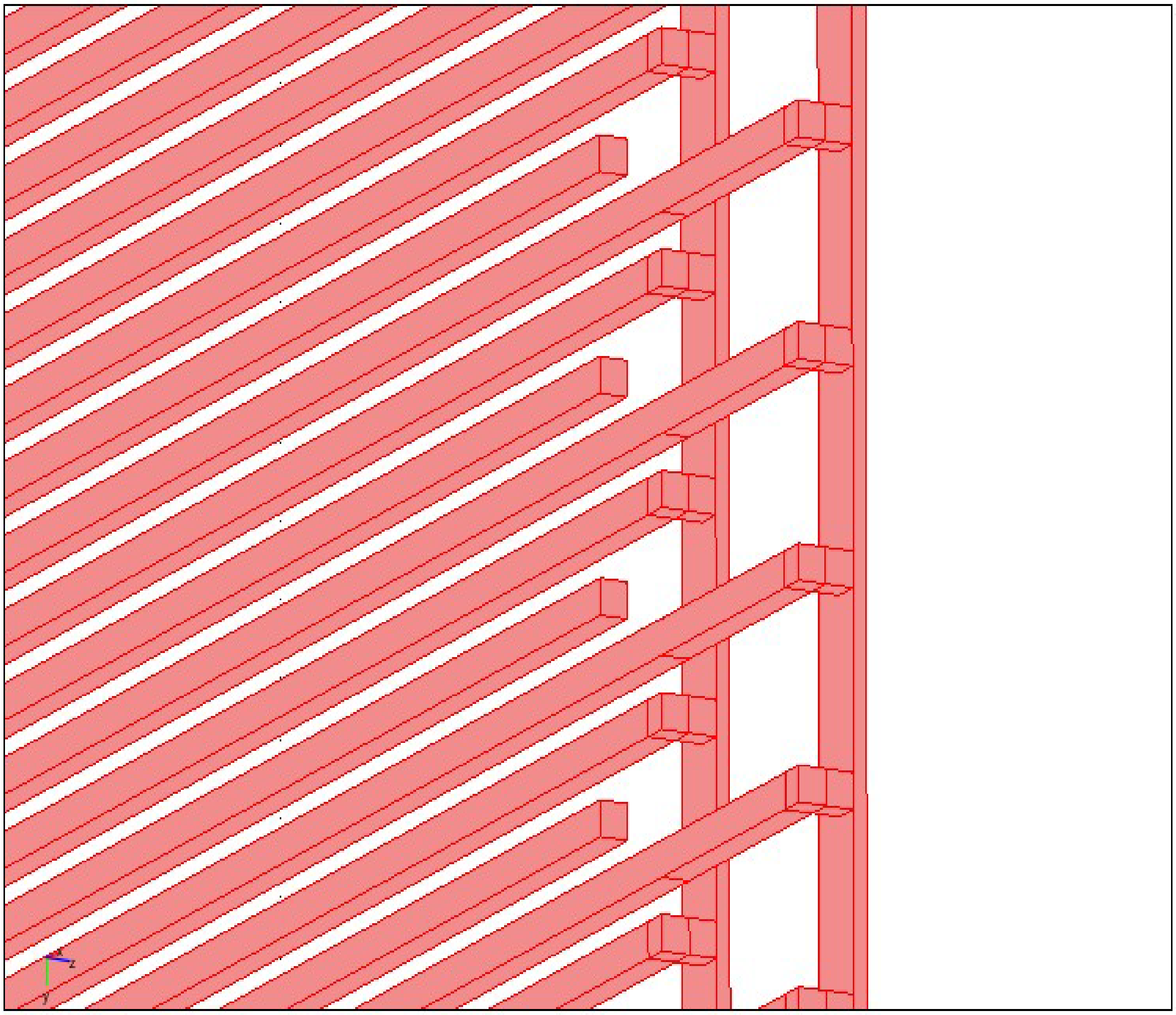

Fig. 7. 7: 3-D highlighted view of the fixed electrodes of the accelerometer

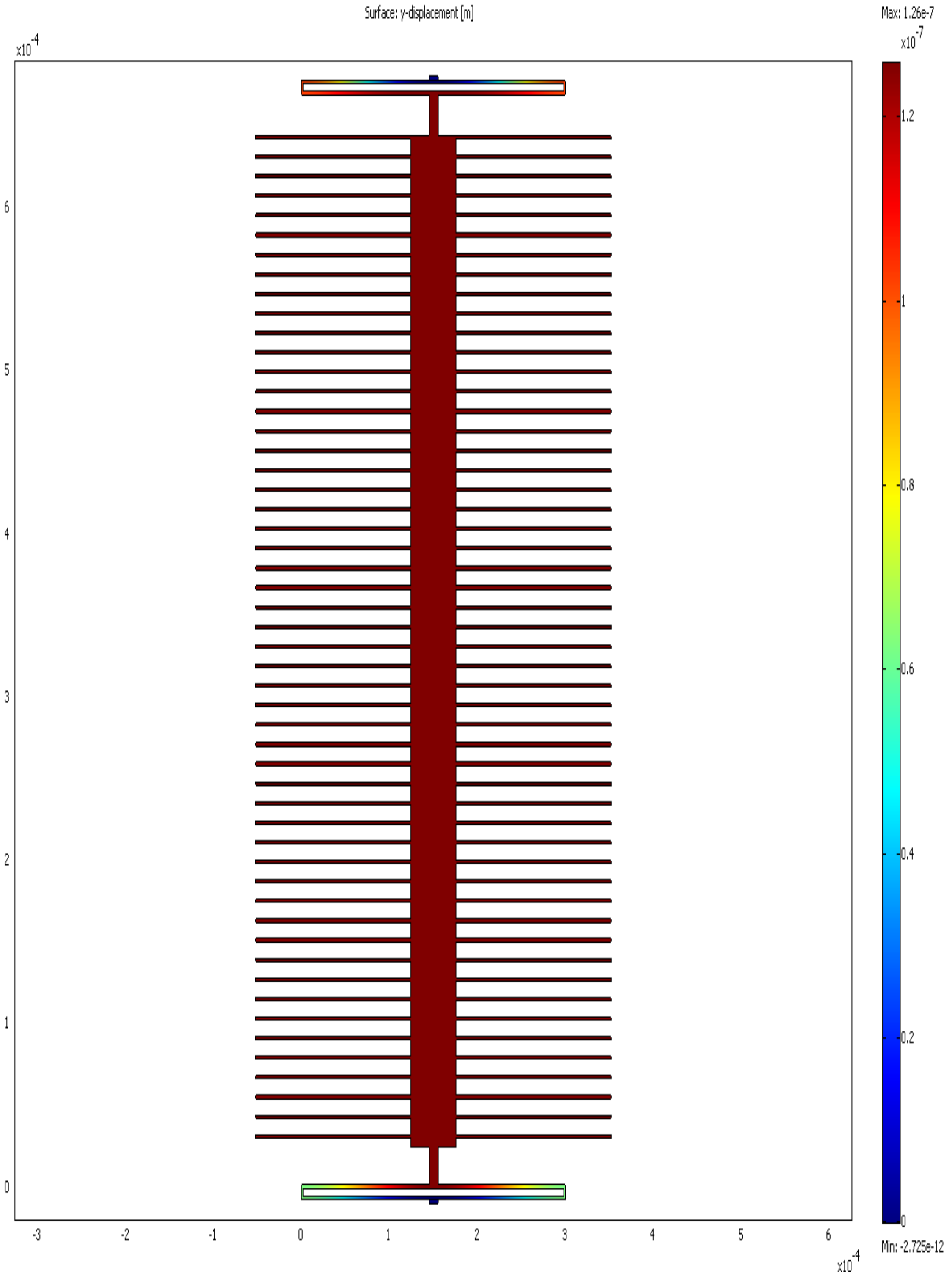

Fig. 7. 8: Displacement of proof mass along with moving electrodes under 50 g force

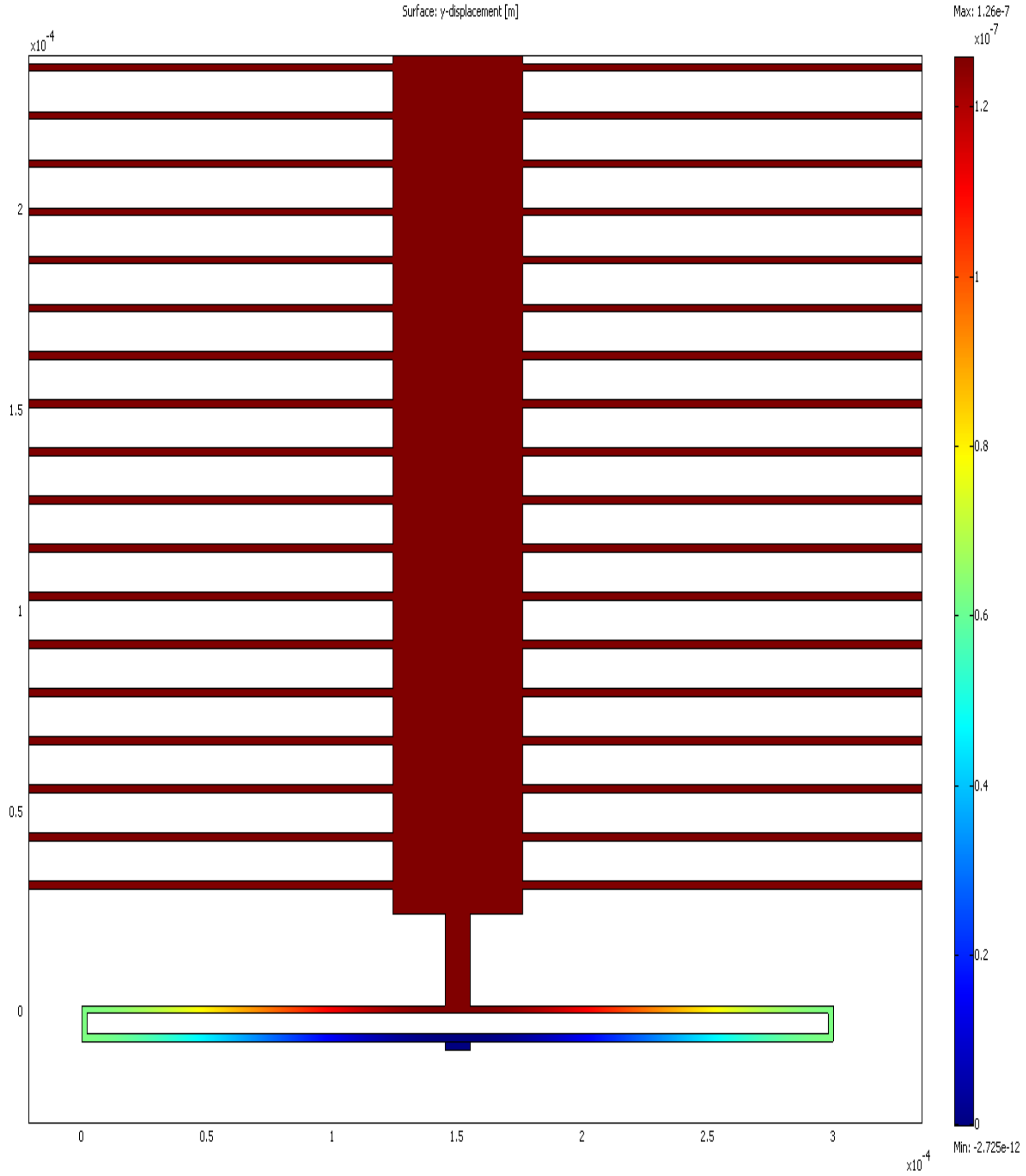

Fig. 7. 9: Expanded view of the spring deflection under 50 g force

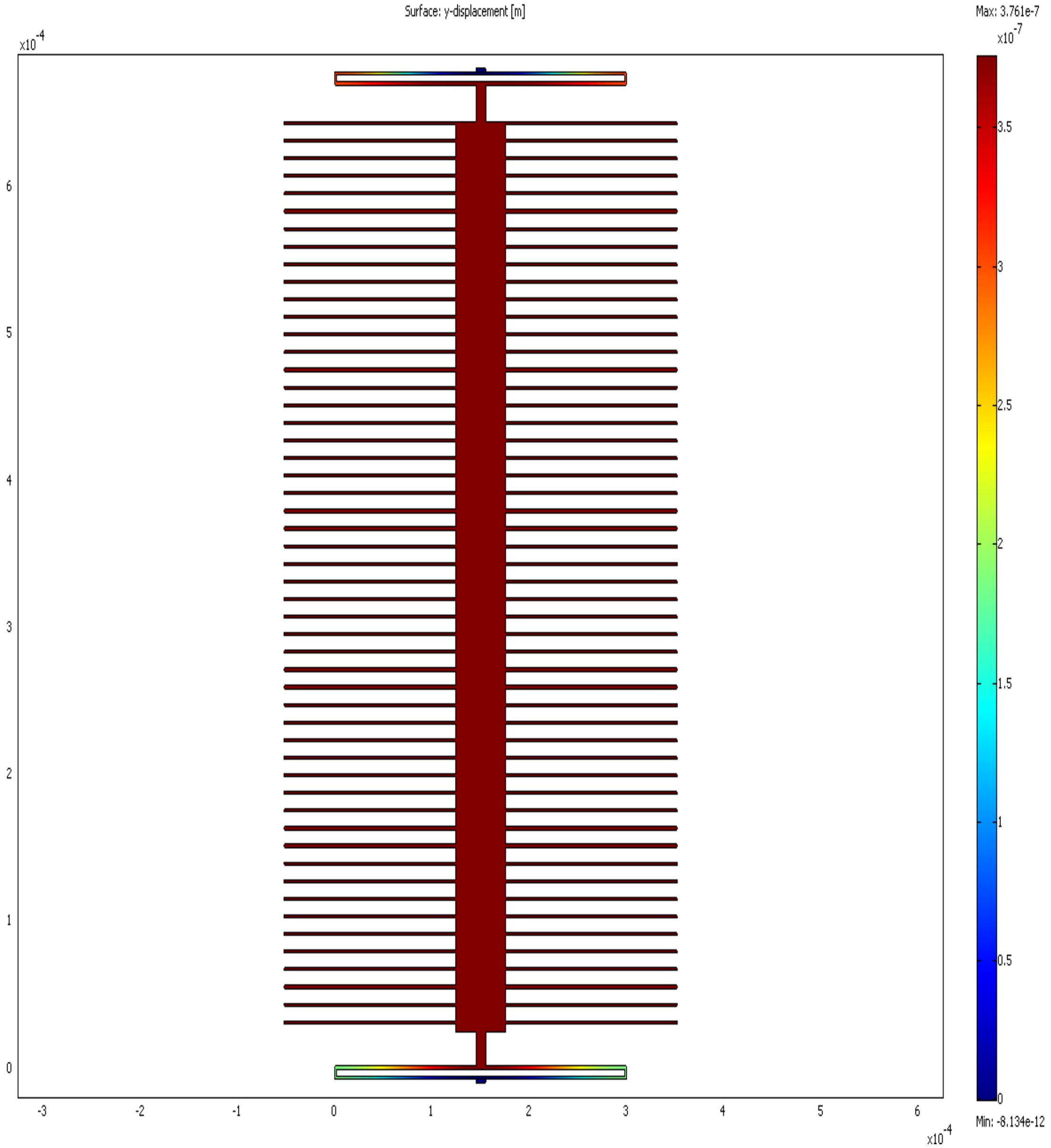

Fig. 7. 10: Displacement of proof mass along with moving electrodes under 150 g force

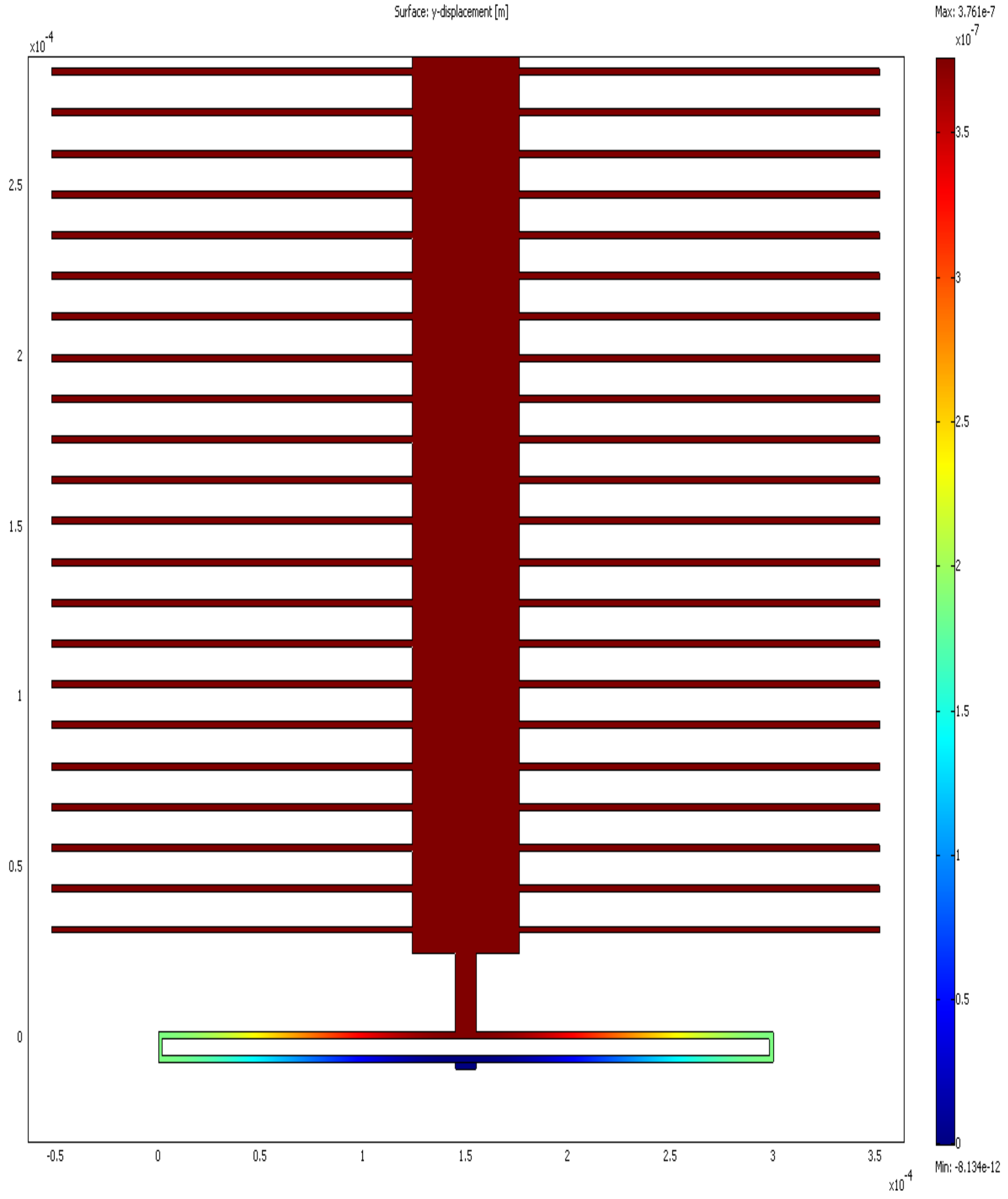

Fig. 7. 11: Expanded view of the spring deflection under 150 g force

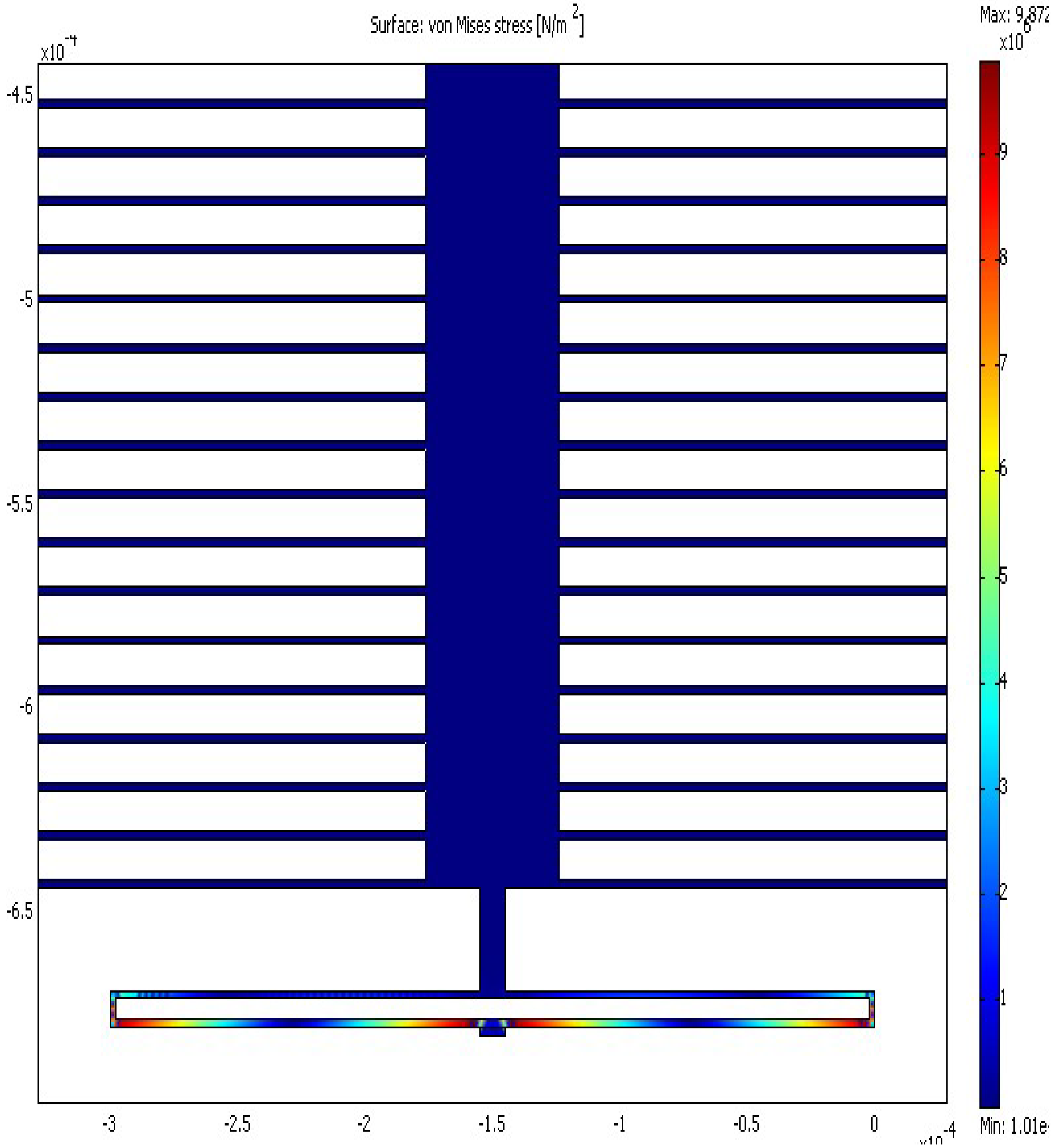

Fig. 7. 12: Stress in y-direction under 150 g force

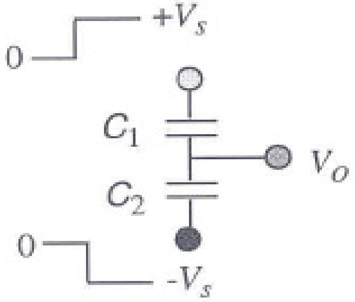

Fig. 7. 13: Equivalent electrical circuit of the accelerometer

The output voltage (V_o) of the circuit in Fig. 7.13 can be written as [185]:

$$V_o = -V_s + \frac{C_1}{C_1 + C_2}(2V_s) = \frac{C_1 - C_2}{C_1 + C_2}V_s \tag{7.11}$$

The capacitances C_1 and C_2 are not fixed due to the motion of the electrodes attached to the proof mass. When the moveable electrodes are at rest position, the two capacitances are equal and the output voltage is zero. However, under acceleration, the movable electrodes will displace and the gaps between fixed and movable electrodes will change by amount of δx as shown in Fig. 7.14.

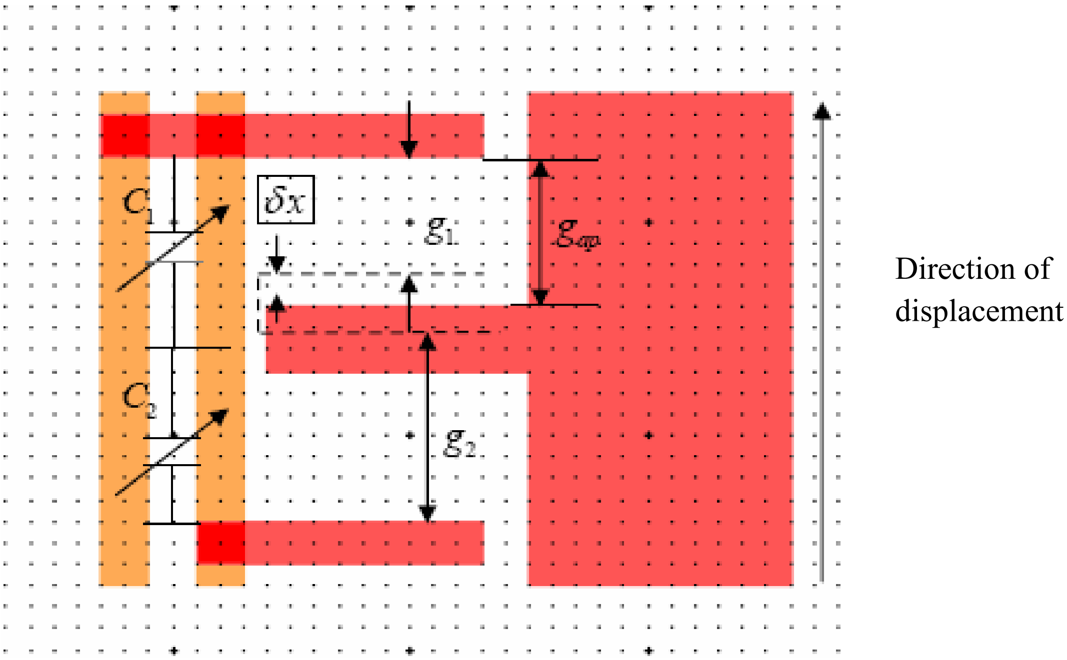

Fig. 7. 14: Displacement of moveable electrode due to acceleration.

Thus, the output voltage as a function of displacement (δx), original gap (g_{ap}) and input voltage magnitude (V_s) can be written as:

$$g_1 = g_{ap} - \delta x \text{ and } g_2 = g_{ap} + \delta x \tag{7.12}$$

$$V_o = \frac{C_1 - C_2}{C_1 + C_2} V_s = \frac{\frac{\varepsilon A}{g_1} - \frac{\varepsilon A}{g_2}}{\frac{\varepsilon A}{g_1} - \frac{\varepsilon A}{g_2}} V_s = \frac{\frac{g_2 - g_1}{g_1 g_2}}{\frac{g_2 + g_1}{g_1 g_2}} V_s = \frac{\delta x}{g_{ap}} V_s \tag{7.13}$$

The relationship between displacement and acceleration can be written as:

$$\delta x = \frac{ma}{K_C} = \frac{a}{\frac{K_C}{m}} = \frac{a}{\omega_0^2} \tag{7.14}$$

Hence, the relationship between the output voltage and the applied acceleration can be obtained as:

$$V_o = \frac{\delta x}{g_{ap}} V_s = \frac{a}{g_{ap}\omega_0^2} V_s \qquad (7.15)$$

The V_o is then calculated using the design parameters for a given acceleration (10 to 50 g) and the results are shown in Fig. 7.15. In addition, the output voltage is also estimated using the simulated displacement values obtained from COMSOL software. From the Fig. 7.15, it can be seen that the calculated and simulated output voltages are analogous. The linear relationship, as shown in Fig. 7.15, is resulted from the linear dependence of output voltage with displacement.

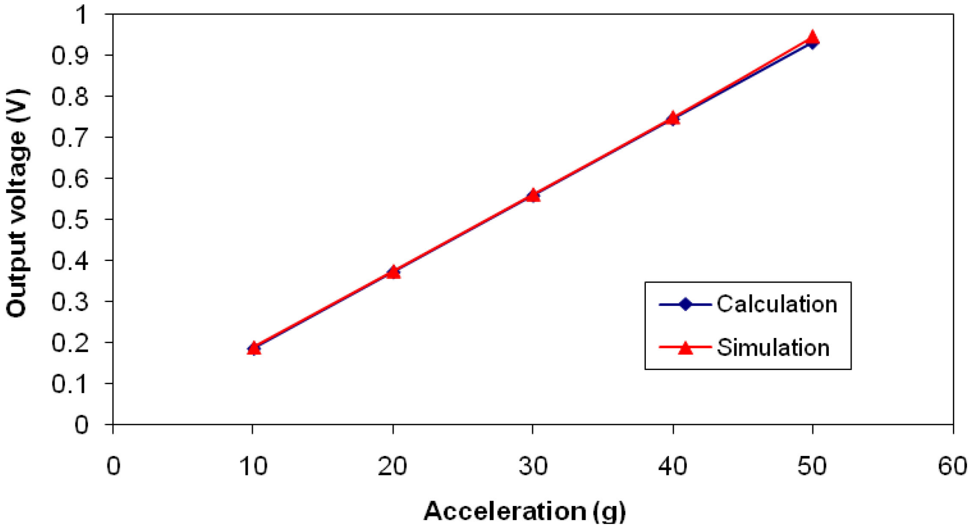

Fig. 7. 15: Comparison of calculated and simulated output voltages.

7.6.2 Stability and sensitivity analysis:

The purpose of the stability analysis is to check whether the movable electrodes will remain within the stable equilibrium range when the various accelerations are applied. If the net force approaches an unstable point, the electrodes would have the possibility to hit the fixed structures and/or brake away. At pull-in voltage, the displacement is equal to $g_{ap}/3$ and the magnitude of the pull-in voltage can be obtained as [185]:

$$V_{pi} = \sqrt{\frac{8K_C g_{ap}^3}{27\varepsilon A_0}} \tag{7.16}$$

Using Eqn. 7.16, it is found that the pull-in voltage of the proposed accelerometer is obtained as 33.1V. Thus, the input DC voltage of 7.58 V to achieve 150 g during the self-test will not push the accelerometer into the unstable region.

The sensitivity of the accelerometer for a given acceleration can be estimated as [185]:

$$V_o = \frac{a}{g_{ap}\omega_0^2} V_s \tag{7.17}$$

Using the design parameters, the sensitivity of the accelerometer is found to be about 7.2 mV/g. This corresponded to an output voltage of 0.36 V at 50 g acceleration. It can be seen from Eqn. (7.17) that the sensitivity is strongly dependent on the resonant frequency, which is further depended on the required bandwidth of operation.

7.7 SUMMARY

The characteristic of the impact acceleration due to a haversine wheel flat is investigated by a three-dimensional vehicle model supported on the three-dimensional 2-layer track. In the design of the accelerometer, two main functions are performed. Initially, the sensing region is designed to measure the acceleration, which produces a change in displacement of the proof mass. This, in turns, changes the distance between electrodes and produces a change in capacitance that can be easily measured. Finally, a self-test region is designed within the accelerometer to facilitate the self-tests/diagnostics of each individual accelerometer.

Finite element simulations are performed and their results are in very good agreement with the calculated results. The results from simple calculations vary 1% to 2% from the highly complex and time consuming simulations.

The current design resulted in a very high spring force, which is strong enough to prevent the movable electrodes from hitting the fixed electrodes under the largest foreseeable accelerations (150 g). This is favorable for stability, as the current design will never reach the unstable region of operations.

CHAPTER 8

CONCLUSIONS AND RECOMMENDATIONS

8.1 INTRODUCTION

As set out in chapter 1, the overall objective of the present dissertation to study the railway wheel-rail impact forces and accelerations caused by single and multiple wheel flats through developing a comprehensive three-dimensional railway vehicle-track model that considers the pitch and roll motion of the car body and bogie on overall wheel-rail impact responses. The specific objectives include: analysis of the two-parameter Pasternak foundation under moving load and moving mass; develop a comprehensive three-dimensional 17-DOF railway vehicle and three-dimensional nonlinear two-layer track model based on Timoshenko beam theory; natural frequency analysis of railway vehicle and track systems; coupling of the vehicle and track interaction model through nonlinear Hertzian contact spring; carry out simulations to determine wheel-rail impact forces and accelerations for various operating and wheel flat parameters; develop a smart wheelset that can detect its flat automatically; and modeling and analysis of a MEMS based accelerometer for automatic detection of the wheel flats.

Modal analysis method incorporating the MATLAB predefined function was applied to solve coupled ordinary and partial differential equations representing the vehicle and track components motions, respectively. A thorough investigation of wheel-rail impact force due to a single wheel flat was conducted considering both linear and nonlinear track parameters. The results obtained from the developed mathematical model were compared with the reported analytical and measured data in the presence of a single wheel flat. Impact accelerations develop at both the defective wheel and flat-free wheel were investigated. The results obtained from the simulations are employed to develop a smart wheelset. Based on the outcomes, some general and specific conclusions are drawn and a direction for future investigations is established.

8.2 HIGHLIGHTS OF THE PRESENT WORK

From the review of relevant literature, it was concluded that the accurate prediction of wheel-rail impact forces and acceleration responses are mainly dependent on the accurate formulation of the vehicle-track model. The most common vehicle-track model used in such studies is a simple wheel that represents the vehicle moving on two-dimensional single- or double-layer track. The rail beam is usually modeled as a continuous Euler-Bernoulli beam, which does not consider the effect of rotary inertia of the beam cross section and beam deformation due to shear force. Although the presence of multiple flats within a wheel or different wheels in same or different axles have been widely noticed in practice, the vast majority of the efforts focus on the impact interactions due to a single flat only. The influences of multiple flats and their consequences have not been adequately quantified. Furthermore, under certain conditions, the pitch and roll motions of the car body and bogie could enhance the wheel-rail impact force caused by the wheel and rail irregularities, which has not been adequately investigated.

In this study, the effect of moving load and moving mass on a continuous one-or two-parameter finite or infinite beam is investigated. After that, a three-dimensional vehicle-track model is developed in order to incorporate pitch and roll motion of the bogie in overall wheel-rail impact responses. The developed model can simulate the wheel-rail impact responses for both single and multiple flats within a wheel or wheelsets or within a bogie. The foremost contributions of the dissertation research are summarized below:

- Formulation of both one-parameter Winkler and two-parameter Pasternak foundation model in order to analyze the vibration of beam under moving load or moving mass with both finite and infinite length.
- Formulation of a three-dimensional railway vehicle-track model in order to study the wheel-rail interactions in the presence of single and multiple wheel flats, while the contribution due to the vehicle pitch and roll motions are considered.
- Formulation of a three-dimensional track system using two Timoshenko beams supported by discrete non-linear elastic supports, while the contribution due to the shear parameter of the rail beam is also considered. The natural frequencies of the developed three-dimensional vehicle-track model have also been investigated.
- Validation of the developed model with the existing theoretical and measured data available in literature considering both linear and nonlinear properties of the railpad and ballast stiffness and damping. The validated model is employed to investigate the vertical dynamic wheel accelerations and wheel-rail impact forces induced by single and multiple wheel flats.
- Evaluation of the impact accelerations arising from single as well as multiple wheel flats and investigation of the influences of one wheel flat on accelerations imparted at the interface of the adjacent wheel.
- Development of a smart wheelset that can detect its defect automatically, and design and analysis of a MEMS based accelerometer.

8.3 CONCLUSIONS

The major conclusions drawn from the present research work are summarized below:

a) The study showed that both the moving load and moving mass have significant effect on the vibration of the beam. The study further revealed that moving mass has significantly higher effect on dynamic responses of the beam over the moving load for both displacement and bending moment responses. The simulation results for a single moving mass over two-parameter finite Pasternak foundation showed that the results obtained from the modal analysis method are comparable to those obtained from exact analytical method**.**

b) This study with three-dimensional railway vehicle-track model showed that railway bogie pitch and roll motions have strong influence on peak wheel acceleration for all considered speed range, in case of multiple flats in phase. However, the car body pitch and roll motions do not have any effect on peak wheel acceleration with multiple flats in-phase condition.

c) The study showed that nonlinear railpad and ballast model gives better prediction of the wheel-rail impact force than that of the linear model when compared with the experimental data. The study further showed that speed has significant effect on peak wheel-rail impact force for both linear and nonlinear railpad and ballast models. However, linear railpad and ballast predict higher peak wheel-rail impact forces for the selected speed range.

d) The study clearly showed that presence of wheel flat within the same wheelset has significant effect on the impact force, displacement and acceleration responses of that wheelset. This study further revealed that the effect of the transmitted force on the rear bogie due to the presence of the wheel flat within the front bogie is little of negligible which can be attributed to the low suspension spring stiffness.

e) This study showed that wheel flat on one side has influence on the wheel-rail interaction of other side. The magnitude of the peak impact accelerations largely depends on both length and depth of the wheel flats.

f)When multiple flats are present within one wheel, wheel-rail impact load that arises at the position of second flat is mostly affected by the location of the first flat within the same wheel. The effects are significant when the locations of the flats are close to each other.

g) This study further showed the development of a smart wheelset for automatic detection of wheel defects through the design and analysis of a MEMS based accelerometer.

8.4 RECOMMENDATIONS FOR FUTURE WORK

The present work provided significant insights on the issues associated with wheel-rail impact loads and impact accelerations in the presence of single and multiple wheel flats. Although this study clearly demonstrates reasonably accurate results compare to the experimental data, the potential usefulness and accuracy can be further enhanced upon some other more considerations. In view of the potential benefits of the present research, further detailed modeling and through investigations are required in order to improve accuracy of the prediction tools to ensure safe operation and low cost maintenance. A list of further studies that can be carried out with the developed model along with recommendations for model improvement is presented in the followings:

- Although two-parameter Pasternak foundation can accurately represent the practical railway track model for investigating the dynamics of moving load and moving mass, further studies with three-parameter Kerr model is required in case of non-cohesive soil foundation in order to study the dynamics of moving mass.

- The developed three-dimensional vehicle-track model utilized nonlinear Hertzian single point contact model. This model is widely used in the study of vertical vehicle-track interaction. However, this model assumes that contact occurs at wheel centre point that may not always accurate especially in case of defective wheel. Thus, a multipoint contact model that can accommodate the partial contact in the presence of wheel defect would be a better alternative to predict the wheel-rail interaction forces, especially in very high speed condition.
- In this study, the developed model is validated with analytical and experimental data available in literature. However, dedicated experiment to validate the present work will enhance the study, especially for multiple wheel flats.
- In development of a smart wheelset, this study developed relationships between the wheel peak acceleration due to presence of flats, vehicle speed and flat sizes for two different wheel load conditions. Further studies with more wheel load conditions are required in order to cover wide variations of wheel load, especially for passenger rail.
- In design of a MEMS based accelerometer, since PolyMUMPS provides three layers to construct the device and since only two layers (poly0 and poly1) are used in the current design, there is one more layer available to extend the accelerometer design. Future work is required to extend this accelerometer into a 3-axis design. Building the third axis on the same planar design space will require some innovation.

REFERENCES:

1. Transport Canada “Railway Freight Car Inspection and Safety Rules” Report no. TC O-06-1, October 25th, 1994

2. Chang, A., “U.S Rail Freight to Invest Record $12B on network in 2011, says AAR” Industry Leaders Magazine April 10, 2011, p 15.

3. Railway Association of Canada yearly report “Rail Trends 2010”, December, 2010

4. Newton, S.G., and Clark, R.A., “An investigation into the dynamic effects on the track of wheel flats on railway vehicles” Journal of Mechanical Engineering Science, 21(4), 1979, pp 287–297.

5. Andersson, C., and Oscarsson, J., “Dynamic train/track interaction including state-dependent track properties and flexible vehicle components”, Vehicle System Dynamics Supplement, 33, 1999, pp 47–58.

6. Jin, X., Wang, K., Wen, Z., and Zhang, W., “Effect of rail corrugation on vertical dynamics of railway vehicle coupled with a track” Acta Mech Sinica, 21, 2005, pp 95–102.

7. Ishida, M., and Ban, T., “Modelling of the wheel flats for track dynamics” 30th Convegno Nazionale AIAS, 12-15 September, Cagliari, Italy, 2001.

8. Dong, R.G., “Vertical dynamics of railway vehicle-track system,” Ph.D. Thesis, Dept. of Mechanical and Industrial Engineering, Concordia University, Montreal, Canada, 1994.

9. Cai, Z., “Modeling of Rail track dynamics and wheel rail interaction” Ph D thesis, Dept. of Civil Engineering, Queen’s University, Kingston, Ontario, Canada, 1992.

10. Dahlberg, T., “Vertical dynamics Train /Track interaction – verifying a theoretical model by full scale experiments” Vehicle system dynamics, supplement, 24, 1995, pp 45-57.

11. Jaschinski, A., “Multibody simulation of flexible vehicles in interaction with flexible guidways” Journal of Vehicle system dynamics, supplement, 24, 1995, pp 31-44.

12. Chudzikiewicz, A., “Simulation of rail vehicle dynamics in MATLAB environment” Vehicle System Dynamics, 33, 2000, pp 107–119.

13. Zhai, W. M., Cai, C. B., Wang, Q. C., Lu, Z.W., and Wu., X. S., “Dynamic effects of Vehicles on Tracks in the case of raising train speed” Proceedings of the Institution of Mechanical Engineers, Part F, 215, 2001, pp 125-135.

14. Jin, X., Wen, Z., Wang, K., and Xiao, X., “Effect of passenger car curving on rail corrugation at a curved track” Wear, 260, 2006, pp 619-633.

15. Zhai, W., and Cai, Z., “Dynamic interaction between a lumped mass vehicle and a discretely supported continuous rail track”, Computers and Structures, 63(5), 1997, pp 987-997.

16. Hou, K., Kalousek, J., Dong, R., “A dynamic model for an asymmetrical vehicle/track system” Journal of Sound and Vibration, 267, 2003, pp 591–604.

17. Sun, Y.Q., and Dhanasekar, M., “A dynamic model for the vertical interaction of the rail track and wagon system” International Journal of Solids and Structures, 39, 2002, pp 1337-1359.

18. Wu, T.X., and D.J. Thompson, “On the impact noise generation due to a wheel passing over rail joints” Journal of Sound and Vibration, 267, 2003, pp 485–496.

19. Johansson, A., and Nielsen, J. C. O., “Out of round railway wheels, wheel rail contact forces and track response derived from the field tests and numerical simulation” Journal of Rail and Rapid Transit, 217, 1995, pp 135-146.

20. Nielsen, J.C.O, and Johansson, A., “Out of round railway wheels a literature survey” Journal of Rail and Rapid Transit, 214,2000, pp 79-91

21. Fermer, M., and Neilson, J. C. O., “Vertical interaction between train and track with soft and stiff rail pads” Proceedings of the Institution of Mechanical Engineers, 209, 1995, pp 39-47.

22. Knothe, K., and Grassie, S.L., “Modeling of railway track and vehicle/track interaction at high frequencies”, Vehicle System Dynamics, 22, 1993, pp. 209-262.

23. Barke, D.W., and Chiu, W. K., “A review of the effects of out-of-round wheels on track and vehicle components” Proceedings of the Institution of Mechanical Engineers, part F, 2005, 219, pp 151-175.

24. Fryba, L., “Vibration of solids and structures under moving loads, third edition”, Thomas Telford Ltd, Prague, Czech Republic, 1999.

25. Sun, L., “Dynamic displacement response of beam-type structures to moving line loads”, International Journal of Solids and Structures, 38, 2001, pp 8869-8878.

26. Patil, S., “Response of infinite railroad track to vibrating mass”, Journal of Engineering Mechanics, ASCE, 114(4), 1998, pp 688-703.

27. Clastornik, J., Eisenberger, M., Yankelevsky, D. Z., and Adin, M. A., "Beams on variable Winkler elastic foundation." Journal of Applied Mechanics, ASME, 53(4), 1986, pp 925-928.

28. Sun, L., and Deng, X., “Dynamic analysis to infinite beam under a moving line load with uniform velocity” Applied Mathematics and Mechanics, 19 (4), 1998, pp 367-373.

29. Eisenberger, M., and Clastornik, J., "Beams on variable two parameter elastic foundation", Journal of Engineering Mechanics, 113(10), 1987, pp 1454-1466.

30. Mackertich, S., "Response of a beam to a moving mass", Journal of Acoustical Society of America, 92(3), 1992, pp 1766-1769.

31. Esmailzadeh, E., and Ghorashi, M., "Vibration analysis of a Timoshenko beam subjected to a travelling mass", Journal of Sound and Vibration, 199(4), 1997, pp 615-628.

32. Michaltsos, G., Sophianopoulos, D., and Kounadis, A. N., "The effect of a moving mass and other parameters on the dynamic response of a simply supported beam" Journal of Sound and Vibration 191(3), 1996, pp 357-362.

33. Lee, H. P., "Dynamic response of a beam with a moving mass", Journal of Sound and Vibration, 191(2), 1996, pp 289-294.

34. Lee, H. P., "On the dynamic behavior of a beam with an accelerating mass", Archive of Applied Mechanics, 65, 1995, pp 564-571.

35. Dehestani, M., Mofid, M., and Vafai, A., "Investigation of critical influential speed for moving mass problems on beams", Applied Mathematical Modeling, 33, 2009, pp 3885–3895.

36. Ting, E. C., Genin, J., and Ginsberg, J. H., "A general algorithm for moving mass problems", Journal of Sound and Vibration, 1974, 33(1), pp 49-58.

37. Foda, M. A., and Abduljabbar, Z., "A dynamic green function formulation for the response of a beam structure to a moving mass", Journal of Sound and Vibration, 210(3), 1998, pp 295-306.

38. Wang, Y. M., "The dynamical analysis of a finite inextensible beam with an attached accelerating mass", International Journal of Solids and Structures, 35(9), 1998, pp 831-854.

39. Sadiku, S., and Leipholz, H. H. E., "On the dynamics of elastic systems with moving concentrated masses" Ingenieur-Arehive, 57, 1987, pp 223-242.

40. Murphy, D. P., "The dynamic response of engineering structures subject to excitation by moving mass systems", Ph.D thesis, University of Wyoming, Laramie, Wyoming, USA, 1984.

41. Akin, J. E., and Mofid, M., "Numerical solution for response of beams with moving mass" Journal of Structural Engineering, 115 (1), 1989, pp 120-131.

42. Bowe, C.J., and Mullarkey, T.P., "Unsprung wheel-beam interactions using modal and finite element models" Advances in Engineering Software, 39, 2008, pp 911–922.

43. Ichikawa, M., Miyakawa, Y., and Matsuda, A., “Vibration analysis of the continuous beam subjected to a moving mass” Journal of Sound and Vibration, 230(3), 2000, pp 493-506.

44. Banerjee, B.B., Das, R.N., and Sahoodynamic, M.C., “Response of a multi-span beam to transverse impact”, Nuclear Engineering and Design, 34, 1975, pp 335-348.

45. Duffy, D. G., “The Response of an Infinite Railroad Track to a Moving, Vibrating Mass”, Journal of Applied Mechanics, 57, 1990, pp 66-73.

46. Stanisic, M. M., and Lafayette, W., “On a new theory of the dynamic behavior of the structures carrying moving masses”, Ingenieur-Archiv, 55, 1985, pp 176-185.

47. Lee, H. P., “Dynamic response of a Timoshenko beam on a Winkler foundation subjected to a moving mass”, Applied Acoustics, 55(3), 1998, pp 203-215.

48. Avramidis, I. E. and Morfidis, K., “Bending of beams on three-parameter elastic foundation” International Journal of Solids and Structures, 43, 2006, pp 357-375.

49. Kerr, A. D., “Elastic and viscoelastic foundation Models”, Journal of Applied Mechanics, 31(3), 1964, pp 491-498.

50. Zhaohua, F., and Cook, R. D., "Beam element on two-parameter elastic foundations", Journal of Engineering Mechanics Division, ASCE, 109(6), 1983, pp 1390-1402.

51. Mallik, A. K., Chandra, S., and Singh, A. B., “Steady-state response of an elastically supported infinite beam to a moving load” Journal of Sound and Vibration, 291, 2006, pp 1148-1169.

52. Kerr, A. D., “A study of a new foundation model”, Acta Mechanica, 1(2), 1965, pp 135-147.

53. Reissner, E., “Note on the formulation of the problem of the plate on an elastic foundation”, Acta Mechanica, 4, 1967, pp 88-91.

54. Horvath, J. S., “New subgrade model applied to Mat foundations”. Journal of Geotechnical Engineering, 109 (12), 1983, pp 1567-1587.

55. Hetenyi, M., “A general solution for the bending of beams on an elastic foundation of arbitrary continuity”, Journal of Applied Physics, 21, 1950, pp 55-58.

56. Criner, H. E., and McCann, G. D., “Rails on elastic foundation under the influence of high-speed travelling loads”, Journal of Applied Mechanics, ASME, 75, 1953, pp 13-22.

57. Chen, Y. H., and Huang, Y. H., “Dynamic stiffness of infinite Timoshenko beam on viscoelastic foundation in moving co-ordinate” International Journal of Numerical Method and Engineering, 48, 2000, pp 1-18.

58. Achenbach, J. D., and Sun, C. T., "Moving load on a flexible supported Timoshenko beam", International Journal of Solids and Structures, 1, 1965, pp 353-370.

59. De Rosa, M. A., "Free vibrations of Timoshenko beams on Two-parameter elastic foundation", Computer and Structure, 57(1), 1995, pp 151-156.

60. Lou, P., Dai, G. L., and Zeng, Q.Y., "Finite-element analysis for a Timoshenko beam subjected to a moving mass", Journal of Mechanical Engineering Science, 220, 2006, pp 669-678.

61. Yavari, A., Nouri, M., and Mofid, M., "Discrete element analysis of dynamic response of Timoshenko beams under moving mass", Advances in Engineering Software, 33, 2002, pp 143-153.

62. Vu-Quoc, L., and Olsson, M., "A computational procedure for interaction of high-speed vehicles on flexible structures without assuming known vehicle nominal motion", Computer Methods in Applied Mechanics and Engineering, 76, 1989, pp 207-244.

63. Bajer, C. I., and Dyniewicz, B., "Numerical modeling of structure vibrations under inertial moving loads", Archive of Applied Mechanics, 79, 2009, pp 499-508.

64. Cifuentes, A. O., "Dynamic response of a beam excited by a moving mass", Finite Elements in Analysis and Design, 5, 1989, pp 237-246.

65. Yong, C. C., and Yang, Z., "Dynamic responses of a beam on a Pasternak foundation and under a moving load" Journal of Chongqing University, 7(4), 2008, pp 311-316.

66. Kargarnovin, M. H., and Younesian, D., "Dynamics of Timoshenko Beams on Pasternak Foundation under Moving Load", Mechanics Research communication, 31(6), 2004, pp 713-723.

67. Zehsaz, M., Sadeghi, M. H., and Asl, A. Z., "Dynamic response of Railway under a moving Load", Journal of Applied sciences, 9(8), 2009, pp 1474-1481.

68. Hardy, M. S. A., and Cebon, D., "Importance of speed and frequency in flexible pavement response", Journal of Engineering Mechanics, ASCE, 120(3), 1994, pp 463-482.

69. Jin, B., "Dynamic displacements of an infinite beam on a poroelastic half space due to a moving oscillating load" Archive of Applied Mechanics, 74, 2004, pp 277-287.

70. Xu, B., Lu, J. F., and Wang, J. H., "Dynamic response of an infinite beam overlying a layered poroelastic half-space to moving loads" Journal of Sound and Vibration, 306, 2007, pp 91-110.

71. Cao, Z. G., Cai, Y. Q., Sun, H. L., and Xu, C. J., "Dynamic responses of a poroelastic half-space from moving trains caused by vertical track irregularities" International Journal for Numerical and Analytical Methods in Geomechanics, 35, 2011, pp 761-786.

72. Kononov, A. V., and Wolfert, R. A. M., "Load motion along a beam on a viscoelastic half-space" European Journal of Mechanics - A/Solids,19, 2000, pp 361-371.

73. Barros, F.C.P., and Luco, J.E., "Response of a layered viscoelastic half-space to a moving point load" Wave Motion, 19, 1994, pp 189-210.

74. Yunmin, C., and Changjing, W., "Steady-state response of a Timoshenko beam on an elastic half-space under a moving load" Acta Mechanica Solida Sinica, 19(1), 2006, pp 26-39.

75. Steenbergen, M. J.M.M., and Metrikine, A. V., "The effect of the interface conditions on the dynamic response of a beam on a half-space to a moving load" European Journal of Mechanics A/Solids, 26, 2007, pp 33-54.

76. Sun, H., Cai, Y., and Xu, C., "Three-dimensional simulation of track on poroelastic half-space vibrations due to a moving point load" Soil Dynamics and Earthquake Engineering, 30, 2010, pp 958-967.

77. Nielsen, J.C.O., and Igeland, A., "Vertical dynamic interaction between train and track-influence of wheel and track imperfections" Journal of Sound and Vibration, 187(5), 1995, pp 825-839.

78. Zhu, J.J., Ahmed, W., Rakheja, S., and Hu, Y.S., "Impact load due to railway wheels with multiple flats predicted using an adaptive contact model Proceedings of the IMechE, Part F, Journal of Rail and Rapid Transit, 223 (4), 2009, pp 391-403.

79. Andersson, C., and Abrahamsson, T., "Simulation of interaction between a train in general motion and a track" Vehicle System Dynamics, 38(6), 2002, pp 433–455.

80. Johansson, A., and Andersson, C., "Out-of-round railway wheels–a study of wheel polygonalization through simulation of three-dimensional wheel–rail interaction and wear", Vehicle System Dynamics, 43(8), 2005, pp 539–559.

81. Wen, Z., Xiao, G., Xiao, X., Jin, X., and Zhu, M., "Dynamic vehicle–track interaction and plastic deformation of rail at rail welds" Engineering Failure Analysis, 16, 2009, pp 1221–1237.

82. Bezin, Y., Iwnicki, S. D., Cavalletti, M., Vries, E., Shahzad, F., and Evans, G., "An investigation of sleeper voids using a flexible track model integrated with railway multi-body dynamics" Journal of Rail and Rapid transit, part F, 223, 2009, pp 597-607.

83. Jin, X., Xiao, X., Wen, Z., Guo, J., and Zhu, M., "An investigation into the effect of train curving on wear and contact stresses of wheel and rail" Tribology International, 42, 2009, pp 475–490.

84. Nejlaoui, M., Zouhaier, A., Ajmi, H., and Lotfi, R., "Analytical modeling of rail vehicle safety and comfort in short radius curved tracks" Comptes Rendus Mecanique, 337, 2009, pp 303–311.

85. Lee, S.Y., Cheng, Y.C., "A New Dynamic Model of High-Speed Railway Vehicle Moving on Curved Tracks" Journal of Vibration and Acoustics, 130 (1), 2008, pp 1-10.

86. Cheng, Y.C., Lee, S.Y., Chen, H.H., "Modeling and nonlinear hunting stability analysis of high-speed railway vehicle moving on curved tracks" Journal of Sound and Vibration, 324, 2009, pp 139–160

87. Sun, Y.Q., and Cole, C., "Comprehensive wagon–track modelling for simulation of three-piece bogie suspension dynamics" Journal of Rail and Rapid transit, part F, 221, 2007, pp 905-917.

88. Zhai, W., Wang, K., and Cai, C., "Fundamentals of vehicle–track coupled dynamics" Vehicle System Dynamics, 47(11), 2009, pp 1349–1376.

89. Dinh, V. N., Kim, K. D., Pennung, W., "Simulation procedure for vehicle–substructure dynamic interactions and wheel movements using linearized wheel–rail interfaces" Finite Elements in Analysis and Design, 45, 2009, pp 341 -356.

90. Hou, K., Kalousek, J., Dong, R., "A dynamic model for an asymmetrical vehicle/track system" Journal of Sound and Vibration, 267, 2003, pp 591–604.

91. Jin, X.S., Wen, Z.F., Wang, K.Y., Zhou, Z.R., Liu, Q.Y., and Li, C.H., "Three-dimensional train–track model for study of rail corrugation", Journal of Sound and Vibration, 293, 2006, pp 830–855.

92. Popp, K., Kaiser, I., Kruse, H., "System dynamics of railway vehicles and track" Archive of Applied Mechanics, 72, 2003, pp 949–961

93. Morys, B., "Enlargement of out-of-round wheel Profiles on high speed trains" Journal of Sound and Vibration, 1999, 227(5), pp 965-978.

94. Dinh, V. N., Kim, K. D., Pennung, W., "Dynamic analysis of three-dimensional bridge-high-speed train interactions using a wheel-rail contact model" Engineering Structures, 31, 2009, pp 3090-3106.

95. Song, M.K., Noh, H.C., and Choi, C.K., "A new three-dimensional finite element analysis model of high-speed train–bridge interactions" Engineering Structures, 25, 2003, pp 1611–1626.

96. Wu, Y.S., Yang, Y.B., and Yau, J.D., "Three-Dimensional Analysis of Train-Rail-Bridge Interaction Problems" Vehicle System Dynamics, 36(1), 2001, pp 1-35.

97. Sun, Y. Q., Dhanasekar, M., and Roach, D., "A three-dimensional model for the lateral and Vertical Dynamics of wagon-track system." Proceedings of the institution of Mechanical Engineers, Part F, 217 (1), 2003, pp 31-45.

98. Ahlbeck, D.R., and Daniels, L.E., "Investigation of rail corrugations on the Baltimore Metro" Wear, 144, 1991, pp 197-210.

99. Chen, Y-H., and Huang, Y-H., "Dynamic characteristics of infinite and finite railways to moving loads" Journal of Engineering Mechanics, 129 (9), 2003, pp 987-995.

100. Bitzenbauer, J., and Dinkel, J., "Dynamic interaction between a moving vehicle and an infinite structure excited by irregularities – Fourier transforms solution" Archive of Applied Mechanics, 72, 2002, pp 199-211.

101. Tassilly, E., and Vincent, N., "A linear model for the corrugation of rail", Journal of Sound and Vibration, 150, 1991, pp 25-45.

102. Thompson, D., "Theoretical modeling of wheel rail noise generation" Journal of Rail and Rapid Transit, 205, 1991, pp 137-149.

103. Wu, T.X., and Thompson, D.J., "A hybrid model for the noise generation due to railway wheel flats." Journal of Sound and Vibration, 251(1), 2002, pp 591-604.

104. Wu, T.X., and Thompson, D.J., "Behavior of the normal contact force under multiple Wheel/Rail interaction." Vehicle System Dynamics, 37 (3), 2002, pp 157–174.

105. Thompson, D., and Wu, T.X., "The effect of non-linearity on wheel/rail impact" Journal of Rail and Rapid transit, 218, 2003, pp 1-15.

106. Dahlberg, T., "Some railroad settlement models—a critical review" Proceedings of the Institution of Mechanical Engineers, Part F, 215 (4), 2001, pp 289-300.

107. Oscarsson, J., "Simulation of Train-Track Interaction with Stochastic Track Properties" Vehicle System Dynamics, 37(6), 2002, pp 449-469.

108. Zhai, W. M., Cai, C. B., Wang, Q. C., Lu, Z.W., and Wu., X. S., "Dynamic effects of Vehicles on Tracks in the case of raising train speed" Proceedings of the Institution of Mechanical Engineers, Part F, 215, 2001, pp 125-135.

109. Zhai, W., and Cai, Z., "Dynamic interaction between a lumped mass vehicle and a discretely supported continuous rail track" Computers and Structures, 63(5), 1997, pp 987-997.

110. Michal, M., and Michael, H., “Effects of speed, load and damping on the dynamic response of railway bridges and vehicles” Computers and Structures, 86, 2008, pp 556–572.

111. Lei, X., “Dynamic analysis of the track structure of a high speed railway using finite elements” Proceedings of Institution of Mechanical Engineers, Part F, 215, 2001, pp 301-309.

112. Nielsen, J.C.O., and Oscarsson, J., “Simulation of dynamic train–track interaction with state-dependent track properties” Journal of Sound and Vibration, 275, 2004, pp 515-532.

113. Yang, S.C., “Enhancement of the finite-element method for the analysis of vertical train–track interactions” Proceedings of the IMechE, Part F, Journal of Rail and Rapid Transit, 223 (6), 2009, pp 609-620.

114. Mazilu, T., “Green’s functions for analysis of dynamic response of wheel/rail to vertical excitation” Journal of Sound and Vibration, 306, 2007, pp 31–58.

115. Zakeri, J.A., Xia, H., and Fan, J.J., “Dynamic responses of train-track system to single rail irregularity” Latin American Journal of Solids and Structures, 6, 2009, pp 89-104.

116. Arnold, D. K., and Joel, E.C., “Analysis and tests of bonded insulated rail joints subjected to vertical wheel loads” International Journal of Mechanical Sciences, 41,1999, pp 1253 - 1272.

117. Dahlberg, T., “Dynamic interaction between train and non-linear railway track model” International conference (EURODYN), 2-5 September, Munich, Germany, 2002.

118. Chen, Y. H., and Huang, Y.H., “Dynamic stiffness of infinite Timoshenko beam on viscoelastic foundation in moving co-ordinate” International Journal of Numerical Method and Engineering, 48, 2000, pp 1-18.

119. Uzzal, R. U. A., Ahmed, W., and Rakheja, S.,, “Analysis of pitch plane railway vehicle-track interactions due to single and multiple wheel flats” Proceedings of the IMechE, Part F, Journal of Rail and Rapid Transit, 223 (4), 2009, pp 375-390.

120. Dukkipati, R.V., and Dong, R., “Impact loads due to wheel flats and shells” Journal of Vehicle System Dynamics, 31,1999, pp 1–22.

121. Thompson, D., Wu, T.X., and Armstrong, T., “Wheel/rail rolling noise - the effects of nonlinearities in the contact zone” Tenth international congress on sound and vibration, 7-10 July, Stockholm, Sweden, 2003.

122. Wu, T.X., and D.J. Thompson, “On the impact noise generation due to a wheel passing over rail joints” Journal of Sound and Vibration, 267, 2003, pp 485–496.

123. Steenbergen, M. J.M.M., “Quantification of dynamic wheel–rail contact forces at short rail irregularities and application to measured rail welds” Journal of Sound and Vibration, 312, 2008, pp 606–629.

124. Cai, Y., Cao, Z., Sun, H., and Xu, C., “Effects of the dynamic wheel–rail interaction on the ground vibration generated by a moving train” International Journal of Solids and Structures, 47, 2010, pp 2246–2259.

125. Tassilly, E., and Vincent, N., “A linear model for the corrugation of rail”, Journal of Sound and Vibration, 150, 1991, pp 25-45.

126. Wu, T.X., and Thompson, D.J., “Theoretical investigation of wheel/rail non-linear interaction due to roughness excitation” Vehicle System Dynamics, 34, 2000, pp 261–282.

127. Matsumoto, A., Sato, Y., Tanimoto, M., and Kang, Q., “Study on the formation mechanism of rail corrugation on curved track”, Vehicle System Dynamics, supplement, 25, 1996, pp 450-465.

128. Grassie, S. L., “A contribution to dynamics design of railway track” Proceedings of 12th IAVSD symposium, Lyon, France, 1991, pp 195-209.

129. Kalker, J.J., “A simplified theory for non-Hertzian contact” Proceedings of 8th IAVSD symposium, Cambridge, Massachusetts, USA, 1983 pp 295-302.

130. Baeza, L., Roda, A., and Nielsen, J.C.O., “Railway vehicle/track interaction analysis using a modal sub-structuring approach” Journal of Sound and Vibration, 293, 2006, pp 112–124.

131. Pascal, J.P., and Sauvage, G., “The available methods to calculate the wheel/rail forces in non Hertzian contact patches and rail damaging” Vehicle System Dynamics, 22, 1993, pp 263-275.

132. Kalker, J. J., “Survey of wheel rail rolling contact theory” vehicle system dynamics, 8, 1979, pp 317-358.

133. Shen, Z.Y., Hedrick, J.K. and Elkins, J.A.,“A Comparison of Alternative Creep Force Models for Rail Vehicle Dynamic Analysis” Proceedings of the 8th IAVSD-Symposium on the Dynamics of Vehicles on Roads and on Tracks. MIT, Cambridge, MA, 1983, pp 591-605.

134. Fingberg, U., “A Model of Wheel-Rail Squealing Noise”, Journal of Sound Vibration, 143, 1990, pp 365– 377.

135. Valdivia, A., “A linear dynamic wear model to explain the initiating mechanism of corrugation” In: Proceedings of the 10th IAVSD-Symposium on the Dynamics of Vehicles on Roads and on Tracks. Amsterdam, 1988, pp 493–496.

136. Jury, A., Enrico, M., Stefano, F., and Monica, M., “Dynamic simulation of railway vehicles: wheel/rail contact analysis” Vehicle System Dynamics, 47(7), 2009, pp 867–899.

137. Piotrowski, J., “Contact loading of a high rail in curves: Physical simulation method to investigate shelling”. Vehicle System Dynamics, 17, 1998, pp 57-79.

138. Kalker, J.J., and Piotrowski, J., “The elastic cross-influence between two quasi-Hertzian contact zones”. Vehicle System Dynamics, 17, 1988, pp 337-355.

139. Piotrowski, J., “A Theory of Wheelset forces for two point contact between wheel and rail”. Vehicle System Dynamics, 11(2), 1982, pp 63–87.

140. Szolc, T., “Medium frequency dynamic investigation of the railway wheelset-track system using a discrete-continuous model”, Archive of Applied Mechanics, 68, 1998, pp 30-45.

141. Moyar, G. J., and Stone, D. H., “An analysis of the thermal contributions to railway wheel Shelling” Wear, 144, 1991, pp 117-138.

142. Jergeus, J., Odenmarck, C., Lunden, R., Sotkovszki, P., Karlsson, B., and Gullers, P., “Full-scale railway wheel flat experiments” Proceedings of Institution of Mechanical Engineers Part F, 213, 1998, pp 1-13.

143. Hempelmann, K., Hiss, F., Knothe, K., and Ripke, B., “The Formation of Wear Patterns on Rail Tread”. Wear, 144, 1991, pp 179–195.

144. Lonsdale, C., Dedmon, S., and Pilch, J., “Effects of increased gross rail load on 36-inch diameter freight car wheels” Railway Wheel Manufacture's Engineering Committee 2001, Technical Conference Proceedings, Chicago, IL, Sep. 25, 2001, pp 12-18.

145. Tajaddini, A., and Kalay, S.F., “Time to revise wheel-removal rules? Association of American Railroads regulations,” Railway Age, 196 (9), 1995, pp 93-98.

146. Reilly, K., “Railway Wheelsets”, Rail Safety and Standards Board, London, UK, 2003.

147. Jenkins, H.H., Stephenson, J.E., Clayton, G.A., and Morland, G.W., “The Effect of Track and Vehicle Parameters on Wheel/Rail Vertical Dynamic Forces” Railway Engineering Journal, 3(1), 1974, pp 2-16.

148. Frederick, C. O., “The effect of wheel and rail irregularities on the track”, Proceedings of Heavy haul railways conference, 18-22, September, Perth, Australia, 1978.

149. Gullers, P., Andersson, L., and Lunden, R., “High-frequency vertical wheel-rail contact forces-field measurements and influence of track irregularities” Wear, 265, 2008, pp 1472-1478.

150. Nordborg, A., "Vertical Rail Vibrations: Parametric Excitation" Acta Acustica, 4, 1998, pp 289-300.

151. Mead, D. J. and Mallik, A.K., "An approximate method of predicting the response of periodically supported beams subjected to random convected loading" Journal of Sound and Vibration, 47 (4), 1976, pp 457-471.

152. Cai, C. W., Cheung, Y. K., and Chan, H. C., "Dynamic response of infinite continuous beams subjected to a moving force-an exact method" Journal of Sound and Vibration, 123 (3), 1988, pp 461-472.

153. Rieker, J., Lin, Y. H., and Trethewey, M., "Discretisation consideration in moving load finite element beam models" Finite Element Analysis and Design, 21, 1996, pp 129-144.

154. Andersen, L., Nielsen, S., and Kirkegaard, P., "Finite element modeling of infinite Euler beams on Kelvin foundations exposed to moving loads in convected coordinates", Journal of Sound and Vibration, 241(4), 2001, pp 587-604.

155. Nguyen, V. H. and Duhamel, D., "Finite element procedures for nonlinear structures in moving coordinates Part II: Infinite beam under moving harmonic loads" Computers and Structures, 86, 2008, pp 2056–2063.

156. Belotti, V., Crenna, F., Michelini, R. C., and Rossi, G. B., "Wheel-flat diagnostic tool via wavelet transform" Mechanical Systems and Signal Processing, 20, 2006, pp 1953–1966.

157. Yue, J., Qiu, Z., and Chen, B., "Application of Wavelet Transform to Defect Detection of Wheelflats of Railway wheels" Proceedings of 6th International Conference on Signal Processing, 26-30 August, Beijing, China, 2002.

158. Anderson, D. R., "Detecting flat wheels with a Fiber-optic sensor" Proceedings of Joint Rail Conference, April 4-6, Atlanta, GA, USA, 2006.

159. Ho, T. K., Liu, S. Y., Ho, Y. T., Ho, K. H., Wong, K. K., Lee, K. Y., Tam, H. Y., and Ho, S. L., "Signature Analysis on Wheel-Rail Interaction for Rail Defect Detection" 4th IET International Conference on Railway Condition Monitoring, Derby, UK, 2008

160. Li, P., Fengping, Y., Zhi, W., Zhi, T., and Shuisheng, J., "Application of an Optical Fiber Grating Pressure Sensor on a High-Speed-Train Real-Time Tracing System" Microwave and Optical Technology Letters, 37(2), 2003, pp 148-151.

161. Peter, H., Joe, N., and Tom, S., "Precision Train Inspection Methods – North American Adoption of Global Technology" General Electric Company, 2005.

162. Kenderian, S., Djordjevic, B. B., Cerniglia, D., and Garcia, G., "Dynamic railroad inspection using the laser-air hybrid ultrasonic technique" Insight, 48(6), 2006, pp 336-341.

163. Tittmann, B., Alers, R., and Lerch, R., "Ultrasonics for Locomotive Wheel Integrity" IEEE Ultrasonics Symposium, 22-25 October, San Juan, Puerto Rico, 2000.

164. Pau, M., Leban, B., and Baldi, A., "Simultaneous subsurface defect detection and contact parameter assessment in a wheel–rail system" Wear, 265, 2008, pp 1837–1847.

165. Brizuela, J., Ibanez, A., and Fritsch, C., "NDE system for railway wheel inspection in a standard FPGA" Journal of Systems Architecture, 56, 2010, pp 616–622.

166. Coccia, S., Bartoli, I., Salamone, S., Phillips, R., Scalea, F. L., Fateh, M., and Carr, G., "Noncontact Ultrasonic Guided Wave Detection of Rail Defects" Journal of the Transportation Research Board, 2117, 2009, pp 77-84.

167. Brizuela, J., Ibanez, A., Nevado, P., and Fritsch, C., "Railway Wheels Flat Detector Using Doppler Effect" Physics Procedia, 3, 2010, pp 811-817.

168. Anastasopoulos, A., Bollas, K., Papasalouros, D., and Kourousis, D., "Acoustic Emission on-line Inspection of Rail Wheels" Ewgae, 8-10 September, Vienna, Austira, 2010.

169. Svet, F. A., "Technique for the detection of flat wheels on railroad cars by acoustical measuring means" available at http://www.freepatentsonline.com/4129276.html

170. Madejski, J., "Automatic detection of flats on the rolling stock wheels" Journal of Achievements in Materials and Manufacturing Engineering, 16 (2), 2006, pp 160-163.

171. Skarlatos, D., Karakasis, K., and Trochidis, A., "Railway wheel fault diagnosis using a fuzzy-logic method", Applied Acoustics, 65, 2004, pp 951-966.

172. Bracciali, A., and Cascini, G., "Detection of corrugation and Wheel flats of railway wheels using energy and cepstrum analysis of rail acceleration, Proc. Inst. Mech. Engrs, Part F, Journal of Rail and Rapid Transit, 21, 1997, pp 109-116.

173. Ahlbeck, D. R., and Hadden, J. A., "Measurement and Prediction of Impact Loads from Worn Railroad Wheel and Rail Surface Profiles" Journal of Engineering for Industry, 107(22), 1985, pp 197-205.

174. Kruger, M., Grosse, C.U., and Marron, P.J., "Wireless Structural Health Monitoring Using MEMS" Key Engineering materials, 2005, 293, pp 625-634.

175. Obadat, M., Lee, H.D., Bhatti, M., and Maclean, M., "Full-scale field evaluation of Micro-electromechanical system-based biaxial strain transducer and its application in fatigue analysis" Journal of Aerospace Engineering, 16(3), 2003, pp 100-107.

176. Lynch, J. P., Partridge, A., Law, K. H., Kenny, T. W., Kiremidjian, A. S., and Carryer, E., "Design of Piezoresistive MEMS-based accelerometer for integration with wireless sensing unit for structural monitoring" Journal of Aerospace Engineering, 16(3), 2003, pp 108-114.

177. Fukuta, Y., "Possibility of sensor network applying for railway signal system" 5th International Conference on Networked Sensing Systems, 17-19 June, 2008, pp 170 - 172.

178. Lee, H., Yun, H. B., and Maclean, B., "Development and field testing of a prototype hybrid uniaxial strain transducer" NDT&E International, 35, 2002, pp 125-134.

179. Brown, J. W., and Churchill, R.V., "Complex Variables and Applications", 7th ed., McGraw-Hill Higher Education, Boston, 2004.

180. Rensburg, N. F. J., and Merwe, A. J., "Natural frequencies and modes of a Timoshenko beam" Wave Motion, 44, 2006, pp 58–69.

181. Lin, H. P. and Chang, S. C., "Free vibration analysis of multi-span beams with intermediate flexible constraints" Journal of Sound and Vibration, 281, 2005, pp 55–169

182. Patil, S. P., "Natural Frequencies of a Railroad Track" Journal of Applied Mechanics, 1987, 54 (2), pp 299-305

183. Snyder, T., Stone, D.H., and Kristan, J., "Wheel Flat and Out-of round formation and growth" Proceedings of the 2003 IEEE/ASME Joint Rail Conference April 22-24, 2003 Chicago, Illinois.

184. http://www.memsrus.com/mumps.pdf; accessed on Nov. 2, 2004

185. Stephen D. Senturia, "Microsystem Design", Kluwer Academic Publishers, 2001

186. http://www.ee.ucla.edu/~wu/ee250b/Case%20study-apacitive%20Accelerometer.pdf